National Technical University of Athens
School of Applied Mathematics & Physical Sciences
Department of Physics

PhD Thesis

Study of (n,x) reactions on Ge isotopes

Sotirios Chasapoglou

Advisory Committee:

Kokkoris Michael
Professor, National Technical University of Athens

Diakaki Maria
Asst. Professor, National Technical University of Athens

Lagoyannis Anastasios
Director of Research, NCSR "Demokritos"

Athens 2024

H.F.R.I.
Hellenic Foundation for Research & Innovation

National Technical University of Athens
School of Applied Mathematics & Physical Sciences
Department of Physics

PhD Thesis

Study of (n,x) reactions on Ge isotopes

Sotirios Chasapoglou

Examination Committee:

Kokkoris Michael Professor, National Technical University of Athens

Vlastou Rosa Professor Emeritus, National Technical University of Athens

Lagoyannis Anastasios Director of Research, NCSR "Demokritos"

Diakaki Maria Asst. Professor, National Technical University of Athens

Patronis Nikolaos Professor, University of Ioannina

Stamatopoulos Athanasios Researcher, Los Alamos National Laboratory

Gastis Panagiotis Researcher, Los Alamos National Laboratory

Εθνικό Μετσόβιο Πολυτεχνείο
Σχολή Εφαρμοσμένων Μαθηματικών και Φυσικών Επιστημών
Τομέας Φυσικής

Διδακτορική Διατριβή

Μελέτη αντιδράσεων νετρονίων σε ισότοπα του Ge

Σωτήριος Χασάπογλου

Συμβουλευτική Επιτροπή:

Κόκκορης Μιχαήλ
Καθηγητής, Εθνικό Μετσόβιο Πολυτεχνείο

Διακάκη Μαρία
Επίκουρη Καθηγήτρια, Εθνικό Μετσόβιο Πολυτεχνείο

Λαγογιάννης Αναστάσιος
Διευθυντής Ερευνών, ΕΚΕΦΕ “Δημόκριτος”

Αθήνα 2024

Εθνικό Μετσόβιο Πολυτεχνείο
Σχολή Εφαρμοσμένων Μαθηματικών και Φυσικών Επιστημών
Τομέας Φυσικής

Διδακτορική Διατριβή

Μελέτη αντιδράσεων νετρονίων σε ισότοπα του Ge

Σωτήριος Χασαάπογλου

Εξεταστική Επιτροπή:

Κόκκορης Μιχαήλ Καθηγητής, Εθνικό Μετσόβιο Πολυτεχνείο
Βλαστού Ρόζα Ομότιμη Καθηγήτρια, Εθνικό Μετσόβιο Πολυτεχνείο
Λαγογιάννης Αναστάσιος Διευθυντής Ερευνών, ΕΚΕΦΕ "Δημόκριτος"
Διακάκη Μαρία Επίκουρη Καθηγήτρια, Εθνικό Μετσόβιο Πολυτεχνείο
Πατρώνης Νικόλαος Καθηγητής, Πανεπιστήμιο Ιωαννίνων
Σταματόπουλος Αθανάσιος Ερευνητής, Los Alamos National Laboratory
Γάστης Παναγιώτης Ερευνητής, Los Alamos National Laboratory

ΕΛ.Ι.Δ.Ε.Κ.
Ελληνικό Ίδρυμα Έρευνας & Καινοτομίας

Η ερευνητική εργασία υποστηρίχτηκε από το Ελληνικό Ίδρυμα Έρευνας και Καινοτομίας (ΕΛ.ΙΔ.Ε.Κ.) στο πλαίσιο της «3ης Προκήρυξης ΕΛ.ΙΔ.Ε.Κ. για Υποψήφιους/ες Διδάκτορες» (Αριθμός Υποτροφίας: 5597)

The research work was supported by the Hellenic Foundation for Research and Innovation (HFRI) under the 3rd Call for HFRI PhD Fellowships (Fellowship Number: 5597)

Στους γονείς μου,
Στον παππού μου...

CONTENTS

Acknowledgments

With this long, exciting and fulfilling journey coming to an end, I would like to take this opportunity to express my heartfelt gratitude to all the people involved. Without their support on so many levels, this thesis could not have been completed.

First of all, I would like to thank my supervisors **Michael Kokkoris** and **Rosa Vlastou**. I do not think that words are enough to express my gratitude towards them. As an undergraduate student, I was fascinated by Nuclear Physics, hence I still remember the day when I received the good news from Michael Kokkoris, that I was accepted as a member of the Nuclear Physics group of the National Technical University of Athens (NTUA), for my diploma thesis. This was the start of an exciting and very rewarding journey, that continued with me being an M.Sc. student and finally a Ph.D. candidate, fortunate enough to keep working with some of the most brilliant minds that I have seen in person, during all these years. Their experience, intelligence and passion for science and research, did not just constitute an irreplaceable characteristic for supervisors, but they also set an example for the morals of a scientist and a person in general. Therefore, I consider them my mentors, and I absolutely admire them both as people and as scientists. They have always encouraged me to pursue my ideas, and they were always willing to help me with whatever came up. 'Mike and Rosa, I know that words are not enough, but thank you for trusting me, for making me part of your group. I will forever treasure the time that I was privileged enough to spend with you...' A special thank you is of course reserved for **Maria Diakaki** that I was lucky enough to meet and work with during my Ph.D. candidacy. Her ideas towards the solution of any problem that came up were simply brilliant and extremely accurate every time. It is an undeniable pleasure to work with Maria, as we did during the irradiations performed at the AMANDE facility (France). If it had not been for Maria, this thesis would have been quite different.

A huge amount of gratitude is of course reserved for the staff of the Tan-

dem laboratory of the Institute of Nuclear and Particle Physics of NCSR 'Demokritos'. This thesis would simply not be possible without the help of **Sotirios Harissopulos**, **Tassos Lagoyannis**, **Michael Axiotis** and **Miltos Andrianis**. They were eager to help me with anything that came up during the experimental part of this work, and for this I will be forever grateful. It has been more than a pleasure collaborating with such skilful and intelligent people. 'Thank you so much for all your irreplaceable support!'

It goes without saying that I could not forget to thank from the bottom of my heart **Ion Stamatelatos, Dora Vassilopoulou** and **Marilia Sava** from the Institute of Nuclear & Radiological Sciences & Technology, Energy & Safety of NSCR 'Demokritos', that helped me greatly with my measurements, creating an extremely friendly and inviting work environment.

I would also like to thank **Richard Babut** and **Nelson Magalotti** from the AMANDE facility in France, where I performed some measurements for my Ph.D. I was very lucky to exchange ideas and share a very fruitful collaboration. 'Thank you for the collaboration, the hospitality and for all your help, both before and after our visit in France!'

I would also like to thank **Nikolas Patronis** for his help and the very interesting discussions that we had. His is indeed a brilliant mind and very eager to help with any problem that comes up. I consider myself very lucky to have met him.

Special thanks to **Claudia Lederer-Woods** for providing the enriched targets that was of course one the most important parts of this thesis!

Moreover, I would like to thank **Thanos Stamatopoulos**, **Antigoni Kalamara** and **Veatriki Michalopoulou**, that offered me a tremendous amount of help, willing to answer whatever question I may had, especially during my early years as a Ph.D. candidate. I would also like to thank all the members of the Nuclear Physics Group of NTUA standing as a unit, ready to help at any time, that will be presented in alphabetical order. I personally thank **George Alamanos, Eleni Alvanou, Labros Amanatidis, Natalia Bligoura, Thymios Daoulas, Nikos Dimitrakopoulos, Christoforos Frantzis, George Gkatis, Maria Kagioglou, Kalliopi Kaperoni, Anna Karakaxi, Anastasia Kotsovolou, Rafail Kourgiantakis, Konstantina Krokidi, Nikos Kyritsis, Despoina Lazaraki, Fotis Maragkos, Eleni Mitsi, Zoi Mpari, Eleni Ntemou, Sofia Pantousa, Filothei Pappa, Kostas Preketes, Anna Skouloudaki, Evangelia Taimpiri, Kalliopi Tsampa, Peli Tsintari, Ioannis Tzormpatzoglou and Anastasia Ziagkova**.

I would also like to thank personally all the members of the examination committee for the overall help through the years.

Finally, I would like to thank my parents for all the support through all these years. They were always there for me and I could not be more grateful.

The research work was supported by the Hellenic Foundation for Research and Innovation (HFRI) under the 3rd Call for HFRI PhD Fellowships (Fellowship Number: 5597). The research work was also funded by the

Basic Research Program PEVE 2021 of the National Technical University of Athens. We acknowledge the support of this work by the project CALIBRA/EYIE (MIS 5002799), which is implemented under the Action “Reinforcement of the Research and Innovation Infras- tructures”, funded by the Operational Program “Competitiveness, Entrepreneurship and Innovation” (NSRF 2014–2020) and co-financed by Greece and the European Union (European Regional Development Fund). This project has received funding from the Euratom researcand training programme 2014-2018 under grant agreement No 847594 (ARIEL).

Extended Abstract in Greek

Εισαγωγή

Οι αντιδράσεις νετρονίων σε ισότοπα του Γερμανίου (Ge) είναι πολύ σημαντικές τόσο για πρακτικές εφαρμογές, όσο και για τη θεμελιώδη έρευνα στον Τομέα της Πυρηνικής Φυσικής. Οι πρακτικές εφαρμογές περιλαμβάνουν τη δοσιμετρία, την αστροφυσική, τεχνολογία αντιδραστήρων, την πυρηνική ιατρική καθώς και την ευρεία χρήση του Ge σε ανιχνευτές ακτινοβολίας-γ. Όσον αφορά στη θεμελιώδη έρευνα, κάποιες από τις αντιδράσεις (n,x) σε ισότοπα του Ge, παράγουν πυρήνες σε ισομερείς καταστάσεις υψηλού σπιν. Η αποδιέγερση τέτοιου είδους πυρήνων εξαρτάται σημαντικά από την κατανομή των σπιν στο συνεχή χώρο των φάσεων, καθώς και των αντίστοιχων τιμών σπιν των διακριτών καταστάσεων. Ακριβή πειραματικά δεδομένα ενεργών διατομών (n,x) αντιδράσεων που παράγουν τέτοιου είδους πυρήνες, παίζουν σημαντικό ρόλο στη μελέτη του παραγόμενου σύνθετου πυρήνα. Μια πληθώρα καναλιών αντίδρασης είναι διαθέσιμα προς μελέτη από τα πέντε σταθερά ισότοπα του Ge (^{70,72,73,74,76}Ge), αποκαλύπτοντας ιδιαίτερα ενδιαφέρουσες συστηματικές, σημαντικές για τη βελτιστοποίηση υπολογισμών στατιστικών μοντέλων. Η ταυτόχρονη αναπαραγωγή όλων των πειραματικά μετρούμενων καναλιών αντίδρασης, χρησιμοποιώντας το ίδιο σύνολο παραμέτρων εισόδου, μπορεί να δράσει ως ένα πολύ ισχυρός περιορισμός σε υπολογισμούς στατιστικών μοντέλων. Επιπροσθέτως, ακριβή δεδομένα ενεργών διατομών σε ενέργειες νετρονίων μεγαλύτερες από τα 15 MeV, είναι πολύ σημαντικές, εφόσον σε αυτή την ενεργειακή περιοχή, η συνεισφορά φαινομένων προ-ισορροπίας στην αποδιέγερση του σύνθετου πυρήνα, γίνεται σημαντική.

Τα περισσότερα από τα υπάρχοντα δεδομένα ενεργών διατομών για αντιδράσεις (n,x) σε ισότοπα του Ge που βρίσκονται στη βιβλιογραφία, έχουν μετρηθεί με χρήση φυσικών στόχων Γερμανίου (^{nat}Ge) και είναι περιορισμένα σε ενέργειες κάτω από 15 MeV, με μεγάλες αποκλίσεις μεταξύ τους. Πρέπει επίσης να υπογραμμιστεί ότι αντίστοιχες αποκλίσεις παρατηρούνται μεταξύ

των υπαρχόντων βιβλιοθηκών αξιολόγησης, οι οποίες γίνονται σημαντικές σε μεγαλύτερες ενέργειες.

Βάσει των παραπάνω, στην παρούσα εργασία, οι αντιδράσεις ^{70}Ge(n,2n)^{69}Ge, ^{72}Ge(n,p)^{72}Ga, ^{72}Ge(n,α)^{69m}Zn, ^{73}Ge(n,p)^{73}Ga, ^{73}Ge(n,np/d)^{72}Ga, ^{73}Ge(n,nα)^{69m}Zn, ^{74}Ge(n,α)^{71m}Zn, ^{74}Ge(n,np/d)^{73}Ga και ^{76}Ge(n,2n)^{75}Ge μελετήθηκαν στο ενεργειακό εύρος 14.0 - 18.9 MeV.

Οι ενεργές διατομές μετρήθηκαν πειραματικά βάσει της μεθόδου της νετρονικής ενεργοποίησης, αξιοποιώντας πέντε ισοτοπικά εμπλουτισμένους στόχους, τους οποίους παρείχε το n_TOF collaboration (CERN). Οι ακτινοβολήσεις έλαβαν χώρα στις νετρονικές εγκαταστάσεις:

- Του επιταχυντή 5.5 MV Tandem Van de Graaff του ΕΚΕΦΕ “Δημόκριτος” (Αθήνα, Ελλάδα).
- Του επιταχυντή 2 MV Tandetron στην εγκατάσταση ”AMANDE”, IRSN (Γαλλία).

Οι παραγωγή των οιονεί-μονοενεργειακών δεσμών νετρονίων βασίστηκε στην αντίδραση ^{3}H(d,n)^{4}He (D-T) και στις δύο νετρονικές εγκαταστάσεις, ενώ η απαραίτητη νετρονική ροή προσδιορίσθηκε μέσω της αντίδρασης αναφοράς ^{27}Al(n,α)^{24}Na. Η ραδιενέργεια που προκλήθηκε στους στόχους Ge καθώς και στα φύλλα αναφοράς Al, μετρήθηκε μέσω φασματοσκοπίς-γ, αξιοποιώντας ανιχνευτές HPGe. Έγινε επίσης συνδυαστική χρήση των κωδίκων NeuSDesc και MCNP5 για την προσομοίωση της διάδοσης της νετρονικής δέσμης, στους στόχους Ge και στα φύλλα αναφοράς.

Τέλος, ακολούθησε μια θεωρητική μελέτη των 9 αντιδράσεων που αναφέρθηκαν παραπάνω μέσω υπολογισμών Hauser-Feshbach μέσω του κώδικα EMPIRE 3.2.3 [1].

Η Μέθοδος της Νετρονικής Ενεργοποίησης

Στα πλαίσια αυτής της διδακτορικής διατριβής, οι ενεργές διατομές των αντιδράσεων ^{70}Ge(n,2n)^{69}Ge, ^{72}Ge(n,p)^{72}Ga, ^{72}Ge(n,α)^{69m}Zn, ^{73}Ge(n,p)^{73}Ga, ^{73}Ge(n,np/d)^{72}Ga, ^{73}Ge(n,nα)^{69m}Zn, ^{74}Ge(n,α)^{71m}Zn, ^{74}Ge(n,np/d)^{73}Ga και ^{76}Ge(n,2n)^{75}Ge μελετήθηκαν στο ενεργειακό εύρος 14.0 - 18.9 MeV μέσω της μεθόδου της νετρονικής ενεργοποίησης.

Η μέθοδος αυτή βασίζεται στη μέτρηση της ακτιβολίας-γ πυρήνων που έχουν παραχθεί, μετά από την ακτινοβόληση ενός πυρήνα στόχου. Όταν μια νετρονική δέσμη προσπίπτει σε έναν πυρήνα-στόχο, παράγεται ο αντίστοιχος σύνθετος πυρήνας, ο οποίος μπορεί να αποδιεγερθεί μέσω ενός συνόλου καναλιών εξόδου. Τα δύνατα προς μελέτη κανάλια με τη μέθοδο της νετρονικής ενεργοποίησης είναι αυτά που οδηγούν στην παραγωγή ραδιενεργών πυρήνων με κατάλληλο χρόνο ημιζωής, ακτίνες-γ κατάλληλης ενέργειας και έντασης.

Πειραματικές Λεπτομέρειες

Οι μετρήσεις πραγματοποιήθηκαν στις νετρονικές εγκαταστάσεις:

- Του επιταχυντή 5.5 MV Tandem Van de Graaff του ΕΚΕΦΕ “Δημόκριτος” (Αθήνα, Ελλάδα).
- Του επιταχυντή 2 MV Tandetron στην εγκατάσταση ”AMANDE”, IRSN (Γαλλία).

Η παραγωγή των νετρονικών δεσμών στο ενεργειακό εύρος 14.0 - 18.9 MeV έγινε μέσω της αντίδρασης ^{3}H(d,n)^{4}He (D-T) και στις δύο νετρονικές εγκαταστάσεις.

Η εγκατάσταση “AMANDE”

Η παραγωγγή της νετρονικής δέσμης σε αυτή την περίπτωση έγινε μέσω της αντίδρασης D-T, με δέσμη δευτερίων 443 keV η οποία επιταχύνεται μέσω του επιταχυντή 2 MV Tandetron (Σχήμα 3.1), φτάνοντας στον πειραματικό χώρο των ακτινοβολήσεων (Σχήμα 2) μέσω μιας γραμμής μεταφοράς στο τέλος της οποίας είναι τοποθετημένος ο στόχος παραγωγής νετρονίων TiT. Ο στόχος αυτός ήταν τοποθετημένος σε μια κινούμενη βάση, η οποία σε συνδυασμό με συνεχή παροχή αέρα κατά τη διάρκεια των ακτινοβολήσεων με σκοπό την αποφυγή θερμικής καταστροφής του στόχου. Η παρακολούθηση πιθανών μεταβολών της νετρονικής δέσμης κατά τη διάρκεια των ακτινοβολήσεων έγινε μέσω ενός αέριου ανιχνευτή ^{3}He. Το σύνολο των στόχων Ge και φύλλων αναφοράς, τοποθετήθηκαν σε γωνία 100° σε σχέση με τον άξονα της νετρονικής δέσμης ώστε να επιτευχθεί τελική ενέργεια νετρονίων 14.0 MeV (Σχήμα 3).

Σχήμα 1: Ο επιταχυντής 2 MV Tandetron™ της εγκατάστασης “AMANDE”

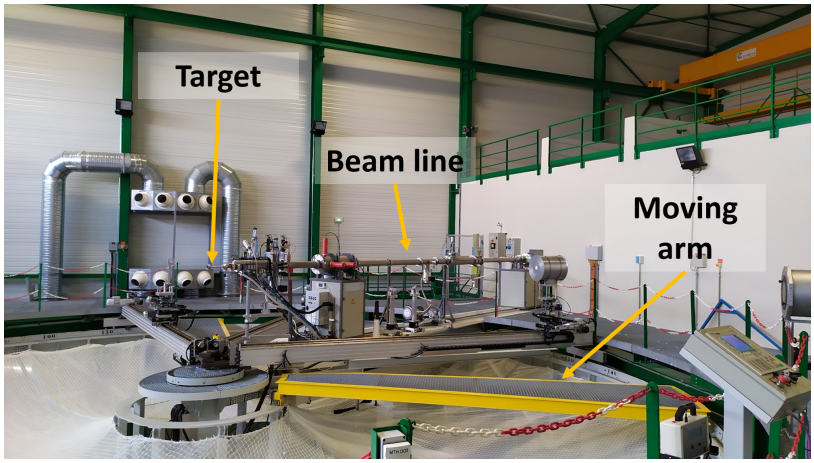

Σχήμα 2: Ο πειραματικός χώρος ακτινοβολήσεων της εγκατάστασης "AMANDE"

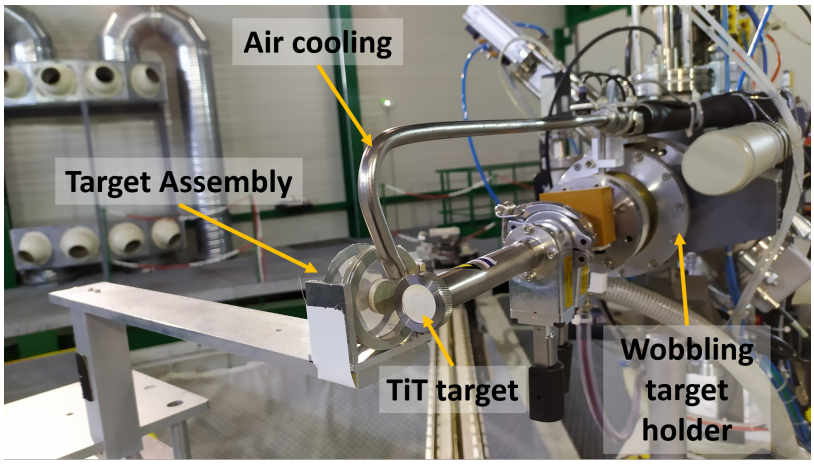

Σχήμα 3: Το τέλος της πειραματικής γραμμής της εγκατάστασης "AMANDE" με τον στόχο TiT και το σύνολο των στόχων Ge και φύλλων αναφοράς τοποθετημένων σε γωνία 100° σε σχέση με τον άξονα της νετρονικής δέσμης.

Η νετρονική εγκατάσταση του ΕΚΕΦΕ "Δημόκριτος"

Σχήμα 4: Ο επιταχυντής 5.5 MV Van de Graaff του ΕΚΕΦΕ "Δημόκριτος"

Η παραγωγή των νετρονικών δεσμών σε αυτή την περίπτωση έγινε και πάλι με δέσμες δευτερίων στο ενεργειακό εύρος 1.8 - 2.8 MeV οι οποίες επιταχύνονται

μέσω του επιταχυντή 5.5 MV Tandem Van de Graaff (Σχήμα 4). Μέσω μιας γραμμής μεταφοράς φτάνουν στον πειραματικό χώρο ακτινοβολήσεων (Σχήμα 5), στο τέλος της οποίας είναι τοποθετημένος ο στόχος παραγωγής νετρονίων TiT (Σχήμα 6). Ο στόχος αυτός ψύχεται κατά τη διάρκεια των ακτινοβολήσεων είτε με αέρα είτε με νερό, ανάλογα με το ρεύμα της δέσμης δευτερίων που προσπίπτουν σε αυτόν. Πιθανές μεταβολές στη νετρονική ροή κατά τη διάρκεια των ακτινοβολήσεων παρακολουθούνται με ανιχνευτή BF_3. Το σύνολο των στόχων Ge και φύλλων αναφοράς τοποθετούνται σε γωνία 0° σε σχέση με τον άξονα των νετρονικών δεσμών, οι οποίες αντιστοιχούν στο ενεργειακό εύρος 15.7 - 18.9 MeV.

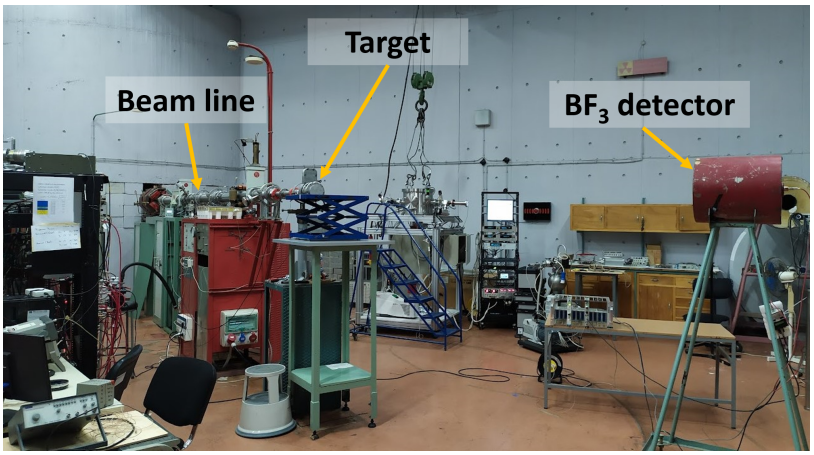

Σχήμα 5: Ο πειραματικός χώρος ακτινοβολήσεων του ΕΚΕΦΕ “Δημόκριτος”

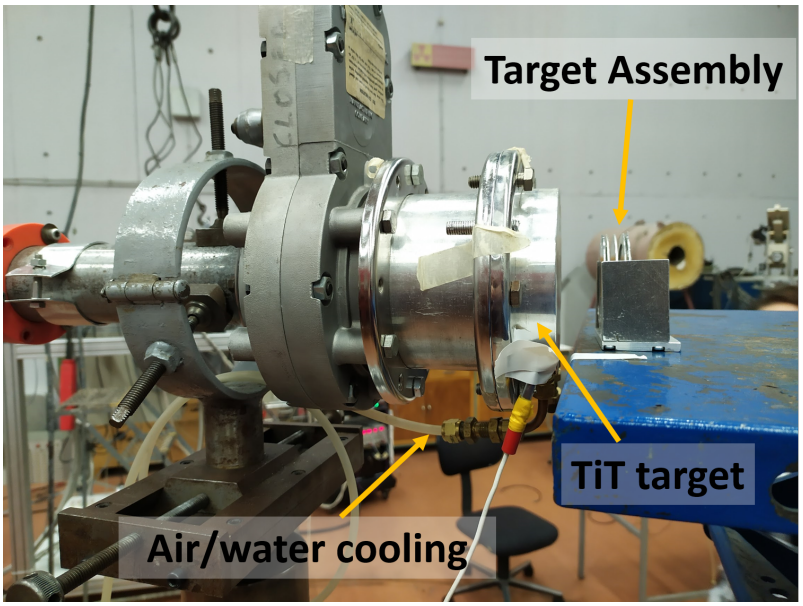

Σχήμα 6: Το τέλος της πειραματικής γραμμής με τον στόχο παραγωγής νετρονίων TiT και το σύνολο των στόχων Ge και φύλλων αναφοράς Al τοποθετημένα σε γωνία 0° σε σχέση με τον άξονα της νετρονικής δέσμης

Στόχοι

Οι ισοτοπικά εμπλουτισμένοι στόχοι που χρησιμοποιήθηκαν για τις μετρήσεις των ενεργών διατομών της παρούσας διατριβής ήταν παστίλιες GeO_2 μάζας ∼2 g η κάθε μια, τις οποίες παρείχε το n_TOF collaboration (CERN). Τα ποσοστά εμπλουτισμού των στόχων παρουσιάζονται στον Πίνακα 1. Για λόγους σύγκρισης, αναφέρεται ότι η φυσική ισοτοπική αναλογία των ισοτόπων ^{70,72,73,74,76}Ge είναι 27.45, 7.76, 36.52 and 7.75 %, αντίστοιχα. Οι στόχοι αυτοί είχαν διάμετρο 20 mm και πάχη μεταξύ ∼2.7 και 3.4 mm. Οι στόχοι ήταν κολλημένοι σε ένα λεπτό φύλο mylar το οποίο με τη σειρά του ήταν κολλημένο σε ένα δαχτυλίδι όπως φαίνεται στο Σχήμα 7.

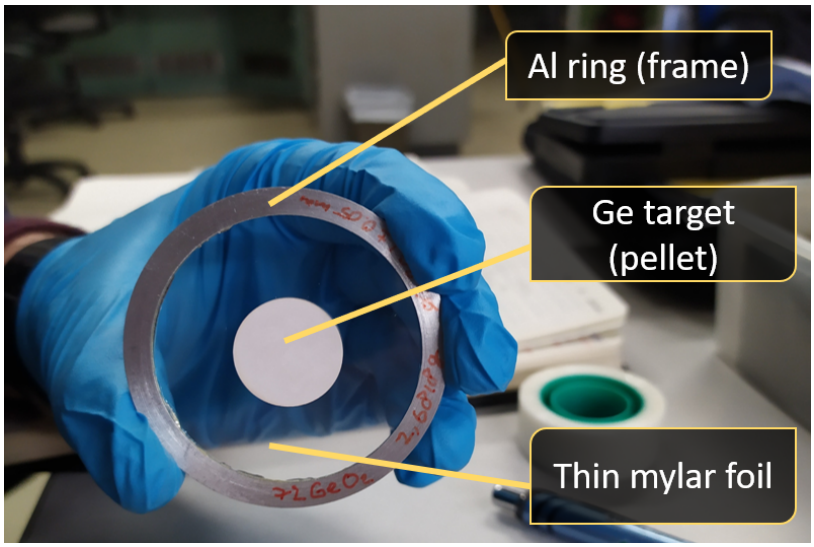

Σχήμα 7: Στόχος GeO_2

Πίνακας 1: Ποσοστά εμπλουτισμού των στόχων GeO_2

Στόχος/ Ισοτοπική αναλογία (%)	^{70}Ge	^{72}Ge	^{73}Ge	^{74}Ge	^{76}Ge
^{70}Ge	97.71	2.23	0.02	0.03	0.01
^{72}Ge	0.35	96.59	2.86	0.20	0.01
^{73}Ge	0.04	2.84	96.07	1.03	0.02
^{74}Ge	1.46	0.18	0.45	95.51	2.40
^{76}Ge	0.06	0.09	0.06	11.33	88.46

Ως στόχοι αναφοράς χρησιμοποιήθηκαν λεπτά μεταλλικά φύλλα Al και Au υψηλής καθαρότητας διαμέτρου ίδιας με αυτή των στόχων Ge. Σημειώνεται ότι κατά τη διάρκεια των ακτινοβολήσεων, οι στόχοι Ge τοποθετούνταν μεταξύ δύο φύλλων αναφοράς.

Τόσο οι στόχοι Ge, όσο και τα μεταλλικά φύλλα αναφοράς τοποθετήθηκαν σε ειδικά σχεδιασμένη θήκη όπως φαίνεται στο σχήμα

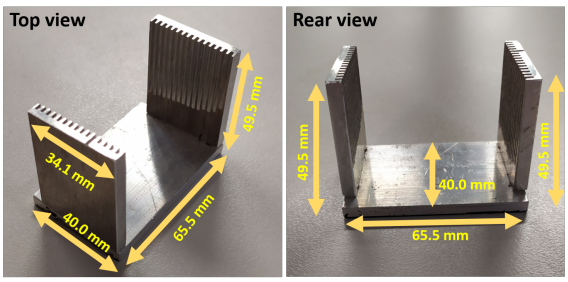

(α΄) Πάνω και πλάγια όψη της θήκης στην οποία τοποθετήθηκαν οι στόχοι Ge και τα φύλλα αναφοράς.

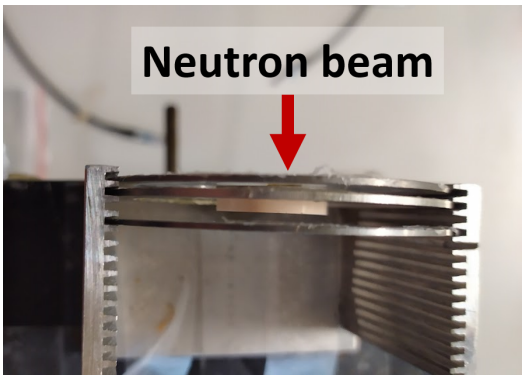

(β΄) Η θήκη των στόχων (όπως φαίνεται από πάνω) με τον στόχο Ge να είναι τοποθετημένος μεταξύ δύο φύλλων Al σε προκαθορισμένες θέσεις

Σχήμα 8: Η θήκη των στόχων που χρησιμοποιήθηκε για την ακτινοβόληση των δειγμάτων.

Ακτινοβολήσεις

Συνολικά πέντε σειρές ακτινοβολήσεων έλαβαν χώρα, κάθε μια από τις οποίες αντιστοιχούσε σε διαφορετική ενέργεια νετρονίων και είχε διάρκεια μιας εβδομάδας. Στον πίνακα 2 παρουσιάζονται κάποιες λεπτομέρειες των ακτινοβολήσεων όπως η ημερομηνία διεξαγωγής τους, η νετρονική εγκατάσταση στην οποία έλαβαν χώρα, η διάρκειά τους, το ρεύμα της ιοντικής δέσμης καθώς και η ενέργεια της δέσμης δευτερίων και της αντίστοιχης παραγόμενης νετρονικής δέσμης. Ο πρώτος στόχος σε κάθε ακτινοβόληση ήταν τοποθετημένος σε απόσταση από 2.5 έως 3.5 cm ωστε να επιτυγχάνεται γωνιακή αποδοχή της τάξης των 20°στην οποία η δέσμη θεωρείται σχεδόν μονοενεργειακή.

Πίνακας 2: Πειραματικές Λεπτομέρειες των Ακτινοβολήσεων

Ημερομηνία	Εγκατάσταση	E_d (MeV)	E_n (MeV)	I (μA)	t_{irr} (h)
Φεβ 2020	ΕΚΕΦΕ ”Δ”	2.90	17.9 ± 0.3	$0.4 - 0.6$	$5 - 25$
Μαϊος 2021	ΕΚΕΦΕ ”Δ”	3.45	18.9 ± 0.3	$0.2 - 0.7$	$3 - 28$
Δεκ 2021	ΕΚΕΦΕ ”Δ”	2.25	16.4 ± 0.4	$0.2 - 0.4$	$7 - 27$
Ιαν 2023	ΕΚΕΦΕ ”Δ”	2.09	15.7 ± 0.5	$2.0 - 3.0$	$5 - 7$
Φεβ 2023	“AMANDE”	0.44	14.0 ± 0.3	$2.0 - 3.0$	$2 - 5$

Ενέργεια Νετρονίων και Προσομοιώσεις Monte Carlo

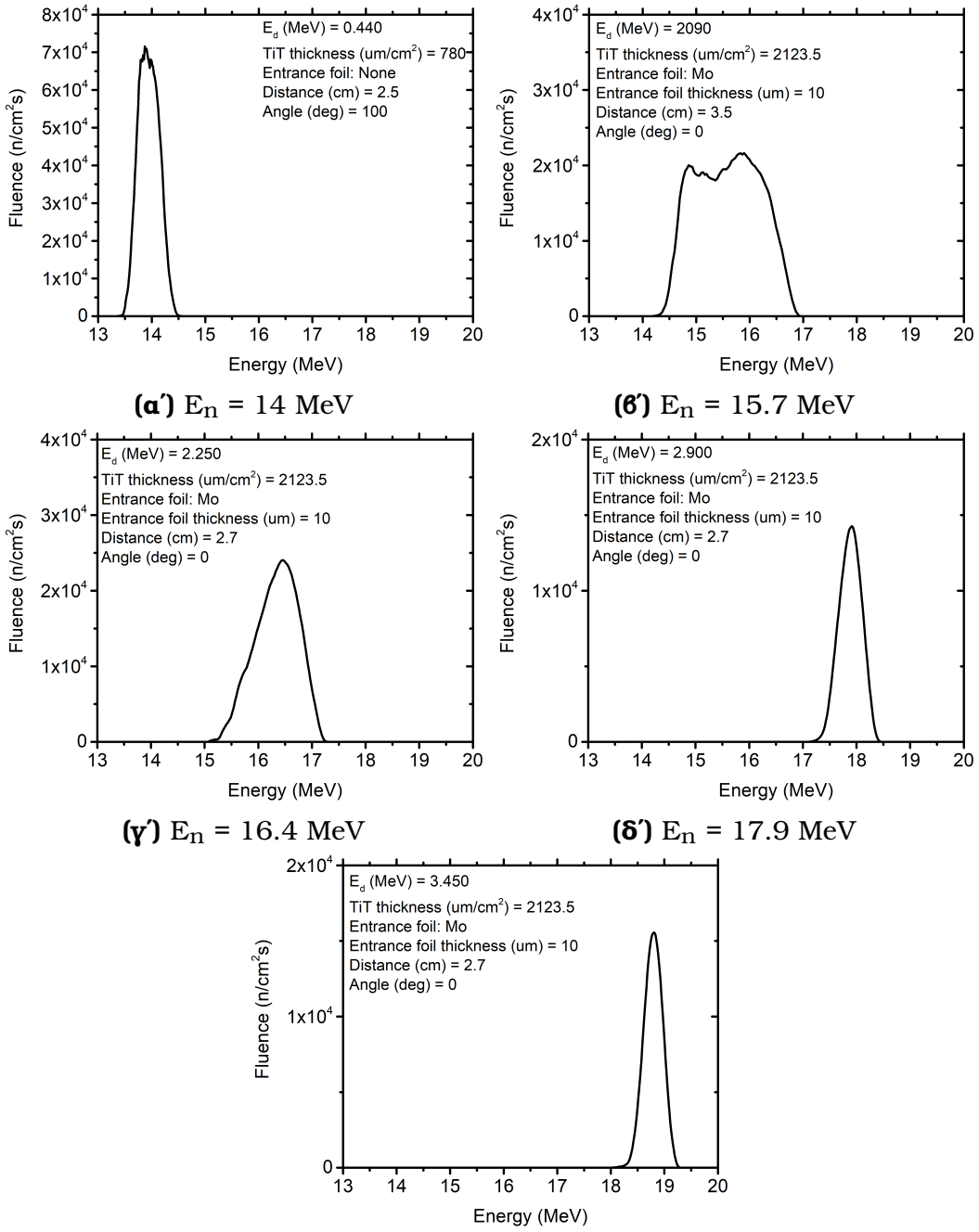

Σχήμα 9: Τα φάσματα των δεσμών νετρονίων όπως αυτά προκύπτουν από τον κώδικα NeuSDesc, λαμβάνοντας υπόψιν τα διαφορετικά χαρακτηριστικά των στόχων παραγωγής νετρονίων για κάθε περίπτωση, όπως το πάχος του στόχου TiT, το πάχος του φύλλου εισόδου καθώς και την απόσταση από τον πρώτο στόχο, όπως επίσης και τη γωνία ανίχνευσης. Για όλες τις περιπτώσεις, το ρεύμα της δέσμης δευτερίων τέθηκε στο 1 μA, ενώ η ακτίνα του ανιχνευτή στο 1 cm.

Η αναπαραγωγή του φάσματος των νετρονίων, με σκοπό τον προδιορισμό της κεντρικής τιμής της ενέργειας των νετρονίων και της αντίστοιχης αβεβαιότητας έγινε μέσω της συνδυαστικής χρήσης των κωδίκων NeuSDesc [2, 3] και MCNP5 [4]. Ο κώδικας NeuSDesc λαμβάνει υπόψιν τη χωρική και ενεργειακή διασπορά της δέσμης δευτερίων μέσω του κώδικα SRIM 2008 [5], και είναι υπεύθυνος για την παραγωγή της πηγής των νετρονίων ως SDEF κάρτας, η οποία στη συνέχεια εισάγεται στον κώδικα MCNP, στον οποίο έχει γίνει ακριβής περιγραφή της πειραματικής διάταξης. Τα αποτελέσματα προσομοίωσης των νετρονικών δεσμών από τον κώδικα NeuSDesc παρουσιάζονται στο Σχήμα 9.

Η νετρονική δέσμη μεταδίδεται μέσω του κώδικα MCNP5 και υπολογίζεται η αντίστοιχη μέση ροή (f4 tally) σε κάθε στόχο Ge και φύλλο αναφοράς. Το αποτέλεσμα αυτού του υπολογισμού φαίνεται στο Σχήμα 10α΄. Η κορυφή που αντιστοιχεί στην κύρια ενέργεια νετρονίων συνοδεύεται από μια χαμηλοενεργειακή παρασιτική ουρά νετρονίων, η οποία οφείλεται σε σκεδάσεις νετρονίων, όπως επίσης και σε αντιδράσεις της δέσμης των δευτερίων με τα υλικά της γραμμής μεταφοράς και του στόχου παραγωγής νετρονίων [6]. Στην κορυφή αυτή προσαρμόζεται μια γκαουσιανή καμπύλη (Σχήμα 10β΄), μέσω των παραμέτρων της οποίας προσδιορίζεται η κεντρική τιμή της ενέργειας των νετρονίων (x_c) και η αντίστοιχη αβεβαιότητα (σ). Ειδικά για την περίπτωση των 15.7 MeV, λόγω απόκλισης από τη γκαουσιανή μορφή, τα αντίστοιχα μεγέθη υπολογίστηκαν βάσει των σχέσεων (4.21) και (4.22) (Αναφορά [7]) για το σταθμισμένο μέσο όρο και την αντίστοιχη διασπορά.

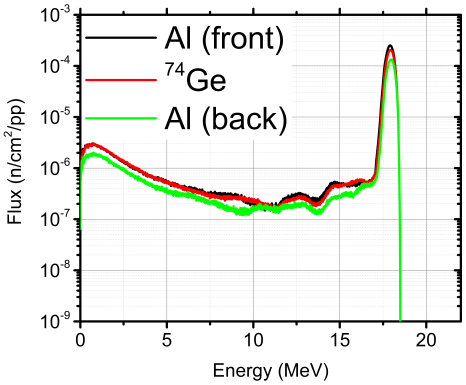

(α΄) Ο υπολογισμός της μέσης ροής νετρονίων από τον κώδικα MCNP5.

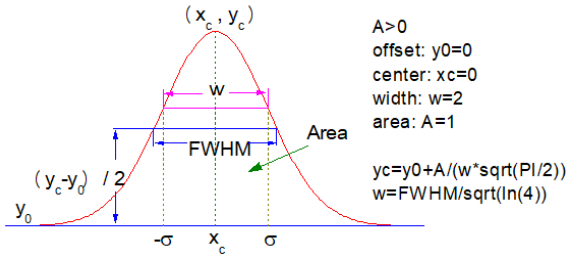

(β΄) Η γκαουσιανή καμπύλη προσαρμογής

Σχήμα 10: 10α΄: Μια τυπική μορφή νετρονικής ροής (f4 tally) ως αποτέλεσμα προσομοίωσης MCNP5, για τα δύο φύλλα αναφοράς Al και για τον στόχο ^{74}Ge. Το σχήμα αναφέρεται σε ενέργεια νετρονικής δέσμης E_n = 17.9 MeV
10β΄: Η γκαουσιανή καμπύλη προσαρμογής που χρησιμοποιείται για τον προσδιορισμό της μέσης ενέργειας νετρονίων και της αντίστοιχης αβεβαιότητας.

Οι εκτενείς αυτές προσομοιώσεις Monte Carlo χρησιμοποιούνται επίσης και για τον προσδιορισμό του λόγου των ροών μεταξύ του φύλου αναφοράς και του προς μέτρηση στόχου (Φ_r/Φ_m). Τα αποτελέσματα των ροών που προκύπτουν από τις προσομοιώσεις αυτές, συγκρίνονται με τις αντίστοιχες πειραματικές τιμές όλων των διαθέσιμων φύλλων αναφοράς, όπως φαίνεται στο Σχήμα 11. Εφόσον η συμφωνία είναι καλή εντός των ορίων των αβεβαιοτήτων των μετρήσεων, οι προσομοιώσεις θεωρούνται αξιόπιστες και μπορούν να χρησιμοποιηθούν για τον προσδιορισμό της νετρονικής ροής στον προς μέτρηση στόχο.

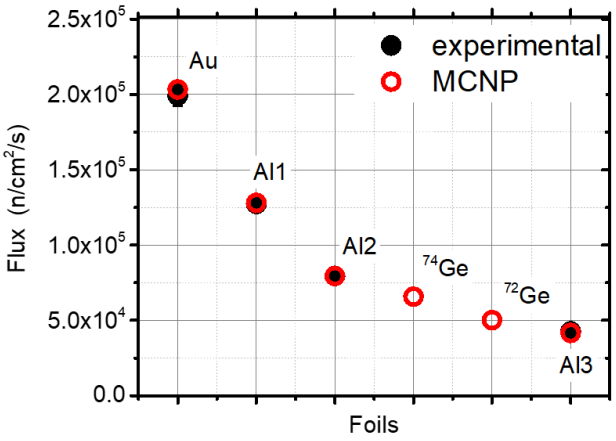

Σχήμα 11: Ένα τυπικό παράδειγμα σύγκρισης τιμών ροής στις θέσεις των φύλλων αναφοράς όπως αυτές προκύπτουν μετά από προσομοίωση και μετά από πειραματική μέτρηση. Το συγκεκριμένο παράδειγμα αναφέρεται στην ακτινοβόληση των στόχων ^{72,74}Ge για ενέργεια νετρονίων E_n = 16.4 MeV

Μετρήσεις σε Ανιχνευτές HPGe

Μετά το πέρας των ακτινοβολήσεων η ενεργότητα των στόχων Ge και των φύλλων αναφοράς μετρήθηκαν με ανιχνευτές Γερμανίου υψηλής καθαρότητας (HPGe) σχετικής ανιχνευτικής απόδοσης από 13 έως 80%. Οι μετρήσεις έγιναν σε απόσταση 7-10 cm από το παράθυρο του ανιχνευτή ώστε να μειωθεί σημαντικά η συνεισφορά φαινομένων συσσώρευσης (pile-up) και άθροισης (summing) παλμών. Στις ίδιες αποστάσεις τοποθετήθηκαν πηγές ^{152}Eu για τον πειραματικό προσδιορισμό της απόδοσης του ανιχνευτή συναρτήσει της ενέργειας. Στο Σχήμα 12 παρουσιάζεται ο ανιχνευτής σχετικής ανιχνευτικής απόδοσης 13% που χρησιμοποιήθηκε στη νετρονική εγκατάσταση “AMANDE”, ενώ στο σχήμα 13 παρουσιάζεται το αντίστοιχο διάγραμμα απόδοσης συναρτήσει των ενεργειών ακτίνων-γ.

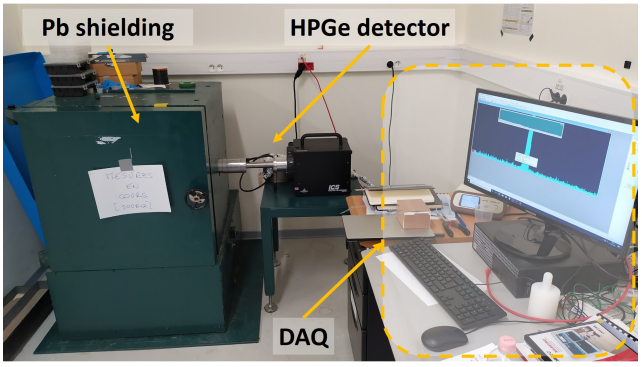

(α′) Ο ανιχνευτής Γερμανίου σχετικής ανιχνευτικής απόδοσης 13% που χρησιμοποιήθηκε στη νετρονική εγκατάσταση "AMANDE". Ο ανιχνευτής αυτός ήταν κατάλληλα θωρακισμένος με Μόλυβδο, ώστε να μειωθεί η συνεισφορά του φυσικού υποβάθρου ακτινοβολίας-γ στις μετρήσεις.

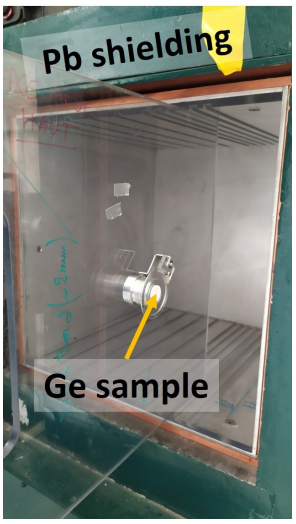

(β′) Η τοποθέτηση ενός δείγματος Ge προς μέτρηση στον ανιχνευτή Γερμανίου της νετρονικής εγκατάστασης "AMANDE".

Σχήμα 12: Ο ανιχνευτής Γερμανίου σχετικής ανιχνευτικής απόδοσης 13% που χρησιμοποιήθηκε στη νετρονική εγκατάσταση "AMANDE"

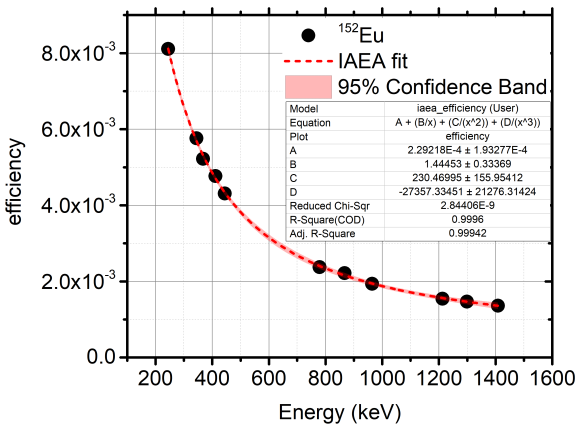

Σχήμα 13: Η απόλυτη απόδοση του ανιχνευτή Γερμανίου σχετικής ανιχνευτικής απόδοσης 13% συναρτήσει της ενέργειας ακτίνων-γ. Τα μαύρα σημεία αντιπροσωπεύουν τις πειραματικές τιμές της απόδοσης του ανιχνευτή βάσει της πηγής ^{152}Eu, τοποθετημένη σε απόσταση 10 cm από το παράθυρο του ανιχνευτή. Η κόκκινη διακεκομμένη γραμμή αναπαριστά την προσαρμογή των σημείων αυτών με την προτεινόμενη από την IAEA συνάρτηση [8], ενώ η γραμμοσκιασμένη περιοχή αναπαριστά τα διαστήματα εμπιστοσύνης εντός 95%.

Μετρούμενες Αντιδράσεις και Πειραματικά Φάσματα

Πίνακας 3: Δεδομένα αποδιέγερσης για τις αντιδράσεις μέτρησης και αναφοράς (^{24}Al(n,α)^{24}Na, ^{197}Au(n,2n)^{196}Au). Οι πιο εντατικές ακτίνες-γ που παρατηρήθηκαν στα πειραματικά φάσματα παρουσιάζονται με τις αντίστοιχες εντάσεις τους.
†: Οι αντιδράσεις (n,np) and (n,d) παράγουν τον ίδιο θυγατρικό πυρήνα και επομένως δεν μπορούν να διαχωριστούν με τη μέθοδο της νετρονικής ενεργοποίησης.

Στόχος	Αντίδραση	Παραγ. Πυρήνας	$t_{1/2}$ (h)	E_γ (keV)	I_γ (%)	Αναφ.
^{70}Ge	(n,2n)	^{69}Ge	39.1	1106.77	36.0 ± 4	[9]
				574.11	13.3 ± 1.8	[9]
				871.98	11.9 ± 1.6	[9]
				1336.60	4.5 ± 0.6	[9]
				318.63	1.6 ± 0.20	[9]
^{72}Ge	(n,p)	^{72}Ga	14.1	834.13	95.45 ± 0.08	[10]
				629.97	26.13 ± 0.04	[10]
				894.33	10.136 ± 0.015	[10]
	(n,α)	^{69m}Zn	13.8	438.63	94.85 ± 0.07	[9]
^{73}Ge	(n,p)	^{73}Ga	4.9	297.32	79.8 ± 1.0	[11]
				325.70	11.2 ± 0.4	[11]
				739.42	4.3 ± 0.3	[11]
	(n,np/d)†	^{72}Ga	14.1	834.13	95.45 ± 0.08	[10]
				629.97	26.13 ± 0.04	[10]
				894.33	10.136 ± 0.015	[10]
	(n,nα)	^{69m}Zn	13.8	438.63	94.85 ± 0.07	[9]
^{74}Ge	(n,α)	^{71m}Zn	4.0	386.28	89.0 ± 1.1	[12]
				487.34	61.9 ± 0.4	[12]
				620.19	54.5 ± 0.7	[12]
	(n,np/d)†	^{73}Ga	4.9	297.32	79.8 ± 1.0	[11]
				325.70	11.2 ± 0.4	[11]
				739.42	4.3 ± 0.3	[11]
^{76}Ge	(n,2n)	^{75}Ge	1.4	264.60	11.4 ± 1.1	[13]
				198.60	1.19 ± 0.12	[13]
^{27}Al	(n,α)	^{24}Na	15.0	1368.63	99.994 ± 0.002	[14]
^{197}Au	(n,2n)	^{196}Au	148.1	355.73	87 ± 3	[15]
				333.03	22.9 ± 0.9	[15]

Στην παρούσα διατριβή μετρήθηκαν οι αντιδράσεις ^{70}Ge(n,2n)^{69}Ge, ^{72}Ge(n,p)^{72}Ga, ^{72}Ge(n,α)^{69m}Zn, ^{73}Ge(n,p)^{73}Ga, ^{73}Ge(n,np/d)^{72}Ga,

^{73}Ge(n,nα)^{69m}Zn, ^{74}Ge(n,α)^{71m}Zn, ^{74}Ge(n,np/d)^{73}Ga και ^{76}Ge(n,2n)^{75}Ge μέσω της μεθόδου της νετρονικής ενεργοποίησης σε σχέση με αντιδράσεις αναφοράς. Τα δεδομένα αποδιέγερσής τους παρουσιάζονται στον Πίνακα 3. Σημειώνεται επίσης πως η συγκεκριμένη μέθοδος βασίζεται στη μέτρηση της ακτινοβολίας που παράγει ο θυγατρικός πυρήνας. Στις αντιδράσεις (n,np) και (n,d) παράγεται ο ίδιος πυρήνας και επομένως τα δύο αυτά κανάλια δεν μπορούν να ξεχωρίσουν μέσω της συγκεκριμένης μεθόδου. Για τον λόγο αυτό, τα κανάλια αυτά μετρούνται αθροιστικά.

Τυπικά φάσματα ακτίνων-γ μετά το πέρας της ακτινοβόλησης ενέργειας νετρονίων 14.0 MeV παρουσιάζονται στα Σχήματα 14 έως 18 κανονικοποιημένα στο χρόνο λήψης αυτών.

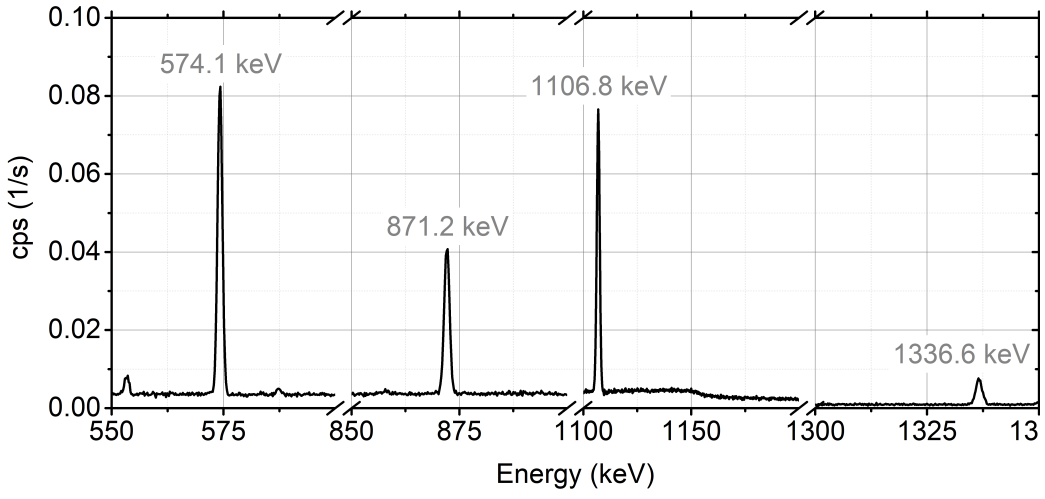

Σχήμα 14: Φάσμα ακτίνων-γ για τον στόχο ^{70}Ge μετά από ακτινοβόληση σε ενέργεια νετρονίων 14.0 MeV. Παρουσιάζονται οι ακτίνες-γ που εκπέμπονται από τον θυγατρικό πυρήνα ^{69}Ge ακολουθώντας την αντίδραση ^{70}Ge(n,2n)^{69}Ge.

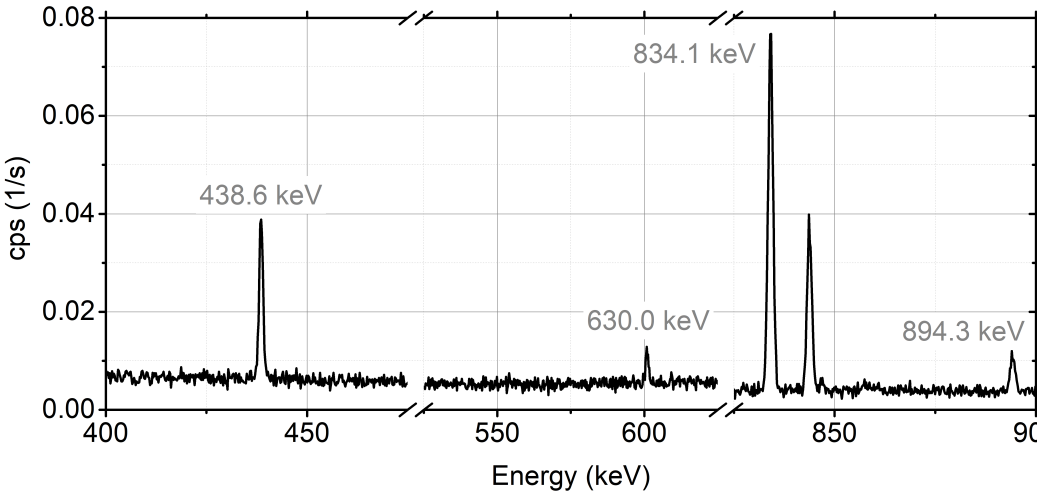

Σχήμα 15: Φάσμα ακτίνων-γ για τον στόχο ^{72}Ge μετά από ακτινοβόληση σε ενέργεια νετρονίων 14.0 MeV. Ακτίνες-γ από δύο διαφορετικές αντιδράσεις παρατηρούνται σε αυτό το φάσμα:
^{72}Ge(n,p)^{72}Ga: 630.0, 834.1 και 894.3 keV
^{72}Ge(n,α)^{69m}Zn: 438.6 keV

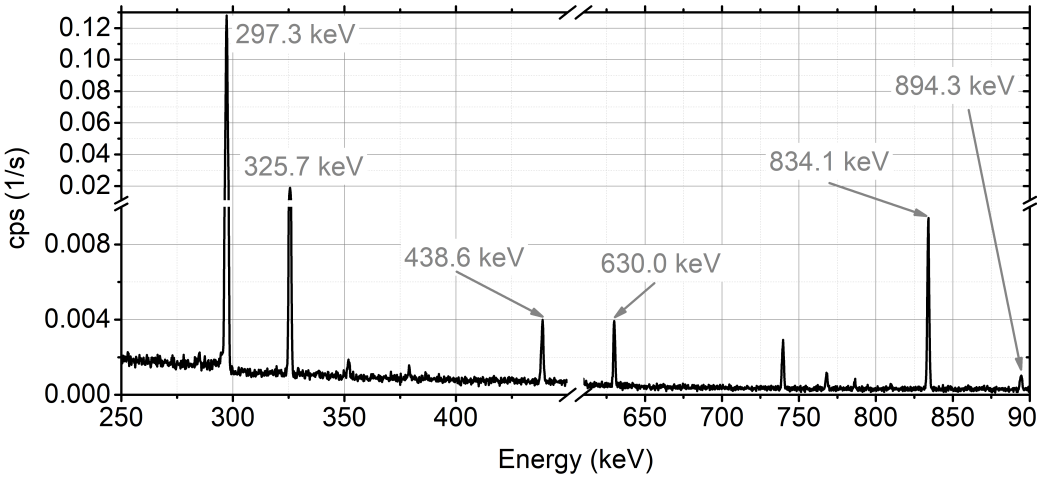

Σχήμα 16: Φάσμα ακτίνων-γ για τον στόχο ^{73}Ge μετά από ακτινοβόληση σε ενέργεια νετρονίων 14.0 MeV. Ακτίνες-γ από τρεις διαφορετικές αντιδράσεις παρατηρούνται σε αυτό το φάσμα: ^{73}Ge(n,p)^{73}Ga: 297.3 και 325.7 keV
^{73}Ge(n,np/d)^{72}Ga: 630.0, 834.1 και 894.3 keV
^{73}Ge(n,nα)^{69m}Zn: 438.6 keV

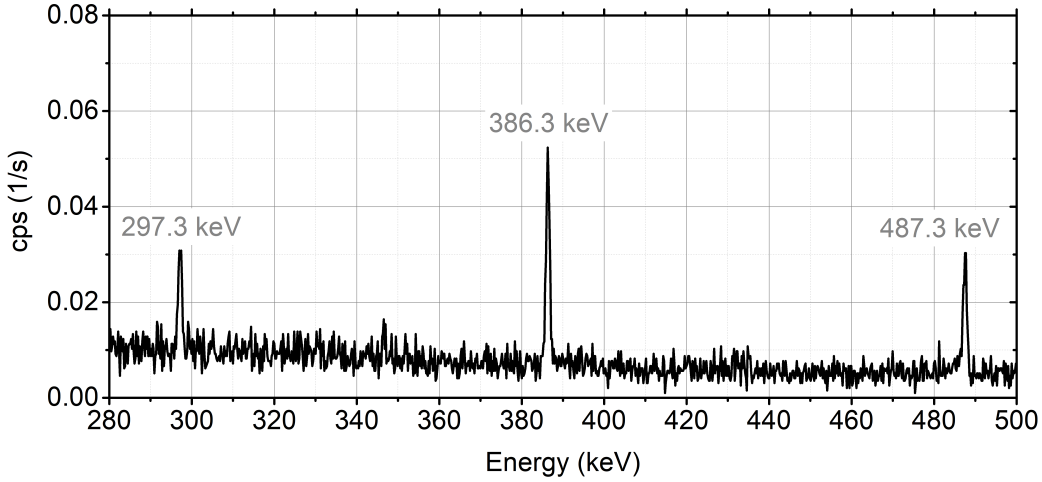

Σχήμα 17: Φάσμα ακτίνων-γ για τον στόχο ^{74}Ge μετά από ακτινοβόληση σε ενέργεια νετρονίων 14.0 MeV. Ακτίνες-γ από δύο διαφορετικές αντιδράσεις παρατηρούνται σε αυτό το φάσμα:
^{74}Ge(n,α)^{71m}Zn: 386.3 και 487.3 keV
^{74}Ge(n,np/d)^{73}Ga: 297.3 keV

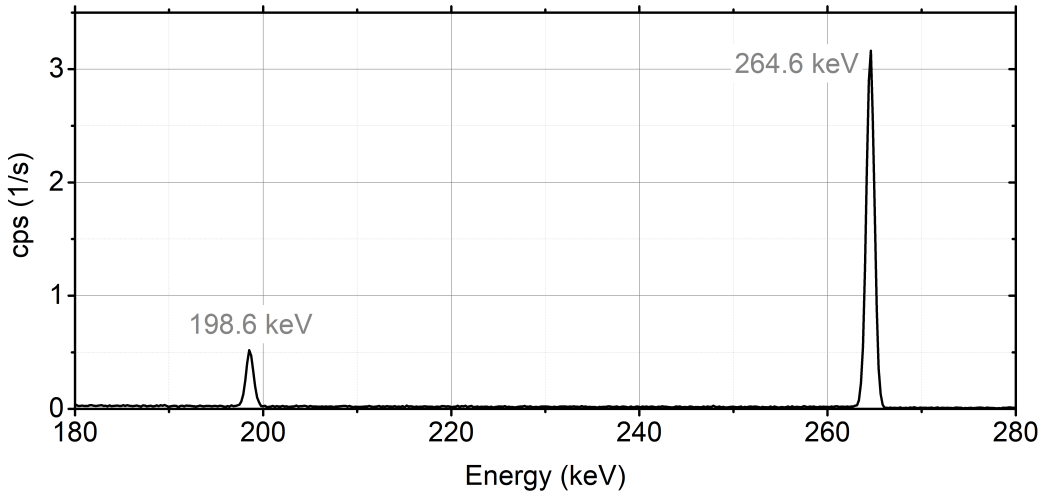

Σχήμα 18: Φάσμα ακτίνων-γ για τον στόχο ^{76}Ge μετά από ακτινοβόληση σε ενέργεια νετρονίων 14.0 MeV. Παρουσιάζονται οι ακτίνες-γ που εκπέμπονται από τον θυγατρικό πυρήνα ^{75}Ge ακολουθώντας την αντίδραση ^{76}Ge(n,2n)^{75}Ge.

Αποτελέσματα και Συζήτηση

Υπολογισμός Ενεργού Διατομής

Ο υπολογισμός της ενεργού διατομής των υπό μελέτη αντιδράσεων βασίστηκε στη σχέση:

$$\sigma_m = \sigma_r \cdot \frac{N_{\gamma,m}}{N_{\gamma,r}} \cdot \frac{(\varepsilon_\gamma \cdot I_\gamma \cdot F \cdot D \cdot f_c \cdot N_t)_r}{(\varepsilon_\gamma \cdot I_\gamma \cdot F \cdot D \cdot f_c \cdot N_t)_m} \cdot \frac{\Phi_r}{\Phi_m} \quad (1)$$

Οι δείκτες “m” και “r” αντίστοιχούν στις λέξεις “measured” και “reference” αντίστοιχα. Οι όροι της σχέσης 1 δίνονται παρακάτω:

Ενεργός διατομή αναφοράς - σ_{ref}

Η ενεργός διατομή για την αντίδραση αναφοράς ^{27}Al(n,α)^{24}Na δίνεται από τη βιβλιοθήκη αξιολόγησης ENDF/B-VIII.0 [16], ενώ η αντίστοιχη αβεβαιότητα της τιμής αυτής εκτιμήθηκε σε ποσοστό 3% για όλες τις περιπτώσεις.

Σύνολο Γεγονότων Φωτοκορυφής - N_γ

Το σύνολο των γεγονότων της εκάστοτε φωτοκορυφής ενδιαφέροντος βρέθηκε από ολοκλήρωση των φασμάτων ακτίνων-γ όπως αυτά προκύπτουν από τον ανιχνευτή Γερμανίου. Για την ανάλυση των φασμάτων χρησιμοποιήθηκε το πρόγραμμα “Tv” [17], από την οποία προέκυψε και η αντίστοιχη αβεβαιότητα για τον εν λόγω όρο.

Απόδοση του ανιχνευτή - ε_γ

Η απόδοση του ανιχνευτή βρέθηκε μετά από κατάλληλη προσαρμογή των πειραματικά μετρούμενων σημείων της απόδοσης όπως αυτά προκύπτουν από σημειακή πηγή ^{152}Eu. Μέσω της καμπύλης προσαρμογής μπορεί να υπολογιστεί η τιμή της απόδοσης του ανιχνευτή στην ενέργεια ενδιαφέροντος καθώς και η αντίστοιχη αβεβαιότητα.

Ενταση ακτίνας-γ - I_γ

Η ένταση για κάθε ακτίνα-γ, καθώς και η αντίστοιχη τιμή αβεβαιότητας προκύπτει από την IAEA για τους πυρήνες ενδιαφέροντος [9–11, 13].

Διορθωτικός Παράγοντας Ενδοαπορρόφησης - F

Ο διορθωτικός αυτός παράγοντας αφορά στο ποσοστό των ακτίνων-γ που απορροφώνται από το ίδιο το δείγμα. Ο προσδιορισμός του επιτυγχάνεται μέσω προσομοιώσεων Monte Carlo ενώ η αβεβαιότητά του είναι αμελητέα.

Διορθωτικός Παράγοντας D

Ο διορθωτικός αυτός παράγοντας αφορά στη διόρθωση για τους πυρήνες οι οποίοι αποδιεγείρονται μετά το πέρας της ακτινοβόλησης. Δίνεται από την σχέση:

$$\mathrm{D} = \mathrm{e}^{-\lambda \mathrm{t}_1} - \mathrm{e}^{-\lambda \mathrm{t}_2} \tag{2}$$

όπου t_1 είναι ο χρόνος που μεσολαβεί μεταξύ του τέλους της ακτινοβόλησης και της αρχής της μέτρησης στον ανιχνευτή Γερμανίου, t_2 είναι το χρονικό διάστημα μέτρησης του δείγματος στον ανιχνευτή και λ αποτελεί τη σταθερά διάσπασης του προς μελέτη ισοτόπου.

Διορθωτικός Παράγοντας $\mathrm{f_c}$

Ο παράγοντας $\mathrm{f_c}$ αφορά στη διόρθωση για πυρήνες που αποδιεγείρονται κατά τη διάρκεια της ακτινοβόλησης, λαμβάνοντας υπόψιν πιθανές μεταβολές της νετρονικής δέσμης κατά τη διάρκεια της ακτινοβόλησης. Δίνεται από τη σχέση:

$$\mathrm{f_c} = \frac{\int_0^{\mathrm{t_{irr}}} \mathrm{e}^{\lambda \mathrm{t}} \mathrm{f(t)dt}}{\int_0^{\mathrm{t_{irr}}} \mathrm{f(t)dt}} \cdot \mathrm{e}^{-\lambda \mathrm{t_{irr}}} \tag{3}$$

όπου ο όρος $\mathrm{f(t)}$ αποτελεί το σύνολο του αριθμού των νετρονίων που καταγράφει ένας απαριθμητής νετρονίων (π.χ. ο ανιχνευτής BF_3) σε διακριτά χρονικά διαστήματα dt, για το σύνολο του χρόνου ακτινοβόλησης ($\mathrm{t_{irr}}$).

Ο αριθμός των πυρήνων στόχου - $\mathrm{N_t}$

Ο αριθμός των πυρήνων $\mathrm{N_t}$ δίνεται συναρτήσει του αριθμού Avogadro ($\mathrm{N_A}$), της μάζας του στόχου (m), της αφθονίας του προς μελέτη ισοτόπου ($\mathrm{a_i}$) και του μαζικού αριθμού (A), βάσει της παρακάτω σχέσης:

$$\mathrm{N_t} = \mathrm{N_A} \cdot \frac{\mathrm{m} \cdot \mathrm{a_i}}{\mathrm{A}} \tag{4}$$

Λόγος Ροών Νετρονίων - $\frac{\Phi_\mathrm{r}}{\Phi_\mathrm{m}}$

Ο λόγος των ροών νετρονίων μεταξύ του στόχου αναφοράς και του προς μέτρηση στόχου υπολογίζεται βάσει προσομοιώσεων MCNP5. Η αξιοπιστία των υπολογισμών αυτών ελέγχεται με χρήση επιπλέον στόχων αναφοράς (π.χ. Al, Au).

Σημειώνεται πως στις περιπτώσεις αντιδράσεων όπου υπήρχε εκπομπή πολλαπλών ακτίνων-γ κατά την αποδιέγερση του παραγόμενου πυρήνα, η ενεργός διατομή της αντίδρασης υπολογίστηκε για κάθε μια από αυτές ξεχωριστά, και η τελική τιμή της ενεργού διατομής προέκυψε ως ο σταθισμένος μέσος όρος των τιμών αυτών, λαμβάνοντας υπόψιν τις συσχετίσεις μεταξύ των επιμέρους μετρήσεων.

Πίνακας 4: Αβεβαιότητηες που εισάγονται στον υπολογισμό της ενεργού διατομής(†: συστηματική αβεβαιότητα)

Παράμετρος	Αβεβαιότητα (%)
Ενεργός διατομή αναφοράς	3
Γεγονότα φωτοκορυφής	$1-10$
Απόδοση του ανιχνευτή HPGe	$2-3$
Διορθωτικός Παράγοντας "F"	–
Ένταση ακτίνας-γ	$0.2-13$
Αριθμός Πυρήνων στόχου	<1
Διορθωτικός Παράγοντας "D"	–
Διορθωτικός Παράγοντας "f_c"	–
Λόγος ροών νετρονίων	–
Παρασιτική ουρά νετρονίων†	<2
Εκτεταμένη γεωμετρία το στόχων Ge†	<3
Συνεισφορά γειτονικών ισοτόπων†	<5

Στον πίνακα 4 παρουσιάζεται το σύνολο των αβεβαιοτήτων οι οποίες αθροίζονται τετραγωνικά για τον υπολογισμό της τελικής αβεβαιότητας στα αποτελέσματα των ενεργών διατομών. Παρουσιάζονται επίσης και συστηματικές αβεβαιότητες οι οποίες δεν αθροίζονται τετραγωνικά, αλλά πρέπει να ληφθούν υπόψιν στα τελικά αποτελέσματα ενεργών διατομών.

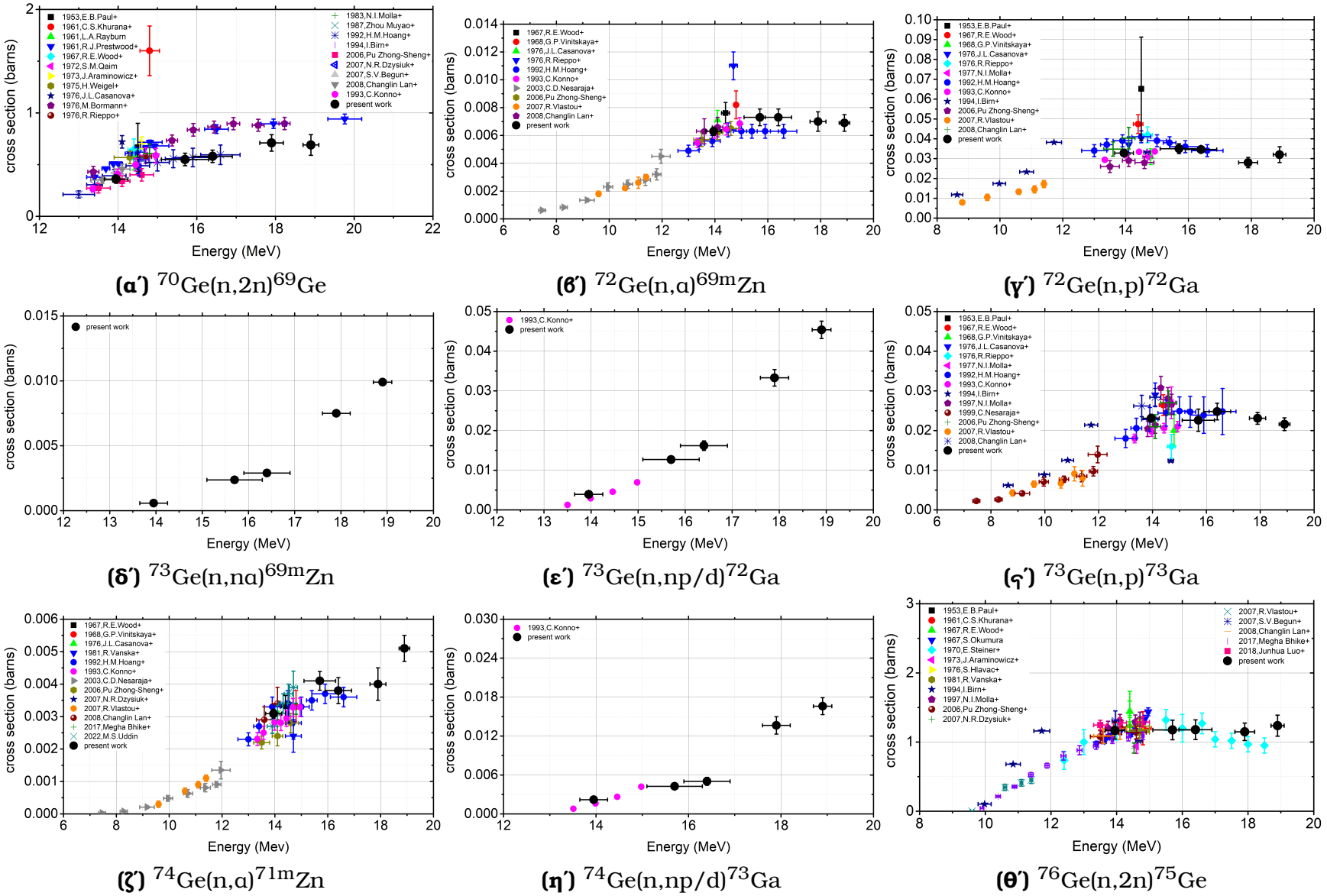

(α′) $^{70}Ge(n,2n)^{69}Ge$ **(β′)** $^{72}Ge(n,α)^{69m}Zn$ **(γ′)** $^{72}Ge(n,p)^{72}Ga$

(δ′) $^{73}Ge(n,nα)^{69m}Zn$ **(ε′)** $^{73}Ge(n,np/d)^{72}Ga$ **(ϛ′)** $^{73}Ge(n,p)^{73}Ga$

(ζ′) $^{74}Ge(n,α)^{71m}Zn$ **(η′)** $^{74}Ge(n,np/d)^{73}Ga$ **(θ′)** $^{76}Ge(n,2n)^{75}Ge$

Σχήμα 19: Πειραματικά δεδομένα ενεργών διατομών

Η αντίδραση ^{70}Ge(n,2n)^{69}Ge

Τα πειραματικά αποτελέσματα ενεργών διατομών για την αντίδραση ^{70}Ge(n,2n)^{69}Ge παρουσιάζονται στο Σχήμα 19α΄ και στον Πίνακα 5 για το ενεργειακό εύρος 14.0-18.9 MeV σε συνδυασμό με υπάρχοντα δεδομένα στη βιβλιογραφία [18]. Ο παραγόμενος πυρήνας ^{69}Ge έχει χρόνο ημιζωής 39.05 h και αποδιεγείρεται στον πυρήνα ^{69}Ga μέσω διάσπασης β^+. Οι πιο εντατικές ακτίνες-γ που συνοδεύουν αυτή την αποδιέγερση έχουν ενέργειες 1106.8, 574.1, 872.0 και 1336.6 keV, και αντίστοιχες εντάσεις 36.0, 13.3, 11.9 και 4.5%. Η τελική τιμή της ενεργού διατομής για την αντίδραση αυτή προέκυψε από το σταθισμένο μέσο όρο των επιμέρους ενεργών διατομών που υπολογίζονται από τις ακτίνες-γ ενεργειών 574.1 και 872.0 keV. Τα αποτελέσματα από τις ακτίνες αυτές είναι μεταξύ τους συνεπή, όπως φαίνεται και στον Πίνακα 5 ενώ η πρώτη έχει επίσης χρησιμοποιηθεί στις πρόσφατες εργασίες των Pu et al. [19] και Lan et. al. [20]. Οι τιμές των ενεργών διατομών που προκύπτουν από τις ακτίνες-γ ενεργειών 1106.8 και 1336.6 keV, από την άλλη είναι συστηματικά χαμηλότερες. Τα αποτελέσματα της παρούσας εργασίας βρίσκονται σε εξαιρετική συμφωνία με τα δεδομένα των Hoang et al. [21] και Pu Zhong-Sheng et al. [19] και αρκετά καλή συμφωνία με τα δεδομένα των of Pu et al., που επίσης χρησιμοποίησαν την ακτίνα-γ ενέργειας 574.1 keV για τον υπολογισμό των ενεργών διατομών. Η συμφωνία με τα δεδομένα των Konno et al. [22] είναι ικανοποιητική. Για τα δεδομένα αυτά χρησιμοποιήθηκε ισοτοπικά εμπλουτισμένος στόχος ^{70}Ge και ακτίνα-γ ενέργειας 1106.8 keV με ένταση $(27 \pm 3)\%$, η οποία είναι κατά 25% μικρότερη από την αντίστοιχη που χρησιμοποιήθηκε στην παρούσα διατριβή.

Πίνακας 5: Αποτελέσματα ενεργών διατομών της αντίδρασης ^{70}Ge(n,2n)^{69}Ge

E_γ (keV)	I_γ (%)	σ_i (b) $E_n = 14.0$ MeV	$E_n = 15.7$ MeV	$E_n = 16.4$ MeV	$E_n = 17.9$ MeV	$E_n = 18.9$ MeV
1106.8	36 ± 4	0.30 ± 0.04	0.46 ± 0.06	0.50 ± 0.06	0.60 ± 0.08	0.63 ± 0.10
1336.6	4.5 ± 0.6	0.28 ± 0.04	0.45 ± 0.07	0.53 ± 0.08	0.55 ± 0.09	-
574.1	13.3 ± 1.8	0.37 ± 0.05	0.56 ± 0.09	0.58 ± 0.09	0.72 ± 0.11	0.73 ± 0.13
872.0	11.9 ± 1.6	0.35 ± 0.05	0.54 ± 0.08	0.58 ± 0.09	0.69 ± 0.11	0.68 ± 0.12
				$\bar{\sigma}$ (b)		
		0.36 ± 0.04	**0.55 ± 0.06**	**0.58 ± 0.06**	**0.71 ± 0.08**	**0.69 ± 0.10**

Η αντίδραση ^{72}Ge(n,α)^{69m}Zn

Τα πειραματικά αποτελέσματα της αντίδρασης ^{72}Ge(n,α)^{69m}Zn παρουσιάζονται στο Σχήμα 19β΄ και στον Πίνακα 6. Ο παραγόμενος πυρήνας ^{69}Zn παράγεται στην ισομερή και στη βασική του στάθμη, ενώ μόνο η ισομερής μπορεί να μελετηθεί μέσω της μεθόδου της νετρονικής ενεργοποίησης. Ο παραγόμενος πυρήνας ^{69m}Zn αποδιεγείρεται προς τη βασική του στάθμη (εσωτερική μετάβαση - IT 94.85%) με χρόνο ημιζωής 13.76 h. Η αποδιέγερση αυτή συνοδεύεται με την εκπομπή της ακτίνας-γ ενέργειας 438.6 keV με αντίστοιχη ένταση 94.85% [9]. Η τιμή της ενεργού διατομής για ενέργεια νετρονίων 14.0 MeV, βρίσκεται σε εξαιρετική συμφωνία με τα δεδομένα των Konno et al. [22], ενώ τα δεδομένα των Hoang et al., φαίνεται να υπερεκτιμούν ελαφρώς τις τιμές των ενεργών διατομών για ενέργειες μεγαλύτερες από 15 MeV.

Πίνακας 6: Αποτελέσματα ενεργών διατομών της αντίδρασης ^{72}Ge(n,α)^{69m}Zn

		σ (b)				
E_γ (keV)	I_γ (%)	$E_n = 14.0$ MeV	$E_n = 15.7$ MeV	$E_n = 16.4$ MeV	$E_n = 17.9$ MeV	$E_n = 18.9$ MeV
438.6	94.85 ± 0.07	$\mathbf{0.0063 \pm 0.0003}$	$\mathbf{0.0073 \pm 0.0006}$	$\mathbf{0.0073 \pm 0.0006}$	$\mathbf{0.0070 \pm 0.0007}$	$\mathbf{0.0069 \pm 0.0006}$

Η αντίδραση ^{72}Ge(n,p)^{72}Ga

Τα πειραματικά αποτελέσματα της αντίδρασης ^{72}Ge(n,p)^{72}Ga παρουσιάζονται στο Σχήμα 19γ΄ και στον Πίνακα 7. Ο παραγόμενος πυρήνας ^{72}Ga αποδιεγείρεται μέσω β^- (100%) διάσπασης στον πυρήνα ^{72}Ge. Η αποδιέγερση του πυρήνα ^{72}Ge προς τη βασική του στάθμη συνοδεύεται από την εκπομπή ακτίνων-γ ενέργειας 834.13, 629.97 και 894.33 keV αντίστοιχων εντάσεων 95.45, 26.13 και 10.14% [10] οι οποίες χρησιμοποιήθηκαν για τον προσδιορισμό της τελικής ενεργού διατομής. Τα αποτελέσματα της ενεργού διατομής για την ενέργεια νετρονίων των 14.0 MeV βρίσκεται σε εξαιρετική συμφωνία με τα δεδομένα των Konno et al., ενώ η τάση των δεδομένων της παρούσας διατριβής για ενέργειες νετρονίων μεγαλύτερες από 15 MeV βρίσκονται σε καλή συμφωνία με τα δεδομένα των Hoang et al.

Πίνακας 7: Αποτελέσματα ενεργών διατομών της αντίδρασης ^{72}Ge(n,p)^{72}Ga

		σ_i (b)				
E_γ (keV)	I_γ (%)	$E_n = 14.0$ MeV	$E_n = 15.7$ MeV	$E_n = 16.4$ MeV	$E_n = 17.9$ MeV	$E_n = 18.9$ MeV
834.1	95.45 ± 0.08	0.0324 ± 0.0015	0.0348 ± 0.0026	0.0361 ± 0.0020	0.0286 ± 0.0027	0.0342 ± 0.0025
630.0	26.13 ± 0.04	0.0340 ± 0.0017	0.0355 ± 0.0027	0.0310 ± 0.0023	0.0269 ± 0.0029	0.0326 ± 0.0026
894.3	10.136 ± 0.015	0.0319 ± 0.0026	0.0347 ± 0.0028	0.038 ± 0.004	0.028 ± 0.004	0.031 ± 0.004
				$\overline{\sigma}$ (b)		
		$\mathbf{0.0328 \pm 0.0014}$	$\mathbf{0.0350 \pm 0.0025}$	$\mathbf{0.0346 \pm 0.0017}$	$\mathbf{0.0280 \pm 0.0026}$	$\mathbf{0.032 \pm 0.004}$

Η αντίδραση ^{73}Ge(n,nα)^{69m}Zn

Τα πειραματικά αποτελέσματα της αντίδρασης ^{73}Ge(n,nα)^{69m}Zn παρουσιάζονται στο Σχήμα 19δ΄ και στον Πίνακα 8. Δεν βρέθηκαν άλλα δεδομένα στη βιβλιογραφία [18] για τη συγκεκριμένη αντίδραση. Το γεγονός αυτό οφείλεται ότι η πλειοψηφία των πειραματικών δεδομένων που υπάρχουν στη βιβλιογραφία χρησιμοποιούν φυσικούς στόχους Γερμανίου. Στη συγκεκριμένη περίπτωση, οι αντιδράσεις up73Ge(n,nα)^{69m}Zn και ^{72}Ge(n,α)^{69m}Zn οδηγούν στην παραγωγή του ίδιου πυρήνα, και επομένως στην περίπτωση των φυσικών η επιμόλυνση του καναλιού ^{72}Ge(n,α)^{69m}Zn είναι αρκετά μεγάλη για την περίπτωση των φυσικών στόχων, κάτι το οποίο δε συμβαίνει στην περίπτωση χρήσης ισοτοπικά εμπλουτισμένων στόχων όπως αυτοί που χρησιμοποιήθηκαν στην παρούσα διατριβή. Ο υπολογισμός της ενεργού διατομής βασίστηκε στην ακτίνα-γ ενέργειας 438.6 keV.

Πίνακας 8: Αποτελέσματα ενεργών διατομών της αντίδρασης ^{73}Ge(n,nα)^{69m}Zn

		σ (mb)				
E_γ (keV)	I_γ (%)	$E_n = 14.0$ MeV	$E_n = 15.7$ MeV	$E_n = 16.4$ MeV	$E_n = 17.9$ MeV	$E_n = 18.9$ MeV
438.6	94.85 ± 0.07	$\mathbf{0.00058 \pm 0.00003}$	$\mathbf{0.00237 \pm 0.00020}$	$\mathbf{0.0029 \pm 0.0005}$	$\mathbf{0.0075 \pm 0.0005}$	$\mathbf{0.0099 \pm 0.0008}$

Η αντίδραση ^{73}Ge(n,np/d)^{72}Ga

Τα πειραματικά αποτελέσματα της αντίδρασης ^{73}Ge(n,np/d)^{72}Ga παρουσιάζονται στο Σχήμα 19ε΄ και στον Πίνακα 9. Λεπτομέρειες για την αποδιέγερση του παραγόμενου πυρήνα ^{72}Ga έχουν αναφερθεί παραπάνω. Τα πειραματικά αποτελέσματα αυτής της διατριβής βρίσκονται σε πολύ καλή συμφωνία με τα μόνα υπάρχοντα δεδομένα των Konno et al. που βρέθηκαν στη βιβλιογραφία για τη συγκεκριμένη αντίδραση, οι οποίοι αξιοποίησαν επίσης ισοτοπικά εμπλουτισμένο στόχο ^{73}Ge. Η αντίδραση αυτή αποτελεί ακόμα ένα παράδειγμα της υπεροχής των ισοτοπικά εμπλουτισμένων στόχων λόγω των σημαντικών επιμολύνσεων στο μετρούμενο φάσμα από την αντίδραση ^{72}Ge(n,p)^{72}Ga στην περίπτωση των φυσικών στόχων Γερμανίου.

Πίνακας 9: Αποτελέσματα ενεργών διατομών της αντίδρασης ^{73}Ge(n,np/d)^{72}Ga

		σ_i (b)				
E_γ (keV)	I_γ (%)	$E_n = 14.0$ MeV	$E_n = 15.7$ MeV	$E_n = 16.4$ MeV	$E_n = 17.9$ MeV	$E_n = 18.9$ MeV
834.1	95.45 ± 0.08	0.00389 ± 0.00018	0.0128 ± 0.0010	0.0162 ± 0.0012	0.0334 ± 0.0022	0.045 ± 0.003
630.0	26.13 ± 0.04	0.00397 ± 0.00021	0.0127 ± 0.0011	–	0.0337 ± 0.0024	0.045 ± 0.004
894.3	10.136 ± 0.015	–	0.0121 ± 0.0013	–	0.0318 ± 0.0003	–
				$\bar{\sigma}$ (b)		
		$\mathbf{0.00392 \pm 0.00017}$	$\mathbf{0.0127 \pm 0.0009}$	$\mathbf{0.0162 \pm 0.0012}$	$\mathbf{0.0333 \pm 0.0021}$	$\mathbf{0.0454 \pm 0.0022}$

Η αντίδραση ^{73}Ge(n,p)^{73}Ga

Τα πειραματικά αποτελέσματα της αντίδρασης ^{73}Ge(n,p)^{73}Ga παρουσιάζονται στο Σχήμα 19ς΄ και στον Πίνακα 10. Ο παραγόμενος πυρήνας ^{73}Ga αποδιεγείρεται μέσω διάσπασης β^- (100%) στον πυρήνα ^{73}Ge. Η αποδιέγερση του πυρήνα αυτού προς τη βασική του στάθμη συνοδεύεται από την εκπομπή ακτίνων-γ ενέργειας 297.3, 325.7,739.4 και 767.8 keV με αντίστοιχες εντάσεις 79.8, 11.2, 4.3 και 1.4% [11]. Τα αποτελέσματα της παρούσας εργασίας βρίσκονται σε εξαιρετική συμφωνία με τα δεδομένα των Hoang et al. εντός των ορίων των αβεβαιοτήτων τους για ενέργειες νετρονίων από 14.0 έως 16.5 MeV, ενώ για την περίπτωση ενέργειας νετρονίων 14.0 MeV υπάρχει μια ασυμφωνία με τα δεδομένα των Konno et al., της τάξης του ∼15 %.

Πίνακας 10: Αποτελέσματα ενεργών διατομών της αντίδρασης ^{73}Ge(n,p)^{73}Ga

		σ_i (b)				
E_γ (keV)	I_γ (%)	$E_n = 14.0$ MeV	$E_n = 15.7$ MeV	$E_n = 16.4$ MeV	$E_n = 17.9$ MeV	$E_n = 18.9$ MeV
297.3	79.8 ± 1.0	0.0217 ± 0.0010	0.0222 ± 0.0016	0.0248 ± 0.0021	0.0231 ± 0.0015	0.0215 ± 0.0016
325.7	11.2 ± 0.4	0.0241 ± 0.0014	0.0232 ± 0.0020	–	0.0256 ± 0.0024	0.024 ± 0.004
739.4	4.3 ± 0.3	0.0273 ± 0.0025	–	–	–	–
767.8	1.44 ± 0.09	0.0264 ± 0.0029	–	–	–	–
				$\bar{\sigma}$ (b)		
		$\mathbf{0.0231 \pm 0.0010}$	$\mathbf{0.0226 \pm 0.0028}$	$\mathbf{0.0248 \pm 0.0021}$	$\mathbf{0.0231 \pm 0.0015}$	$\mathbf{0.0216 \pm 0.0016}$

Η αντίδραση ^{74}Ge(n,α)^{71m}Zn

Τα πειραματικά αποτελέσματα ενεργών διατομών για την αντίδραση ^{74}Ge(n,α)^{71m}Zn παρουσιάζονται στο Σχήμα 19ζ' και στον Πίνακα 11. Ο θυγατρικός πυρήνας ^{71}Zn παράγεται στη βασική και στην μετασταθή του κατάσταση. Στα πλαίσια της διατριβής αυτής, μόνο η μελέτη της αποδιέγερσης της μετασταθούς στάθμης προς τον πυρήνα ^{71}Ga μέσω β^- διάσπασης (100%) με χρόνο ημιζωής 4.14 h, ήταν δυνατή με τη μέθοδο της νετρονικής ενεργοποίησης. Η τελική τιμή της ενεργού διατομής υπολογίστηκε από το σταθμισμένο μέσο όρο των επιμέρους τιμών ενεργών διατομών όπως αυτές προέκυψαν από τις ακτίνες-γ ενέργειας 386.4, 487.4 και 620.1 keV με αντίστοιχες εντάσεις 89.0, 61.9 και 54.5% [12]. Η τιμή της ενεργού διατομής για ενέργεια νετρονίων 14.0 MeV βρίσκεται σε εξαιρετική συμφωνία με την αντίστοιχη τιμή των δεδομένων των Konno et al., ενώ για μεγαλύτερες ενέργειες μέχρι 16 MeV υπάρχει εξαιρετική συμφωνία με τα δεδομένα των Hoang et al.

Πίνακας 11: Αποτελέσματα ενεργών διατομών της αντίδρασης ^{74}Ge(n,α)^{71m}Zn

		σ_i (b)				
E_γ (keV)	I_γ (%)	$E_n = 14.0$ MeV	$E_n = 15.7$ MeV	$E_n = 16.4$ MeV	$E_n = 17.9$ MeV	$E_n = 18.9$ MeV
386.3	89.0 ± 1.1	0.00308 ± 0.00016	0.0041 ± 0.0004	0.0037 ± 0.0005	0.0040 ± 0.0005	0.0049 ± 0.0005
487.3	61.9 ± 0.4	0.00311 ± 0.00017	0.0041 ± 0.0004	0.0038 ± 0.0007	0.0040 ± 0.0005	0.0051 ± 0.0005
620.2	54.5 ± 0.7	0.00308 ± 0.00020	0.0042 ± 0.0005	–	–	0.0059 ± 0.0007
				$\overline{\sigma}$ (b)		
		$\mathbf{0.00309 \pm 0.00014}$	$\mathbf{0.00410 \pm 0.00029}$	$\mathbf{0.0038 \pm 0.0004}$	$\mathbf{0.0040 \pm 0.0005}$	$\mathbf{0.0051 \pm 0.0004}$

Η αντίδραση ^{74}Ge(n,np/d)^{73}Ga

Τα πειραματικά αποτελέσματα ενεργών διατομών για την αντίδραση ^{74}Ge(n,np/d)^{73}Ga παρουσιάζονται στο Σχήμα 19η΄ και στον Πίνακα 12. Η περιγραφή της αποδιέγερσης του θυγατρικού πυρήνα ^{73}Ga έχει ήδη γίνει σε προηγούμενη ενότητα. Τα πειραματικά αποτελέσματα της παρούσας διατριβής βρίσκονται σε καλή συμφωνία τόσο ως προς την τάση τους, όσο και ως προς την τιμή στην περίπτωση της ενέργειας νετρονίων 14.0 MeV με το μοναδικό σύνολο δεδομένο των Konno et al. που υπάρχει για τη συγκεκριμένη αντίδραση.

Πίνακας 12: Αποτελέσματα ενεργών διατομών της αντίδρασης ^{74}Ge(n,np/d)^{73}Ga

		σ (b)				
E_γ (keV)	I_γ (%)	$E_n = 14.0$ MeV	$E_n = 15.7$ MeV	$E_n = 16.4$ MeV	$E_n = 17.9$ MeV	$E_n = 18.9$ MeV
297.3	79.8 ± 1.0	$\mathbf{0.00219 \pm 0.00016}$	$\mathbf{0.0043 \pm 0.0004}$	$\mathbf{0.0050 \pm 0.0006}$	$\mathbf{0.0136 \pm 0.0014}$	$\mathbf{0.0166 \pm 0.0014}$

Η αντίδραση ^{76}Ge(n,2n)^{75}Ge

Τα πειραματικά αποτελέσματα της αντίδρασης ^{76}Ge(n,2n)^{75}Ge παρουσιάζονται στο Σχήμα 19θ΄ και στον Πίνακα 13. Ο θυγατρικός πυρήνας ^{75}Ge παράγεται στη βασική (με χρόνο ημιζωής 82.78 min) και στη μετασταθή του στάθμη (με χρόνο ημιζωής 47.7 sec). Στα πλαίσια αυτής της διατριβής, μετρήθηκε η συνολική ενεργός διατομή σ_{m+g} που αντιστοιχεί στο άθροισμα των ενεργών διατομών για τη βασική και μετασταθή στάθμη, εφόσον η μετασταθής στάθμη αποδιεγείρεται σε ποσοστό 100% προς τη βασική. Ο παραγόμενος πυρήνας ^{75}Ge αποδιεγείρεται εν συνεχεία μέσω διάσπασης β^- (100%) στον πυρήνα ^{75}As εκπέμποντας την χαρακτηριστική ακτίνα-γ ενέργειας 264.6 keV με αντίστοιχη ένταση 11.4% [13], η οποία χρησιμοποιήθηκε για τον προσδιορισμό της ενεργού διατομής. Τα αποτελέσματα της διατριβής αυτής βρίσκονται σε πολύ καλή συμφωνία με τα πειραματικά δεδομένα των Steiner et al. [23], που αποτελεί το μόνο σύνολο δεδομένων για ενέργειες μεγαλύτερες των 15 MeV, ενώ για την περίπτωση των 14 MeV υπάρχει πολύ καλή συμφωνία πρακτικά με κάθε σύνολο δεδομένων, εντός των ορίων των αβεβαιοτήτων των μετρήσεων.

Πίνακας 13: Αποτελέσματα της αντίδρασης ^{76}Ge(n,2n)^{75}Ge

		σ (b)				
E_γ (keV)	I_γ (%)	$E_n = 14.0$ MeV	$E_n = 15.7$ MeV	$E_n = 16.4$ MeV	$E_n = 17.9$ MeV	$E_n = 18.9$ MeV
264.6	11.4 ± 1.1	$\mathbf{1.17 \pm 0.13}$	$\mathbf{1.18 \pm 0.14}$	$\mathbf{1.18 \pm 0.14}$	$\mathbf{1.15 \pm 0.13}$	$\mathbf{1.24 \pm 0.15}$

Σύγκριση αποτελεσμάτων Φυσικών και Ισοτοπικά Εμπλουτισμένων Στόχων

Η μέθοδος της νετρονικής ενεργοποίησης βασίζεται στη μέτρηση της ραδιενέργειας του εκάστοτε παραγόμενου πυρήνα. Σε κάποιες περιπτώσεις όμως, δύο διαφορετικές αντιδράσεις γειτονικών ισοτόπων μπορεί να οδηγήσουν στην παραγωγή του ίδιου πυρήνα. Για παράδειγμα, ο πυρήνας ^{72}Ge μπορεί να παραχθεί από τις αντιδράσεις ^{72}Ge(n,p)^{72}Ga και ^{73}Ge(n,np/d)^{72}Ga. Συνεπώς, ιδιαίτερα στην περίπτωση μετρήσεων ενεργών διατομών με φυσικούς στόχους πρέπει να ποσοτικοποιηθεί η συνεισφορά των 'παρασιτικών' καναλιών που οδηγούν στην παραγωγή του ίδιου πυρήνα με αυτόν που παράγεται από την εκάστοτε προς μελέτη αντίδραση. Η συνεισφορά αυτή μπορεί να υπολογιστεί με θεωρητικούς υπολογισμούς, οι οποίοι ωστόσο συνοδεύονται από τις δικές τους αβεβαιότητες, κυρίως συστηματικές.

Οι μετρήσεις με ισοτοπικά εμπλουτισμένους στόχους από την άλλη, δεν επηρεάζονται τόσο (ανάλογα με τα ποσοστά εμπλουτισμού) από τις συνεισφορές αυτές, οδηγόντας στην παραγωγή αποτελεσμάτων ενεργού διατομής μεγαλύτερης ακρίβειας.

Για τους λόγους αυτούς, στα πλαίσια της διατριβής αυτής, πραγματοποιήθηκαν δύο σειρές μετρήσεων για ενέργεια δέσμης νετρονίων E_n = 17.9 MeV. Στη πρώτη σειρά μετρήσεων χρησιμοποιήθηκε φυσικός στόχος Ge με όλα τα ισότοπα στη φυσική τους αναλογία (^{70}Ge 20.52%, ^{72}Ge 27.45%, ^{73}Ge 7.76%, ^{74}Ge 36.52%, ^{76}Ge 7.75%). Στη δεύτερη σειρά μετρήσεων χρησιμοποιήθηκαν ισοτοπικά εμπλουτισμένοι στόχοι, με σκοπό τον έλεγχο της ακρίβειας και της ευαισθησίας των διορθώσεων που πρέπει να εφαρμοστούν [24]. Η μέθοδος διόρθωσης που εφαρμόστηκε παρουσιάζεται στην επόμενη Παράγραφο.

Διορθώσεις Παρασιτικών Αντιδράσεων

Το σύνολο των γεγονότων (Y) που μετρούνται στο πειραματικό φάσμα ακτινοβολίας-γ μιας 'μολυσμένης' αντίδρασης, αποτελείται από το άθροισμα των γεγονότων της αντίδρασης ενδιαφέροντος (X) και την αντίστοιχη συνεισφορά της παρασιτικής αντίδρασης που οδηγεί στην παραγωγή του ίδιου πυρήνα. Ο λόγος των δύο παραπάνω μεγεθών δίνεται από τη σχέση:

$$\frac{Y}{X} = 1 + \frac{\sigma_1}{\sigma_2} \cdot \frac{Ab_1}{Ab_2} \tag{5}$$

όπου

- Y Το σύνολο των γεγονότων φωτοκορυφής στο φάσμα
- X Τα γεγονότα φωτοκορυφής της προς μελέτη αντίδρασης
- $\boldsymbol{\sigma_1}$ Η τιμή της ενεργού διατομής της 'παρασιτικής' αντίδρασης, η οποία λαμβάνεται από κάποια βιβλιοθήκη αξιολόγησης

- $\boldsymbol{\sigma_2}$ Η τιμή της ενεργού διατομής της προς μελέτη αντίδρασης, η οποία λαμβάνεται από την ίδια βιβλιοθήκη αξιολόγησης

- $\mathrm{Ab_1}$ Η αφθονία του ισοτόπου που είναι υπεύθυνο για την παρασιτική συνεισφορά

- $\mathrm{Ab_2}$ Η αφθονία του ισοτόπου του οποίου η αντίδραση μελετάται

Όπως παρουσιάζεται στην Εξίσωση 5, η μεθοδολογία αυτή εξαρτάται έντονα από την επιλογή της βιβλιοθήκης αξιολόγησης για τον προσδιορισμό του λόγου των ενεργών διατομών σ_1/σ_2. Η επιλογή της ίδιας βιβλιοθήκης αξιολόγησης για τις δύο τιμές ενεργών διατομών υποθέτει ότι οι υπολογισμοί στατιστικών μοντέλων γίνονται με συστηματικό τρόπο για όλα τα κανάλια αντίδρασης, και οι διάφορες πιθανές συστηματικές αβεβαιότητες απαλείφονται με τη χρήση του λόγου σ_1/σ_2, καθιστώντας τη μεθοδολογία αξιόπιστη.

Η μεθοδολογία θα εφαρμοστεί στις αντιδράσεις ^{76}Ge(n,2n)^{75}Ge, ^{72}Ge(n,α)^{69m}Zn και ^{72}Ge(n,p)^{72}Ga. Σημειώνεται ότι η πρώτη αντίδραση δε μολύνεται από κάποιο γειτονικό ισότοπο, και θα χρησιμοποιηθεί σαν έλεγχος της μεθοδολογίας, ενώ οι δύο τελευταίες μολύνονται από αντιδράσεις γειτονικών ισοτόπων.

Η αντίδραση ^{76}Ge(n,2n)^{75}Ge - μη μολυσμένη

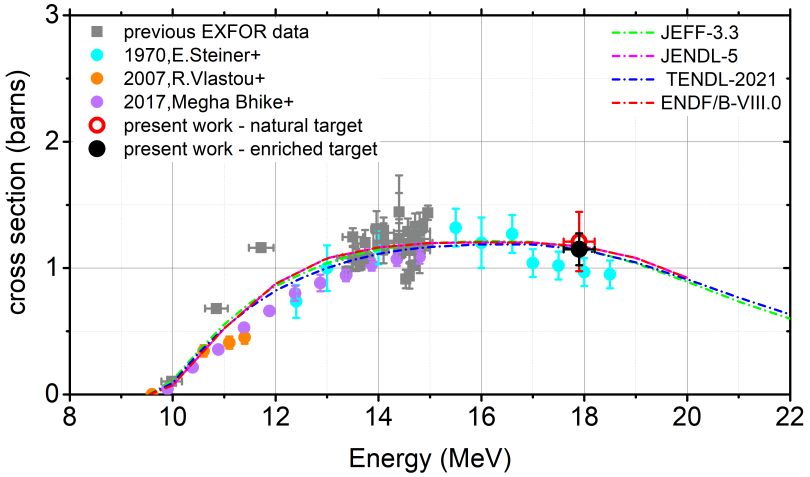

Σχήμα 20: Τα αποτελέσματα ενεργού διατομής της αντίδρασης ^{76}Ge(n,2n)^{75}Ge

Τα πειραματικά αποτελέσματα της αντίδρασης ^{76}Ge(n,2n)^{75}Ge παρουσιάζονται στο Σχήμα 20 μαζί με προηγούμενα δεδομένα της βιβλιογραφίας [18] και βιβλιοθήκες αξιολόγησης [16, 25–27]. Στον Πίνακα 14 παρουσιάζονται οι ακτίνες-γ που χρησιμοποιήθηκαν και τα τελικά αποτελέσματα ενεργών διατομών για τις μετρήσεις με φυσικό και ισοτοπικά εμπλουτισμένο στόχο.

Παρατηρείται εξαιρετική συμφωνία μεταξύ των δύο ανεξάρτητων μετρήσεων, εντός των ορίων των αβεβαιοτήτων τους, κάτι το οποίο υποδεικνύει ότι δεν υπήρχαν συστηματικές διαφορές μεταξύ τους, όσον αφορά στην ανάλυση των δεδομένων ή τη συνολική πειραματική διαδικασία που ακολουθήθηκε. Επομένως μπορεί να γίνει αξιόπιστη σύγκριση των αποτελεσμάτων των πιο σύνθετων περιπτώσεων που ακολουθούν.

Πίνακας 14: Η ακτίνα-γ που χρησιμοποιήθηκε, μαζί με την έντασή της και την αντίστοιχη αβεβαιότητα [13] για την αντίδραση ^{76}Ge(n,2n)^{75}Ge. Παρουσιάζονται επίσης και οι υπολογισμένες ενεργές διατομές με τις αντίστοιχες αβεβαιότητές τους.

τύπος στόχου	E_γ (keV)	I_γ (%)	**σ(b)**
natural	264.6	11.4 ± 1.1	$\mathbf{1.21 \pm 0.24}$
enriched	264.6	11.4 ± 1.1	$\mathbf{1.15 \pm 0.13}$

Η αντίδραση ^{72}Ge(n,α)^{69m}Zn - μολυσμένη

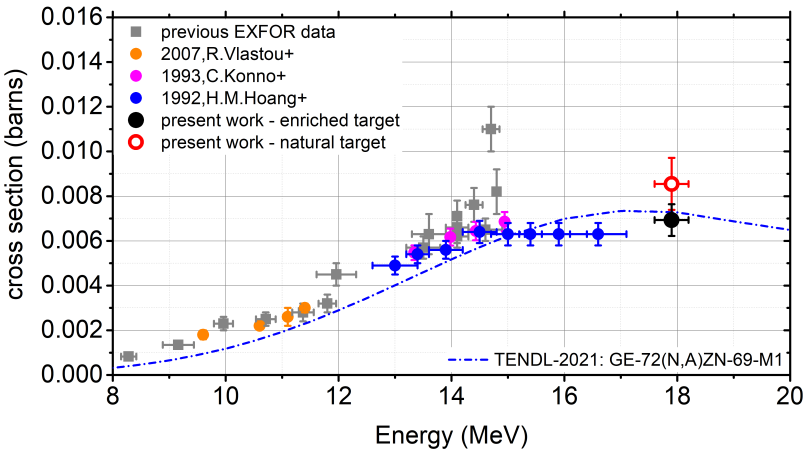

Σχήμα 21: Τα αποτελέσματα ενεργού διατομής της αντίδρασης ^{72}Ge(n,α)^{69m}Zn

Τα αποτελέσματα της αντίδρασης ^{72}Ge(n,α)^{69m}Zn παρουσιάζονται στο Σχήμα 21 για την περίπτωση του φυσικού και ισοτοπικά εμπλουτισμένου στόχου, μαζί με προηγούμενα δεδομένα της βιβλιογραφίας και τη βιβλιοθήκη αξιολόγησης TENDL-2021. Στον Πίνακα 15 παρουσιάζεται η ακτίνα-γ που χρησιμοποιήθηκε και τα τελικά αποτελέσματα ενεργών διατομών μαζί με τις αντίστοιχες αβεβαιότητές τους.

Παρατηρείται μια διαφορά της τάξης του 18% μεταξύ των δύο μετρήσεων. Σημειώνεται ότι η συγκεκριμένη αντίδραση μολύνεται από την αντίδραση ^{73}Ge(n,nα)^{69m}Zn στην περίπτωση του φυσικού στόχου. Η διόρθωση που ακο-

λουθήθηκε σε αυτή την περίπτωση βάσει της εξίσωσης 5 και της βιβλιοθήκης EAF 2010 [28] παρουσιάζεται παρακάτω,

Πίνακας 15: Η ακτίνα-γ που χρησιμοποιήθηκε, μαζί με την ένταση της και την αντίστοιχη αβεβαιότητα [9] για την αντίδραση ^{72}Ge(n,α)^{69m}Zn. Παρουσιάζονται επίσης και οι υπολογισμένες ενεργές διατομές με τις αντίστοιχες αβεβαιότητές τους.

τύπος στόχου	E_γ (keV)	I_γ (%)	**σ(b)**
natural	438.63	94.85 ± 0.07	$\mathbf{0.0085 \pm 0.0012}$
enriched	438.63	94.85 ± 0.07	$\mathbf{0.0070 \pm 0.0007}$

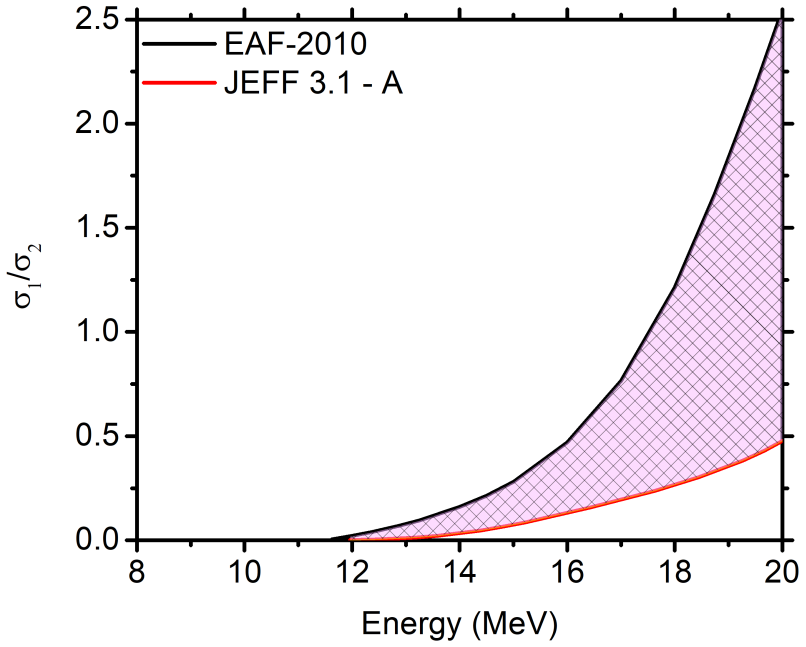

Σχήμα 22: Ο λόγος σ_1/σ_2 για την παρασιτική αντίδραση ^{73}Ge(n,nα) ως συνάρτηση της ενέργειας νετρονίων.

Παρασιτικό Κανάλι για την αντίδραση ^{73}Ge(n,nα)^{69m}Zn Ο λόγος των ενεργών διατομών σ_1/σ_2 της Εξίσωσης 5 υπολογίστηκε βάσει της βιβλιοθήκης αξιολόγησης EAF 2010. Ο λόγος αυτός παρουσιάζεται συναρτήσει της ενέργειας νετρονίων στο Σχήμα 22 για τις βιβλιοθήκες EAF-2010 [28] και JEFF 3.1-A [29]. Οι αποκλίσεις του λόγου αυτού αυξάνονται σημαντικά συναρτήσει της ενέργειας, οδηγώντας σε πολύ διαφορετικά αποτελέσματα διόρθωσης της τελικής τιμής ενεργού διατομής ανάλογα με την επιλογή της τιμής του λόγου αυτού. Για την περίπτωση των 17.9 MeV, οι διορθώσεις κυμαίνονται από 7.3 έως 32.7% εντός του διαστήματος της γραμμοσκιασμένης περιοχής του Σχήματος 22, που ορίζεται από τις δύο βιβλιοθήκες. Αυτό το γεγονός θα μπορούσε να δικαιολογήσει την απόκλιση της τάξης του 18% που παρατηρήθηκε.

Σημειώνεται πως η συγκεκριμένη μεθοδολογία θεωρείται αξιόπιστη για ενέργειες νετρονίων μικρότερες των 12 MeV ανεξάρτητα από την επιλογή βιβλιοθήκης (το εύρος των διορθώσεων δεν ξεπερνά το 3%). Επίσης στην περίπτωση του ισοτοπικά εμπλουτισμένου στόχου ^{72}Ge, η διόρθωση των 17.9 MeV δεν ξεπερνά σε ποσοστό το 3.5% ανεξάρτητα από την επιλογή βιβλιοθήκης.

Η αντίδραση ^{72}Ge(n,p)^{72}Ga - μολυσμένη

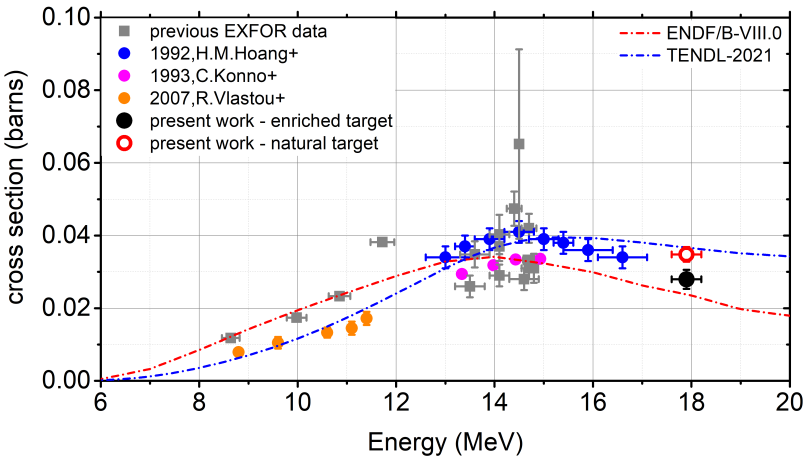

Σχήμα 23: Τα αποτελέσματα ενεργού διατομής της αντίδρασης ^{72}Ge(n,p)^{72}Ga

Τα αποτελέσματα ενεργών διατομών της αντίδρασης ^{72}Ge(n,p)^{72}Ga παρουσιάζονται στο Σχήμα 23 για την περίπτωση φυσικού και ισοτοπικά εμπλουτισμένου στόχου μαζί με προηγούμενα δεδομένα της βιβλιογραφίας και τις βιβλιοθήκες αξιολόγησης ENDF/B-VIII.0 [16] και TENDL-2021 [25]. Στον Πίνακα 16 παρουσιάζονται οι ακτίνες-γ που χρησιμοποιήθηκαν για τον υπολογισμό των ενεργών διατομών με τις εντάσεις τους και τις αντίστοιχες αβεβαιότητες.

Πίνακας 16: Λίστα των ακτίνων-γ που χρησιμοποιήθηκαν στον υπολογισμό της ενεργού διατομής, μαζί με τις εντάσεις και τις αντίστοιχες αβεβαιότητές τους [10] για την αντίδραση ^{72}Ge(n,p)^{72}Ga. Παρουσιάζονται και οι τελικές τιμές ενεργών διατομων με τις αντίστοιχες αβεβαιότητες.

τύπος στόχου	E_γ (keV)	I_γ (%)	σ_i (b)	**σ(b)**
natural	834.13	95.45 ± 0.08	0.0361 ± 0.0027	$\mathbf{0.0348 \pm 0.0020}$
	629.97	26.13 ± 0.04	0.031 ± 0.005	
	2201.59	26.87 ± 0.12	0.031 ± 0.005	
enriched	834.13	95.45 ± 0.08	0.0286 ± 0.0026	$\mathbf{0.0280 \pm 0.0026}$
	629.97	26.13 ± 0.04	0.0269 ± 0.0027	
	894.33	10.14 ± 0.02	0.0284 ± 0.004	

Παρατηρείται μια διαφωνία της τάξης του 20% μεταξύ των δύο μετρήσεων. Σημειώνεται ότι στην περίπτωση του φυσικού στόχου, χρησιμοποιήθηκε η βιβλιοθήκη αξιολόγησης TENDL-2021 για τον υπολογισμό της συνεισφοράς των παρασιτικών αντιδράσεων ^{73}Ge(n,np)^{72}Ga και ^{73}Ge(n,d)^{72}Ga, μέσω του λόγου σ_1/σ_2.

Παρασιτικά Κανάλια για την αντίδραση ^{72}Ge(n,p)^{72}Ga Ο λόγος σ_1/σ_2 των ενεργών διατομών της εξίσωσης 5 υπολογίστηκε βάσει της βιβλιοθήκης αξιολόγησης TENDL-2021 για τον προσδιορισμό της συνεισφοράς των παρασιτικών αντιδράσεων ^{73}Ge(n,np)^{72}Ga και ^{73}Ge(n,d)^{72}Ga.

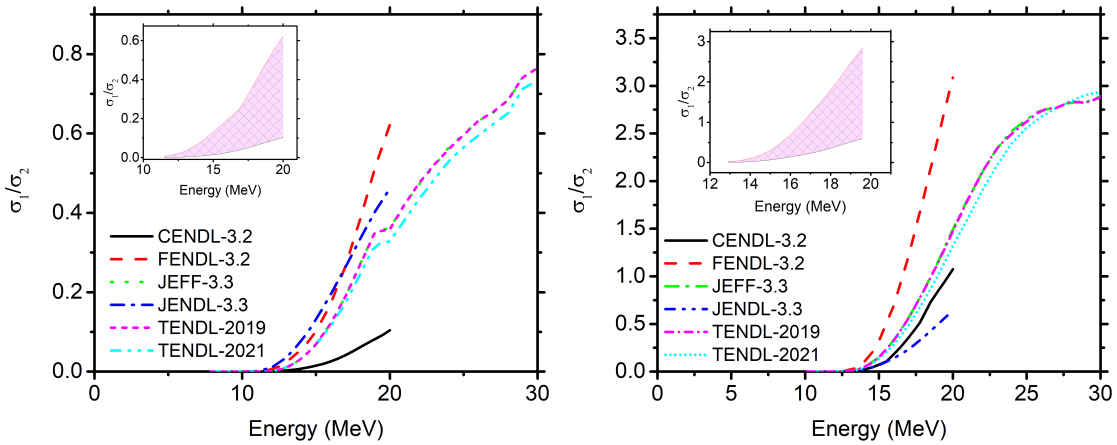

(α′) ^{73}Ge(n,d)^{72}Ga **(β′)** ^{73}Ge(n,np)^{72}Ga

Σχήμα 24: Ο λόγος σ_1/σ_2 των παρασιτικών αντιδράσεων ^{73}Ge(n,d/np)^{72}Ga ως συνάρτηση της ενέργειας νετρονίων.

Ο λόγος αυτός παρουσιάζεται συναρτήσει της ενέργειας νετρονίων στο Σχήμα 24 για βιβλιοθήκες [25, 27, 30–33] που βρέθηκαν να έχουν πληροφορίες ενεργών διατομών τόσο για τις παρασιτικές αντιδράσεις, όσο και για τη μετρούμενη αντίδραση.

Η ελάχιστη και μέγιστη τιμή του λόγου σ_1/σ_2 δημιουργεί τη γραμμοσκιασμένη περιοχή που παρουσιάζεται στα Σχήματα 24α′ και 24β′, εντός της οποίας μπορεί να επιλεχθεί κάποια τιμή για τον λόγο σ_1/σ_2. Οι έντονες διαφορές μεταξύ των βιβλιοθηκών, ειδικά σε μεγαλύτερες ενέργειες οδηγούν σε πολύ διαφορετικά αποτελέσματα διορθώσεων ενεργών διατομών στη περίπτωση των φυσικών στόχων. Για παράδειγμα, για ενέργεια νετρονίων 17.9 MeV οι διορθώσεις κυμαίνονται μεταξύ:

- 1.7 έως 10.6% για την αντίδραση ^{73}Ge(n,d)^{72}Ga
- 9.7 εως 49.2% για την αντίδραση ^{73}Ge(n,np)^{72}Ga

Και για τις δύο παρασιτικές αντιδράσεις, η συνεισφορά δεν ξεπέρασε σε ποσοστό το 3% για ενέργειες νετρονίων μικρότερες των ∼14.5 MeV, στις οποίες

η συγκεκριμένη μεθοδολογία μπορεί να θεωρηθεί αξιόπιστη. Οι έντονες διαφορές μεταξύ των βιβλιοθηκών μπορεί να είναι ο λόγος των διαφοροποιήσεων των μετρήσεων με φυσικό και ισοτοπικά εμπλουτισμένο στόχο που έγιναν στα πλαίσια αυτής της διατριβής.

Σημειώνεται τέλος ότι στην περίπτωση του ισοτοπικά εμπλουτισμένου στόχου ^{72}Ge, η συνεισφορά των παρασιτικών αντιδράσεων δεν ξεπέρασε σε ποσοστό το 5%, επιβεβαιώνοντας την αξιοπιστία των αποτελεσμάτων ενεργών διατομών που προκύπτουν από ισοτοπικά εμπλουτισμένους στόχους.

Θεωρητικοί Υπολογισμοί

Εκτός από τις πειραματικές μετρήσεις, στα πλαίσια της παρούσας διατριβής έγιναν θεωρητικοί υπολογισμοί με χρήση του κώδικα EMPIRE 3.2.3 [1], ο οποίος εκτελεί υπολογισμούς Hauser-Feshbach [34] με σκοπό την αναπαραγωγή των αντιδράσεων ^{70}Ge(n,2n)^{69}Ge, ^{72}Ge(n,α)^{69m}Zn, ^{72}Ge(n,p)^{72}Ga, ^{73}Ge(n,nα)^{69m}Zn, ^{73}Ge(n,np/d)^{72}Ga, ^{73}Ge(n,p)^{73}Ga, ^{74}Ge(n,α)^{71m}Zn, ^{74}Ge(n,np/d)^{73}Ga και ^{76}Ge(n,2n)^{75}Ge) που μελετήθηκαν, με ένα συνεκτικό σύνολο παραμέτρων εισόδου. Οι υπολογισμοί έγιναν στο ενεργειακό εύρος 5 - 20 MeV.

Ο κώδικας EMPIRE επιτρέπει την επιλογή διάφορων οπτικών μοντέλων δυναμικού (μέσω της εντολής "OMPOT") από την πιο πρόσφατη βιβλιοθήκη RIPL-3 (Reference Input Parameter Library), για διάφορα είδη σωματιδίων. Οι υπολογισμοί των συντελεστών διέλευσης γίνεται μέσω του κώδικα ECIS [35, 36] επηρεάζονται κυρίως από την επιλογή του οπτικού δυναμικού, και είναι πιο ευαίσθητοι στην χαμηλοενεργειακή περιοχή μερικών MeV (κοντά στο ενεργειακό κατώφλι των αντιδράσεων). Οι υπολογισμοί στην περιοχή υψηλότερων ενεργειών από την άλλη, είναι πιο ευαίσθητοι στην επιλογή των διάφορων μοντέλων πυκνότητας ενεργειακών καταστάσεων (τα διαθέσιμα μοντέλα στον κώδικα του EMPIRE είναι τα εξής: Μοντέλο Αερίου Φέρμι - Fermi-Gas Model [37], Μοντέλο Gilbert-Cameron - Gilbert-Cameron Model [38], Γενικευμένο Μοντέλο Υπερρεσυτού - Generalized Superfluid Model [39, 40] και το Βελτιωμένο Γενικευμένο Μοντέλο Υπερρεσυτού - Enhanced Generalized Superfluid Model [41]) καθώς και φαινομένων προ-ισορροπίας. Τα φαινόμενα αυτά περιγράφονται μέσω των κβαντομηχανικών μοντέλων Multi-step Direct [42] (μέσω της εντολής του EMPIRE "MSD") και Multi-step Compound [43] (μέσω της εντολής του EMPIRE "MSC"), καθώς και του φαινομενολογικού μοντέλου εξιτονίων [44, 45] (μέσω της εντολής του EMPIRE "PCROSS").

Ο σκοπός της θεωρητικής αυτής μελέτης ήταν η επιλογή ενός συνεκτικού συνόλου παραμέτρων εισόδου με σκοπό την ταυτόχρονη αναπαραγωγή όλων των καναλιών που μελετήθηκαν λαμβάνοντας υπόψιν όλα τα διαθέσιμα πειραματικά δεδομένα.

Η σειρά των βημάτων που ακολουθήθηκε είχε ως εξής: Εφόσον τα κανάλια (n,2n) έχουν τη μεγαλύτερη τιμή ενεργού διατομής και τα ισότοπα ^{70,76}Ge διαφέρουν μόνο κατά 3 ζεύγη νετρονίων, το πρώτο βήμα περιελάμ-

βανε την ταυτόχρονη μελέτη των αντιδράσεων ^{70,76}Ge(n,2n)^{69,75}Ge. Έγιναν όλοι οι συνδυασμοί των διαθέσιμων οπτικών δυναμικών από τη βιβλιοθήκη RIPL-3 και των διαθέσιμων μοντέλων πυκνότητας ενεργειακών καταστάσεων από τον κώδικα EMPIRE 3.2.3. Ο βέλτιστος συνδυασμός βρέθηκε να είναι το οπτικό δυναμικό νετρονίων B. Morillon and P. Romain [46] (RIPL-3 OMP index: 2411) και το Βελτιωμένο Γενικευμένο Μοντέλο Υπερρεσυτού - Enhanced Generalized Superfluid Model [41] (μέσω της εντολής "levden=0" στον κώδικα του EMPIRE). Τα οπτικά δυναμικά για πρωτόνια, σωματίδια-α, δευτέρια, τρίτια και ^{3}He αφέθηκαν στις προκαθορισμένες τους τιμές σε αυτή την πρώτη προσέγγιση. Οι μηχανισμοί προ-ισορροπίας ενεργοποιήθηκαν μέσω των κβαντομηχανικών μοντέλων Multi-step Direct [42] (μέσω της εντολής του EMPIRE "MSD=1") και Multi-step Compound [43] (μέσω της εντολής του EMPIRE "MSC=1") και του φαινομενολογικού μοντέλου εξιτονίων (PCROSS=1.5 - μέση τιμή). Ακολουθώντας τον παραπάνω συνδυασμό παραμέτρων, η ταυτόχρονη αναπαραγωγή των καναλιών ^{70,76}Ge(n,2n)^{69,75}Ge είναι πάρα πολύ καλή όπως φαίνεται και στο Σχήμα 25. Οι υπολογισμοί αυτοί στη συνέχεια επεκτάθηκαν και σε χαμηλότερες ενέργειες (από 0.1 μέχρι 20 MeV) και τα αποτελέσματα της παραμετροποίησης που αναφέρθηκε παραπάνω ήταν επίσης σε πολύ καλή συμφωνία με δεδομένα αντιδράσεων (n,tot) όταν αυτά ήταν διαθέσιμα στη βιβλιογραφία.

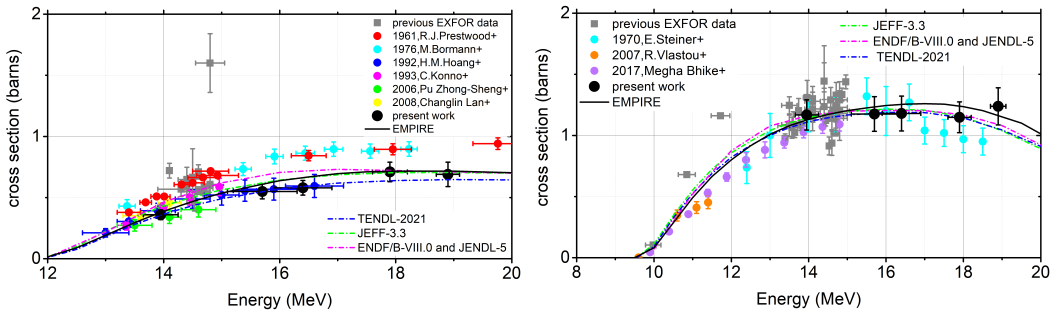

(α′) ^{70}Ge(n,2n)^{69}Ge **(β′)** ^{76}Ge(n,2n)^{75}Ge

Σχήμα 25: Υπολογισμοί EMPIRE για τις αντιδράσεις ^{70,76}Ge(n,2n)^{69,75}Ge

Με δεσμευμένο οπτικό δυναμικό νετρονίων και δεσμευμένο μοντέλο πυκνότητας ενεργειακών καταστάσεων, το δεύτερο βήμα ήταν η αναπαραγωγή των καναλιών αντίδρασης που είχαν ένα πρωτόνιο στο κανάλι εξόδου. Αυτές ήταν οι αντιδράσεις ^{72,73}Ge(n,p)^{72,73}Ga και ^{73,74}Ge(n,np/d)^{72,73}Ga. Το οπτικό δυναμικό των A.J.Koning και J.P.Delaroche [47] υιοθετήθηκε σε αυτή την περίπτωση (RIPL-3 OMP index: 5405), ενώ η συνεισφορά φαινομένων προ-ισορροπίας τροποποιήθηκαν ελαφρώς μέσω του μοντελου των εξιτονίων (PCROSS=1.2, 0.6 και 0.6 για τους πυρήνες ^{72,73,74}Ge αντίστοιχα). Τα οπτικά δυναμικά για σωματίδια-α, δευτέρια, τρίτια και ^{3}He αφέθηκαν και πάλι στις προκαθορισμένες τους τιμές. Η αναπαραγωγή των καναλιών ^{72,73}Ge(n,p)^{72,73}Ga είναι πολύ καλή όπως φαίνεται στα Σχήματα 26α′ και 26β′, η οποία περιλαμβάνει εκτός από τα αποτελέσματα της παρούσας ερ-

γασίας, και αποτελέσματα μετρήσεων των αντιδράσεων ^{72,73}Ge(n,p)^{72,73}Ga από παλαιότερες μετρήσεις της ομάδας Πυρηνικής Φυσικής του ΕΜΠ [48]. Οι υπολογισμοί των αντιδράσεων ^{73,74}Ge(n,np/d)^{72,73}Ga, φαίνεται να υποτιμούν ελαφρώς τις τιμές των μετρούμενων ενεργών διατομών, όπως φαίνεται στα Σχήματα 5.7c και 5.7d.

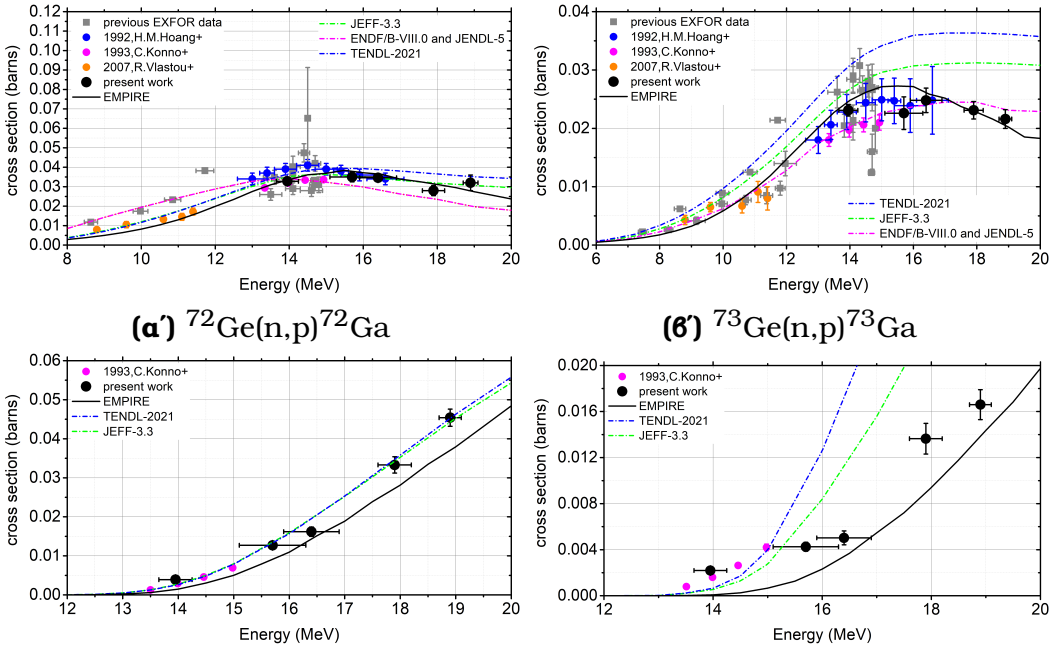

(α′) ^{72}Ge(n,p)^{72}Ga **(β′)** ^{73}Ge(n,p)^{73}Ga

(γ′) ^{73}Ge(n,np/d)^{72}Ga **(δ′)** ^{74}Ge(n,np/d)^{73}Ga

Σχήμα 26: Υπολογισμοί EMPIRE για τα κανάλια αντίδρασης με πρωτόνιο (p) στο κανάλι εξόδου

Με δεσμευμένα τα οπτικά δυναμικά νετρονίων και πρωτονίων, καθώς και το μοντέλο πυκνότητας ενεργειακών καταστάσεων, το τρίτο και τελευταίο βήμα ήταν η αναπαραγωγή των καναλιών αντίδρασης με σωματίδιο-α στο κανάλι εξόδου, μέσω κατάλληλης επιλογής οπτικού δυναμικού σωματιδίων-α. Επιλέχθηκε το οπτικό δυναμικό των V.Avrigeanu, P.E.Hodgson, and M.Avrigeanu [49] RIPL-3 OMP index: 9600), ενώ τροποποιήθηκε η παράμετρος $\tilde{a}$ (εντολή EMPIRE "ATILNO") κατά 19% ($\tilde{a} = 0.81$) για τον παραγόμενο πυρήνα ^{69}Zn και 16% ($\tilde{a} = 0.84$) για τον παραγόμενο πυρήνα ^{70}Zn, αφήνοντας πρακτικά ανεπηρέαστα τα υπόλοιπα προς μελέτη κανάλια αντίδρασης. Η αναπαραγωγή των καναλιών ^{72}Ge(n,α)^{69m}Zn και ^{73}Ge(n,nα)^{69m}Zn είναι πολύ καλή όπως φαίνεται στα Σχήματα 27α′ και 27γ′, κάτι το οποίο δε συμβαίνει για την περίπτωση της αντίδρασης ^{74}Ge(n,α)^{71m}Zn, όπως φαίνεται στο Σχήμα 27δ′.

Σημειώνεται ότι όλες οι τροποποιήσεις που έγιναν στα δεδομένα εισόδου κατά τη διάρκεια μελέτης των εννέα αντιδράσεων που μελετήθηκαν, έγιναν με συνεπή τρόπο και δεν επηρέασαν προηγούμενα βήματα της μελέτης.

Πρέπει επίσης να δοθεί έμφαση στο γεγονός ότι η ικανοποιητική αναπαραγωγή 9 καναλιών αντίδρασης σε πέντε ισότοπα του Ge συμπεριλαμβάνο-

ντας βασικές και μετασταθείς στάθμες, με συνεκτικό τρόπο, επιβεβαιώνει την αξιοπιστία της παραμετροποίησης που υιοθετήθηκε στους αντίστοιχους υπολογισμούς στατιστικών μοντέλων.

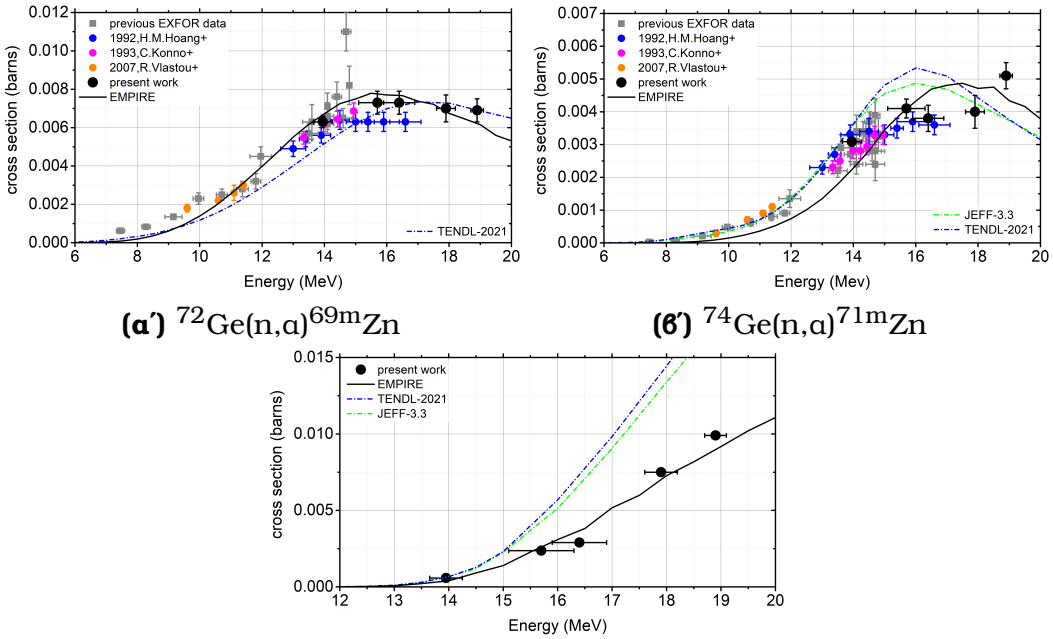

(α΄) ^{72}Ge(n,α)^{69m}Zn **(β΄)** ^{74}Ge(n,α)^{71m}Zn

(γ΄) ^{73}Ge(n,nα)^{69m}Zn

Σχήμα 27: Υπολογισμοί EMPIRE για όλες τις αντιδράσεις με σωματίδιο-α στο κανάλι εξόδου

Συμπεράσματα και Προοπτικές

Στην παρούσα διατριβή, μετρήθηκαν οι ενεργές διατομές των αντιδράσεων ^{70}Ge(n,2n)^{69}Ge, ^{72}Ge(n,α)^{69m}Zn, ^{72}Ge(n,p)^{72}Ga, ^{73}Ge(n,nα)^{69m}Zn, ^{73}Ge(n,np/d)^{72}Ga, ^{73}Ge(n,p)^{73}Ga, ^{74}Ge(n,α)^{71m}Zn, ^{74}Ge(n,np/d)^{73}Ga και ^{76}Ge(n,2n)^{75}Ge μέσω της μεθόδου της νετρονικής ενεργοποίησης ως προς την ενεργό διατομή της αντίδρασης αναφοράς ^{27}Al(n,α)^{24}Na. Η παραγωγή των νετρονικών δεσμών έγινε μέσω της αντίδρασης ^{3}H(d,n)^{4}He στις νετρονικές εγκαταστάσεις του ΕΚΕΦΕ “Δημόκριτος” (Ελλάδα) και “AMANDE”, IRSN (Γαλλία). Οι στόχοι που χρησιμοποιήθηκαν ήταν ισοτοπικά εμπλουτισμένοι στόχοι ^{70,72,73,74,76}Ge σε μορφή παστίλιας GeO_2, και τους παρείχε το n_TOF collaboration (CERN).

Τα περισσότερα από τα πειραματικά δεδομένα που βρίσκονται στη βιβλιογραφία χρησιμοποιούν στόχους ^{nat}Ge για τις μετρήσεις ενεργών διατομών. Στην περίπτωση αυτή όμως δημιουργούνται μολύνσεις από γειτονικά ισότοπα που οδηγούν στη δημιουργία του ίδιου παραγόμενου πυρήνα[1] και συνεισφέ-

[1]Η τεχνική της νετρονικής ενεργοποίησης βασίζεται στη μέτρηση της ραδιενέργειας του παραγόμενου πυρήνα. Επομένως αν δύο κανάλια αντίδρασης οδηγούν στην παραγωγή του

ρουν στο μετρούμενο φάσμα, καθιστώντας αναγκαία την εφαρμογή θεωρητικών διορθώσεων, οι οποίες συνοδεύονται από τις δικές τους αβεβαιότητες. Οι συνεισφορές αυτές γίνονται μεγαλύτερες συναρτήσει της ενέργειας νετρονίων, οδηγόντας σε διορθωμένα δεδομένα ενεργών διατομών αμφισβητίσιμης ακρίβειας. Αυτός θα μπορούσε να είναι ο λόγος για τη σημαντική έλλειψη πειραματικών δεδομένων στις αντιδράσεις που μελετήθηκαν για ενέργειες νετρονίων μεγαλύτερες των 15 MeV, καθώς και για τις ασυμφωνίες μεταξύ των υπάρχοντων πειραματικών δεδομένων ενεργών διατομών.

Η χρήση ισοτοπικά εμπλουτισμένων στόχων από την άλλη, παράγει δεδομένα υψηλότερης ακρίβειας, εφόσον τέτοιου είδους μετρήσεις δεν επηρεάζονται σημαντικά από τα είδη των μολύνσεων που αναφέρθηκαν παραπάνω. Επομένως τα αποτελέσματα της παρούσας διατριβής, παρέχουν απαραίτητα δεδομένα ενεργών διατομών σε μια ενεργειακή περιοχή που υπάρχουν πολύ λίγα ή και καθόλου αντίστοιχα δεδομένα. Επιπρόσθετα, η χρήση ισοτοπικά εμπλουτισμένων στόχων επιτρέπει τη μέτρηση αντιδράσεων με πολύ χαμηλές τιμές ενεργού διατομής (π.χ. ^{73}Ge(n,nα)^{69m}Zn). Ταυτόχρονα, αυτά τα ακριβή δεδομένα, μπορούν να δράσουν ως ένας ευαίσθητος έλεγχος για την ακρίβεια και τα όρια της μεθοδολογίας που ακολουθήθηκε στην περίπτωση χρήσης φυσικών στόχων Γερμανίου (^{nat}Ge). Σε αυτό το πλαίσιο, προτάθηκε μια μεθοδολογία διόρθωσης για τέτοιου είδους διορθώσεις, η ακρίβεια και τα όρια εφαρμογής της οποίας ελέγχθηκαν πειραματικά με δύο σειρές μετρήσεων σε ενέργεια νετρονίων 17.9 MeV. Η πρώτη σειρά μετρήσεων πραγματοποιήθηκε με χρήση στόχου ^{nat}Ge και τα διορθωμένα αποτελέσματα συγκρίθηκαν με τα αντίστοιχα αποτελέσματα της δεύτερης σειράς μετρήσεων που πραγματοποιήθηκαν με χρήση των αντίστοιχων ισοτοπικά εμπλουτισμένων στόχων Ge.

Την πειραματική μελέτη ακολούθησε μια θεωρητική, μέσω του κώδικα EMPIRE 3.2.3. Ο στόχος ήταν η ταυτόχρονη και ικανοποιητική αναπαραγωγή των εννέα καναλιών αντίδρασης που μελετήθηκαν λαμβάνοντας υπόψιν, εκτός από τα αποτελέσματα της εργασίας αυτής, μετρήσεις ενεργών διατομών της βιβλιογραφίας και από παλαιότερες μετρήσεις της ομάδας Πυρηνικής Φυσικής του ΕΜΠ, χρησιμοποιόντας ένα συνεκτικό σύνολο παραμέτρων εισόδου. Η ακριβής περιγραφή των καναλιών αυτών στα πέντε φυσικά ισότοπα του Ge, στα οποία συμπεριλαμβάνεται η παραγωγή θυγατρικών πυρήνων τόσο στη βασική όσο και σε ισομερή στάθμη, αποτελεί έναν πολύ ισχυρό περιορισμό στις παραμέτρους εισόδου υπολογισμών στατιστικών μοντέλων, επιβεβαιώνοντας την ακρίβεια και αξιοπιστία τους.

Υπάρχει όμως η ανάγκη ελέγχου της παραμετροποίησης αυτής και σε άλλα ισότοπα γειτονικής μαζικής περιοχής που παρουσιάζουν τεχνολογικό ή και θεωρητικό ενδιαφέρον (για παράδειγμα το ισότοπο ^{75}As αναγράφεται στην NEA Nuclear data high priority request list για εφαρμογές δοσιμετρίας). Επιπλέον θα παρουσίαζε μεγάλο ενδιαφέρον να γίνουν in-beam μετρήσεις, ειδικά για την περίπτωση συγκεκριμένων αντιδράσεων με σκοπό τον διαχωρισμό

ίδιου θυγατρικού πυρήνα, δεν υπάρχει τρόπος διαχωρισμού των δύο συνεισφορών.

των συζευγμένων καναλιών (n,d) και (n,np). Τέλος, μετρήσεις ενεργών διατομών με χρήση ισοτοπικά εμπλουτισμένων στόχων σε συγκεκριμένους μεσοβαρείς πυρήνες (π.χ. τα στοιχεία άρτιου Z Fe, Ni, Zn, Se, Sr με πολλά φυσικά ισότοπα), ανεξάρτητα από το κόστος τους και τη δυσκολία απόκτησής τους, θα ήταν πάρα πολύ σημαντικές για τη βελτιστοποίηση υπολογισμών στατιστικών μοντέλων, και θα οδηγούσαν σε ακριβέστερες μελλοντικές προσπάθειες αξιολόγησης, ιδιαίτερα στην υψηλοενεργειακή περιοχή των MeV, όπου παρατηρείται έλλειψη πειραματικών δεδομένων μεγάλης ακρίβειας.

Chapter 1

Introduction

Neutron-induced reaction cross sections are of major importance concerning both practical applications and fundamental research in the Nuclear Physics field. Practical applications include dosimetry, astrophysical projects, reactor technology, nuclear medicine, and the wide use of Ge in γ-ray detectors. Regarding the fundamental research interest, some (n,x) reaction channels on Ge isotopes produce residual nuclei in high-spin isomeric states. The de-excitation of such nuclei is heavily dependent on the spin distribution of the continuum phase space and the spins of the respective discrete levels involved. Accurate experimental cross-section data of (n,x) reactions that produce such residual nuclei can play a significant role in the study of the residual compound nucleus. A plethora of reaction channels is produced from the five natural occurring isotopes of Ge (^{70,72,73,74,76}Ge), revealing very interesting systematics, crucial for the optimization of statistical model calculations. The simultaneous reproduction of all the experimentally studied reaction channels, with the same set of input parameters, can act as a very important constraint in statistical model calculations. In addition, accurate cross-section data above 15 MeV are very important, since in this energy region, the contribution of the pre-equilibrium effect in the de-excitation of the compound nucleus becomes more significant.

Most of the experimental cross-section data of (n,x) reactions on Ge isotopes found in literature, are measured with ^{nat}Ge targets and are limited to energies below 15 MeV, with large discrepancies among them. It should also be underlined that similar discrepancies are observed among the different evaluation libraries, that become more prominent at higher energies.

In this scope, in the present work the ^{70}Ge(n,2n)^{69}Ge, ^{72}Ge(n,p)^{72}Ga, ^{72}Ge(n,α)^{69m}Zn, ^{73}Ge(n,p)^{73}Ga, ^{73}Ge(n,np/d)^{72}Ga, ^{73}Ge(n,nα)^{69m}Zn, ^{74}Ge(n,α)^{71m}Zn, ^{74}Ge(n,np/d)^{73}Ga and ^{76}Ge(n,2n)^{75}Ge reactions have been studied in the energy range between 14-18.9 MeV.

The cross sections were experimentally measured via the activation technique implementing five isotopically enriched Ge targets provided by the n_TOF collaboration (CERN). The irradiations were performed at the neutron beam facilities of:

- The 5.5 MV Tandem Van de Graaff Accelerator of NCSR "Demokritos" (Athens, Greece).
- The 2 MV Tandetron Accelerator of AMANDE, IRSN (France).

The quasi-monoenergetic neutron beams were produced via the ^{3}H(d,n)^{4}He (D-T) reaction in both facilities, while the necessary neutron flux was determined via the ^{27}Al(n,α)^{24}Na reference reaction. The induced radioactivity on the Ge targets and Al reference foils was measured by γ-ray spectroscopy employing HPGe detectors. The combined use of the NeuSDesc and MCNP5 codes, was implemented for the simulation of the propagation of the neutron beam through the consecutive stack of targets and reference foils.

Finally, a subsequent theoretical study of the nine aforementioned reactions was performed by Hauser-Feshbach calculations via the EMPIRE 3.2.3 code.

Chapter 2

Activation Method & Residual Nuclei

In this chapter, the basic formalism of the activation technique that was used in this work for the calculation of the cross section values of the ^{70}Ge(n,2n)^{69}Ge, ^{72}Ge(n,p)^{72}Ga, ^{72}Ge(n,α)^{69m}Zn, ^{73}Ge(n,p)^{73}Ga, ^{73}Ge(n,np/d)^{72}Ga, ^{73}Ge(n,nα)^{69m}Zn, ^{74}Ge(n,α)^{71m}Zn, ^{74}Ge(n,np/d)^{73}Ga and ^{76}Ge(n,2n)^{75}Ge reactions will be presented, along with the decay properties of the residual nuclei that were studied.

2.1 Activation Method

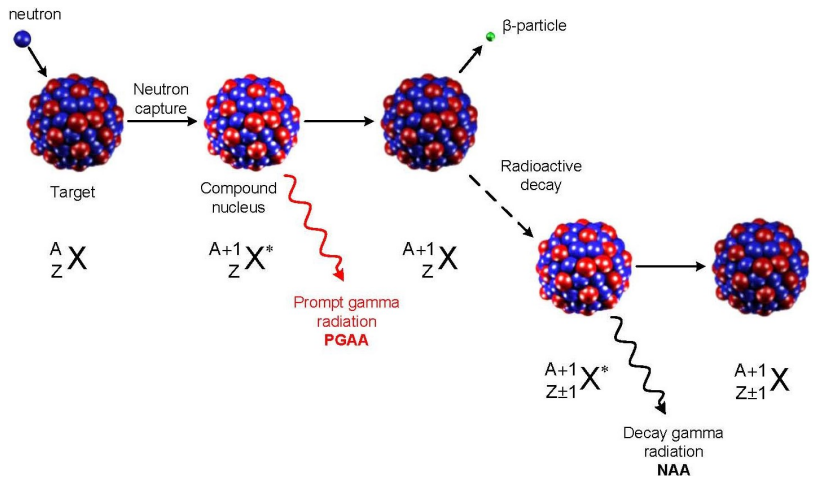

Figure 2.1: Schematic representation of the Neutron Activation Analysis method [50]

The activation method is a very precise and non-destructive technique that can be used for neutron flux determination, or for a qualitative and quantitative analysis of elements of an unknown sample. This method is based on the measurement of the prompt (Prompt Gamma Neutron Activation Analysis - PGNAA) or delayed (Delayed Gamma Neutron Activation Analysis - DGNAA) γ-ray emission from a sample that has been irradiated at a specific neutron field. In the present work, the DGNAA was employed for the cross-section measurements of reactions that will be presented in section 2.3, leading to residual nuclei with half-lives of a few hours.

As seen in Fig. 2.1, when an incident particle (e.g. neutron) impinges on a target nucleus ${}^{A}_{Z}X$, the compound nucleus ${}^{A}_{Z}X^{*}$ is formed, and may de-excite through the emission of a prompt γ-ray and a prompt particle. Then, the residual nucleus ${}^{A+1}_{Z\pm1}X$ de-excites most commonly by $\beta^{\pm}$ decay accompanied by the emission of the delayed γ-rays.

The excited nucleus produced during the neutron irradiation starts decaying at the moment of their production. In this scope, the net production of the radioactive nuclei can be described by the following differential equation:

$$\frac{dN}{dt} = \text{production} - \text{decay} \Rightarrow \frac{dN}{dt} = \sigma \cdot f(t) \cdot N_t - \lambda \cdot N \tag{2.1}$$

where:

- σ: the cross section of the reaction
- $f(t)$: the time-dependent neutron flux impinging on the target
- N_t: the number of nuclei in the target
- N: the number of the produced radioactive nuclei

The general solution of equation 2.1 is:

$$N(t) = \frac{\int e^{\lambda dt} \sigma N_t f(t) + C}{e^{\lambda dt}} \tag{2.2}$$

Assuming that the total irradiation time is t_{irr}, the total neutron flux impinging on the target will be:

$$\Phi = \int_0^{t_{irr}} f(t)dt \tag{2.3}$$

where λ is the decay constant of the produced radioactive nuclei. In this case, equation 2.1 becomes:

$$N_p(t_{irr}) = \sigma N_t \Phi \frac{\int_0^{t_{irr}} e^{\lambda dt} f(t)dt}{\int_0^{t_{irr}} f(t)dt} e^{-\lambda t_{irr}} \tag{2.4}$$

Equation 2.4 represents the total number of radioactive nuclei produced during an irradiation that lasted for $t = t_{irr}$.

Assuming

$$f_c = \frac{\int_0^{t_{irr}} e^{\lambda dt} f(t) dt}{\int_0^{t_{irr}} f(t) dt} e^{-\lambda t_{irr}} \tag{2.5}$$

as a correction factor that takes into account the produced nuclei that decayed during the irradiation, equation 2.4 becomes:

$$N_p = \sigma \cdot N_t \cdot \Phi \cdot f_c \tag{2.6}$$

In this work, the cross-section calculation of each measured reaction is performed relative to a reference one. Equation 2.6 is then applied both for the reference and the measuring target:

$$N_p^{ref} = \sigma^{ref} \cdot N_t^{ref} \cdot \Phi^{ref} \cdot f_c^{ref} \tag{2.7a}$$

$$N_p^{tar} = \sigma^{tar} \cdot N_t^{tar} \cdot \Phi^{tar} \cdot f_c^{tar} \tag{2.7b}$$

The expression for the calculation of the measured cross-section value presented in equation (2.8) is obtained by the division of equations (2.7a) and (2.7b):

$$\sigma^{tar} = \sigma^{ref} \cdot \frac{N_p^{tar}}{N_p^{ref}} \cdot \frac{N_t^{ref}}{N_t^{tar}} \cdot \frac{f_c^{ref}}{f_c^{tar}} \cdot \frac{\Phi^{ref}}{\Phi^{tar}} \tag{2.8}$$

2.2 Energy Diagrams

In this section, the energy diagrams for all the studied nuclei will be presented in Figures 2.2 to 2.6. When a neutron beam impinges on a target nucleus, the respective compound nucleus is formed in an excited state. Depending on the excitation energy provided by the neutron, the compound nucleus can de-excite via several exit channels. This mechanism can be schematically described by an energy diagram. All the energy levels described in an energy diagram are calculated with the ground state of the compound nucleus as the level of reference. It should be underlined, that in Figures 2.2 to 2.6, the solid colored lines represent the neutron beam energy in the laboratory system, while the dashed colored lines, represent the respective excitation energy of the compound nucleus in the center of mass system.

It is noted that from all the available exit channels presented in Figures 2.2 to 2.6, the ones that were available to be studied with the activation technique were the ^{70}Ge(n,2n)^{69}Ge, ^{72}Ge(n,p)^{72}Ga, ^{72}Ge(n,α)^{69m}Zn, ^{73}Ge(n,p)^{73}Ga, ^{73}Ge(n,np/d)^{72}Ga, ^{73}Ge(n,nα)^{69m}Zn, ^{74}Ge(n,α)^{71m}Zn, ^{74}Ge(n,np/d)^{73}Ga and ^{76}Ge(n,2n)^{75}Ge ones, that will be described in section 2.3.

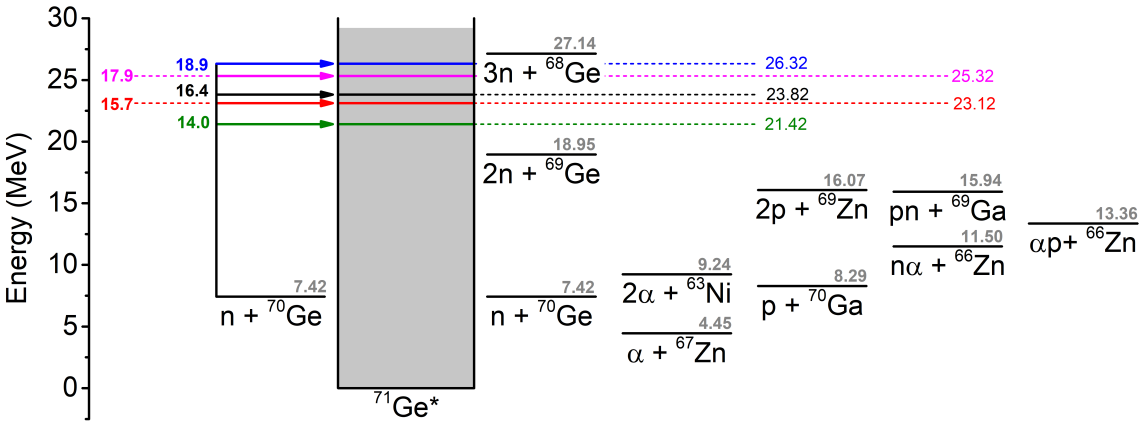

Figure 2.2: The energy diagram of the n+^{70}Ge system.

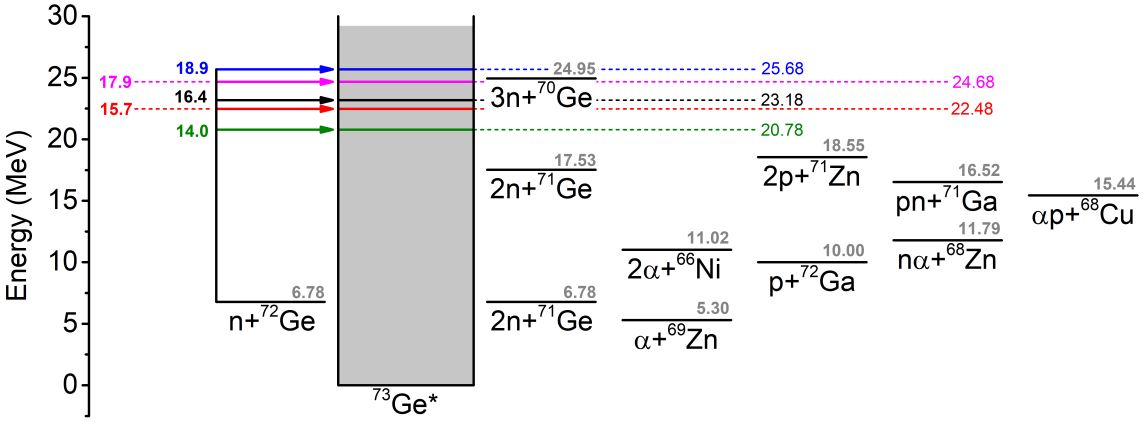

Figure 2.3: The energy diagram of the n+^{72}Ge system.

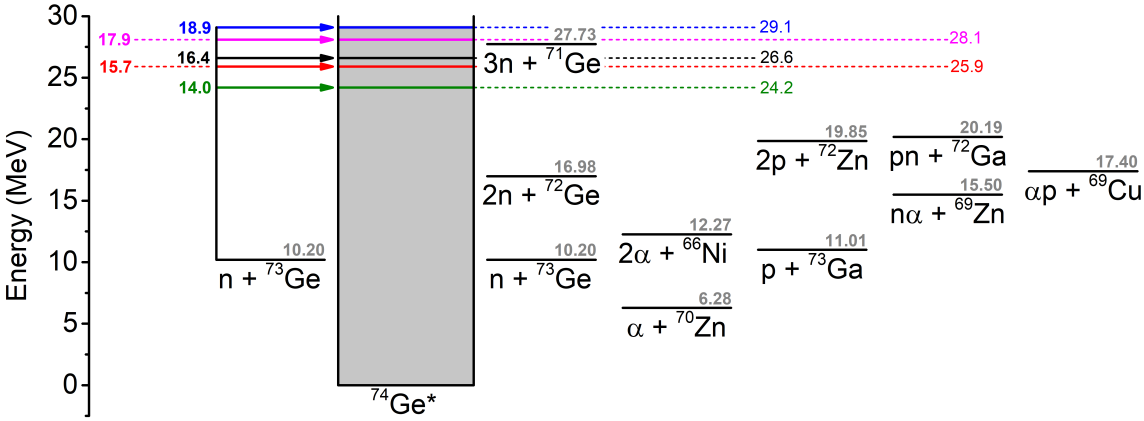

Figure 2.4: The energy diagram of the n+^{73}Ge system.

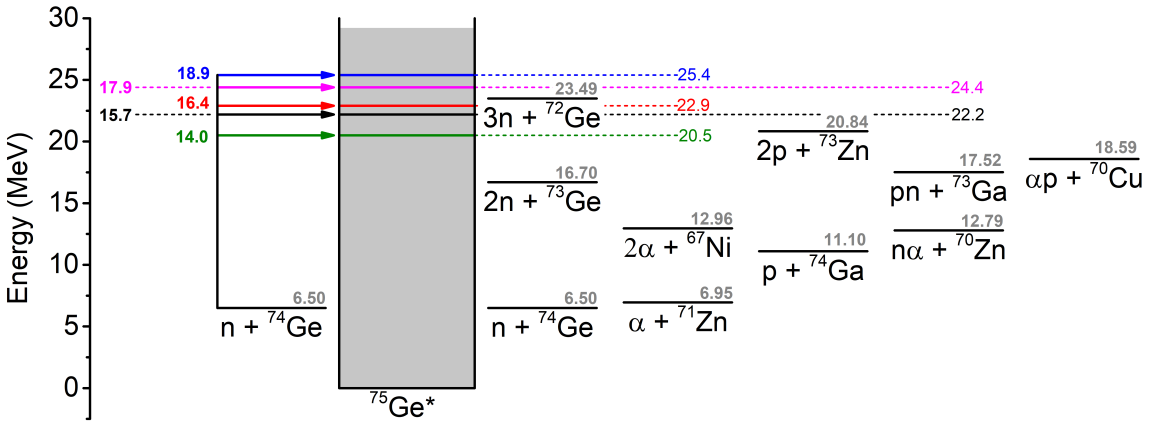

Figure 2.5: The energy diagram of the n+^{74}Ge system.

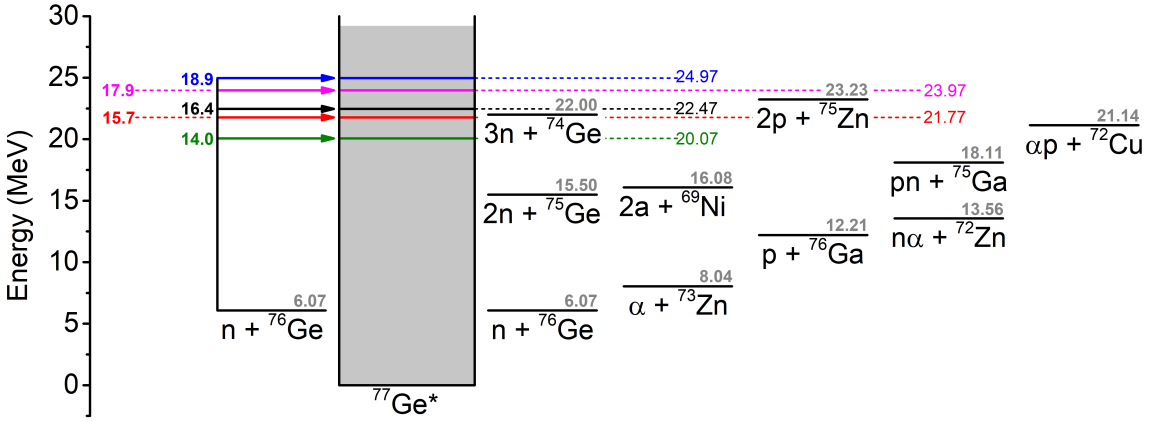

Figure 2.6: The energy diagram of the n+^{76}Ge system.

2.3 Residual Nuclei

In this section, the residual nuclei produced from the ^{70}Ge(n,2n)^{69}Ge, ^{72}Ge(n,p)^{72}Ga, ^{72}Ge(n,α)^{69m}Zn, ^{73}Ge(n,p)^{73}Ga, ^{73}Ge(n,np/d)^{72}Ga, ^{73}Ge(n,nα)^{69m}Zn, ^{74}Ge(n,α)^{71m}Zn, ^{74}Ge(n,np/d)^{73}Ga and ^{76}Ge(n,2n)^{75}Ge reactions studied in this work will be presented. The characteristic γ-rays from the de-excitation of these residual nuclei will be measured with γ-spectroscopy after the irradiation of each Ge target and eventually will be used for the cross section determination of the relevant reactions.

2.3.1 The ^{69}Ge residual nucleus

The ^{69}Ge residual nucleus is produced from the ^{70}Ge(n,2n)^{69}Ge reaction. The residual nucleus ^{69}Ge de-excites with a half life of 39.05 h (100% β^-) to ^{69}Ga (see Figure 2.7), which in turn de-excites to its ground state via emission of several γ-rays. Some of the most prominent are the 1106.77, 574.11 and 871.98 keV ones, with intensities of 36%, 13.3% and 11.9%

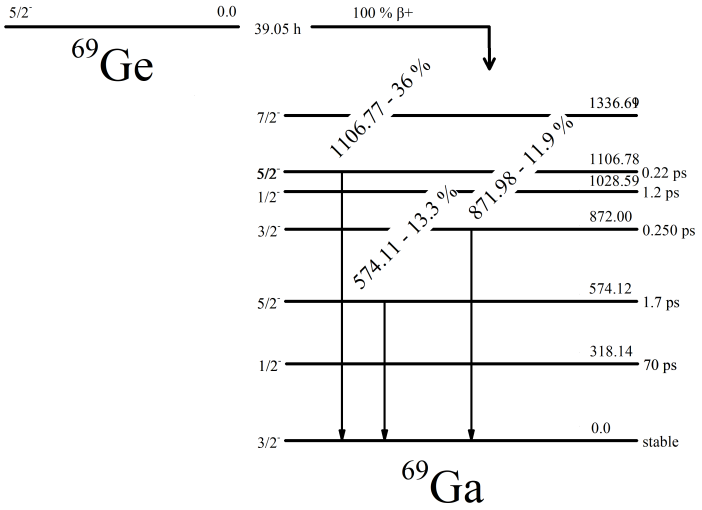

Figure 2.7: Simplified decay scheme for the de-excitation of the ^{69}Ge residual nucleus. The intensities of the γ-rays are obtained from Ref. [9].

respectively obtained from Ref. [9].

2.3.2 The ^{69}Zn residual nucleus

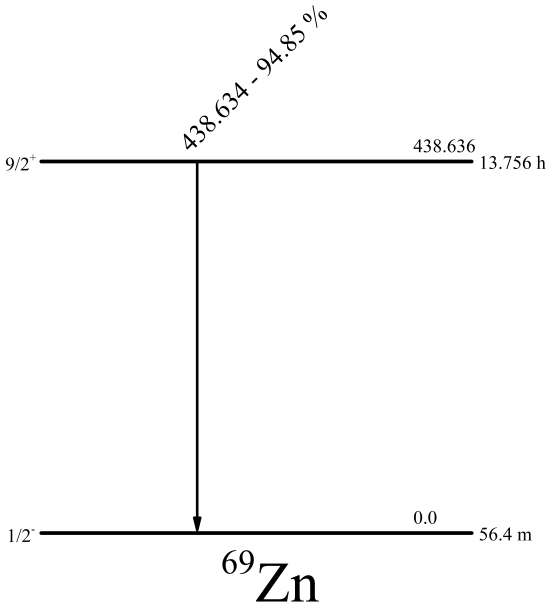

Figure 2.8: Simplified decay scheme for the de-excitation of the ^{69}Zn residual nucleus. The intensity of the characteristic γ-ray is obtained from Ref. [9].

The ^{69}Zn residual nucleus is produced from both the ^{72}Ge(n,α)^{69m}Zn and ^{73}Ge(n,nα)^{69m}Zn reactions, in both its ground and isomeric state. The

ground state of ^{69}Zn decays directly to the ground state of ^{69}Ge and could not be measured in the present work. The isomeric state (with a half-life of 13.76 h) decays to the ground state of ^{69}Zn, (see Figure 2.8), with the emission of the characteristic 438.6 keV γ-ray (with an intensity of 94.85 %, obtained from Ref. [9]).

2.3.3 The ^{71}Zn residual nucleus

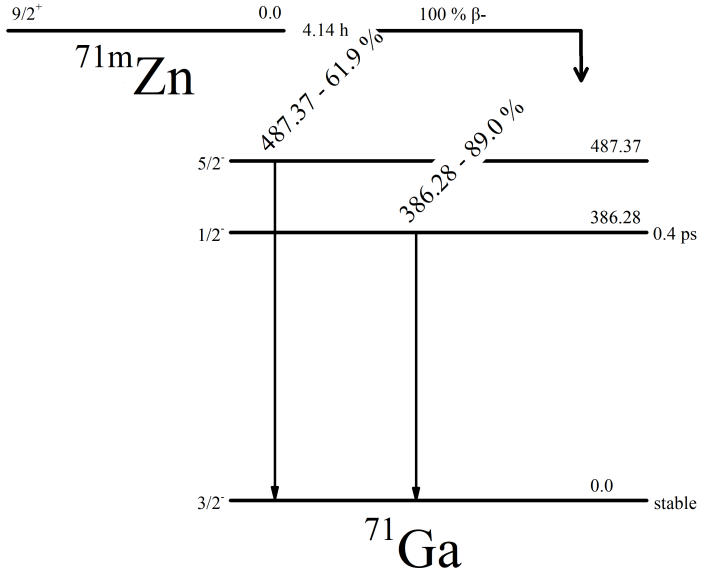

Figure 2.9: Simplified decay scheme for the de-excitation of the ^{71}Zn residual nucleus. The intensities of the γ-rays are obtained from Ref. [12].

The residual nucleus ^{71}Zn is produced from the ^{74}Ge(n,α)^{71m}Zn reaction in both its ground and metastable state, as seen in Figure 2.9. Due to the short half-life of the ground state of ^{71}Zn ($t_{1/2}$ = 2.45 m), only the activity of the metastable state ($t_{1/2}$ = 4.14 h) can be measured via the activation technique. The de-excitation of the metastable state of ^{71}Zn produces the characteristic 386.28 and 487.34 keV γ-rays with intensities of 91.4 and 61.2 % respectively as obtained from Ref. [12].

2.3.4 The ^{72}Ga residual nucleus

The ^{72}Ga residual nucleus is produced from both ^{72}Ge(n,p)^{72}Ga and ^{73}Ge(n,np/d)^{72}Ga reactions. It decays with a half-life of 14.1 h (100% β^-) to ^{72}Ge that de-excites to its ground state with the emission of several γ-rays as shown in Figure 2.10. Some of the most intense are the 834.13, 629.97 and 894.33 keV ones, with intensities of 95.45%, 26.13% and 10.14% respectively. The intensity values were obtained from Ref. [10].

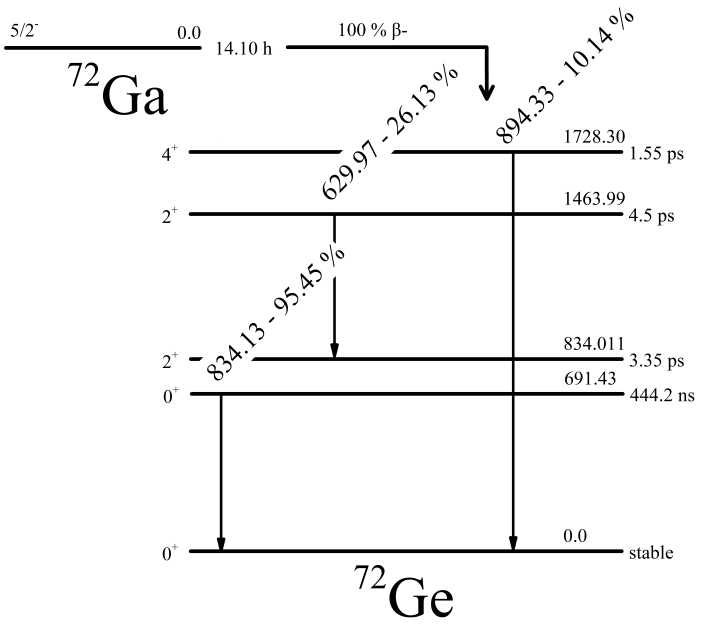

Figure 2.10: Simplified decay scheme for the de-excitation of the ^{72}Ga residual nucleus. The intensities of the γ-rays are obtained from Ref. [10]

2.3.5 The ^{73}Ga residual nucleus

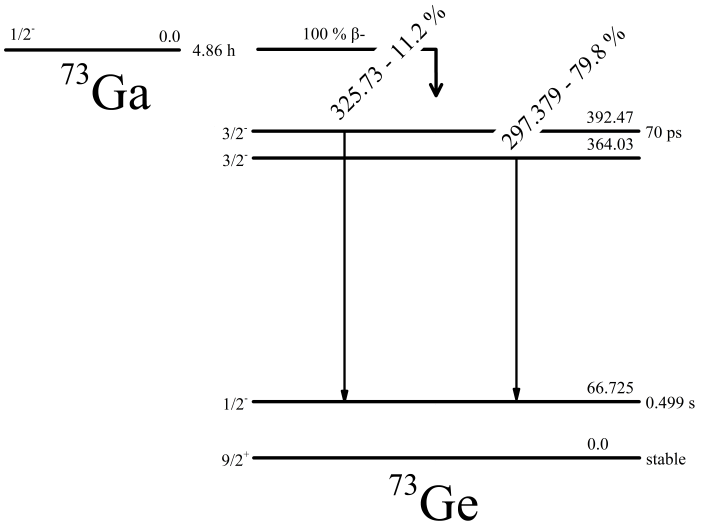

Figure 2.11: Simplified decay scheme for the de-excitation of the ^{73}Ga residual nucleus. The intensities of the γ-rays are obtained from Ref. [11].

The ^{73}Ga residual nucleus is produced from both the ^{73}Ge(n,p)^{73}Ga and ^{74}Ge(n,np/d)^{73}Ga reactions. As seen in Figure 2.11, it decays to ^{73}Ge (100% β^-) with a half life of 4.86 h, emitting the characteristic 297.38 and 325.73 keV γ-rays with respective intensities of 79.8% and 11.2%, values

obtained from Ref. [11].

2.3.6 The ^{75}Ge residual nucleus

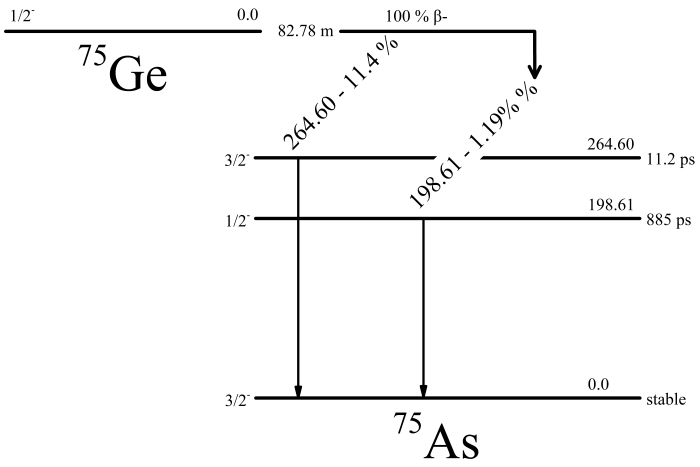

Figure 2.12: Simplified decay scheme for the de-excitation of the ^{75}Ga residual nucleus. The intensities of the ɣ-rays are obtained from Ref.[13]

.

The ^{75}Ge residual nucleus is produced from the ^{76}Ge(n,2n)^{75}Ge reaction. It decays to ^{75}As (100% β^-) with a half-life of 82.78 min. Its decay to the ground state of ^{75}As is presented in Figure 2.12 and is accompanied by the emission of the characteristic 264.60 and 198.61 keV ɣ-rays with 11.4% and 1.19% respective intensities, values obtained from Ref. [13].

Chapter 3

Experimental Details

In this chapter, the experimental details of the present work will be presented such as the neutron facilities, the neutron monitoring, information about the irradiations and the measurement of the residual radioactivity of the targets.

The measurements were performed at the neutron beam facilities of:

- The 2 MV Tandetron Accelerator of "AMANDE", IRSN, France.
- The 5.5 MV Tandem Van de Graaff Accelerator of NCSR "Demokritos", Athens, Greece.

The quasi-monoenergetic neutron beams in the 14-18.9 MeV energy range were produced via the ^{3}H(d,n)^{4}He (D-T) reaction with a Q-value of 17.59 MeV at both experimental facilities.

3.1 The "AMANDE" Facility

The Amande facility (Accelerator for metrology and neutron applications for external dosimetry) is located at the Cadarache site (Bouches-du-Rhône, France) and is run by the Microirradiation, Neutron Metrology and Dosimetry Laboratory (LMDN), which is part of IRSN's Dosimetry Research Service (SDOS) [51–53].

3.1.1 Deuteron Beam

The deuteron beam was generated from D^- ions accelerated by a voltage at the center of the accelerator, that passed through a nitrogen gas flow, stripping two of the electrons from the D^- ions, reversing their initial charge. The accelerator used is a 2 MV Tandetron™ (see Figure 3.1).

Figure 3.1: The 2 MV Tandetron™ Accelerator of the "AMANDE" facility

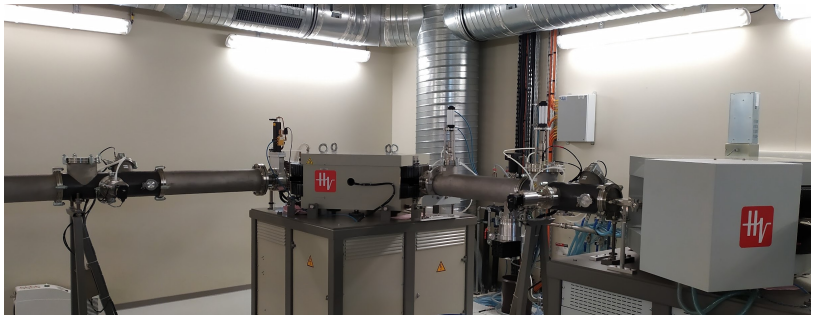

Figure 3.2: The 90° magnet of the "AMANDE" facility.

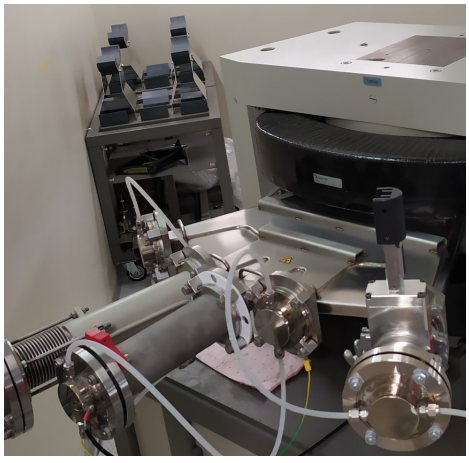

Figure 3.3: The "switching" magnet of the "AMANDE" facility.

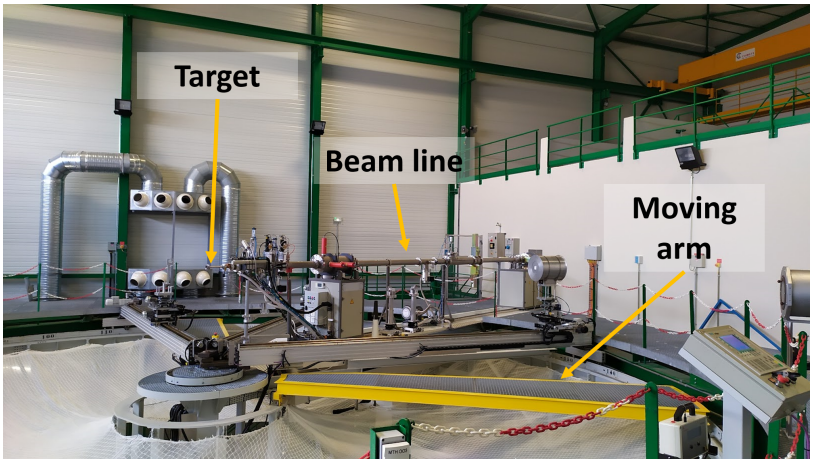

Figure 3.5: The experimental hall of the “AMANDE” facility

The deuteron beam was accelerated at 443 keV, an energy defined from the voltage in the accelerator’s terminal and the magnetic field of the 90° magnet, controlled by an NMR Tesla meter (see Figure 3.2).

Finally, the deuteron beam was driven towards the experimental hall area with the help of a “switching” magnet (see Figure 3.3). The 400 m^2 experimental hall of the facility (see Figure 3.5) is specially designed to reduce the scattering of the produced neutrons, with minimum use of material and optimized thin metallic walls. At the end of the beam line, the deuteron beam impinged on the Tritiated Ti (TiT) target, placed at a distance of 7.2 meters above the ground, producing the quasi-monoenergetic neutron beam of 13.95 MeV at an angle of 100° with respect to the axis of the deuteron beam, as shown in Figure 3.4.

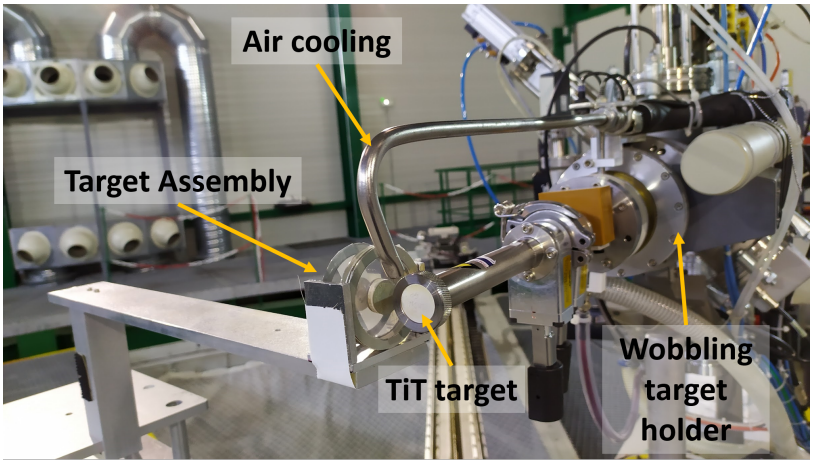

Figure 3.4: The end of the beam line with the TiT target and the target assembly placed at 100° with respect to the axis of the neutron beam.

3.1.2 The TiT target

The TiT target had a surface thickness of 780 μg/cm^2 and a T/Ti ratio of 1.62. It was placed at the end of the beam line on a wobbling target holder, and was air-cooled during the irradiations.

3.1.3 Neutron Monitoring

A 'long counter' detector is used for the determination of the neutron fluence. This detector has a tube filled with ^{3}He gas surrounded by a moderator, consisting of polyethylane and borated polyethylane. Cadmium sheets are placed at the front and at the back of the detector [54]. The data from this detector that acts as a counter, can be stored in short time intervals and used for the estimation of the neutron beam instabilities during the irradiations.

3.2 The "Demokritos" facility

The neutron beam facility of NCSR "Demokritos" is located at Aghia Paraskevi, Athens, Greece and belongs to the Institute of Nuclear and Particle Physics (INPP) [55], which is one of the eight Institutes of the National Centre for Scientific Research "Demokritos" (NCSRD), hosting the only research accelerator operating in Greece [56].

3.2.1 Deuteron Beam

Figure 3.6: The 5.5 MV Van de Graaff accelerator of the "Demokritos" facility

The deuteron beam was generated from D^- ions accelerated by a voltage at the center of the accelerator, that was stripped by two electrons when passing through either a Carbon foil or a nitrogen gas flow. This stripping process reversed the initial charge of the ion beam, enabling it to reach the final acceleration energy. The accelerator is an electrostatic Van de Graaff accelerator with a maximum voltage of 5.5 MV (see Figure 3.6).

The deuteron beam was accelerated at energies ranging from 1.8-2.8 MeV, energies defined from the voltage in the accelerator's terminal and

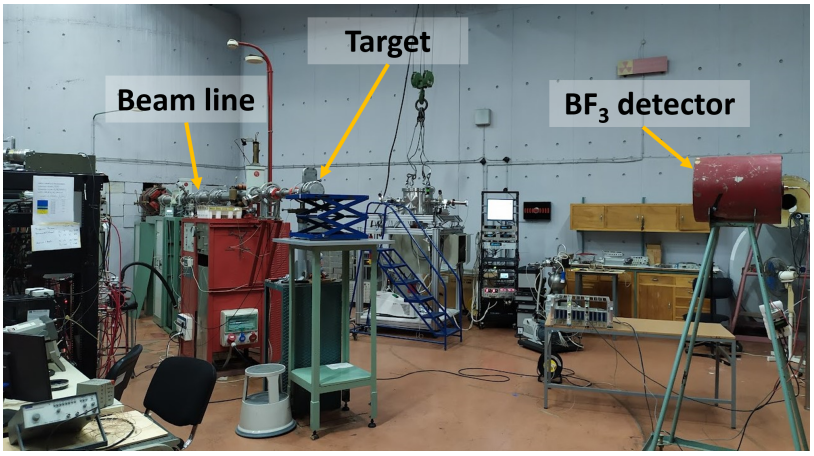

Figure 3.7: The experimental hall of the “Demokritos” facility

the 90° analyzing magnet. The ion beam is then driven towards the experimental hall with the help of a switching magnet, reaching the Tritiated Titanium (TiT) target at the end of the beam line. The 297.5 m^2 and 6.8 m height experimental hall is specially designed for neutron fields, minimizing the neutron scattering from the room, equipped with borated concrete walls up to 1.2 m thickness for radioprotection reasons (see Figure 3.7).

3.2.2 The TiT target

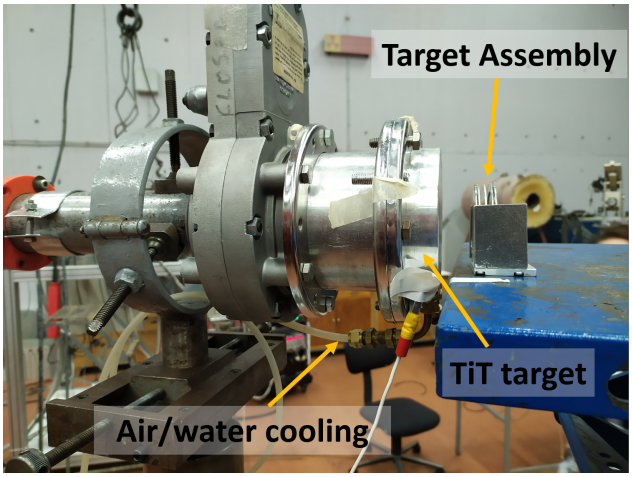

Figure 3.8: The end of the beam line with the TiT target and the target assembly placed at 0° with respect to the axis of the neutron beam

The TiT target used at the “Demokritos” facility had a surface thickness of 2123.5 μm/cm^2 and a T/Ti ratio of 1.54. The TiT target was placed in an aluminum flange equipped with a 10 μm Mo entrance foil and a 1 mm Cu backing that acted as a beam stop. The flange was kept in high vacuum

during the experiments acting also as a Faraday cup for the measurement of the charge of the ion beam reaching the target. The target was either air or water cooled (depending on the ion beam current value, reaching the TiT target) during the irradiations to prevent any potential thermal damage caused by the impinging ion beam (see Figure 3.8).

3.2.3 Neutron Monitoring

The neutron beam fluctuations during the irradiations were measured with a BF_3 detector placed at ∼3 m from the neutron producing target, and at a large forward angle relative to the axis of the neutron beam to minimize the effect of backscattering. BF_3 is a gas detector, acting as a proportional counter. The signals from this detector come from the energy deposition of α particles and ^{7}Li nuclei stemming from the reactions:

$$^{10}\mathrm{B(n,\alpha)^7Li} \qquad \mathrm{Q-value} = 2.792\,\mathrm{MeV}\ (6\%)$$
$$^{10}\mathrm{B(n,\alpha)^7Li^*} \qquad \mathrm{Q-value} = 2.310\,\mathrm{MeV}\ (94\%)$$

The ^{7}Li residual nucleus is produced either at the ground or at an isomeric state for 6 and 94% of the reactions respectively. Both of those reactions have very high cross-section values in the thermal energy region. For that reason, the BF_3 detector is surrounded by a parafin cylinder that thermalizes the neutrons. The data from this detector are stored in short time intervals in multichannel scaling mode, providing information about the neutron beam instabilities during the irradiation. It should be noted here, that the BF_3 detector is used only as a counter and does not provide information about the neutron energy spectrum.

3.3 Targets

3.3.1 Ge Targets

The isotopically enriched Ge targets used in this work were in the form of GeO_2 pellets of ∼2 g each, and were provided by the n_TOF collaboration (CERN). The enrichment levels of the targets are presented in Table 3.1[1]. The GeO_2 pellets were glued on a thin mylar foil, attached to a frame in the form of a ring (see Figure 3.9). Each frame had an outer radius of 29.8 mm and an inner one of 24.3 mm, while the thickness of each of the support rings was 1.4 mm. The diameter of each Ge pellet was 20 mm. The material of the frame was either Al or plastic and the thickness of the Ge pellets varied between ∼2.7 and 3.4 mm.

[1]For comparison purposes, it is noted that the natural abundance for the ^{70,72,73,74,76}Ge isotopes is 20.52, 27.45, 7.76, 36.52 and 7.75 %, respectively.

Table 3.1: Enrichment Levels of the GeO_2 pellets

Target/ Isotopic distribution (%)	^{70}Ge	^{72}Ge	^{73}Ge	^{74}Ge	^{76}Ge
^{70}Ge	97.71	2.23	0.02	0.03	0.01
^{72}Ge	0.35	96.59	2.86	0.20	0.01
^{73}Ge	0.04	2.84	96.07	1.03	0.02
^{74}Ge	1.46	0.18	0.45	95.51	2.40
^{76}Ge	0.06	0.09	0.06	11.33	88.46

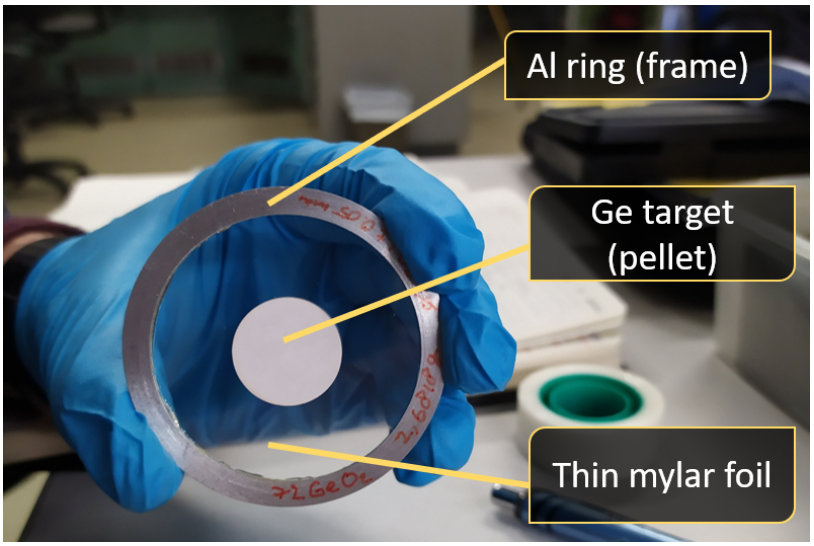

Figure 3.9: Each enriched Ge pellet was glued on a thin mylar foil, attached to a ring.

3.3.2 Reference Targets

Since the activation method is performed in a relative way (as it will be explained in detail in Chapter 4), reference targets were used in this work for the neutron flux determination. More specifically, Al and Au reference targets were implemented in the form of high purity metallic foils. The mass of the Al foils was in the order of 0.4 g, with a thickness of 5 mm, while the Au foil used had a mass in the order of $\sim$ 3.3 g with a thickness of 6 mm. The diameter of the reference foils matched the one of the Ge pellets being 20 mm. They were also glued on a thin mylar foil attached to a Fe ring of 1.4 mm thickness, having the same outer and inner radius as the one referring to the Ge pellets. It is underlined here, that for each irradiation, each Ge target was placed between two reference foils.

3.3.3 Target Holder

The target assembly of Ge targets and reference foils was placed at a specially designed target holder (presented in Figure 3.10), with fixed positions for each support ring having an accurate placement-reproducibility. The distance between two consecutive positions in the target holder is 2 mm.

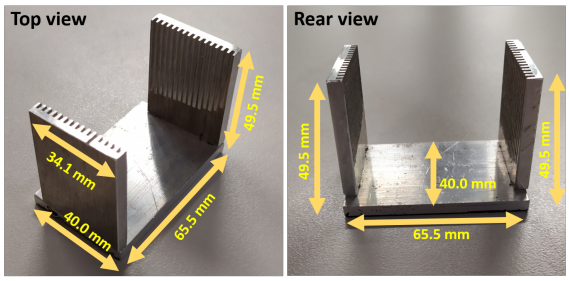

(a) Top and rear view of the target holder for the Ge targets and the reference foils.

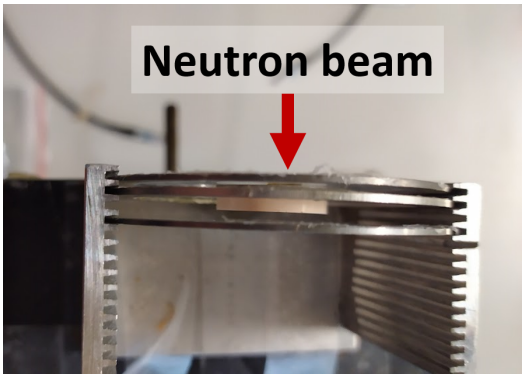

(b) The target holder (seen from the top) with a Ge sample (white pellet) placed between two Al reference foils at fixed positions.

Figure 3.10: The target holder used for the target assembly.

3.4 Irradiations

Five irradiations were performed, each referring to a different neutron energy. Each irradiation lasted for a week, with each day reserved for a different Ge isotopic target. In Table 3.2 some experimental details about the different irradiations are provided such as the date and facility in which the measurements were carried out, the deuteron and neutron energy (in the laboratory system), along with typical ion beam current values and irradiation times.

Table 3.2: Experimental details about the irradiations

Date	Facility	E_d (MeV)	E_n (MeV)	I (μA)	t_{irr} (h)
Feb 2020	NCSRD	2.90	17.9 ± 0.3	$0.4 - 0.6$	$5 - 25$
May 2021	NSCRD	3.45	18.9 ± 0.3	$0.2 - 0.7$	$3 - 28$
Dec 2021	NCSRD	2.25	16.4 ± 0.4	$0.2 - 0.4$	$7 - 27$
Jan 2023	NCSRD	2.09	15.7 ± 0.5	$2.0 - 3.0$	$5 - 7$
Feb 2023	AMANDE	0.44	14.0 ± 0.3	$2.0 - 3.0$	$2 - 5$

3.4.1 Irradiation Setups

The irradiation setup in each case consisted of a Ge sample "sandwiched" between two reference foils (see Figure 3.10b). The distance between the first sample and the neutron producing target varied between 2.5 and 3.7 cm, thus ensuring a maximum angular acceptance of $\pm 20^{\circ}$, where the neutron beam produced by the D-T reaction can be considered almost monoenergetic.

3.4.2 Neutron Energy and Uncertainty - Monte Carlo Simulations

The reproduction of the neutron spectra, for the determination of the neutron energy, the respective uncertainty and relative flux values between the measuring targets and the reference foils, was achieved via the combined use of NeuSDesc [2, 3] and MCNP5 [4] Monte Carlo codes.

NeuSDesc code takes into account the energy loss, energy and angular straggling of the deuterons incorporating the characteristics of the different elements of the neutron producing target (entrance foil material and respective thickness, type of target with the respective surface concentration, Ti/T ratio in the case of TiT target etc) via the SRIM-2008 Monte Carlo code [5]. It calculates average neutron energies, fluences and resolutions. NeuSDesc also offers the choice of producing a source-definition (SDEF) card for the MCNP code, at a specific point in the xyz space. A typical NeuSDesc input used in this work, included the description of the:

- Type and thickness of entrance foil
- TiT target (TiT ratio, thickness)
- Deuteron beam energy
- The x,y,z coordinates of the neutron point(s) generation, along with the directional cosines relative to the neutron beam axis for the production of a SDEF card

The calculated neutron energy spectra from the NeuSDesc code are presented in Figure 3.11, taking into account the energy and angular straggling of the ion beam by the SRIM 2008 code.

The NeuSDesc output in this case is an SDEF card, that will be fed into the MCNP5 code. The geometry of the TiT target and the target holder assembly is also described in the MCNP5 code (see Figure 3.12). The next step in order to determine the neutron energy and respective uncertainty is to propagate the produced neutron beam and "score" it (f4 tally) to the consecutive set of Ge targets and reference foils (see Figure 3.13a).

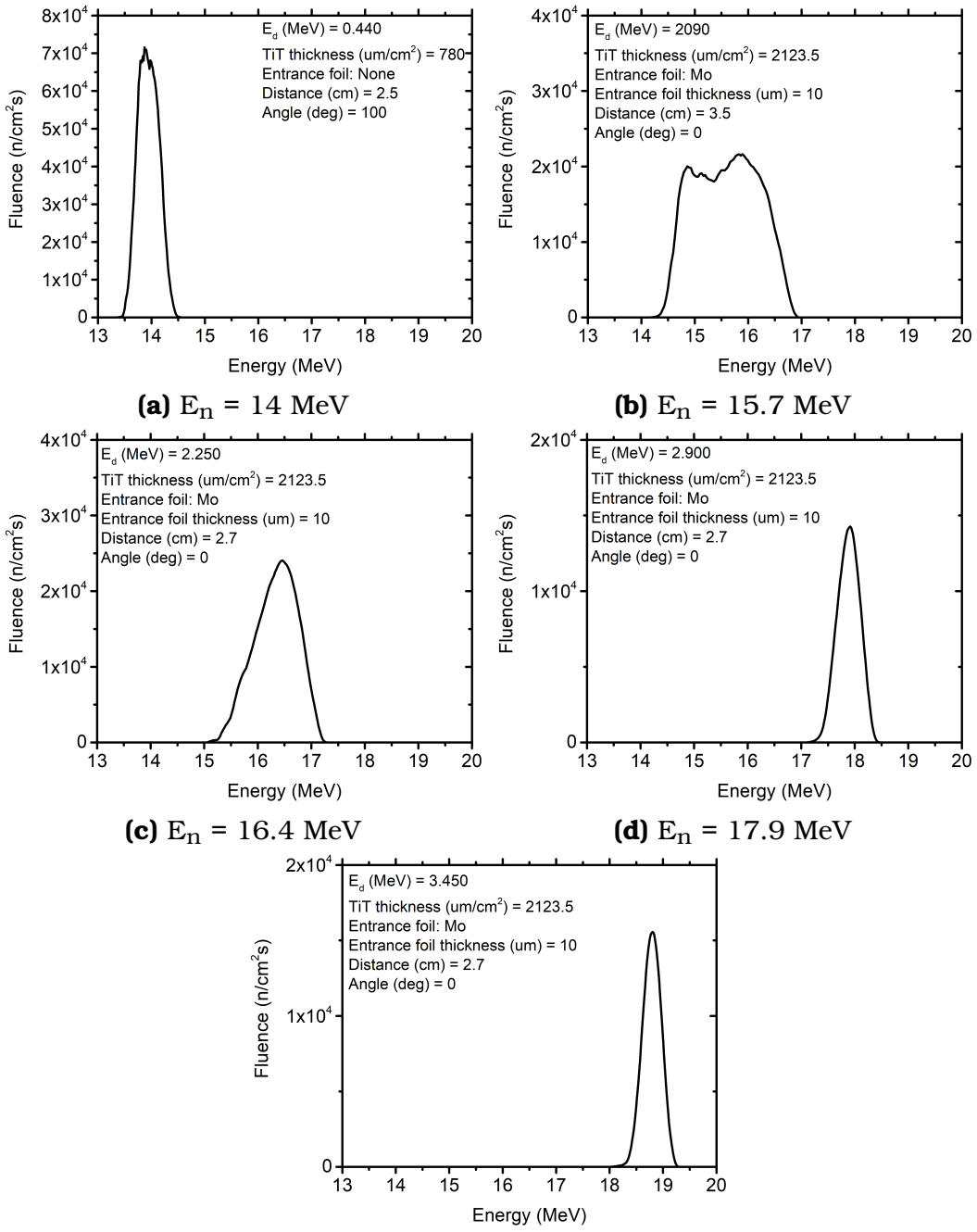

Figure 3.11: The neutron spectra as an output of the NeuSDesc code, taking into account the different experimental characteristics in each case (TiT target, entrance foil thickness, distance of the first foil from the TiT target and detection angle). For all cases, the deuteron beam current was assumed to be 1 μA and the detector radius 1 cm.

As presented in Figure 3.13a, the main beam is accompanied by a tail of low energy parasitic neutrons. The source of these parasitic neutrons in-

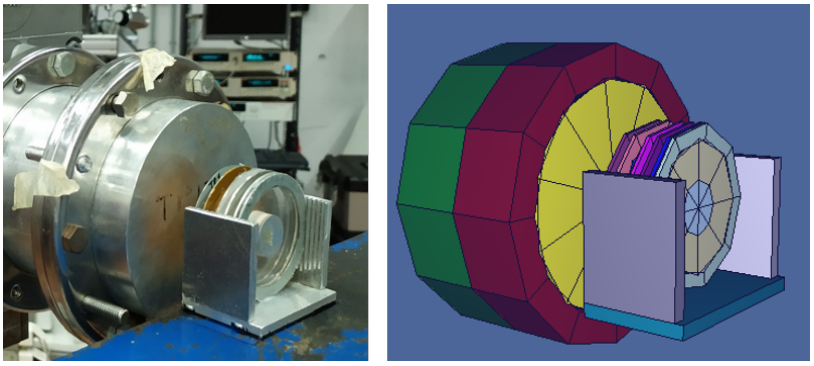

Figure 3.12: The description of the TiT target and the target holder assembly via the MCNP5 code (right panel) and an actual picture of the setup (left panel).

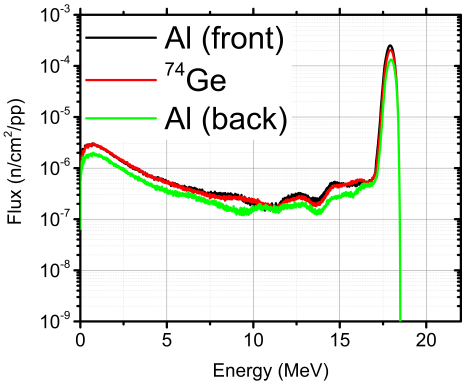

(a) The neutron flux scoring from the MCNP f4 tally.

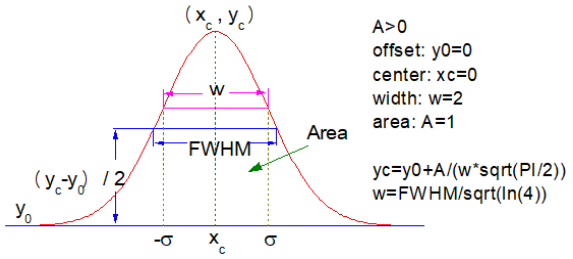

(b) The Gaussian fitting function

Figure 3.13: 3.13a: A typical shape of the neutron flux as a result of the MCNP5 f4 tally scoring in the two Al reference foils and the Ge target. This plot refers to the 17.9 MeV neutron energy case.
3.13b: The fitting function used for the neutron energy and the respective uncertainty determination.

clude break-up reactions (with significant contributions for deuteron energies higher than 3.7 MeV), neutron scattering and ^{12}C(d,n)^{13}N and ^{16}O(d,n)^{17}F reactions due to the carbon build-up process in the beam line and vacuum system, as well as oxidation processes. Furthermore, due to the implantation of deuterons in the target, the ^{2}H(d,n)^{4}He reaction can also produce parasitic neutrons [6]. The main energy peak is fitted with a gaussian function:

$$y_c = y_0 + \frac{A}{w \cdot \sqrt{\pi/2}}, \qquad w = \frac{FWHM}{\sqrt{\ln(4)}}$$

It should be underlined that specifically for the 15.7 MeV case, the shape of the neutron flux significantly deviated from a gaussian shape. Thus,

using the formulas (4.21) and (4.22) of Ref. [7] for the weighted average and the corresponding variance, the mean energy value and the associated uncertainty were determined.

The mean neutron energy values and the corresponding uncertainties are presented in Table 3.2.

The integration of the main peak is used for the determination of the Φ_r/Φ_m factor of equation 4.1 in Chapter 4. This factor is used for the determination of the neutron flux at the position of a measured Ge target, based on Monte Carlo simulations. In order to test the validity of the simulated neutron flux values the following methodology is followed:

1. The neutron flux is experimentally measured for all the available reference foils (e.g. Al, Au).

2. Monte Carlo simulations are performed and the respective simulated neutron flux value is obtained via the Φ_r/Φ_m ratio.

3. The two aforementioned values are compared, and if the agreement is satisfactory, the Monte Carlo simulations can be considered reliable for the calculation of the neutron flux at the position of the Ge measured target.

A typical example of such as comparison is presented in Figure 3.14. Since the agreement between the experimentally calculated and simulated (MCNP) flux values is excellent within the statistical uncertainties of the measurements, the simulations can be trusted for the estimation of the neutron flux at the position of the Ge targets.

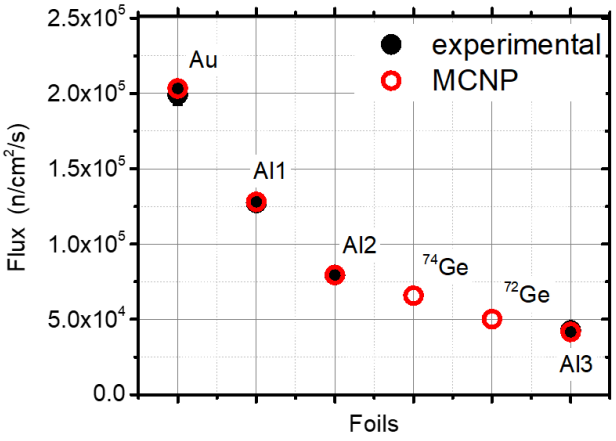

Figure 3.14: A typical example for the experimental and simulated neutron fluxes, obtained from the irradiation of the ^{72,74}Ge targets at neutron energy of E_n = 16.4 MeV.

3.5 HPGe Measurements

Following the irradiations, the induced radioactivity of the measured Ge targets and reference foils was measured via high purity Ge (HPGe) detectors of 13% - 80% relative efficiency. Typical examples of HPGe detectors are presented in Figures 3.15 and 3.16 The measurements were performed at a distance of 7-10 cm from the detector window considering the counting rate of the measuring sample. The distance was chosen in order to minimize the pile-up or true coincidence summing effect corrections (for more information see Appendix B). The absolute efficiency of each detector was experimentally measured, via the use of a ^{152}Eu point source, placed at the same distance as the measuring sample. A typical spectrum of a ^{152}Eu source is presented in Figure 3.17, while the absolute efficiency curve as a function of γ-ray energy is presented in Figure 3.18, obtained from a HPGe detector with a 13% relative efficiency.

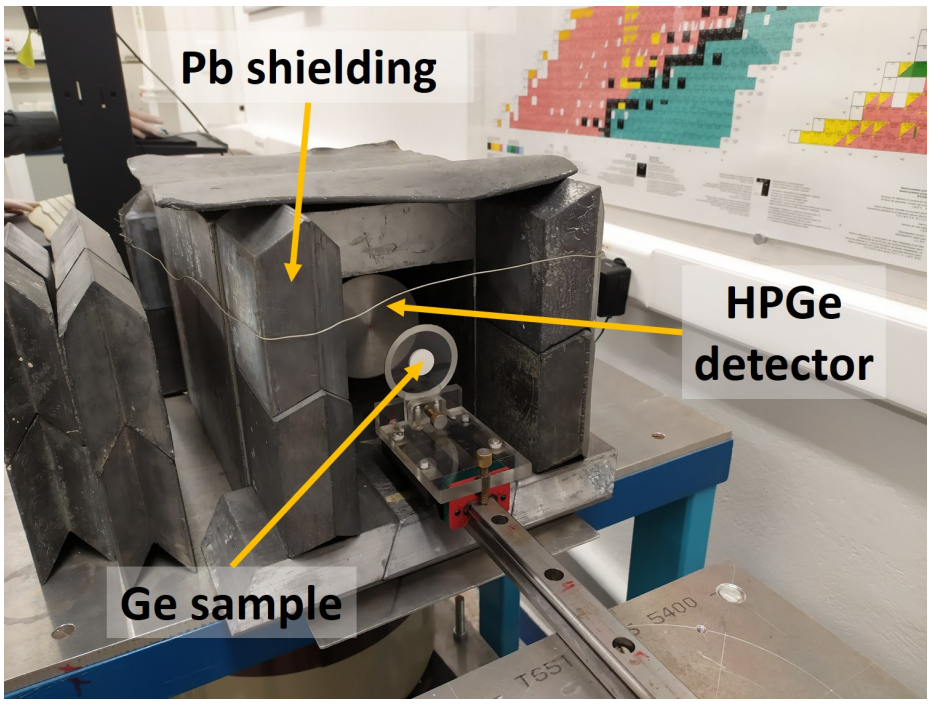

Figure 3.15: An 80% HPGe detector of the "Demokritos" facility properly shielded with a stack of Pb blocks to minimize the contribution of γ-ray background in the measured spectra

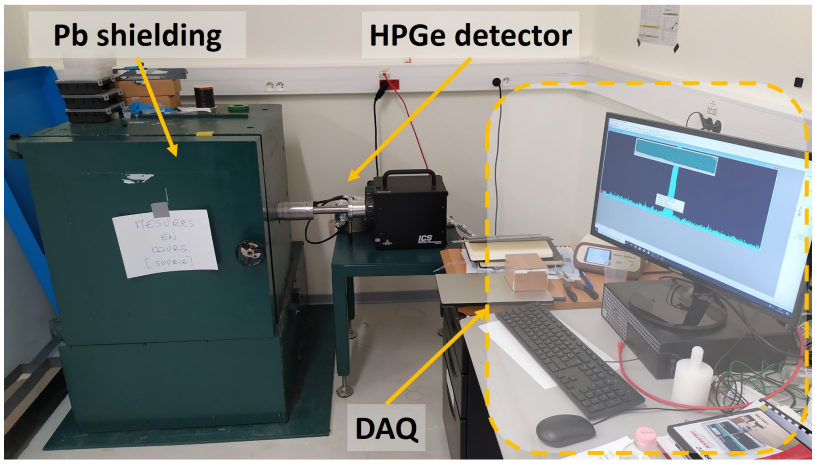

(a) The HPGe detector of the "AMANDE" facility properly shielded with a Pb box to minimize the contribution of γ-ray background in the measured spectra

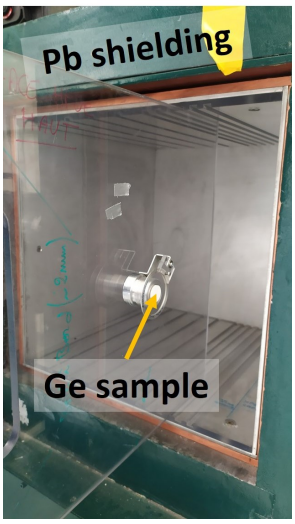

(b) The placement of the Ge sample in front of the HPGe detector of the "AMANDE" facility

Figure 3.16: The 13% HPGe detector of the AMANDE facility

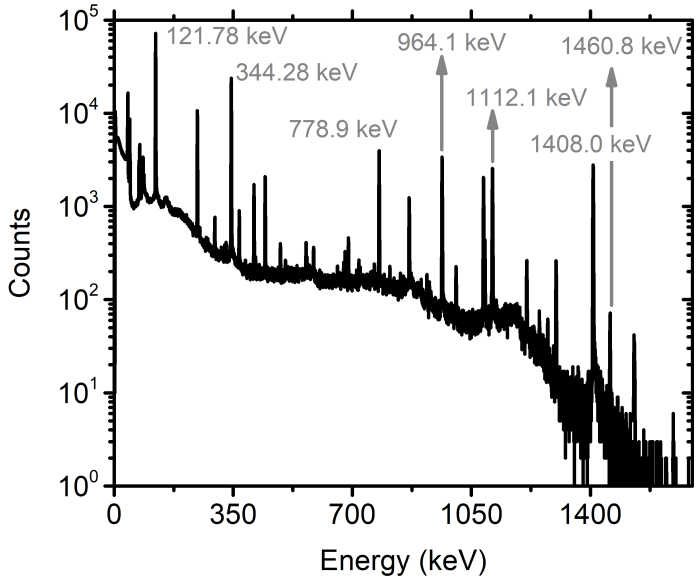

Figure 3.17: A typical γ-ray spectrum of a ^{152}Eu point source obtained from a HPGe detector of 13% relative efficiency. Some characteristic γ-ray lines from the ^{152}Eu decay are presented, along with the 1460.8 keV line from ^{40}K (natural γ-ray background).

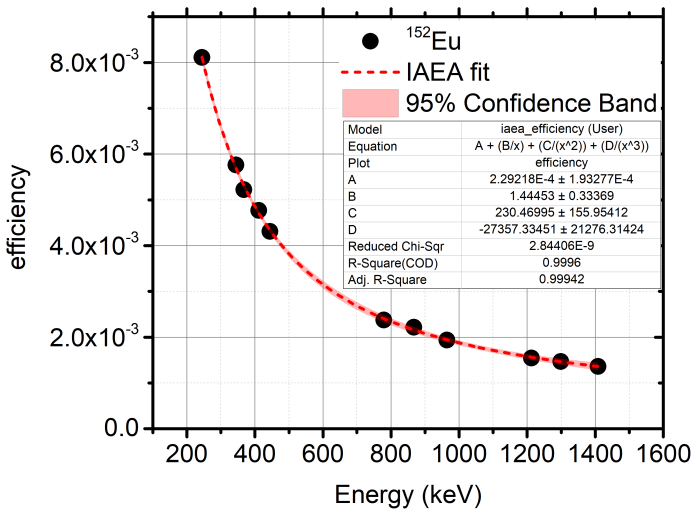

Figure 3.18: The absolute efficiency of a HPGe detector of 13% relative efficiency as a function of γ-ray energy. The black solid points represent the experimental absolute efficiency points calculated via the ^{152}Eu point source, placed at 10 cm from the detector window. The red dashed line represents the fitting of the experimental points via the standard IAEA function [8], while the shaded region represents the 95% level confidence level band.

3.5.1 Measured Reactions

In the present work, the cross sections of the ^{70}Ge(n,2n)^{69}Ge, ^{72}Ge(n,p)^{72}Ga, ^{72}Ge(n,α)^{69m}Zn, ^{73}Ge(n,p)^{73}Ga, ^{73}Ge(n,np/d)^{72}Ga, ^{73}Ge(n,nα)^{69m}Zn, ^{74}Ge(n,α)^{71m}Zn, ^{74}Ge(n,np/d)^{73}Ga and ^{76}Ge(n,2n)^{75}Ge reactions have been experimentally measured via the activation technique, which is based on the measurement of the induced radioactivity of the daughter nuclei produced from each reaction. The decay data of the measured reactions (half life of daughter nucleus, γ-ray energies and respective intensities) are presented in Table 3.3. It should be underlined at this point, that since the activation technique is based on the measurement of the decay properties of the residual nucleus produced from each measured reaction, in the case of (n,np) and (n,d) reactions, the same residual nucleus is produced, and these two reaction channels cannot be distinguished with the activation technique. Therefore, the cross-section result in this case will be the sum of the aforementioned reaction channels.

Typical experimental γ-ray spectra obtained from a HPGe detector (of 13% relative efficiency) are presented in Figures 3.19, 3.20, 3.21, 3.22 and 3.23, time normalized in their respective (live) time acquisitions. These off-beam γ-ray spectra were obtained following the irradiation at the 14.0 MeV neutron beam energy.

Table 3.3: The decay data of the measured and reference (^{24}Al(n,α)^{24}Na, ^{197}Au(n,2n)^{196}Au) reactions. The most intense γ-rays observed in the experimental spectra are presented with their respective intensities.
†: The (n,np) and (n,d) reaction channels produce the same residual nucleus and cannot thus be distinguished via the activation technique.

Target	Reaction	Daughter Nucleus	$t_{1/2}$ (h)	E_γ (keV)	I_γ (%)	Ref
^{70}Ge	(n,2n)	^{69}Ge	39.1	1106.77	36.0 ± 4	[9]
				574.11	13.3 ± 1.8	[9]
				871.98	11.9 ± 1.6	[9]
				1336.60	4.5 ± 0.6	[9]
				318.63	1.6 ± 0.20	[9]
^{72}Ge	(n,p)	^{72}Ga	14.1	834.13	95.45 ± 0.08	[10]
				629.97	26.13 ± 0.04	[10]
				894.33	10.136 ± 0.015	[10]
	(n,α)	^{69m}Zn	13.8	438.63	94.85 ± 0.07	[9]
^{73}Ge	(n,p)	^{73}Ga	4.9	297.32	79.8 ± 1.0	[11]
				325.70	11.2 ± 0.4	[11]
				739.42	4.3 ± 0.3	[11]
	(n,np/d)†	^{72}Ga	14.1	834.13	95.45 ± 0.08	[10]
				629.97	26.13 ± 0.04	[10]
				894.33	10.136 ± 0.015	[10]
	(n,nα)	^{69m}Zn	13.8	438.63	94.85 ± 0.07	[9]
^{74}Ge	(n,α)	^{71m}Zn	4.0	386.28	89.0 ± 1.1	[12]
				487.34	61.9 ± 0.4	[12]
				620.19	54.5 ± 0.7	[12]
	(n,np/d)†	^{73}Ga	4.9	297.32	79.8 ± 1.0	[11]
				325.70	11.2 ± 0.4	[11]
				739.42	4.3 ± 0.3	[11]
^{76}Ge	(n,2n)	^{75}Ge	1.4	264.60	11.4 ± 1.1	[13]
				198.60	1.19 ± 0.12	[13]
^{27}Al	(n,α)	^{24}Na	15.0	1368.63	99.994 ± 0.002	[14]
^{197}Au	(n,2n)	^{196}Au	148.1	355.73	87 ± 3	[15]
				333.03	22.9 ± 0.9	[15]

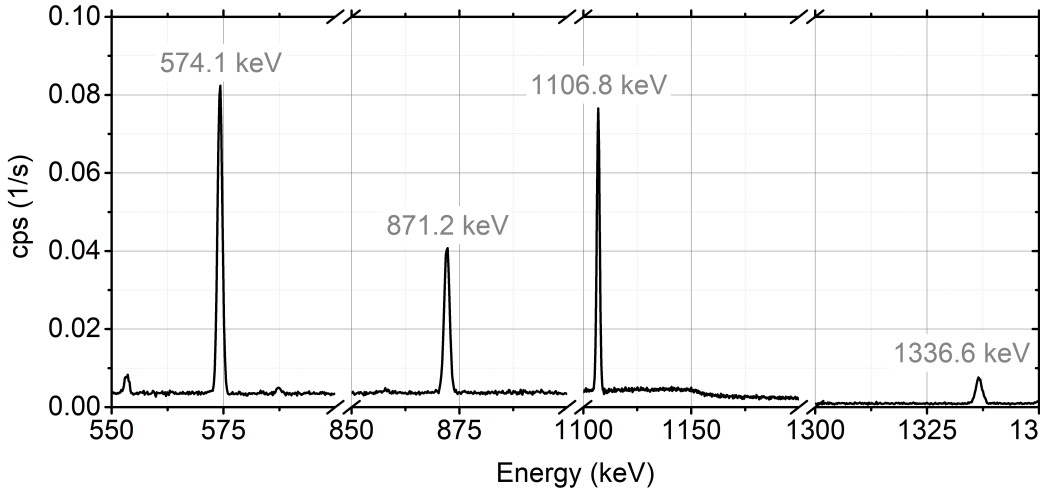

Figure 3.19: The γ-ray spectrum obtained from the ^{70}Ge sample at the 13.95 MeV neutron energy. The γ-rays emitted from the ^{69}Ge residual nucleus following the ^{70}Ge(n,2n)^{69}Ge reaction are presented.

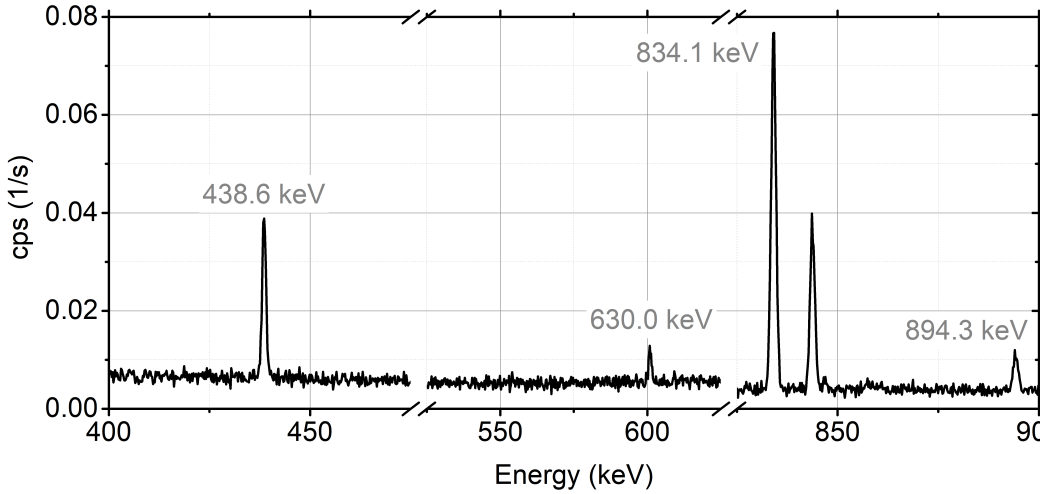

Figure 3.20: The γ-ray spectrum obtained from the ^{72}Ge sample at the 13.95 MeV neutron beam energy. γ-rays from two different reactions are observed in this spectrum:
^{72}Ge(n,p)^{72}Ga: 630.0, 834.1 and 894.3 keV
^{72}Ge(n,α)^{69m}Zn: 438.6 keV

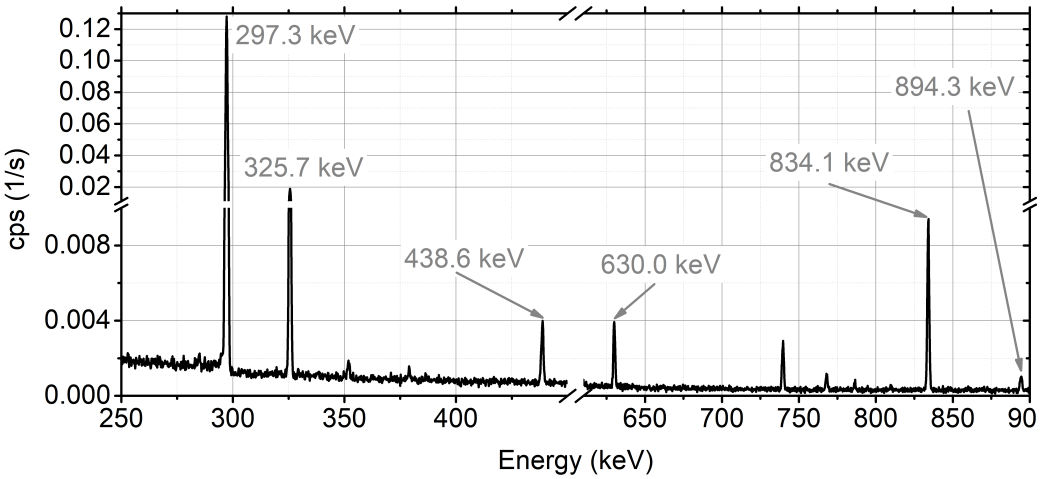

Figure 3.21: The γ-ray spectrum obtained from the ^{73}Ge sample at the 13.95 MeV neutron beam energy. γ-rays from three different reactions are observed in this spectrum: ^{73}Ge(n,p)^{73}Ga: 297.3 and 325.7 keV
^{73}Ge(n,np/d)^{72}Ga: 630.0, 834.1 and 894.3 keV
^{73}Ge(n,nα)^{69m}Zn: 438.6 keV

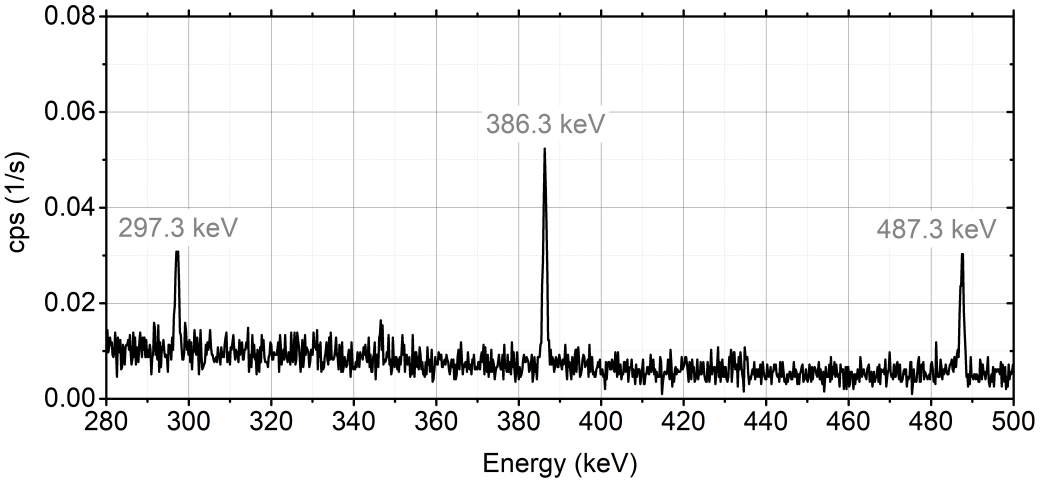

Figure 3.22: The γ-ray spectrum obtained from the ^{74}Ge sample at the 13.95 MeV neutron beam energy. γ-rays from two different reactions are observed in this spectrum:
^{74}Ge(n,α)^{71m}Zn: 386.3 and 487.3 keV
^{74}Ge(n,np/d)^{73}Ga: 297.3 keV

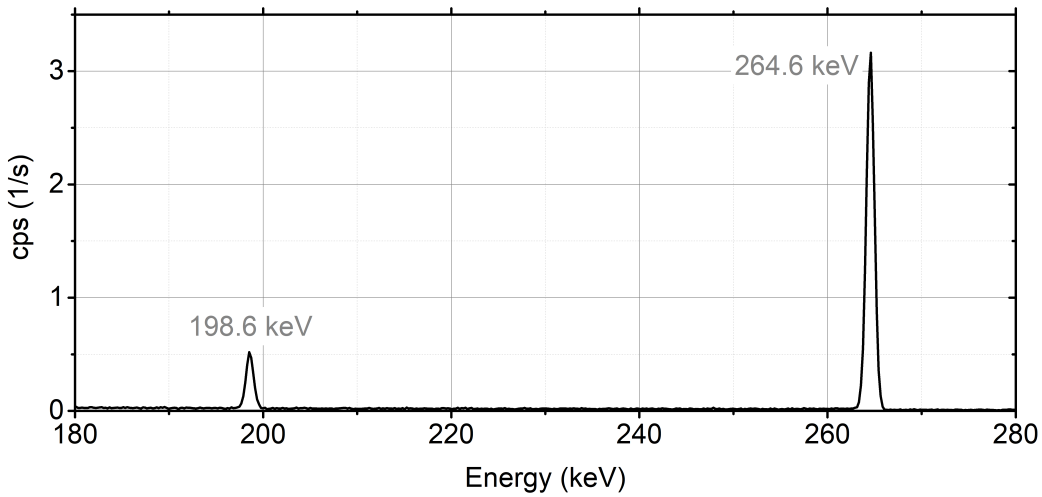

Figure 3.23: The γ-ray spectrum obtained from the ^{76}Ge sample at the 13.95 MeV neutron beam energy. The γ-rays emitted from the ^{75}Ge residual nucleus following the ^{76}Ge(n,2n)^{75}Ge reaction are presented.

Chapter 4

Results & Discussion

4.1 Cross-Section Calculation

The experimental cross-section values based on the activation method were calculated via the following expression:

$$\sigma_m = \sigma_r \cdot \frac{N_{\gamma,m}}{N_{\gamma,r}} \cdot \frac{(\varepsilon_\gamma \cdot I_\gamma \cdot F \cdot D \cdot f_c \cdot N_t)_r}{(\varepsilon_\gamma \cdot I_\gamma \cdot F \cdot D \cdot f_c \cdot N_t)_m} \cdot \frac{\Phi_r}{\Phi_m} \tag{4.1}$$

where the subscripts “m” and “r” refer to “measured” and “reference” respectively. The factors of equation 4.1 are explained below, accompanied by their respective uncertainties.

In the following sections, the calculation of each factor, along with its respective uncertainty is presented in more detail.

4.1.1 Reference Cross Section - σ_r

The cross-section value of the reference ^{27}Al(n,α)^{24}Na reaction was obtained from the ENDF/B-VIII.0 library [16], using the interpolation button at the ENDF website [57], for the five energies of interest.

σ_r - uncertainty

The uncertainty in the interpolated cross-section value was estimated to be 3% for all cases.

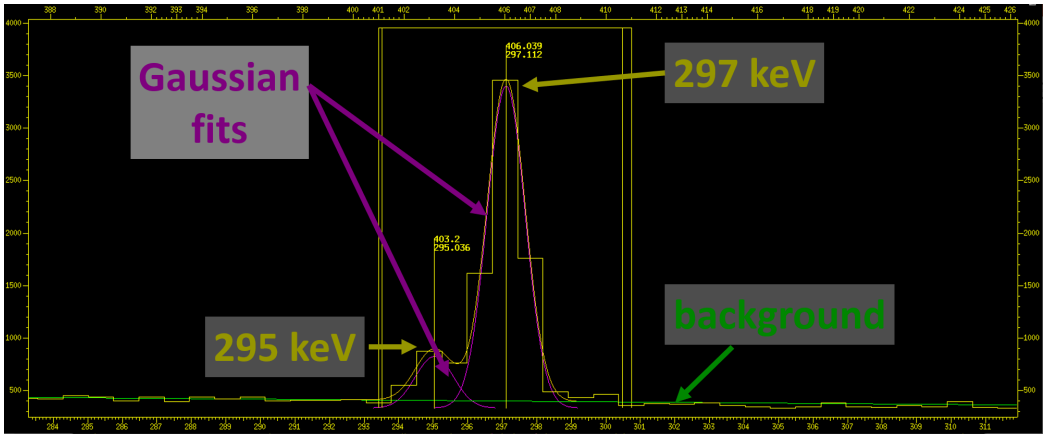

Figure 4.1: The γ-ray spectrum obtained from the irradiated ^{73}Ge target. The left tail of the 295 keV line stemming from the natural γ-ray background [59], overlaps with the left tail of the 297 keV γ-ray emitted from the ^{73}Ga residual nucleus, produced from the ^{73}Ge(n,p)^{73}Ga reaction. A double gaussian fit (magenta color) was performed via the "Tv" software to estimate the yield of each γ-ray. An assumed linear background (green color) was subtracted from the corresponding integrals of the peaks.

4.1.2 γ-ray yield - N_γ

The induced radioactivity of the Ge targets and the reference Al foils was measured via HPGe detectors, with relative efficiencies[1] of 13-80%. All the γ-ray spectra were analyzed via the "Tv" software [17]. The "N_γ" factor was calculated from the integration of the γ-ray peak of interest in the γ-ray spectrum, with subtraction of the background of the spectrum. As presented in Table 3.3, some measured residual (or daughter) nuclei, emit more than one γ-rays. If the difference in energy of these γ-rays (or the difference between the measured γ-ray and a γ-ray from natural background) is similar to the energy resolution of the HPGe detector, a double gaussian fit had to be applied (an example is hown in Figure 4.1).

N_γ - uncertainty

The uncertainty of both the measured γ-ray yield and the total background yield in the area of the γ-ray peak, is given by the square root of the respective yield. The uncertainty in the "N_γ" factor is calculated by propagating the uncertainty of the two yields, following their subtraction.

Furthermore, systematic errors stem from corrections to the measured yield which are introduced due to the parasitic tail contribution of the neutron yield (see Appendix B), as well as the contribution of parasitic reactions

[1]The relative efficiency of a HPGe detector is calculated relative to the efficiency of a 3"× 3" NaI detector for the 1332.5 keV line emitted from a ^{60}Co source, positioned at a 25 cm distance from the detector [58].

(see Section 4.12).

4.1.3 Efficiency - ε_γ

The efficiency $\varepsilon_\gamma(E_\gamma)$ at a specific γ-ray energy is obtained by the IAEA fitting function [8]. First, a calibrated ^{152}Eu point source[2] was placed in front of the HPGe detector, at the same distance as the measured samples. A typical spectrum from this measurement is presented in Figure 3.17. The efficiency of the detector is given by the fraction of the detected over the emitted γ-rays :

$$\varepsilon(E_\gamma) = \frac{N_{\gamma,\text{detected}}}{N_{\gamma,\text{emitted}}} \tag{4.2}$$

Assuming that the calibration source had a R_0 activity at the time of its creation, the activity at the calibration time would be:

$$R(t) = R_0 \cdot e^{-\lambda t} \tag{4.3}$$

where $\lambda = \frac{\ln(2)}{t_{1/2}}$ is the decay constant of the radioactive calibration source, and t is the time elapsed between the creation of the calibration source and the time of the measurement in the HPGe detector. ^{152}Eu emits a number of different γ-rays (E_i) [60] with different intensities $I_{\gamma,\,i}$. The total number $N_{\gamma,i}$ of a specific γ-ray E_i emitted during the measurement time (t_{spectrum}) is:

$$N_{\gamma,i,\text{emitted}} = R(t) \cdot I_{\gamma,i} \cdot t_{\text{spectrum}} \tag{4.4}$$

Equation 4.2 then becomes:

$$\varepsilon(E_\gamma) = \frac{N_{\gamma,\text{detected}}}{R(t) \cdot I_{\gamma,i} \cdot t_{\text{spectrum}}} \tag{4.5}$$

where the $N_{\gamma,\,\text{detected}}$ factor is obtained by integration (or fitting) of the γ-rays from the experimental γ-ray spectrum of the ^{152}Eu source (see Figure 3.17), following the methodology described in section 4.1.2.

In this way, the experimental efficiency points presented in Figure 3.18 are obtained. These points, are then fitted with a suitable fitting function (in the present work the fitting function proposed by IAEA [8] was implemented), from which the efficiency value at a specific γ-ray energy $\varepsilon(E_\gamma)$ is then obtained.

[2]It is noted, that the methodology described in this section can be applied for more calibration sources. The choice of more than one calibration sources for the efficiency curve determination is recommended in order to cover a wider energy range, with more experimental efficiency points, rendering the fitting process more reliable.

ε_γ - uncertainty

The uncertainty of the efficiency experimental points is calculated by the error propagation formula:

$$\delta\varepsilon = \sqrt{\left(\frac{\partial\varepsilon}{\partial N_{\gamma,detected}}\right)^2 + \left(\frac{\partial\varepsilon}{\partial R_0}\right)^2} \Rightarrow$$

$$\delta\varepsilon = \varepsilon\sqrt{\left(\frac{\delta N_{\gamma,detected}}{N_{\gamma,detected}}\right)^2 + \left(\frac{\delta R_0}{R_0}\right)^2}$$

These experimental points are then fitted by the IAEA fitting function, and the uncertainty at a specified γ-ray energy is estimated by the confidence bands of the fitting curve at a 95% level (Figure 3.18).

It must also be underlined that the difference between the extended geometry of the samples and the point ^{152}Eu source was estimated by Monte Carlo simulations to be less than 3% and was introduced as a systematic uncertainty in the measurements.

4.1.4 γ-ray Intensity - I_γ

The values for the γ-ray intensity and their respective uncertainties were obtained from IAEA [9–11, 13].

4.1.5 Correction Factor "F"

The correction factor "F" is needed in order to take into account the self attenuation of the γ-ray within the sample itself. The estimation of this correction factor is achieved with a simple Monte Carlo simulation implementing the MCNP5 code. The first step is to model the HPGe detector and the measuring foil. Then two successive runs are performed. In the first run, the modeled foil is described with its full physical characteristics (diameter, thickness, density etc), and the emitted γ-rays are scored in the HPGe detector volume. In the second run, the material of the foil is replaced with air, while the respective γ-rays are emitted from the foil volume and the γ-rays are again scored in the HPGe detector volume. The "F" factor is subsequently calculated as the ratio of the number of γ-rays that are recorded in the HPGe detector volume.

4.1.6 Correction Factor "D"

The correction factor "D" takes into account the decaying nuclei during the "cooling time" t_1 (time interval between the end of the irradiation and the

start of the measurement in the HPGe detector) and the measurement time t_2 in the HPGe detector. This correction factor is given by the expression:

$$D = e^{-\lambda t_1} - e^{-\lambda t_2} \tag{4.6}$$

with λ being the decaying constant of the corresponding residual nucleus (see also Appendix A).

4.1.7 Correction Factor "f_c"

The correction factor "f_c" concerns the decaying nuclei during the irradiation time (t_{irr}), taking into account any instabilities of the neutron beam. This factor is described by the following expression:

$$f_c = \frac{\int_0^{t_{irr}} e^{\lambda t} f(t) dt}{\int_0^{t_{irr}} f(t) dt} \cdot e^{-\lambda t_{irr}} \tag{4.7}$$

where $f(t)$ is the neutron beam flux expressed in arbitrary units and obtained at fixed, short time intervals from a neutron counter (e.g. a BF_3 detector).

4.1.8 Number of target nuclei - N_t

N_t is the number of nuclei of the measured isotope:

$$N_t = N_A \cdot \frac{m \cdot a_i}{A} \tag{4.8}$$

where N_A is the Avogadro's number, m is the mass of the target, with a_i and A being the abundance and the mass number of the measured isotope, respectively.

4.1.9 Neutron Flux Ratio - $\frac{\Phi_r}{\Phi_m}$

Φ_r/Φ_m is the neutron flux ratio between the reference and the measuring target. This factor is found from MCNP5 simulations by integrating the flux in the main beam region, as described in Section 3.4.2 (see Figure 3.13a), for the reference and measured reaction respectively. The validity of the simulated neutron flux is tested via multiple reference foils (e.g. Al, Au) as explained in Section 3.4.2.

4.2 Weighted Average Cross Sections - Uncertainty Calculation

All parameters used for the cross-section calculation following equation 4.1 were considered to be uncorrelated. Therefore, the uncertainty of the cross-

section value calculated from one γ-ray is given by the quadratic summation of each of the factors of equation 4.1.

However, as presented in Table 3.3, in many cases the cross-section values were calculated from the weighted average of two or three γ-rays, taking into consideration the correlation between the measurements.

As a simple example, let's assume that one residual nucleus emits two different γ-rays. Following equation 4.1, two cross-section values would be calculated, with their respective uncertainty ($\sigma_1 \pm \delta\sigma_1$, $\sigma_2 \pm \delta\sigma_2$). The weighted average and the uncertainty for this case is given by equations (27) reported in [61]:

$$\bar{\sigma} = \frac{\left(\delta\sigma_2^2 - V_{12}\right)\sigma_1 + \left(\delta\sigma_1^2 - V_{12}\right)\sigma_2}{\delta\sigma_1^2 + \delta\sigma_2^2 - 2V_{12}} \tag{4.9}$$

$$\delta\sigma = \sqrt{\frac{\delta\sigma_1^2\delta\sigma_2^2 - V_{12}}{\delta\sigma_1^2 + \delta\sigma_2^2 - 2V_{12}}} \tag{4.10}$$

where V_{12} is the covariance of σ_1 and σ_2 values:

$$\begin{aligned}
V_{12} &= \mathrm{cov}\left(\sigma_1, \sigma_2\right) \\
&= \left(\frac{\partial\sigma}{\partial\sigma_{\mathrm{ref}}}\right)_1 \mathrm{cov}\left(\sigma_{\mathrm{ref},1}, \sigma_{\mathrm{ref},2}\right) \left(\frac{\partial\sigma}{\partial\sigma_{\mathrm{ref}}}\right)_2 + \\
&+ \left(\frac{\partial\sigma}{\partial N_{\gamma,\mathrm{tar}}}\right)_1 \mathrm{cov}\left(N_{\gamma,\mathrm{tar},1}, N_{\gamma,\mathrm{tar},2}\right) \left(\frac{\partial\sigma}{\partial N_{\gamma,\mathrm{tar}}}\right)_2 + \\
&+ \left(\frac{\partial\sigma}{\partial N_{\gamma,\mathrm{ref}}}\right)_1 \mathrm{cov}\left(N_{\gamma,\mathrm{ref},1}, N_{\gamma,\mathrm{ref},2}\right) \left(\frac{\partial\sigma}{\partial N_{\gamma,\mathrm{ref}}}\right)_2 + \\
&+ \left(\frac{\partial\sigma}{\partial\varepsilon_{\mathrm{ref}}}\right)_1 \mathrm{cov}\left(\varepsilon_{\mathrm{ref},1}, \varepsilon_{\mathrm{ref},2}\right) \left(\frac{\partial\sigma}{\partial\varepsilon_{\mathrm{ref}}}\right)_2 + \\
&+ \left(\frac{\partial\sigma}{N_{\mathrm{t,ref}}}\right)_1 \mathrm{cov}\left(N_{\mathrm{t,ref},1}, N_{\mathrm{t,ref},2}\right) \left(\frac{\partial\sigma}{N_{\mathrm{t,ref}}}\right)_2 + \\
&+ \left(\frac{\partial\sigma}{\partial N_{\mathrm{t,tar}}}\right)_1 \mathrm{cov}\left(N_{\mathrm{t,tar},1}, N_{\mathrm{t_tar_2}}\right) \left(\frac{\partial\sigma}{\partial N_{\mathrm{t,tar}}}\right)_2 + \\
&+ \left(\frac{\partial\sigma}{\partial\varepsilon_{\mathrm{tar}}}\right)_1 \mathrm{cov}\left(\varepsilon_{\mathrm{tar},1}, \varepsilon_{\mathrm{tar}_2}\right) \left(\frac{\partial\sigma}{\partial\varepsilon_{\mathrm{tar}}}\right)_2 + \\
&+ \left(\frac{\partial\sigma}{\partial I_{\gamma,\mathrm{tar}}}\right)_1 \mathrm{cov}\left(I_{\gamma,\mathrm{tar},1}, I_{\gamma,\mathrm{tar}_2}\right) \left(\frac{\partial\sigma}{\partial I_{\gamma,\mathrm{tar}}}\right)_2 + \\
&+ \left(\frac{\partial\sigma}{\partial I_{\gamma,\mathrm{ref}}}\right)_1 \mathrm{cov}\left(I_{\gamma,\mathrm{ref},1}, I_{\gamma,\mathrm{ref}_2}\right) \left(\frac{\partial\sigma}{\partial I_{\gamma,\mathrm{ref}}}\right)_2
\end{aligned} \tag{4.11}$$

In the case when the weighted average of three different cross-section values was used ($\sigma_1 \pm \delta\sigma_1$, $\sigma_2 \pm \delta\sigma_2$, $\sigma_3 \pm \delta\sigma_3$), stemming from three different

γ-rays, the more general formalism of Appendix 2 of [62] was employed, following the expressions:

$$\bar{\sigma} = \Sigma \cdot W^{\intercal} = \begin{bmatrix} \sigma_1 \\ \sigma_2 \\ \sigma_3 \end{bmatrix} \cdot \begin{bmatrix} w_1 & w_2 & w_3 \end{bmatrix} \Rightarrow$$
$$\bar{\sigma} = \sigma_1 \cdot w_1 + \sigma_2 \cdot w_2 + \sigma_3 \cdot w_3 \tag{4.12}$$

where σ_i are the different cross-section values and w_i are the corresponding weights.

The weights are described by the following equation:

$$w_i = \frac{\sum_j V_{ji^{-1}}}{\sum_k \sum_l V_{kl}^{-1}} \tag{4.13}$$

The uncertainty in the weighted average value is calculated by the following equation:

$$(\delta\sigma)^2 = W \cdot V \cdot W^{\intercal} \Rightarrow (\delta\sigma)^2 = \begin{bmatrix} w_1 & w_2 & w_3 \end{bmatrix} \begin{bmatrix} V_{11} & V_{12} & V_{13} \\ V_{21} & V_{22} & V_{23} \\ V_{31} & V_{32} & V_{33} \end{bmatrix} \begin{bmatrix} w_1 \\ w_2 \\ w_3 \end{bmatrix} \Rightarrow$$
$$(\delta\sigma)^2 = w_1 \cdot (w_1 V_{11} + w_2 V_{21} + w_3 V_{31}) + w_2 \cdot (w_1 V_{12} + w_2 V_{22} + w_3 V_{32}) + w_3 \cdot (w_1 V_{13} + w_2 V_{23} + w_3 V_{33}) \tag{4.14}$$

More information about the calculation of weighted average cross sections along with their corresponding uncertainties is given in Appendix C.

Finally, a summary of the statistical uncertainties that are quadratically summed and presented in the cross-section results of the Sections 4.3 to 4.11 as well as the systematic uncertainties introduced in the analysis is presented in Table 4.1.

Table 4.1: Uncertainties introduced in the cross-section calculation (†: systematic uncertainty)

Parameter	Uncertainty (%)
Reference cross section†	3
γ-ray yield	1 – 10
Efficiency	2 – 3
Correction factor "F"	–
γ-ray intensity	0.2 – 13
Number of target nuclei	< 1
Correction factor "D"	–
Correction factor "f_c"	–
Neutron flux ratio	–
Parasitic tail contribution†	< 2
Extended geometry of the Ge samples†	< 3
Contributions from neighboring isotopes†	< 5

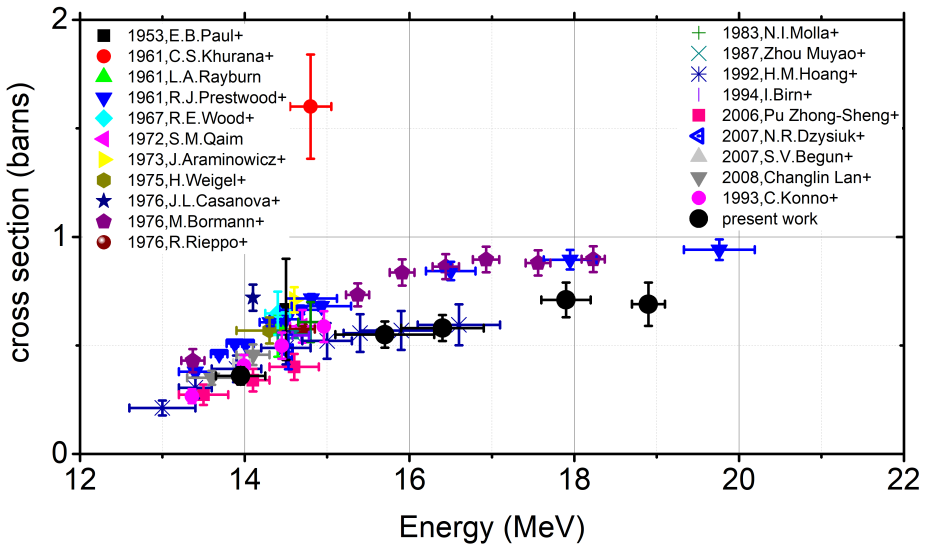

Figure 4.2: The cross-section results of the ^{70}Ge(n,2n)^{69}Ge reaction, along with previous data found in literature [18].

4.3 The ^{70}Ge(n,2n)^{69}Ge reaction

The experimental cross-section results of the present work in the energy range between 14.0-18.9 MeV are presented in Figure 4.2, along with previous data found in literature [18]. The residual nucleus ^{69}Ge is produced only from the ^{70}Ge(n,2n)^{69}Ge reaction. This reaction is not contaminated by other reaction channels from neighboring isotopes. In other words, datasets that implement natural targets for the measurements are just as reliable as the ones that employ enriched samples. Its decay is described in section 2.3.1. In the γ-ray spectra following the ^{70}Ge target irradiation four γ-rays were observed (see Figure 3.19). From each of these γ-rays a different cross-section value was calculated. It was observed that the cross-section values obtained from the 1106.8 and 1336.6 keV γ-rays were systematically lower than the ones calculated from the 574.1 and 872.0 keV ones (see Table 4.2). This systematic behavior could be explained from erroneous γ-ray intensities in literature [9]. Furthermore, two general trends are observed from the existing data, with the results of the present work being in agreement with the "lower" trend.

The results of the present work are in excellent agreement with the dataset of Hoang et al. [21] within the statistical uncertainties of the measurements. Hoang et al. used the 574 keV γ-ray for the cross section calculation. The trend of the dataset of Konno et al. [22] slightly overestimates the cross-section values, possibly due to a different value in the γ-ray intensity of the 1106 keV peak. In this publication [22], the branching ratio for the 1106 keV γ-ray is reported to be (27 ± 3) %, whereas the respective value obtained from IAEA [9] holds the value of (36 ± 4) %. This

correction in the γ-ray intensity would result in cross-section results in agreement with the ones of the present work, calculated from the same γ-ray (see Figure 4.3). In Figure 4.3, the cross-section values have been calculated from the weighted average of two γ-rays each time, following the formalism described in Appendix C. More specifically, the solid black points stem from the weighted average of the cross-section values from the 1106.8 and 1336.6 keV, and the solid red points from the weighted average of the cross-section values from the 574.1 and 872.0 keV γ-rays.

Table 4.2: ^{70}Ge(n,2n)^{69}Ge cross-section results

		σ_i (b)				
E_γ (keV)	I_γ (%)	$E_n = 14.0$ MeV	$E_n = 15.7$ MeV	$E_n = 16.4$ MeV	$E_n = 17.9$ MeV	$E_n = 18.9$ MeV
1106.8	36 ± 4	0.30 ± 0.04	0.46 ± 0.06	0.50 ± 0.06	0.60 ± 0.08	0.63 ± 0.10
1336.6	4.5 ± 0.6	0.28 ± 0.04	0.45 ± 0.07	0.53 ± 0.08	0.55 ± 0.09	-
574.1	13.3 ± 1.8	0.37 ± 0.05	0.56 ± 0.09	0.58 ± 0.09	0.72 ± 0.11	0.73 ± 0.13
872.0	11.9 ± 1.6	0.35 ± 0.05	0.54 ± 0.08	0.58 ± 0.09	0.69 ± 0.11	0.68 ± 0.12
				$\overline{\boldsymbol{\sigma}}$ (b)		
		$\mathbf{0.36 \pm 0.04}$	$\mathbf{0.55 \pm 0.06}$	$\mathbf{0.58 \pm 0.06}$	$\mathbf{0.71 \pm 0.08}$	$\mathbf{0.69 \pm 0.10}$

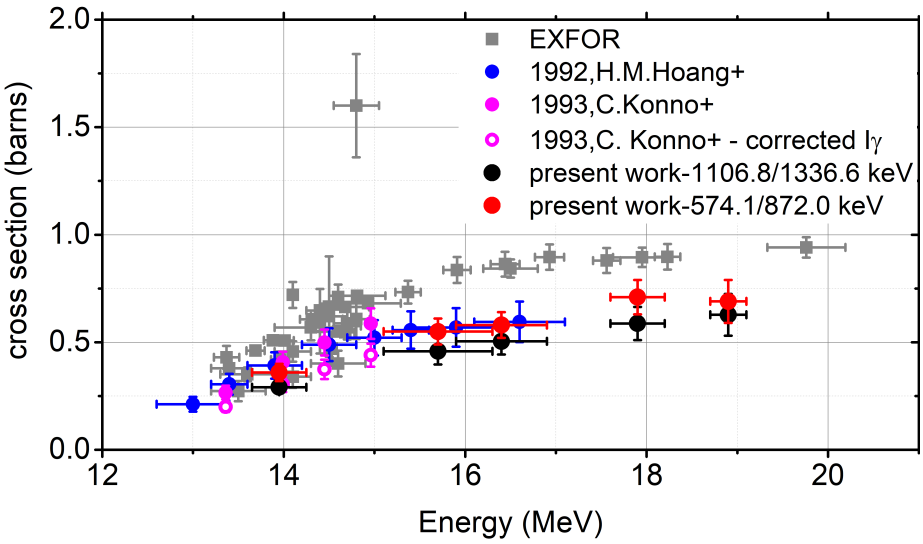

Figure 4.3: The cross-section results for the ^{70}Ge(n,2n)^{69}Ge reaction, along with the datasets of Hoang et al. [21] and Konno et al. [22]. The cross-section values calculated from the 574.1 and 872.0 keV γ-rays (solid red points) are systematically higher than the ones calculated from the 1106.8 and 1336.6 keV ones (solid black points). The dataset of Konno et al. (solid magenta points) has been corrected in terms of the I_γ value for the 1106.8 keV γ-ray (hollow magenta points), and is in very good agreement with the cross section-results of the present work based on the same γ-ray.

It should be noted that datasets before 1983 are the ones responsible for the higher trend, possibly due to different decay data such as I_γ values and half lives of the measuring isotopes.

Finally, the cross-section values presented in Figure 4.2 are the result of the weighted average of the 574.1 and 872.0 keV γ-rays yielding consistent results, while the former was also used in the recent works of Pu et al. [19] and Lan et. al. [20]. These results are presented in Table 4.2.

4.4 The ^{76}Ge(n,2n)^{75}Ge reaction

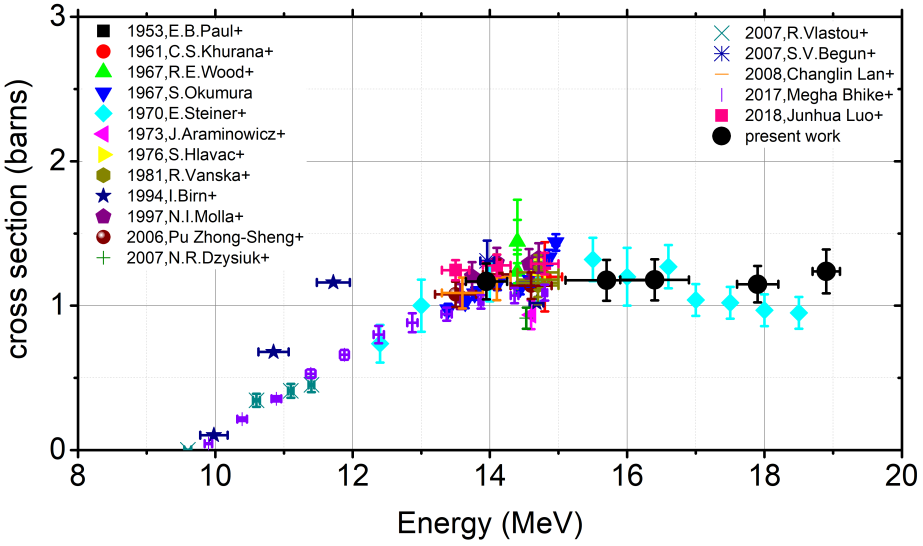

Figure 4.4: The cross-section results of the ^{76}Ge(n,2n)^{75}Ge reaction, along with previous data found in literature [18].

Alongside with earlier data from the literature [18], the experimental cross-section results of the current work for the ^{76}Ge(n,2n)^{75}Ge reaction in the energy range between 14-19 MeV are shown in Figure 4.4. The reactions ^{74}Ge(n,γ)^{75}Ge and ^{76}Ge(n,2n)^{75}Ge yield the residual nucleus ^{75}Ge. Using the methods outlined in Ref. [6], the ^{74}Ge(n,γ)^{75}Ge reaction's contribution to the observed yield was determined to be insignificant. The present work's results have been calculated using the 264.6 keV γ-ray (which is referred to Table 4.3). The results show good agreement with the dataset of Steiner et al. [23], the only dataset above 15 MeV, within statistical uncertainties; at 14.0 MeV, the agreement is satisfactory with all datasets in this region. Furthermore, the current work's results and those from our group's earlier study [48] both follow the trend of the data from Megha Bhike et al. [63], which also used enriched ^{76}Ge samples for the measurements.

Table 4.3: ^{76}Ge(n,2n)^{75}Ge cross-section results

E_γ (keV)	I_γ (%)	σ (b) $E_n = 14.0$ MeV	$E_n = 15.7$ MeV	$E_n = 16.4$ MeV	$E_n = 17.9$ MeV	$E_n = 18.9$ MeV
264.6	11.4 ± 1.1	$\mathbf{1.17 \pm 0.13}$	$\mathbf{1.18 \pm 0.14}$	$\mathbf{1.18 \pm 0.14}$	$\mathbf{1.15 \pm 0.13}$	$\mathbf{1.24 \pm 0.15}$

4.5 The ^{72}Ge(n,p)^{72}Ga reaction

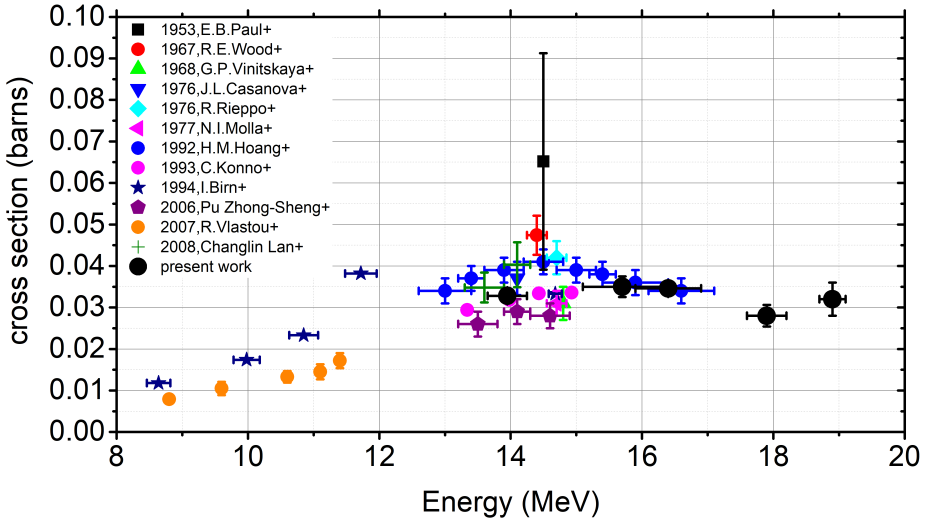

Figure 4.5: The cross-section results of the ^{72}Ge(n,p)^{72}Ga reaction, along with previous data found in literature [18].

Figure 4.5 presents the experimental cross-section results of the current work for the ^{72}Ge(n,p)^{72}Ga reaction in the energy range between 14-19 MeV, together with earlier data obtained in literature [18]. The ^{72}Ge(n,p)^{72}Ga measured reaction produces the residual nucleus ^{72}Ga, as do the parasitic ^{73}Ge(n,np)^{72}Ga and ^{73}Ge(n,d)^{72}Ga reactions. Section 2.3.4 provides details on the de-excitation of the ^{72}Ga residual nucleus. The weighted average of the cross-section values obtained from the 834.1, 630.0, and 894.3 keV γ-rays was used to determine the final cross-section results. The dataset of Konno et al. [22], which likewise used an enriched ^{72}Ge sample for the measurements, followed the overall trend of the data in the current work. The cross-section values in the energy range of 13–15 MeV appear to be overestimated by Hoang et al. [21]. Within the statistical uncertainties, there is a very strong agreement with the data of the current work above 15 MeV. It should be mentioned that Hoang et al. utilized a ^{nat}Ge target, which required theoretical corrections using the EMPIRE code [64] to account for the parasitic channel contributions. It is important to emphasize that theoretical corrections of this kind come with their own set of systematic uncertainties. Additionally, highly enriched targets, like those employed in this study (refer to Table 3.1), are not impacted by the previously mentioned parasitic contributions.

Table 4.4: ^{72}Ge(n,p)^{72}Ga cross-section results

		σ_i (b)				
E_γ (keV)	I_γ (%)	$E_n = 14.0$ MeV	$E_n = 15.7$ MeV	$E_n = 16.4$ MeV	$E_n = 17.9$ MeV	$E_n = 18.9$ MeV
834.1	95.45 ± 0.08	0.0324 ± 0.0015	0.0348 ± 0.0026	0.0361 ± 0.0020	0.0286 ± 0.0027	0.0342 ± 0.0025
630.0	26.13 ± 0.04	0.0340 ± 0.0017	0.0355 ± 0.0027	0.0310 ± 0.0023	0.0269 ± 0.0029	0.0326 ± 0.0026
894.3	10.136 ± 0.015	0.0319 ± 0.0026	0.0347 ± 0.0028	0.038 ± 0.004	0.028 ± 0.004	0.031 ± 0.004
				$\overline{\boldsymbol{\sigma}}$ (b)		
		$\mathbf{0.0328 \pm 0.0014}$	$\mathbf{0.0350 \pm 0.0025}$	$\mathbf{0.0346 \pm 0.0017}$	$\mathbf{0.0280 \pm 0.0026}$	$\mathbf{0.032 \pm 0.004}$

4.6 The ^{73}Ge(n,p)^{73}Ga reaction

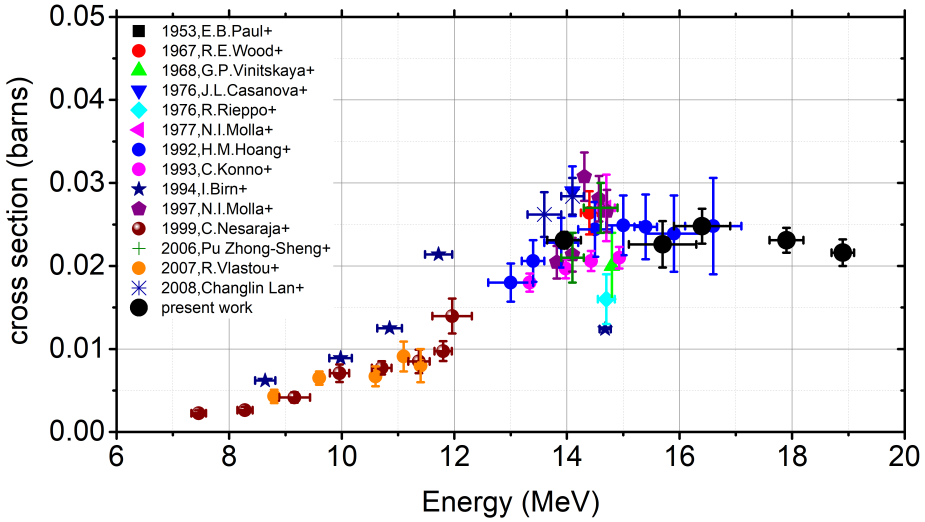

Figure 4.6: The cross-section results of the ^{73}Ge(n,p)^{73}Ga reaction, along with previous data found in literature [18].

Together with earlier data from the literature [18], Figure 4.6 displays the experimental cross-section results for the ^{73}Ge(n,p)^{73}Ga reaction in the energy range of 14–19 MeV. The parasitic reactions ^{74}Ge(n,np)^{73}Ga, ^{74}Ge(n,d)^{73}Ga, and ^{76}Ge(n,α)^{73}Zn also yield the ^{73}Ga residual nucleus, as the measured ^{73}Ge(n,p)^{73}Ga reaction; the de-excitation of the ^{73}Ga residual nucleus is described in section 2.3.5. The final cross-section results were produced using a weighted average of the cross-section values obtained from the 297.3, 325.7, 739.4, and 767.8 keV γ-rays. The trend of the Konno et al. dataset [22], which also employed an enriched ^{73}Ge sample for the cross-section measurements, is again in fair agreement with the trend of the data of the present work. The agreement within the statistical uncertainties is again quite satisfacrory with the dataset of Hoang et al. [21]. It is reminded at this point, that Hoang et al. utilized a ^{nat}Ge target, which required theoretical corrections. Such corrections were not necessary in the frame of this work, since a highly enriched ^{72}Ge target (refer to Table 3.1) was employed for the cross-section measurements.

Table 4.5: ^{73}Ge(n,p)^{73}Ga cross-section results

		σ_i (b)				
E_γ (keV)	I_γ (%)	$E_n = 14.0$ MeV	$E_n = 15.7$ MeV	$E_n = 16.4$ MeV	$E_n = 17.9$ MeV	$E_n = 18.9$ MeV
297.3	79.8 ± 1.0	0.0217 ± 0.0010	0.0222 ± 0.0016	0.0248 ± 0.0021	0.0231 ± 0.0015	0.0215 ± 0.0016
325.7	11.2 ± 0.4	0.0241 ± 0.0014	0.0232 ± 0.0020	–	0.0256 ± 0.0024	0.024 ± 0.004
739.4	4.3 ± 0.3	0.0273 ± 0.0025	–	–	–	–
767.8	1.44 ± 0.09	0.0264 ± 0.0029	–	–	–	–
				$\overline{\sigma}$ (b)		
		$\mathbf{0.0231 \pm 0.0010}$	$\mathbf{0.0226 \pm 0.0028}$	$\mathbf{0.0248 \pm 0.0021}$	$\mathbf{0.0231 \pm 0.0015}$	$\mathbf{0.0216 \pm 0.0016}$

4.7 The ^{72}Ge(n,α)^{69m}Zn reaction

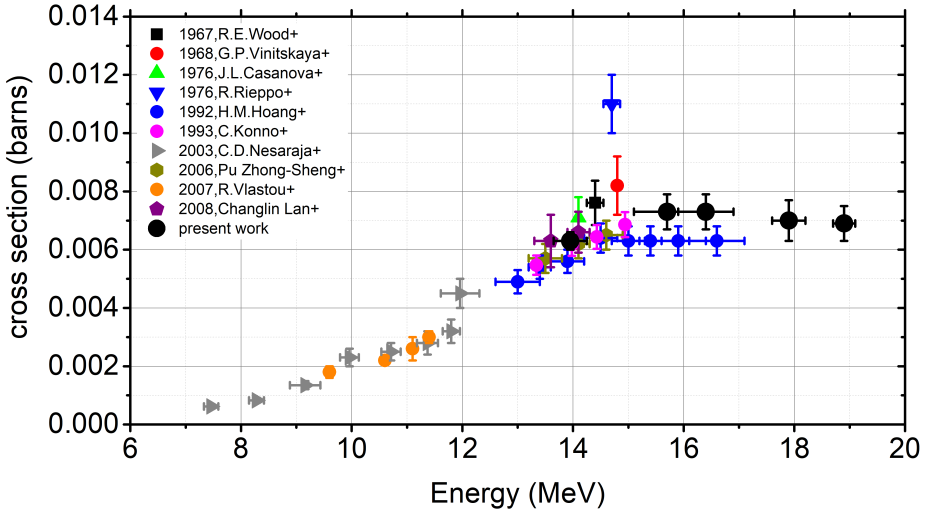

Figure 4.7: The cross-section results of the ^{72}Ge(n,α)^{69m}Zn reaction, along with previous data found in literature [18].

Figure 4.7 provides the experimental cross-section results for the ^{72}Ge(n,α)^{69m}Zn reaction in the energy range between 14-19 MeV, together with previous data obtained in the literature [18]. Both the ^{73}Ge(n,nα)^{69m}Zn parasitic reaction and the ^{72}Ge(n,α)^{69m}Zn measured reaction yield the residual nucleus ^{69}Zn. Section 2.3.2 describes the de-excitation of the ^{69}Zn residual nucleus, and the 438.6 γ-ray was used to determine the final cross-section results. The result of the present work is in very good agreement with the results of Changlin Lan et al. [65] and Pu Zhong-Sheng et al. [19] for the cross-section point at 14.0 MeV, while the present work's overall trend of data, is again followed by the respective trend of the dataset of Konno et al. [22], also employing an enriched ^{72}Ge sample for the measurements. The points of Hoang et al. [21] appear to slightly underestimate the cross-section values in the energy region between 13 and 15 MeV.

Table 4.6: ^{72}Ge(n,α)^{69m}Zn cross-section results

		σ (b)				
E_γ (keV)	I_γ (%)	$E_n = 14.0$ MeV	$E_n = 15.7$ MeV	$E_n = 16.4$ MeV	$E_n = 17.9$ MeV	$E_n = 18.9$ MeV
438.6	94.85 ± 0.07	$\mathbf{0.0063 \pm 0.0003}$	$\mathbf{0.0073 \pm 0.0006}$	$\mathbf{0.0073 \pm 0.0006}$	$\mathbf{0.0070 \pm 0.0007}$	$\mathbf{0.0069 \pm 0.0006}$

4.8 The ^{74}Ge(n,α)^{71m}Zn reaction

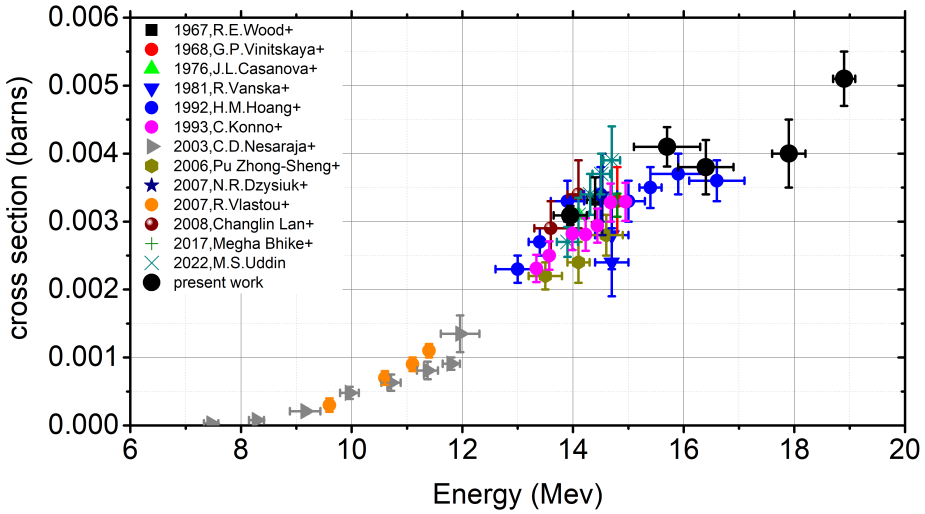

Figure 4.8: The cross-section results of the ^{74}Ge(n,α)^{69m}Zn reaction, along with previous data found in literature [18].

The experimental cross-section results of the present work for the ^{74}Ge(n,α)^{71m}Zn reaction in the energy range between 14-19 MeV are presented in Figure 4.8 along with previous data found in literature [18]. The residual nucleus ^{71}Zn is produced only from the ^{74}Ge(n,α)^{71m}Zn measured reaction, and the de-excitation of the ^{71}Zn residual nucleus has been already been described in section 2.3.3. The final cross-section results were the result from the weighted average of the 386.3, 487.3 and 620 keV γ-rays. The result of the present work for the neutron beam energy of 14 MeV, is in very good agreement with the results of Changlin Lan et al. [65], Uddin [66] and Konno et al. [22]. The dataset of Pu Zhong-Sheng et al. [19] seems to underestimate the cross-section values. The trend of the data of the present work is again followed by the trend of the datasets of Konno et al. [22] and Hoang et al. [21].

Table 4.7: ^{74}Ge(n,α)^{71m}Zn cross-section results

		σ_i (b)				
E_γ (keV)	I_γ (%)	$E_n = 14.0$ MeV	$E_n = 15.7$ MeV	$E_n = 16.4$ MeV	$E_n = 17.9$ MeV	$E_n = 18.9$ MeV
386.3	89.0 ± 1.1	0.00308 ± 0.00016	0.0041 ± 0.0004	0.0037 ± 0.0005	0.0040 ± 0.0005	0.0049 ± 0.0005
487.3	61.9 ± 0.4	0.00311 ± 0.00017	0.0041 ± 0.0004	0.0038 ± 0.0007	0.0040 ± 0.0005	0.0051 ± 0.0005
620.2	54.5 ± 0.7	0.00308 ± 0.00020	0.0042 ± 0.0005	–	–	0.0059 ± 0.0007
				$\overline{\sigma}$ (b)		
		$\mathbf{0.00309 \pm 0.00014}$	$\mathbf{0.00410 \pm 0.00029}$	$\mathbf{0.0038 \pm 0.0004}$	$\mathbf{0.0040 \pm 0.0005}$	$\mathbf{0.0051 \pm 0.0004}$

4.9 The ^{73}Ge(n,np/d)^{72}Ga reaction

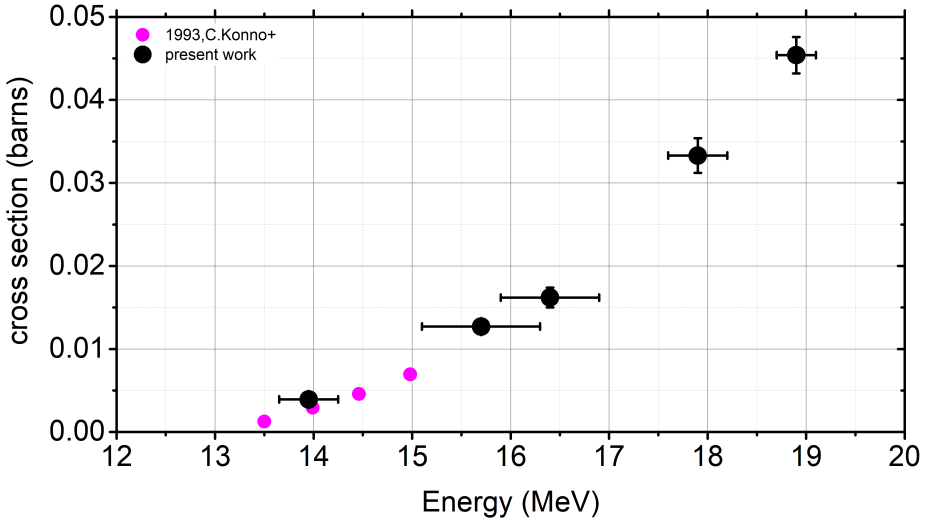

Figure 4.9: The cross-section results of the ^{73}Ge(n,np/d)^{72}Ga reaction, along with the dataset of Konno et al. [22], which was the only one found in literature [18].

The experimental cross-section results of the present work for the ^{73}Ge(n,np/d)^{72}Ga reaction in the energy range between 14-19 MeV are presented in Figure 4.9 along with the dataset of Konno et al. [22], which is the only one found in literature [18]. The residual nucleus ^{72}Ga is produced from the ^{73}Ge(n,np/d)^{72}Ga measured reaction, as well as from the ^{72}Ge(n,p)^{72}Ga one. This is the reason why this measurement can only be performed with the use of enriched samples. The de-excitation of the ^{72}Ga residual nucleus has been already described in section 2.3.4. It should be underlined that following the activation technique, only the radioactivity of the residual nucleus is being measured. Therefore, the different contributions of the ^{73}Ge(n,np)^{72}Ga and ^{73}Ge(n,d)^{72}Ga cannot be separated via the activation technique, and the final cross-section result is the sum of the (n,np) and (n,d) reaction channels. The final cross-section results were calculated from the weighted average of the 834.1, 630.0 and 894.3 keV γ-rays. The trend of the data of the present work is reproduced by the only available dataset of Konno et al.

Table 4.8: ^{73}Ge(n,np/d)^{72}Ga cross-section results

		σ_i (b)				
E_γ (keV)	I_γ (%)	$E_n = 14.0$ MeV	$E_n = 15.7$ MeV	$E_n = 16.4$ MeV	$E_n = 17.9$ MeV	$E_n = 18.9$ MeV
834.1	95.45 ± 0.08	0.00389 ± 0.00018	0.0128 ± 0.0010	0.0162 ± 0.0012	0.0334 ± 0.0022	0.045 ± 0.003
630.0	26.13 ± 0.04	0.00397 ± 0.00021	0.0127 ± 0.0011	–	0.0337 ± 0.0024	0.045 ± 0.004
894.3	10.136 ± 0.015	–	0.0121 ± 0.0013	–	0.0318 ± 0.0003	–
		$\bar{\sigma}$ (b)				
		$\mathbf{0.00392 \pm 0.00017}$	$\mathbf{0.0127 \pm 0.0009}$	$\mathbf{0.0162 \pm 0.0012}$	$\mathbf{0.0333 \pm 0.0021}$	$\mathbf{0.0454 \pm 0.0022}$

4.10 The ^{74}Ge(n,np/d)^{73}Ga reaction

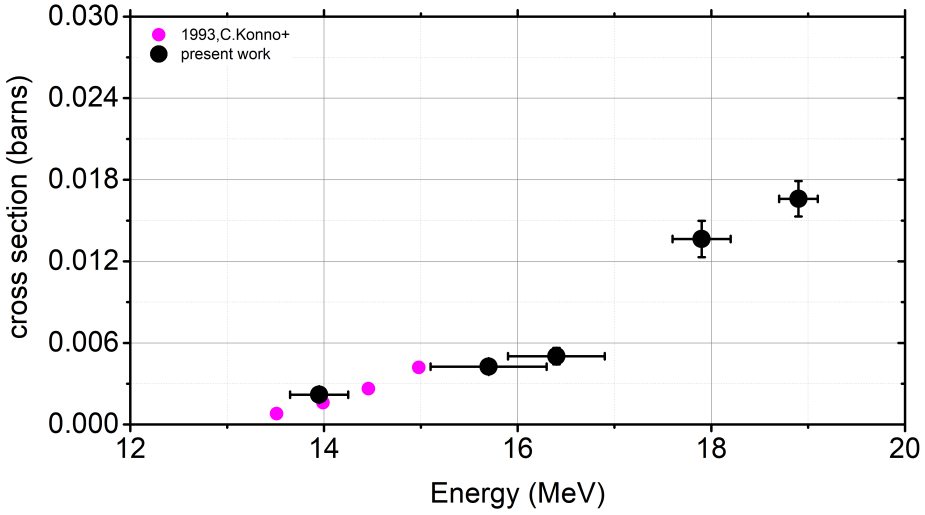

Figure 4.10: The cross-section results of the ^{74}Ge(n,np/d)^{74}Ga reaction, along with the dataset of Konno et al. [22], which was the only one found in literature [18].

Figure 4.10 presents the experimental cross-section results of the current work for the ^{74}Ge(n,np/d)^{73}Ga reaction in the energy range between 14-19 MeV along with the dataset of Konno et al. [22], which is again the only one found in literature [18]. The residual nucleus ^{73}Ga is produced from the ^{74}Ge(n,np/d)^{73}Ga measured reaction, as well as from the ^{73}Ge(n,p)^{73}Ga and ^{76}Ge(n,α)^{73}Zn ones. This is the reason why, once again, this measurement can only be performed with the use of enriched samples. Section 2.3.5 provides details on the de-excitation of the ^{73}Ga residual nucleus. It is important to emphasize again that just the radioactivity of the residual nucleus is being measured after the end of the irradiation according to the activation technique. As a result, as was already noted, the activation technique is unable to distinguish between the distinct contributions of the ^{74}Ge(n,np)^{73}Ga and ^{74}Ge(n,d)^{73}Ga. As a result, the final cross-section result is the sum of the (n,np) and (n,d) reaction channels. The final cross-section values were computed using the 297.3 keV γ-ray. The trend of the data Konno et al. seems to slightly overestimate the cross-section values in this particular case and there is no obvious explanation for this discrepancy.

Table 4.9: ^{74}Ge(n,np/d)^{73}Ga cross-section results

		σ (b)				
E_γ (keV)	I_γ (%)	$E_n = 14.0$ MeV	$E_n = 15.7$ MeV	$E_n = 16.4$ MeV	$E_n = 17.9$ MeV	$E_n = 18.9$ MeV
297.3	79.8 ± 1.0	$\mathbf{0.00219 \pm 0.00016}$	$\mathbf{0.0043 \pm 0.0004}$	$\mathbf{0.0050 \pm 0.0006}$	$\mathbf{0.0136 \pm 0.0014}$	$\mathbf{0.0166 \pm 0.0014}$

4.11 The ^{73}Ge(n,nα)^{69m}Zn reaction

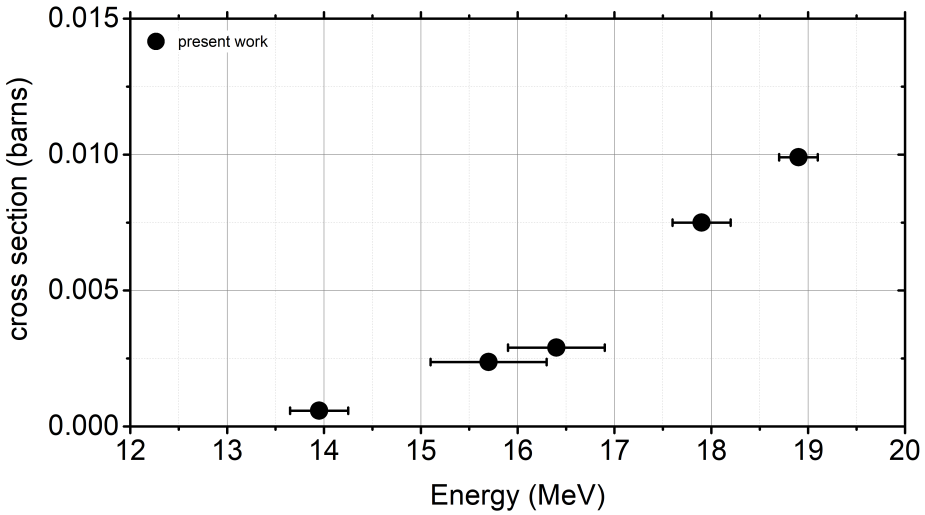

Figure 4.11: The cross-section results of the ^{73}Ge(n,nα)^{69m}Zn reaction

Figure 4.11 shows the experimental cross-section results for the ^{73}Ge(n,nα)^{69m}Zn reaction in the energy range of 14-19 MeV. There were no more data for this reaction available in the literature [18]. Both the ^{73}Ge(n,nα)^{69m}Zn measured reaction and the ^{72}Ge(n,α)^{69m}Zn one yield the residual nucleus ^{69}Zn. This is the primary cause for which enriched samples are required in order to carry out this measurement. Section 2.3.2 describes the de-excitation of the ^{73}Ga residual nucleus, while the 438.6 keV γ-ray was used to determine the final cross-section values.

Table 4.10: ^{73}Ge(n,nα)^{69m}Zn cross-section results

		σ (b)				
E_γ (keV)	I_γ (%)	E_n = 14.0 MeV	E_n = 15.7 MeV	E_n = 16.4 MeV	E_n = 17.9 MeV	E_n = 18.9 MeV
438.6	94.85 ± 0.07	$\mathbf{0.00058 \pm 0.00003}$	$\mathbf{0.00237 \pm 0.00020}$	$\mathbf{0.0029 \pm 0.0005}$	$\mathbf{0.0075 \pm 0.0005}$	$\mathbf{0.0099 \pm 0.0008}$

4.12 Enriched VS Natural Targets

The activation method is based on the measurement of the induced radioactivity of the residual nucleus. However, as shown in section 2.3, the same residual nucleus can, in some cases, be produced from different reaction channels from neighboring natural occurring isotopes. For example, the ^{72}Ga residual nucleus is produced from both ^{72}Ge(n,p)^{72}Ga and ^{73}Ge(n,np/d)^{72}Ga reactions. Therefore, when measuring such reactions with a natural target, the contribution of the different reaction channels (that will be called "parasitic channels") leading to the production of the same residual nucleus, needs to be estimated and subsequently subtracted from the measured yield. This estimation can be achieved via theoretical calculations or existing evaluation libraries, however, such corrections are accompanied by their own uncertainties, predominantly systematic.

The measurements of cross sections with isotopically enriched targets on the other hand, such as the ones used in the present work, do not suffer significantly (depending on the enrichment levels) from such contaminations, deeming the aforementioned corrections negligible and the cross-section data much more reliable.

It should be underlined, that most data found in literature implement ^{nat}Ge targets for the measurement of (n,x) reactions on Ge isotopes, and the contribution of the parasitic channels becomes larger as a function of energy. This could be one of the reasons why only very few of the existing data found in literature exceed the 15 MeV neutron beam energy.

In order to examine the consequences of this issue, two sets of measurements were performed. The first measurements were performed with a ^{nat}Ge target with all the isotopes in their natural abundances (^{70}Ge 20.52%, ^{72}Ge 27.45%, ^{73}Ge 7.76%, ^{74}Ge 36.52%, ^{76}Ge 7.75%). The second set of measurements was performed with the use of enriched targets, that acted as a test for the accuracy and sensitivity of the theoretical corrections that must be applied [24]. Both of these sets of measurements were performed at the neutron energy of 17.9 MeV and the methodology proposed and followed will be outlined in the next section (Section 4.12.1).

4.12.1 Corrections for parasitic reactions

The measurement of the net γ-ray yield (Y) of a contaminated reaction will be the sum of the γ-ray yield of the measured reaction (X) and the contribution from the 'parasitic' reaction that leads to the production of the same residual nucleus, acting as a contamination. The ratio between the yield of the measured and the parasitic reaction is given by Equation (4.15):

$$\frac{Y}{X} = 1 + \frac{\sigma_1}{\sigma_2} \cdot \frac{Ab_1}{Ab_2} \tag{4.15}$$

Where:

- Y is the total γ-ray yield in the spectrum
- X is the γ-ray yield only from the measured reaction
- $\boldsymbol{\sigma_1}$ is the cross-section value of the parasitic reaction, obtained from an evaluated library
- $\boldsymbol{\sigma_2}$ is the cross-section value of the measured reaction, obtained from the same library
- Ab_1 is the abundance of the isotope that produces the parasitic contribution
- Ab_2 is the abundance of the isotope whose reaction is measured

This methodology is heavily dependent on the cross-section ratio of the parasitic over the measured reaction (σ_1/σ_2), which in turn depends on the choice of a specific evaluation library. Whenever possible, these chosen libraries were based on Hauser-Feshbach theoretical model evaluations, such as TALYS (TENDL 2021 library [25]). Alternative libraries were chosen (eg EAF 2010 [28]), in the case when the aforementioned libraries were not available. This approach relies on the assumption that any evaluation or statistical model calculation is performed in a consistent way for all the reaction channels involved, and any possible systematic errors involved will be canceled out via the use of the σ_1/σ_2 ratio, making this adopted methodology robust.

The main idea is that the accuracy and the limits of the corrections following the methodology of Equation (4.15) will also be applied in contaminated reactions (^{72}Ge(n,α)^{69m}Zn and ^{72}Ge(n,p)^{72}Ga) and the results will then be tested with the respective accurate results that are produced from the adequately enriched Ge samples used in this work, that do not suffer from such contaminations. As a confirmation of the two sets of measurements regarding the whole experimental procedure, the non-contaminated ^{76}Ge(n,2n)^{75}Ge reaction will also be presented.

In this scope, results for the ^{76}Ge(n,2n)^{75}Ge, ^{72}Ge(n,α)^{69m}Zn and ^{72}Ge(n,p)^{72}Ga reactions will be presented, both for the ^{nat}Ge and enriched Ge target cases for the neutron beam energy of 17.9 MeV. Both of these sets of measurements were performed at the neutron beam facility of NCSR 'Demokritos' and the data analysis followed is presented in Section 4.1.

4.12.2 The ^{76}Ge(n,2n)^{75}Ge reaction - not contaminated

The experimental results for the ^{76}Ge(n,2n)^{75}Ge reaction are presented in Figure 4.12, for the natural and the enriched target case, along with previous data found in literature [18] and evaluated libraries [16, 25–27]. The γ-rays used for the cross-section calculation are reported in Table 4.11, along with the final results and their corresponding uncertainties.

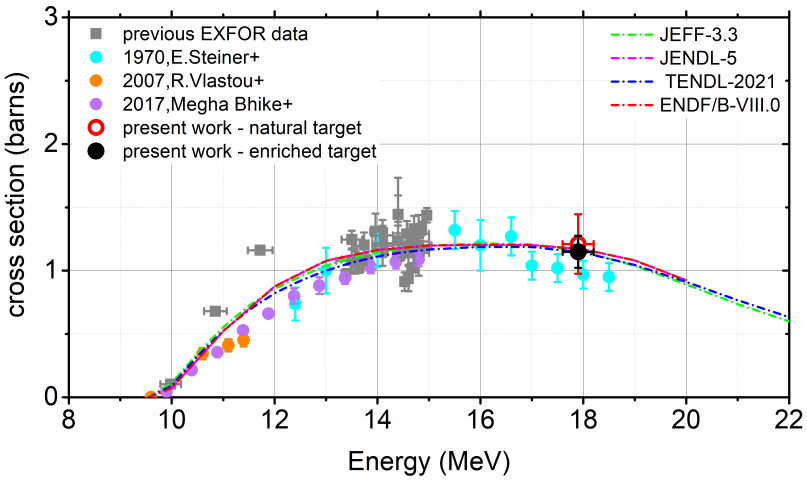

Figure 4.12: The cross-section result for the uncontaminated ^{76}Ge(n,2n)^{75}Ge reaction

Table 4.11: A list of the γ-rays used in the analysis, along with their intensities and their corresponding uncertainties [13] for the ^{76}Ge(n,2n)^{75}Ge reaction. Additionally, the calculated cross-section values and uncertainties are provided.

target type	E_γ (keV)	I_γ (%)	**σ(b)**
natural	264.6	11.4 ± 1.1	$\mathbf{1.21 \pm 0.24}$
enriched	264.6	11.4 ± 1.1	$\mathbf{1.15 \pm 0.13}$

The cross-section results both for the ^{nat}Ge and the enriched Ge target case are in excellent agreement within their uncertainties, as well as with the evaluated curves and the dataset of Steiner et. al. which is the only one exceeding the neutron beam energy of 15 MeV. The excellent agreement between the two independent sets of measurements proves that there exist no substantial systematic differences between them, acting as a validation for the experimental setup and the analysis procedure followed for the comparison of the results in the more complicated cases which will be presented in the following paragraphs.

4.12.3 The ^{72}Ge(n,α)^{69m}Zn reaction - contaminated

The results of the present work for the ^{72}Ge(n,α)^{69m}Zn reaction are presented in Figure 4.13 both for the ^{nat}Ge and enriched Ge target case along with previous data found in literature and the TENDL-2021 library, while in Table 4.12, the γ-rays used for the final cross-section results, along with their intensities and corresponding uncertainties are presented.

The comparison between the two sets of measurements yields a ∼18 % difference between them, with the cross-section result calculated from

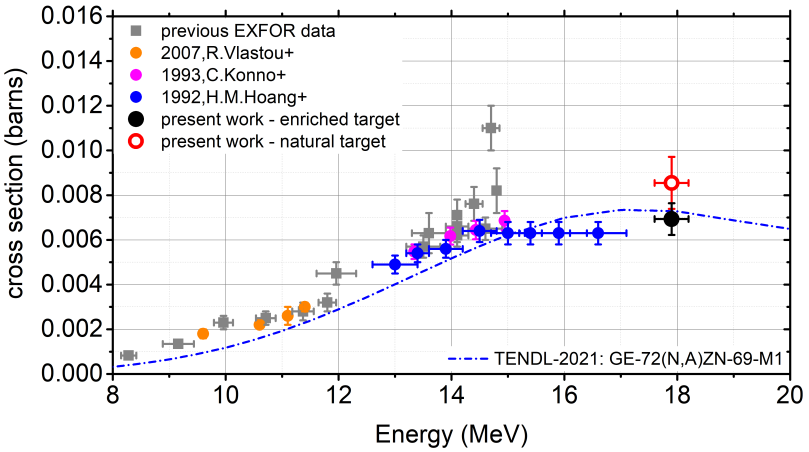

Figure 4.13: The cross-section result for the contaminated ^{72}Ge(n,α)^{69m}Zn reaction

Table 4.12: The γ-ray used for the calculation of the ^{72}Ge(n,α)^{69m}Zn reaction, together with its intensity, the calculated cross-section value and the corresponding uncertainties [9].

target type	E_γ (keV)	I_γ (%)	**σ(b)**
natural	438.63	94.85 ± 0.07	$\mathbf{0.0085 \pm 0.0012}$
enriched	438.63	94.85 ± 0.07	$\mathbf{0.0070 \pm 0.0007}$

the enriched target, being in good agreement with the general trend of the dataset of Konno et al. [22]. It is underlined, that Konno et al. [22] also used an enriched target (97.8 % enrichment level).

It is also noted that this particular reaction is contaminated by the ^{73}Ge(n,nα)^{69m}Zn in the ^{nat}Ge sample case. In the following paragraph, the correction methodology illustrated in Equation (4.15) and its limits will be presented, adopting the cross-section values of the EAF-2010 library.

Parasitic Channel for the ^{72}Ge(n,α)^{69m}Zn reaction

The σ_1/σ_2 cross-section ratio was calculated via the EAF-2010 library to correct for the contribution of the parasitic ^{73}Ge(n,nα)^{69m}Zn reaction to the measured ^{72}Ge(n,α)^{69m}Zn one. This ratio is plotted as a function of energy in Figure 4.14 for the EAF-2010 [28] and JEFF 3.1-A [29] libraries that hold information both for the measured, as well as, for the contaminating channel. This correction was found to be in the order of 3% or lower for energies below 12 MeV, and thus the results obtained using a natural target could be considered reliable only in this energy region. For higher energies, as illustrated in Figure 4.14, the increasing discrepancy between the libraries could yield very different corrections in the final cross-section results. For example, for E_n=17.9 MeV, depending on the choice of the

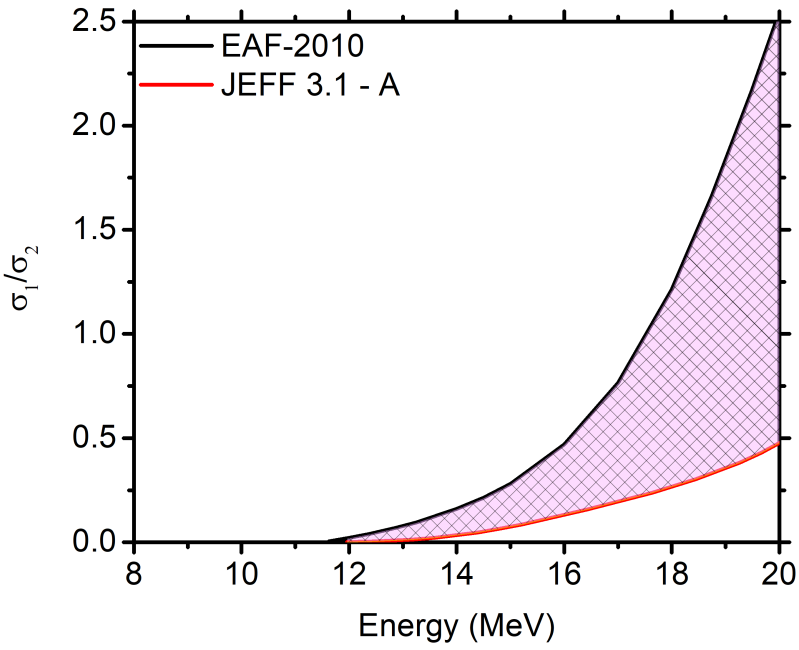

Figure 4.14: The σ_1/σ_2 ratio regarding the ^{73}Ge(n,na) parasitic reaction that contaminates the measured one as a function of energy.

library, the final correction ranges from 7.3 to 32.7%. This could be the source of the ∼18 % discrepancy between the two sets of measurements.

Finally, it should be underlined that the enriched ^{72}Ge target used for the validation of the aforementioned methodology was not entirely mono-isotopic, containing the 'parasitic' ^{73}Ge isotope in a percentage of 2.86%. Nevertheless, the corrections adopting the methodology of Equation (4.15) did not surpass 3.5% for any chosen library, a correction well within the statistical and systematic uncertainties of the measurement.

4.12.4 The ^{72}Ge(n,p)^{72}Ga reaction - contaminated

The results of the present work for the ^{72}Ge(n,p)^{72}Ga reaction are presented in Figure 4.15 both for the ^{nat}Ge and the enriched Ge target case, along with previous data found in literature and the ENDF/B-VIII.0 [16] and TENDL-2021 [25] evaluated libraries. In Table 4.13 the γ-rays used for the final cross-section result along with their intensities and corresponding uncertainties are presented.

There exists a ∼20% discrepancy between the two sets of measurements, with the result obtained from the enriched ^{72}Ge target being again lower than the respective one from the ^{nat}Ge target. The general trend of the dataset of Konno et al. [22] (that used an enriched ^{72}Ge target for the measurements) is in good agreement with the result of the enriched target, while the trend of the dataset of Hoang et al. [21] (that used a ^{nat}Ge target for the cross-section measurements) is in good agreement with the cross-

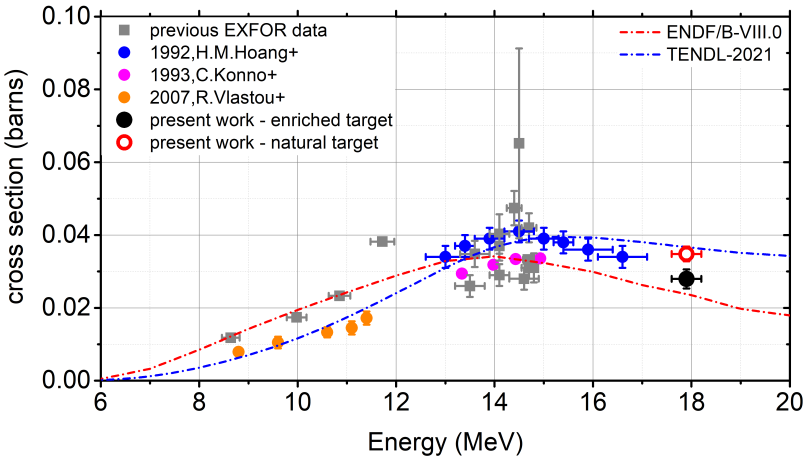

Figure 4.15: The cross-section results for the contaminated ^{72}Ge(n,p)^{72}Ga reaction

Table 4.13: A list of the γ-rays used in the cross-section calculation, along with their intensities and respective uncertainties [10] for the ^{72}Ge(n,p)^{72}Ga reaction. The cross-section values and their respective uncertainties are also presented.

target type	E_γ (keV)	I_γ (%)	σ_i (b)	**σ(b)**
natural	834.13	95.45 ± 0.08	0.0361 ± 0.0027	$\mathbf{0.0348 \pm 0.0020}$
	629.97	26.13 ± 0.04	0.031 ± 0.005	
	2201.59	26.87 ± 0.12	0.031 ± 0.005	
enriched	834.13	95.45 ± 0.08	0.0286 ± 0.0026	$\mathbf{0.0280 \pm 0.0026}$
	629.97	26.13 ± 0.04	0.0269 ± 0.0027	
	894.33	10.14 ± 0.02	0.0284 ± 0.004	

section result of the present work regarding a ^{nat}Ge target. It is noted that Hoang et al. [21] implemented statistical model calculations via the EMPIRE code for the estimation of the contribution of the parasitic reaction channels to the measured yield.

The ^{73}Ge(n,np)^{72}Ga and ^{73}Ge(n,d)^{72}Ga reactions act as a contamination to the measured one in the ^{nat}Ge case. The theoretical correction applied employing the TENDL-2021 library, following the Equation (4.15) will be presented in the following section

Parasitic Channels for the ^{72}Ge(n,p)^{72}Ga reaction

The σ_1/σ_2 cross-section ratio was calculated via the TENDL-2021 library to correct for the contribution of the ^{73}Ge(n,np)^{72}Ga and ^{73}Ge(n,d)^{72}Ga reaction channels. This ratio is plotted as a function of energy in Figure 4.16 for the libraries found in literature, with information regarding both the

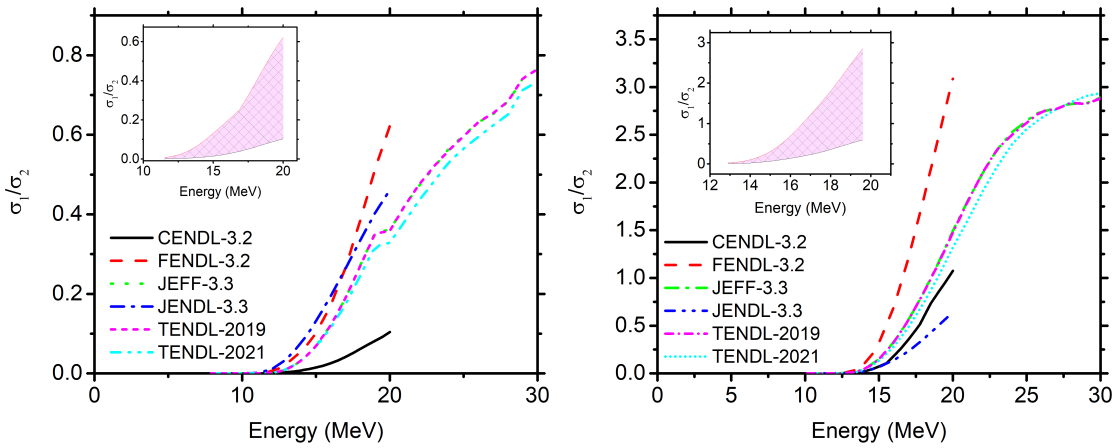

(a) ^{73}Ge(n,d)^{72}Ga **(b)** ^{73}Ge(n,np)^{72}Ga

Figure 4.16: The σ_1/σ_2 ratio regarding the ^{73}Ge(n,d/np)^{72}Ga parasitic reaction that contaminate the measured one as a function of energy.

measured and the parasitic reactions [25, 27, 30–33]. The area between the lower and higher value of the σ_1/σ_2 cross-section ratio is presented in the insets of Figures 4.16a and 4.16b, within which a value for the cross-section ratio can be chosen. The discrepancies between the libraries, especially in higher energies could subsequently yield quite discrepant corrected cross-section results. For the neutron energy of E_n=17.9 MeV for example:

- for the ^{73}Ge(n,d)^{72}Ga reaction the correction ranges from 1.7 to 10.6%
- for the ^{73}Ge(n,np)^{72}Ga reaction the correction ranges from 9.7 to 49.2%

For both contaminating reactions, the 'parasitic' contribution does not exceed 3% for energies below ∼14.5 MeV, an energy region where these theoretical corrections could be considered reliable. The large variations between the libraries could be the reason behind the discrepancy between the two sets of measurements.

It is finally noted that the ^{72}Ge target is not entirely mono-isotopic since it contains 2.86% ^{73}Ge. Nevertheless, the contribution of the parasitic reactions following Equation (4.15) did not surpass 5% for any chosen library, once more validating the accuracy of the cross-section data employing enriched targets.

Chapter 5

Theoretical Calculations

5.1 Nuclear Reaction Mechanisms

Nuclear reactions can be classified into three main types, regarding the mechanism followed. These categories are:

- compound nucleus reactions
- direct reactions
- pre-equilibrium reactions

5.1.1 Compound nucleus reactions

In compound nucleus reactions, the incident particle enters the target nucleus and transfers its energy to the nucleons of the target possibly through scattering. The recoiling nucleon and the incident particle continue to transfer energy through successive collisions. After several such interactions, the incident particle energy is statistically distributed to the particle-nucleus system after a thermodynamic equilibrium is reached, rather than transferred to a single nucleon after a single collision. The probability of a single nucleon to escape the nucleus, following the statistical distribution of energy, is rather small, resembling molecules evaporating from a hot liquid [67]. Therefore, there is a discrete "intermediate" state between the absorption of the incident particle and the emission of the outgoing particle(s), that is characterized by the statistical distribution of energy between the nucleons, depending only in the total energy provided to the nucleus. This state is also known as the compound nucleus that "lives" for a time scale of 10^{-18} - 10^{-16} s. The probability of its decay is independent of the way of its formation, also known as the Bohr's independence hypothesis.

The compound nucleus reaction mechanism is best followed for projectile energies between 1 - 20 MeV/nucleon and for medium-heavy nuclei, cases when the incident particle has a small chance of escaping, keeping its identity and energy, and the target nucleus is large enough to distribute the incident energy among the nucleons.

Finally, due to the statistical nature of the energy distribution among the nucleons, the outgoing particles are expected to have an isotropic angular distribution.

5.1.2 Direct reactions

In direct reactions, the incident particle mainly interacts with peripheral nucleons of the target nucleus, transferring part of its energy, without the formation of a compound nucleus, as an intermediate step. The direct reaction mechanism is a very fast process (10^{-22} s) and is characterized by a sharp forward peak angular distribution of the outgoing particles. The contribution of the direct reaction mechanism becomes more significant at higher nucleon energies, since the de Broglie wavelength decreases as a function of energy, and the incident particle is more likely to interact with individual, peripheral nucleons rather than with the whole nucleus, as is the case for the compound nucleus reaction mechanism, where the energy of the incident particle is more evenly spread.

Some characteristic examples of direct reactions are the elastic and inelastic scattering, transfer, knock-out, charge-exchange and break-up reactions.

5.1.3 Pre-equilibrium reactions

Pre-equlibrium (or pre-compound) reactions are essentially an intermediate state between the rapid process of a direct reaction and the slower exchange of energy between the incident particle and the target nucleus, that constitutes the compound nucleus reaction mechanism. With the borders of the two aforementioned reaction mechanisms, not being explicit, at intermediate energies the incident particle gradually loses energy as it enters the target nucleus. However, the target nucleus-incident particle system decays before a thermodynamic equilibrium is reached, partially retaining some information regarding the input channel.

5.2 The EMPIRE 3.2.3 code

EMPIRE is a modular system of nuclear reaction codes, that can be used for theoretical investigations of nuclear reactions in a wide energy range. The available projectiles to be chosen are photons, nucleons, deuterons, tritons,

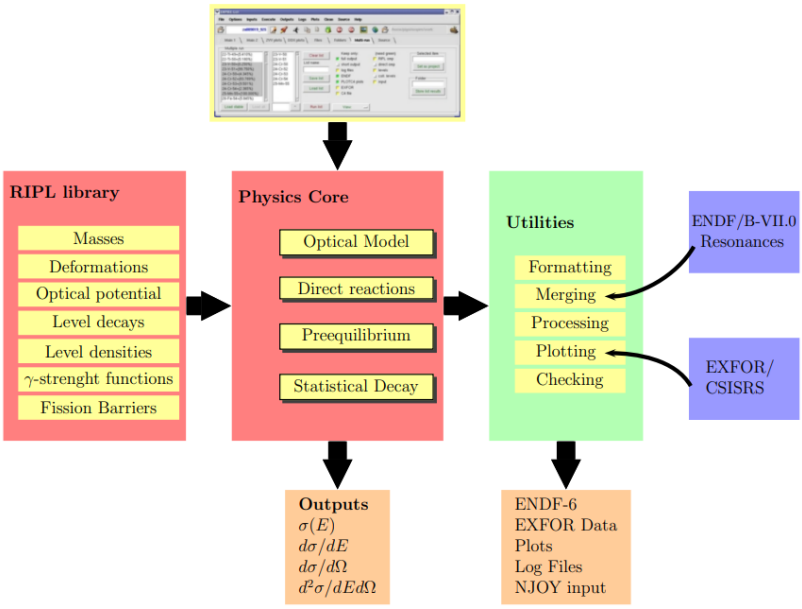

Figure 5.1: Flow-chart of the EMPIRE system showing the major components of the system as obtained from Ref. [1]

helium-3 nuclei (^{3}He), alphas, and light or heavy ions. The function of the code is illustrated as a flow-chart in Figure 5.1.

The code accounts for the major nuclear reaction models, such as optical model, Coupled Channels and DWBA (ECIS06 [35, 36] and OPTMAN [68–70]), Multi-step Direct [42] (ORION + TRISTAN), NVWY Multi-step Compound [43], exciton model [44, 45] (PCROSS), hybrid Monte Carlo simulation (DDHMS), and the full featured Hauser-Feshbach model [34] including width fluctuations and the optical model for fission. A comprehensive library of input parameters based on the RIPL-3 [71] library covers nuclear masses, optical model parameters, ground state deformations, discrete levels and decay schemes, level densities, fission barriers, and γ-ray strength functions.

In the following sections, some basic theoretical models will be described, that can be handled by the EMPIRE code via the use of specific keywords, necessary for theoretical calculations performed by the EMPIRE 3.2.3 code. These models are the optical model (EMPIRE keyword 'OMPOT'), the Hauser-Feshbach theory, the exciton model (EMPIRE keyword 'PCROSS') and the nuclear level density models (EMPIRE keyword 'LEVDEN'). Each of the aforementioned keywords can be assigned a specific value. More details will be presented in the Sections 5.2.1, 5.2.3 and 5.2.4.

5.2.1 The Optical Model

The optical model is used to describe an interaction between an incident particle and a target nucleus, including both the elastic and all the compet-

ing non-elastic channels. The whole interaction process can be envisioned as light impinging on an opaque glass sphere, where light is only partially absorbed [67]. It is described by a complex mean field potential $U(r)$ as follows:

$$U(r) = V(r) + iW(r) \tag{5.1}$$

where the real part $(V(r))$ of eq. 5.1 represents the elastic scattering, and the imaginary part $(W(r))$ of eq. 5.1 represents the inelastic scattering (or absorption effects).

Adopting for example the formalism followed in Ref. [72], eq. 5.1 can be rewritten as :

$$\begin{aligned} U(r,E) = &- \underbrace{V_V(r,E)}_{\text{real volume term}} - \underbrace{iW_V(r,E)}_{\text{imaginary volume term}} - \\ &- \underbrace{iW_D(r,E)}_{\text{imaginary surface term}} + \\ &+ \underbrace{V_{SO}(r,E)\cdot l\cdot\sigma}_{\text{real spin-orbit term}} + \underbrace{iW_{SO}(r,E)\cdot l\cdot\sigma}_{\text{imaginary spin-orbit term}} + \\ &+ \underbrace{V_C(r)}_{\text{Coulomb term}} \end{aligned} \tag{5.2}$$

Each term of eq. 5.2 can be separated by energy-dependent well depths ($V_V(E)$, $W_V(E)$, $W_D(E)$, $V_{SO}(E)$ and $W_{SO}(E)$) and energy independent radial parts "f" as follows:

$$V_V(r,E) = V_V(E) f(r, R_V, a_V) \tag{5.3}$$

$$W_V(r,E) = W_V(E) f(r, R_v, a_V) \tag{5.4}$$

$$W_D(r,E) = -4a_D W_D(E) \frac{d}{dr} f(r, R_D, a_D) \tag{5.5}$$

$$V_{SO}(r,E) = V_{SO}(E) \left(\frac{\hbar}{m_\pi c}\right)^2 \frac{1}{r}\frac{d}{dr} f(r, R_{SO}, a_{SO}) \tag{5.6}$$

$$W_{SO}(r,E) = W_{SO}(E) \left(\frac{\hbar}{m_\pi c}\right)^2 \frac{1}{r}\frac{d}{dr} f(r, R_{SO}, a_{SO}) \tag{5.7}$$

Using Equations (5.3) to (5.7), Equation (5.2) becomes:

$$U(r,E) = V_C(r) - V_V(E) f(r, R_V, a_V) -$$

$$
\begin{aligned}
&- i\left(W_V(E)f(r,R_V,a_V) - 4a_D W_D(E)\frac{d}{dr}f(r,R_D,a_D)\right) + \\
&+ V_{SO}(E)\left(\frac{\hbar}{m_\pi c}\right)^2 \frac{1}{r}\frac{d}{dr}f(r,R_{SO},a_{SO})\cdot l\cdot \sigma + \\
&+ iW_{SO}(E)\left(\frac{\hbar}{m_\pi c}\right)^2 \frac{1}{r}\frac{d}{dr}f(r,R_{SO},a_{SO})\cdot l\cdot \sigma
\end{aligned} \tag{5.8}
$$

The form factor $f(r,R_i,a_i)$ is a Woods-Saxon shape:

$$f(r,R_i,a_i) = \frac{1}{1+e^{(r-R_i)/a_i}}$$

where the geometry parameters are the radius $R_i = r_i A^{1/3}$, with A being the atomic mass number, and a_i the diffuseness parameters. For charged projectiles, the Coulomb term V_C, is given by that of a uniformly charged sphere [72]:

$$V_C(r) = \begin{cases} \frac{Zze^2}{2R_C}\left(3-\frac{r^2}{R_C^2}\right), & r \le R_C \\ \frac{Zze^2}{r}, & r \ge R_C \end{cases}$$

where $Z(z)$ is the charge of the projectile and $R_C = r_C A^{1/3}$ is the Coulomb radius.

It is underlined that EMPIRE 3.2.3 enables the user to choose different optical models that are available from the Reference Input Parameter Library (RIPL-3) via the 'OMPOT' keyword.

5.2.2 The Hauser-Feshbach theory

The Hauser-Feshbach theory [34] is used to describe nuclear reactions performed via the formation of a compound nucleus. Such reactions can be represented as:

$$a + A \rightarrow C^* \rightarrow B + b$$

The probability for an incident particle a with kinetic energy ε_a to form the compound nucleus C^* and subsequently decay to nucleus B via the emission of a b particle with a respective kinetic energy ε_b (see Figure 5.2), following the Bohr's hypothesis (see Section 5.1.1) is given by:

$$\sigma_{a,b} = \sum_{J\pi} \sigma_a(E,J\pi)P_b(E,J\pi) \tag{5.9}$$

where $\sigma_a(E,J\pi)$ represents the probability of the formation of the compound nucleus C in a state of spin and parity $J\pi$. $P_b(E,J\pi)$ represents the probability for the compound nucleus C to decay to the exit channel b. If

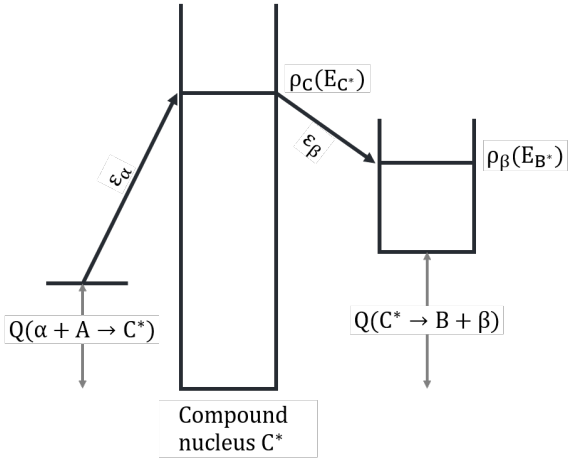

Figure 5.2: Representation of the $a + A \rightarrow B + b$ reaction via the formation of a compound nucleus C^* in an excited state. $\rho(E)$ represents the level density, while ε represents the nuclei kinetic energies in the center of mass system.

the produced compound nucleus is in an excited state E_C^*, then the decay probability is expressed in terms of transmission coefficients:

$$P_b(E, J\pi) = \frac{T_b(E_C^*, J\pi)}{\sum_C T_C(E_C^*, J\pi)} \tag{5.10}$$

where T_b is the transmission coefficient of channel b. The denominator $\sum_C T_C(E_C^*, J\pi)$ represents the sum of all possible decay channels, including particle emission, photon emission and fission. If the residual nucleus B is produced in an excited state E_B^*, with a respective level density of states $\rho_B(E_B^*)$ Equation (5.10) becomes:

$$P_b^{l_\pi} = \frac{T_l(\varepsilon_b)\rho_B(E_B^*)}{\sum_\gamma T_{\gamma,l}\rho_c(E_C^*, J\pi)} \tag{5.11}$$

However, if spin is also taken into account, the calculation of the cross section regarding the entrance channel, is obtained by the Optical Model. In this case, the final cross-section calculation involves the sums of all the possible spin additions of the entrance and exit channel, taking into account the energy conversion and selection rules.

$$\sigma_{a,b(E)} = \frac{\pi}{k^2}\sum_J \frac{2J+1}{(2s+1)(2S+1)} \frac{\sum_{l,j,l',j'} T_l(\varepsilon_a)T_{l'}(\varepsilon_b)\rho_B(E_B^*, S')}{\sum_{\gamma,l'',j''} T_{\gamma,l''}\rho_G(E_G^*)} \tag{5.12}$$

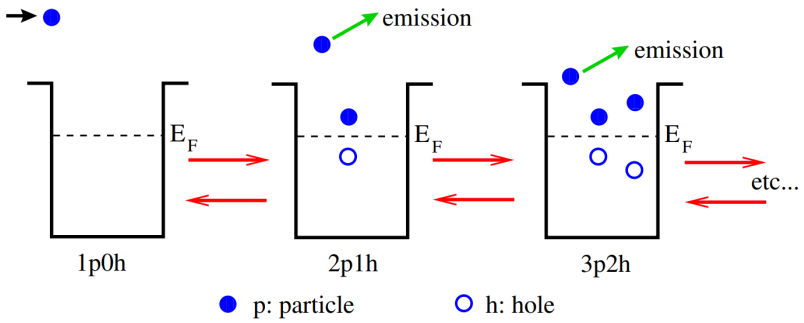

Figure 5.3: A schematic representation of the creation of excitons as a function of time as an incident particle impinges on a target nucleus. This figure is obtained from Ref. [73]

where the primed symbols represent the exit channel and the unprimed ones represent the entrance channel. More specifically j and J represent the angular momenta of the entrance channel and the compound nucleus respectively, s, S and S' represent the spins of the incident particle, the target and residual nucleus respectively. It should also be underlined that selection rules are applied in the sums of both the entrance and the exit channel, and thus the denominator includes all the possible exit channels. Furthermore, if the residual nucleus B is produced in a discrete excited level, the level density function $\rho_B(E^*_B, S')$ should be replaced by δ-functions.

5.2.3 Pre-equilibrium models

EMPIRE can handle the pre-equilibrium reaction mechanism with:

- the quantum mechanical models:
  - Multistep Direct (MSD) [42]
    As the incident energy rises, there is a greater chance that one particle will stay in the continuum and resulting in a strong memory of the projectile's initial trajectory, leading to a multistep direct reaction. The cross sections are forward peaked in this instance because there is constructive interference between matrix components affecting the same change in the particle's momentum in the continuum.
  - Multistep Compound (MSC) [43]
    All of the particles remain bound through the cascade that leads to the equilibrium during a multistep compound reaction. It is assumed that the phases of the matrix elements (J, parity, etc.) that are necessary to define a channel are random in order to eliminate any interference terms following averaging. The energy averaged cross sections are therefore approximately 90° symmetric.

- the phenomenological approach of the exciton model [44, 45]

In this section the phenomenological approach of Griffin [44, 45] (usually referred to as the exciton model) will be presented. It is mentioned that the MSC and MSD models can be activated in the EMPIRE code via the respective keywords (MSC=MSD=1). The exciton model is handled by the 'PCROSS' keyword with values ranging from 0.5 to 3, if enabled. If the value PCROSS = 0 is assigned, then the exciton model will be disabled.

According to the exciton model, the incident particle interacts with the target nucleus, exciting a single nucleon above the Fermi surface, leaving at the same time, a 'hole' behind, lying below the Fermi level. In this sense, an excited nuclear state can be characterized by the particles (p) above the Fermi level, and the holes (h) that exist below the Fermi level. The particles could either stem from protons (p_π) or neutrons (p_ν), creating the respective holes (h_π or h_ν). The sum of particles and holes is called number of excitons n, following the relation $n = p + h$.

The successive interactions between the incident particle and the target nucleus will result in an increasing number of excitons and more degrees of freedom, that will end up in an equilibrium, following the selection rules:

$$\Delta n = 0, \pm 2, \qquad \Delta p = \Delta h = 0, \pm 1$$

In Figure 5.3 the time evolution of the exciton number is presented after the interaction of an incident particle with a target nucleus. In the case of a neutron, the energy of the incident particle should be greater than the separation energy (Q-value), while in the case of protons, the Coulomb barrier should also be surpassed. If an excited particle has enough energy, it could escape the nucleus.

According to Griffin's model, the transition rate of a nucleus from an n-exciton state to other states with $n' = n$ or $n' = n \pm 2$ excitons is given by the Fermi's Gold Rule:

$$\lambda_{n\to n'} = \frac{2\pi}{\hbar}|M|^2 \rho_{n'}(E) \Rightarrow \lambda_{ph\to p'h'} = \frac{2\pi}{\hbar}|M|^2 \rho_{p'h'}(E)$$

where $|M|^2$ is the average squared matrix element for the $n \to n'$ transition. The density of p' particle and h' hole states at a specific excitation energy E is given by the expression [74, 75]:

$$\rho_{p'h'}(E) = \frac{g(gE - A_{p'h'})^{p'+h'-1}}{p'!h'!(p'+h'-1)!}$$

where:

$$A_{p'h'} = \frac{1}{4}(p'^2 + h'^2 + p' - 3h')$$

and g is the density of single-particle states.

The probability for an excited nucleus (at a specific energy E) to be in a configuration of $n = p + h$ excitons is called the occupational probability and noted as: $P(n, E, t)$. It satisfies the relation [76] :

$$\begin{aligned}\frac{dP(n,E,t)}{dt} &= P(n-2,E,t)\lambda_{n-2,n}(E)+ \\ &+ P(n+2,E,t)\lambda_{n+2,n}(E)- \\ &- P(n,E,t)\left(\lambda_{n,n+2}(E)+\lambda_{n,n-2}+\lambda_{n,c}(E)\right) \Rightarrow \qquad (5.13)\\ -P(n,E,0) &= t_{n-2}(E)\lambda_{n-2,n}(E)+ \\ &+ t_{n+2}(E)\lambda_{n+2,n}(E)- \\ &- t_n(E)\left(\lambda_{n,n+2}(E)+\lambda_{n,n-2}+\lambda_{n,c}(E)\right) \qquad (5.14)\end{aligned}$$

where $\lambda_{n,c}$ is the total decay rate for emission to the continuum and t_n is the lifetime of an n-exciton state. These factors follow the relations:

$$\lambda_{n,c}(E) = \sum_{c'} \int_0^{E_{c',max}} \lambda_{n,c}(E,\varepsilon_{c'})d\varepsilon_{c'}, \quad \varepsilon_c = \varepsilon - B$$

and

$$t_n = \int_0^{t_{eq}} P(n,E,t)dt$$

where ε_c is the energy of the particle reduced by its binding energy in the nucleus and t_{eq} is the time needed for equilibrium to be reached.

The cross section for particle emission in channel c follows the expression:

$$\sigma_c(E,\varepsilon_c) = \sigma_R \int_0^{t_{eq}} \sum_{n,\Delta n=2} P(n,E,t)\lambda_{n,c}(E,\varepsilon_c)dtd\varepsilon_c$$

where σ_R is the incident channel reaction cross section.

5.2.4 Nuclear level density models

The nuclear level densities play a crucial role in Hauser-Feshbach calculations performed by the EMPIRE 3.2.3 code. Three of the available level density models in EMPIRE are phenomenological (Gilbert-Cameron Model (GCM), Generalized Superfluid Model (GSM), Enhanced Generalized Superfluid Model (EGSM)) and one is based on Hartree-Fock-Bogoliubov microscopic model (HFBM) which will be presented in the following sections. The Fermi Gas Model (FGM) [37] is implemented in all the aforementioned

models and will be separately described, since the most commonly used level density analytical expression was derived from FGM. The different level density models are chosen in the EMPIRE code via different values to the 'LEVDEN' keyword.

The Fermi Gas Model

The Fermi Gas Model is based on the assumption of the equal spacing of the single particle states and the absence of collective effects. The density of the levels with spin J, parity π and excitation energy E can be distinguished in terms of state density and spin and parity contribution as:

$$\rho(E_x, J, \pi) = \underbrace{\rho(E_x)}_{\text{state density}} \cdot \underbrace{\rho(J, \pi)}_{\text{spin and parity dependence}} \tag{5.15}$$

where

$$\rho(E_x) = \frac{e^S}{\sqrt{Det}} \tag{5.16}$$

where S is the entropy and $Det = 114a^3T^5/\pi$ and

$$\rho(J, \pi) = \frac{1}{2}\frac{(2J+1)}{\sqrt{8\pi\sigma^3}}\exp\left[-\frac{(J+1/2)^2}{2\sigma^2}\right] \tag{5.17}$$

where the factor $1/2$ corrects for the equiparity distribution, and σ^2 is the spin cut-off parameter. The state density follows the relation:

$$\rho^{FG}(E) = \frac{\sqrt{\pi}}{12a^{1/4}U^{5/4}}\exp(2\sqrt{aU}) \tag{5.18}$$

Combining Equations (5.17) and (5.18), Equation (5.15) becomes:

$$\rho^{FG}(E, J, \pi) = \frac{2J+1}{48\sqrt{2}\sigma^{3/2}a^{1/4}U^{5/4}}\exp\left[2\sqrt{aU} - \frac{(J+1/2)^2}{2\sigma^2}\right] \tag{5.19}$$

where U is the effective excitation energy and is equal to

$$U = E_x - \Delta$$

, where Δ equal or closely related to the pairing energy. Equation (5.19) implies that the level densities in the Fermi Gas model depend on the parameters a, σ and Δ.

The energy dependence of the a-parameter, taking into account shell effects was proposed by Ignatyuk [77]:

$$a(E) = \tilde{a}\left[1 + f(U)\frac{\delta W}{U}\right] \tag{5.20}$$

where δW is the shell correction, $\tilde{a}$ is the asymptotic value of the a-parameter and

$$f(U) = 1 - e^{-\gamma U}$$

where γ is the shell effects damping parameter.

Gilbert-Cameron Model - LEVDEN 2

According to the Gilbert-Cameron model [78] (EMPIRE keyword LEVDEN=2) the excitation energy is separated in two regions. For energies below the matching point (U_x), the constant temperature formula applies, while for energies above the matching point, the Fermi Gas formula is used:

$$\rho^{GC}(E_x) = \begin{cases} \rho^{CT}(E_x)\,, & E_x \leq U_x \\ \rho^{FG}(E_x)\,, & E_x > U_x \end{cases} \tag{5.21}$$

The level density for the constant temperature follows the relation:

$$\rho^{GC}(E_x, J, \pi) = \rho^{GC}(E_x)\rho(J, \pi)$$

where $\rho(J, \pi)$ is given by Equation (5.17) and the state density by:

$$\rho^{CT}(E_x)\frac{1}{T}\exp\left(\frac{E_x - E_0}{T}\right)$$

with T being the nuclear temperature and E_0 a free parameter. The Fermi Gas state density $\rho^{FG}(E_x)$ is given by Equation (5.19). The pairing energy Δ is given by:

$$\Delta = n\frac{12}{\sqrt{A}}\,, \quad n = \begin{cases} 0\,, & \text{for odd-odd nuclei} \\ 1\,, & \text{for odd-A nuclei} \\ 2\,, & \text{for even-even nuclei} \end{cases}$$

The a-parameter could be energy-dependent or not, while the spin cut-off parameter $\sigma(E_x)$ is given by the expression:

$$\sigma^2(E_x) = 0.146A^{2/3}\sqrt{aU}$$

Generalized Superfluid Model - LEVDEN 1

In the Generalized Superfluid Model (GSM) [39, 40] (EMPIRE keyword LEVDEN=1) the level density is divided in two parts. Low energies are characterized by a superfluid behavior where pairing correlations strongly affect the level density. The high energy region is described by the Fermi Gas Model (FGM). The two regions are separated by the 'critical energy' U_c.

It can be expressed as:

$$U_c = a_c T_c^2 + E_{cond}$$

where T_c is the critical temparature and E_{cond} is the condensation energy.

$$E_{cond} = \frac{3}{2\pi^2} a_c \Delta_0^2$$

The critical values for the determinant and the entropy are given by the following expressions:

$$S_c = 2a_c T_c$$

$$Det_c = \left(\frac{12}{\sqrt{\pi}}\right)^2 a_c^3 T_c^3$$

Both below and above the critical energy, the quasi-particle level density follows this relation, but with different definitions of the thermodynamic quantities:

$$\rho_{qp}(E_x, J, \pi) = \frac{e^S}{\sqrt{Det}} \frac{1}{2} \frac{2J+1}{\sqrt{8\pi\sigma_{eff}^3}} \exp\left[-\frac{(J+1/2)^2}{2\sigma_{eff}^2}\right] \tag{5.22}$$

Calculations are performed for the excitation energy:

$$U = E_x + n\Delta_0 + \delta_{shift}\,, \quad n = \begin{cases} 0\,, & \text{for odd-odd nuclei} \\ 1\,, & \text{for odd-A nuclei} \\ 2\,, & \text{for even-even nuclei} \end{cases}$$

where $\Delta_0 = 12/\sqrt{A}$ and the δ_{shift} adjustable shift parameter is used for better description of experimental data.

If the rotational and vibrational enhancements (K_{rot}, K_{vib}) and their damping with increasing energy (Q_{rot}, Q_{vib}) are added in an adiabatic form to Equation (5.22) the final expression of the GSM level density is produced:

$$\rho(E_x, J, \pi) = \rho_{qp}(E_x, J, \pi) K_{rot} Q_{rot} K_{vib} Q_{vib} \tag{5.23}$$

Enhanced Generalized Superfluid Model - LEVDEN 0

The Enhanced Generalized Superfluid Model (EGSM) (EMPIRE keyword LEVDEN=0) is also referred to as 'Empire Global Specific Model'. It uses the superfluid model below the critical excitation energy U_c and the Fermi Gas above, as the Generalized Superfluid Model (GSM) does. The difference between the EGSM and the GSM is the more accurate treatment of high angular momenta [1] in the former case.

In EGSM, the rotational energy is subtracted from the intrinsic excitation energy, while in the other level density models the spin dependence is treated as a separate factor characterized by the spin cut-off parameter σ^2. In the EGSM, the non-adiabatic form of nuclear rotation leads to the collective enhancement of the level density, leading to a more dynamical approach regarding the shape of the nucleus. Thus deformation is taken into account via the level density parameter a that increases as a function of the nucleus' surface.

The effective excitation in EGSM is defined as:

$$U = E_x + n\Delta_0\,, \quad n = \begin{cases} 0\,, & \text{for even-even nuclei} \\ 1\,, & \text{for odd-A nuclei} \\ 2\,, & \text{for odd-odd nuclei} \end{cases} \tag{5.24}$$

where $\Delta_0 = 12\sqrt{A}$. For excitation energies below the critical energy E_c, the nuclear level density is given by Equation (5.23).

For energies above the critical energy E_c an energy shift is introduced, equal to the condensation energy:

$$U* = U - E_{cond}$$

With the assumption that the prolate nuclei rotate along the axis perpendicular to the symmetry axis, the level density becomes:

$$\begin{aligned} \rho(E_x, J, \pi) = & \frac{1}{16\sqrt{6\pi}} \left(\frac{\hbar^2}{\Im_\parallel}\right)^{1/2} a^{-1/4} \\ & \sum_{K=-J}^{J} \left(U^* - \frac{\hbar^2 K^2}{2\Im_{eff}}\right)^{-5/4} \\ & \exp\left\{2\left[a\left(U^* - \frac{\hbar^2 K^2}{2\Im_{eff}}\right)\right]^{\frac{1}{2}}\right\} Q_{rot} K_{vib} Q_{vib} \end{aligned} \tag{5.25}$$

, while assuming similarly that the oblate nuclei rotate parallel to the symmetry axis, the level density becomes:

$$\begin{aligned} \rho(E_x, J, \pi) = & \frac{1}{16\sqrt{6\pi}} \left(\frac{\hbar^2}{\Im_\parallel}\right)^{1/2} a^{-1/4} \\ & \sum_{K=-J}^{J} \left(U^* - \frac{\hbar^2[J(J+1) - K^2]}{2|\Im_{eff}|}\right)^{-5/4} \\ & \exp\left\{2\left[a\left(U^* - \frac{\hbar^2[J(J+1) - K^2]}{2|\Im_{eff}|}\right)\right]^{\frac{1}{2}}\right\} Q_{rot} K_{vib} Q_{vib} \end{aligned} \tag{5.26}$$

The rotational enhancement is taken into account in Equations (5.25) and (5.26) via the summation over projection of the angular momentum K. $\mathfrak{I}_{eff}$ represents the effective moment of inertia defined as a function of the parallel and perpednicular moments of inertia as follows:

$$\frac{1}{\mathfrak{I}_{eff}} = \frac{1}{\mathfrak{I}_{\parallel}} - \frac{1}{\mathfrak{I}_{\perp}}$$

If $J >> K$, Equations (5.25) and (5.26) become:

$$\rho(E_x, J, \pi) = \frac{e^S}{\sqrt{Det}} \cdot \frac{1}{2} \cdot \frac{2J+1}{\sqrt{8\pi\sigma_{eff}^2}} exp\left[-\frac{(J+1/2)^2}{2\sigma_{eff}^2}\right] K_{rot} Q_{rot} K_{vib} Q_{vib} \qquad (5.27)$$

Microscopic combinatorial level densities - LEVDEN 3

In EMPIRE, there is also the possibility to describe the nuclear level density via a combinatorial approach. Single-particle level schemes are obtained from the Hartree-Fock-Bogoliubov method (HFBM), based on the BSk14 Skyrme force [79] (EMPIRE keyword LEVDEN=3). This way, incoherent particle hole densities $\omega_{ph}(E_x, M, \pi)$ are constructed as a function of the excitation energy (E_x), the spin projection (M) and the parity (π).

If the studied nucleus exhibits spherical symmetry, the level density follows the relation:

$$\rho_{sph}(E_x, J, \pi) = \omega_{int}(E_x, M = J, \pi) - \omega_{int}(E_x, M = J = 1, \pi) \qquad (5.28)$$

where ω_{int} is the vibrational state density $\omega_{vib}(E_x, M, \pi)$ folded with the incoherent particle-hole state density $\omega_{ph}(E_x, M, \pi)$.

For a deformed nucleus, with an axial mirror symmetry, the level density follows the relation:

$$\begin{aligned}\rho_{def}(E_x, J, \pi) = \frac{1}{2} \sum_{K=-J, K\neq 0}^{J} & \omega_{int}(E_x - E_{rot}^{J,K}, K, \pi) + \\ & + \delta_{J=even}\delta_{\pi=+}\omega_{int}\omega_{int}(E_x - E_{rot}^{J,0}, 0, \pi) + \\ & + \delta_{J=odd}\delta_{\pi=-}\omega_{int}\omega_{int}(E_x - E_{rot}^{J,0}, 0, \pi) \end{aligned} \qquad (5.29)$$

where K are the spin projections and $E_{rot}^{J,K}$ is the rotational energy.

5.3 EMPIRE 3.2.3 calculations

In this section, the steps followed for the theoretical reproduction of the ^{70}Ge(n,2n)^{69}Ge, ^{72}Ge(n,α)^{69m}Zn, ^{72}Ge(n,p)^{72}Ga, ^{73}Ge(n,nα)^{69m}Zn,

^{73}Ge(n,np/d)^{72}Ga, ^{73}Ge(n,p)^{73}Ga, ^{74}Ge(n,α)^{71m}Zn, ^{74}Ge(n,np/d)^{73}Ga and ^{76}Ge(n,2n)^{75}Ge reaction channel results with a coherent set of input parameters via the EMPIRE 3.2.3 code [1] will be presented. The calculations were performed in the neutron energy range from 5 to 20 MeV.

The aim of this theoretical investigation was the use of a coherent set of input parameters for the simultaneous reproduction of all the aforementioned studied reaction channels, taking into account all the available experimental data in literature. The procedure that was followed towards this goal can be divided into three steps:

1. choice of the neutron Optical Model potential and the appropriate level density model
2. choice of the proton Optical Model potential
3. choice of the α-particle Optical Model potential

These steps will be discussed in Sections 5.3.1 to 5.3.3 that follow.

5.3.1 Neutron Optical Model potential and level density model

For the first step of the theoretical investigation, the ^{70,76}Ge(n,2n)^{69,75}Ge reaction channels were chosen, in order to be simultaneously reproduced, since the (n,2n) reaction channels are the most dominant ones regarding their cross-section values. Furthermore, the ^{70,76}Ge isotopes differ only by three neutron pairs and they are both even-even nuclei, so they can be expected to follow similar systematics.

All the combinations between all the available optical model potentials from the RIPL-3 library and the available level density models provided by the EMPIRE 3.2.3 code were performed. The ideal combination between these two parameters for the simultaneous reproduction of the ^{70,76}Ge(n,2n)^{69,75}Ge reaction channels was found to be:

- the global optical model potential of Morillon and Romain [46] (RIPL-3 OMP index: 2411)
- the Enhanced Generalized Superfluid Model (EGSM) (EMPIRE keyword: levden=0)

As presented in Figure 5.4, all the level density models except the one from Morillon and Romain [46] seem to overestimate the experimental cross-section values, especially for energies below ∼18 MeV.

It is also noted, that during this first approach, the optical model potential for protons, alphas, deuterons, tritons and ^{3}He were left at default values in the EMPIRE input file.These were:

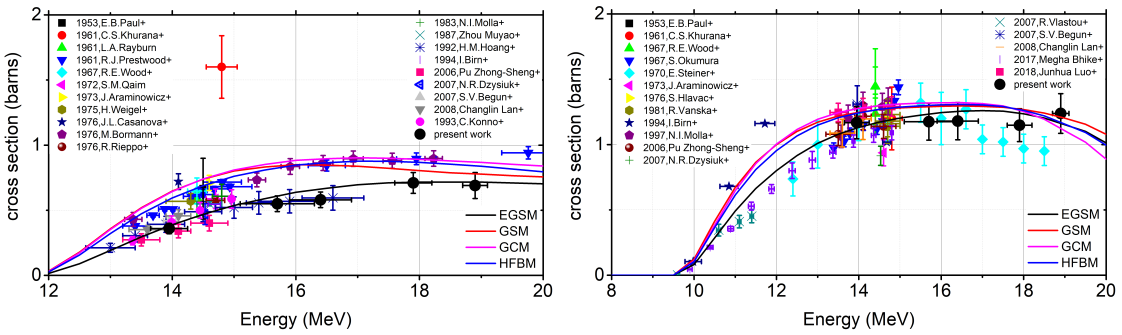

(a) ^{70}Ge(n,2n)^{69}Ge **(b)** ^{76}Ge(n,2n)^{75}Ge

Figure 5.4: EMPIRE calculations for the ^{70,76}Ge(n,2n)^{69,75}Ge reaction channels for all the available level densities in the EMPIRE 3.2.3 code:
EGSM: Enhanced Generalized Superfluid Model
GSM: Generalized Superfluid Model
GCM: Gilbert-Cameron Model
HFBM: Hartree-Fock-Bogoliubov Model
All these calculations were performed with the global optical model potential of Morillon and Romain [46]

- The proton optical model potential of Koning and Delaroche [47] (RIPL-3 OMP index: 5405)
- The α-particle optical model potential of Avrigeanu, Hodgson, and Avrigeanu [49] (RIPL-3 OMP index: 9600)
- The deuteron optical model potential of An and Cai [80] (RIPL-3 OMP index: 6200)
- The triton optical model potential of F.D.Becchetti and G.W.Greenlees [81] (RIPL-3 OMP index: 7100)
- The ^{3}He optical model potential of F.D.Becchetti and G.W.Greenlees [81] (RIPL-3 OMP index: 8100)

The pre-equilibrium mechanism was also activated in both cases (MSD=1, MSC=1, PCROSS=1.5).

As presented in Figure 5.5, the simultaneous reproduction of the ^{70,76}Ge(n,2n)^{69,75}Ge reaction channels is quite satisfactory, with the adopted input parameters.

Nevertheless, the calculations were extended to lower energies (from 0.1 to 20 MeV) with the same parametrization, in order to check the reproduction of the (n,total) channel for both the ^{70,76}Ge isotopes, as presented in Figure 5.6. There is a very nice reproduction of these channels, further validating the choice of the input parameters in the calculations.

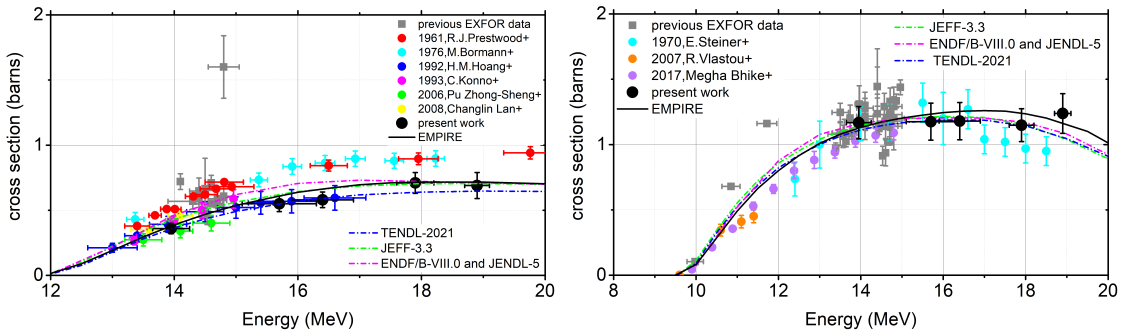

(a) ^{70}Ge(n,2n)^{69}Ge **(b)** ^{76}Ge(n,2n)^{75}Ge

Figure 5.5: EMPIRE calculations for the ^{70,76}Ge(n,2n)^{69,75}Ge reaction channels adopting the global optical model potential of Morillon and Romain [46] and the EGSM level density model, along with JEFF-3.3 [27], JENDL-5 [26], TENDL-2021 [25] and ENDF/B-VIII.0 [16] evaluation libraries.

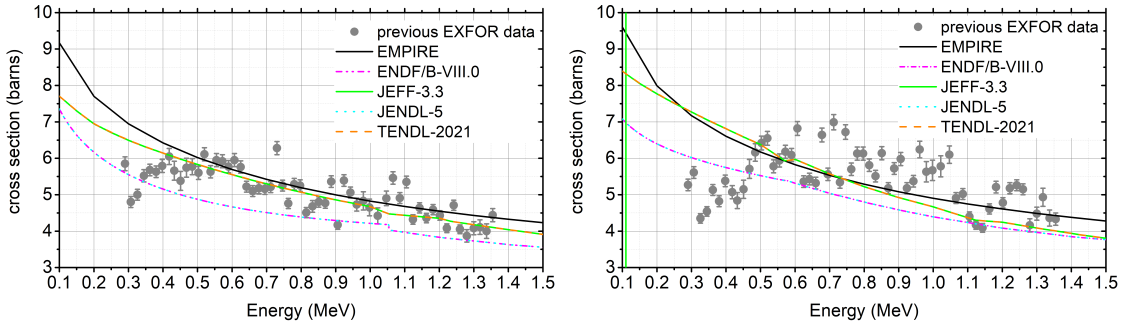

(a) ^{70}Ge(n,tot) **(b)** ^{76}Ge(n,tot)

Figure 5.6: The EMPIRE calculation for the (n,tot) reaction channels for the ^{70,76}Ge isotopes, along with previous data found in literature [18] and the JEFF-3.3 [27], JENDL-5 [26], TENDL-2021 [25] and ENDF/B-VIII.0 [16] evaluation libraries.

5.3.2 Proton Optical Model potential

The second step was to reproduce all the reactions with a proton on the exit channel, namely the ^{72,73}Ge(n,p)^{72,73}Ga and the ^{73,74}Ge(n,np/d)^{72,73}Ga ones, with the optical model potential for neutrons and the level density model fixed from the previous step. The most appropriate global optical model potential for protons was found to be the one of Koning and Delaroche [47] (RIPL-3 OMP index: 5405). The contribution of the pre-equilibrium mechanism was modified via the PCROSS EMPIRE keyword for the nuclei ^{72,73,74}Ge with respective values of 1.2, 0.6 and 0.6, while the MSD and MSC models were also activated (MSD=MSC=1). The optical model potentials for alphas, deuterons, tritons and ^{3}He were once more

left at their default values.

There is a satisfactory agreement with the experimental cross-section results of the present work, regarding the simultaneous reproduction of all the reaction channels with a proton (p) on the exit channel as presented in Figure 5.7. Furthermore, this parametrization also reproduces experimental cross-section results from previous measurements of our group (Vlastou et al. [48]) as presented in Figures 5.7a and 5.7b.

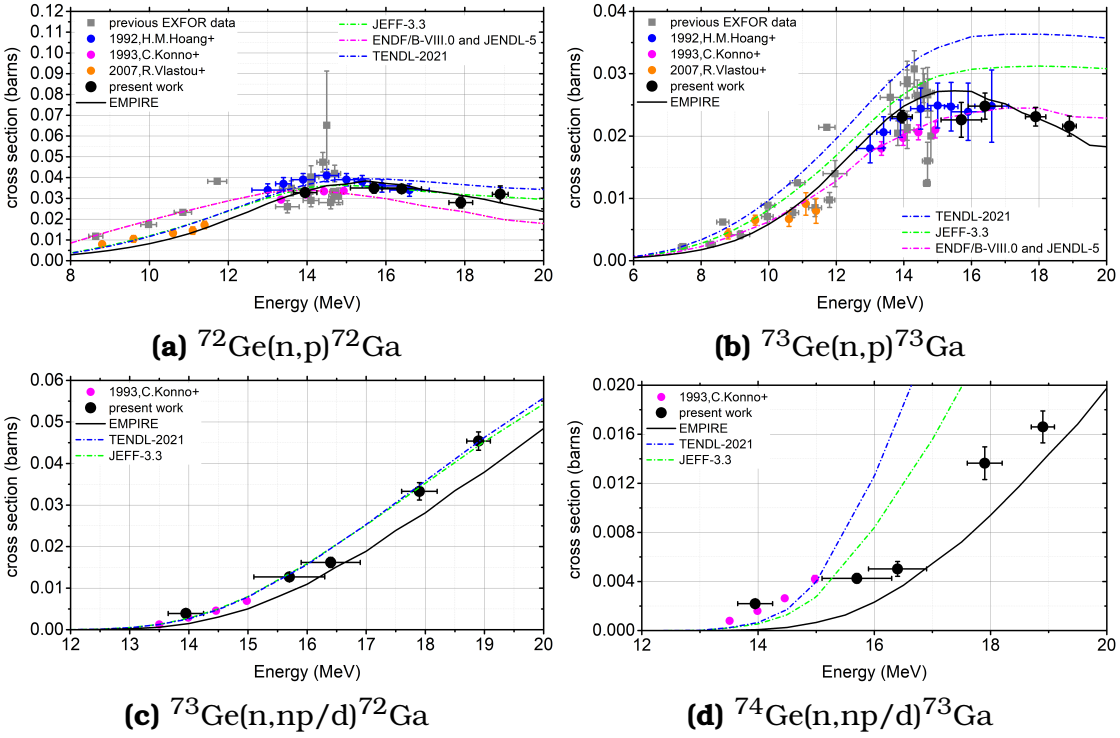

(a) ^{72}Ge(n,p)^{72}Ga **(b)** ^{73}Ge(n,p)^{73}Ga

(c) ^{73}Ge(n,np/d)^{72}Ga **(d)** ^{74}Ge(n,np/d)^{73}Ga

Figure 5.7: EMPIRE calculations, along with JEFF-3.3 [27], JENDL-5 [26], TENDL-2021 [25] and ENDF/B-VIII.0 [16] evaluation libraries for all the reaction channels with a proton (p) in the exit channel. The optical model potential of Koning and Delaroche [47] was adopted.

5.3.3 α-particle Optical Model potential

Having the optical model for neutrons, protons and the level density fixed from the previous two steps, the final step was to simultaneously reproduce all the studied reaction channels with an α-particle on the exit channel. These reactions were the ^{72,74}Ge(n,α)^{69m,71m}Zn and the ^{73}Ge(n,nα)^{69m}Zn ones. The most suitable was the one from Avrigeanu, Hodgson, and Avrigeanu [49] (RIPL-3 OMP index: 9600). In this case the level density parameter $\tilde{a}$ ("ATILNO" EMPIRE keyword) was modified by 19% ($\tilde{a} = 0.81$) and by 16% ($\tilde{a} = 0.84$) for the residual nuclei ^{69}Zn and ^{70}Zn respectively, leaving all the remaining studied channels unaffected.

The reproduction of the ^{72}Ge(n,α)^{69m}Zn reactions with this parametrization is quite satisfactory as presented in Figures 5.8a and 5.8c, something which is not the case for the ^{73}Ge(n.nα)^{69m}Zn reaction as illustrated in Figure 5.8b.

It should also be emphasized that the main contributions to the studied reactions were the neutron and proton and alpha optical model potentials (in this order), with the respective optical model potentials for deuterons, tritons and ^{3}He having a very small contribution to the final theoretical cross-section result. Nevertheless, after each step involving a change in the input parameters, all the previous ones were repeated, in order to ensure the validity of the whole EMPIRE calculation.

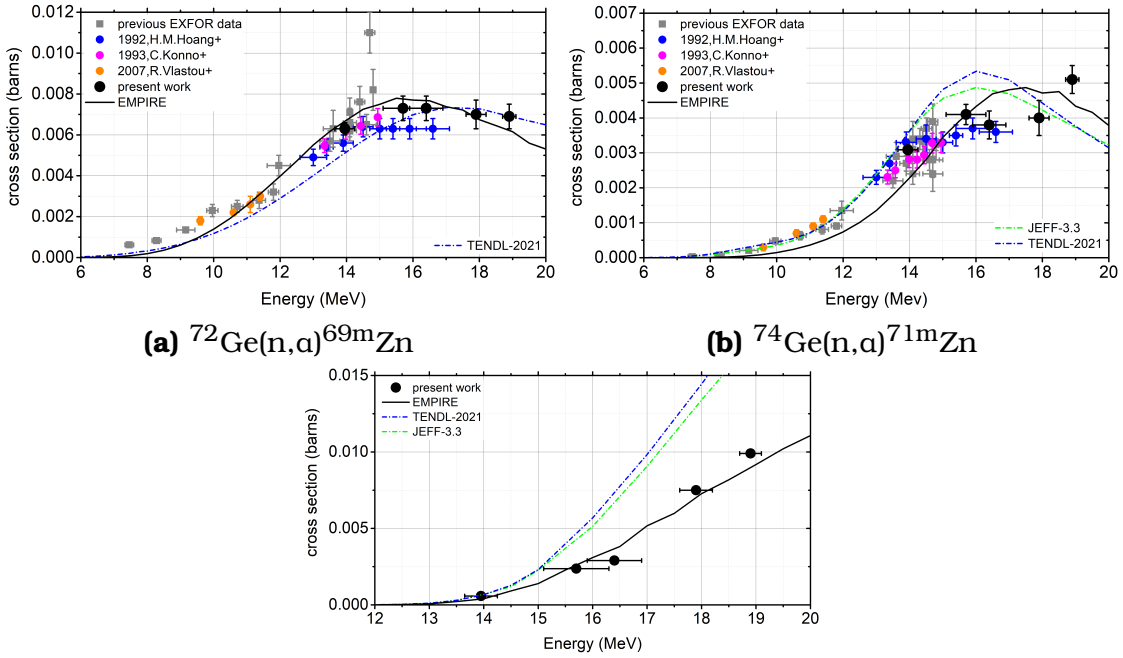

(a) ^{72}Ge(n,α)^{69m}Zn **(b)** ^{74}Ge(n,α)^{71m}Zn

(c) ^{73}Ge(n,nα)^{69m}Zn

Figure 5.8: EMPIRE calculations, along with JEFF-3.3 [27] and TENDL-2021 [25] evaluation libraries for all the reaction channels with an alpha (α) particle in the exit channel. The optical model potential of Avrigeanu, Hodgson, and Avrigeanu [49] was adopted.

It should also be underlined that the modification of the input parameters during the EMPIRE calculations for the nine reaction channels that were presented above, were performed in a consistent manner, not affecting any previous steps during the whole procedure.

Finally, it should be highlighted that the satisfactory reproduction of nine different reaction channels on the five isotopes of Ge, with a coherent set of input parameters, constitutes a very important constraint in the statistical model calculations performed, thus confirming the validity and reliability of the adopted parametrization.

Finally, the parametrization mentioned above was applied in some reactions that were not measured in the present work, but other experimental data were found in literature. These reactions were the ^{70}Ge(n,p)^{70}Ga (presented in Figure 5.9) and the ^{76}Ge(n,2n)^{75m}Ge (presented in Figure 5.10) reactions.

There is a good reproduction for most of the recent experimental data of the ^{70}Ge(n,p)^{70}Ga reaction, while the EMPIRE calculation for the ^{76}Ge(n,2n)^{75m}Ge reaction is also in excellent agreement with the recent dataset of Megha Bhike [63] that also utilized an enriched ^{76}Ge target for the cross-section measurements. The reproduction of both ground and isomeric state of the ^{76}Ge(n,2n)^{75}Ge reaction further confirms the validity and reliability of the adopted parametrization.

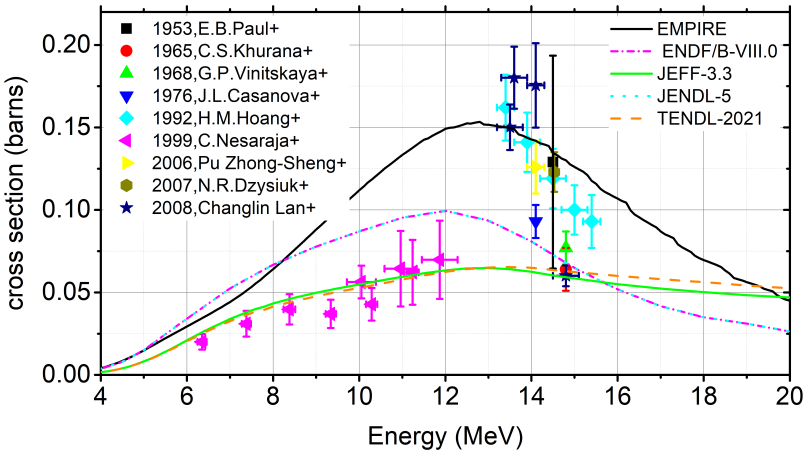

Figure 5.9: EMPIRE calculation for the ^{70}Ge(n,p)^{70}Ga reaction

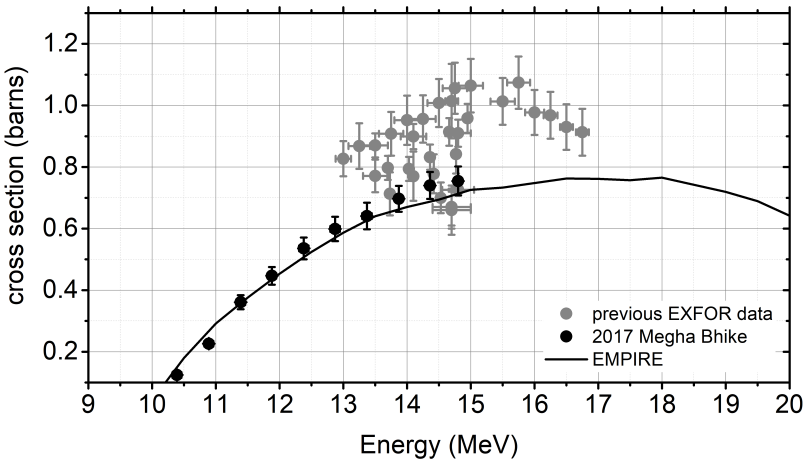

Figure 5.10: EMPIRE calculation for the ^{76}Ge(n,2n)^{75m}Ge reaction

Chapter 6

Conclusions & Perspectives

In this work, the total cross-sections of the ^{70}Ge(n,2n)^{69}Ge, ^{72}Ge(n,α)^{69m}Zn, ^{72}Ge(n,p)^{72}Ga, ^{73}Ge(n,nα)^{69m}Zn, ^{73}Ge(n,np/d)^{72}Ga, ^{73}Ge(n,p)^{73}Ga, ^{74}Ge(n,α)^{71m}Zn, ^{74}Ge(n,np/d)^{73}Ga and ^{76}Ge(n,2n)^{75}Ge reactions have been experimentally determined by means of the activation technique, relative to the reference ^{27}Al(n,α)^{24}Na reaction, and cross-checked by the ^{197}Au(n,2n)^{196}Au reference reaction. The quasi-monoenergetic neutron beams were produced in the energy range between 14.0-18.9 MeV via the ^{3}H(d,n)^{4}He reaction at the neutron beam facilities of NSCR 'Demokritos' (Greece) and the 'AMANDE', IRSN facility (France). The targets that were used in this work were enriched ^{70,72,73,74,76}Ge samples, in the form of GeO_2 pellets provided by the n_TOF collabaration (CERN).

Most of the data found in literature implement ^{nat}Ge targets for the cross-section measurements. Contaminations from neighboring isotopes' reactions that lead to the production of the same residual nucleus[1], could then contribute to the yield of the measured reaction, thus necessitating theoretical corrections that bear their own uncertainties. These contributions become larger as a function of neutron energy, leading to less trustworthy theoretically corrected cross-section results. This could be the reason why there is a considerable lack of experimental data for most of the studied reactions above 15 MeV and discrepancies among the existing data.

The use of highly enriched samples, on the other hand, can yield much more accurate cross-section data since the latter does not suffer from such contaminations. In this scope, the results of this work provide much needed accurate data in an energy region where very few or none of them exists. Furthermore, reactions with very low cross-section values can be measured

[1]The activation technique is based on the measurement of the radioactivity emitted from a residual nucleus. Therefore if two reaction channels lead to the production of the same residual nucleus, there is no way to distinguish between the two contributions.

with the use of isotopically enriched samples (e.g. ^{73}Ge(n,nα)^{69m}Zn). At the same time, these accurate results can act as a test for the validity and limits of the correction methodologies followed, in the case of ^{nat}Ge targets. Within the scope of this work, a methodology for such corrections was proposed, the accuracy and limits of which were tested experimentally with two sets of measurements at the neutron beam energy of 17.9 MeV. The first set of measurements was performed with a ^{nat}Ge target and the corrected results were compared to the ones produced from the second set of measurements carried out with the respective enriched samples.

Following the experimental work, a theoretical investigation was performed with statistical model calculations via the EMPIRE 3.2.3 code. The goal was to achieve a satisfying reproduction for the nine reaction channels studied, taking into account, not only the accurate cross-section data calculated in the frame of this work, but also previous measurements from our group and previous experimental data found in literature, with a coherent set of input parameters. The accurate simultaneous description of nine reaction channels on five isotopes of Ge, including isomer production, is a very important constraint in the input parameters of statistical model calculations, verifying their accuracy and robustness.

However, there is a need for testing the parametrization used in the theoretical study of the present work, to other isotopes, of technological or theoretical interest in the same mass region (for example ^{75}As is reported in the NEA Nuclear data high priority request list for dosimetry applications). Furthermore, it would be very interesting to perform in-beam measurements, especially in some of the measured reactions in order to distinguish between the (n,d) and (n,np) coupled channels. In conclusion, cross-section measurements employing highly isotopically enriched targets of key medium-heavy elements (such as e.g. the even-Z Fe, Ni, Zn, Se, Sr elements, with many natural occurring isotopes), despite their cost and difficulty to obtain, could vastly improve statistical model calculations and lead towards more successful evaluation attempts, especially in the high-MeV energy region, where there is a lack of accurate experimental data.

Appendix A

Activation Method & Correction Factors

As described in section 2.1, the activation method is based on the measurement of the induced radioactivity of a residual nucleus produced from a nuclear reaction described as[1]:

$$\mathrm{x} + \mathrm{X} \rightarrow \mathrm{Y} + \mathrm{y}$$

where:

- x is the projectile (in the present work a neutron beam)
- X is the target nucleus (in the present work, one of the ^{70,72,73,74,76}Ge isotopes)
- y is the ejectile
- Y is the residual nucleus whose radioactivity is being measured

The production of the residual nucleus Y is described by the differential equation A.1[2]:

$$\frac{\mathrm{dN_p}}{\mathrm{dt}} = \underbrace{\sigma \cdot \mathrm{f(t)} \cdot \mathrm{N_t}}_{\text{production}} - \underbrace{\lambda \mathrm{N_p}}_{\text{destruction}} \tag{A.1}$$

where:

[1] Or in a more compact form: $\mathrm{X(x,y)Y}$

[2] It is assumed that the produced radioactive nuclei do not undergo nuclear reactions with the neutron beam. In other words, the number of the produced radioactive nuclei that is "destroyed" by secondary nuclear reactions is negligible.

- σ is the cross section of the $X(x,y)Y$ reaction.
- $f(t)$ is the neutron flux integrated in fixed (preferably small-in the order of a few minutes) time intervals, denoted as "dt" in chapters 2 and 4. It is expressed in arbitrary units, hence a "neutron counter" such as a BF_3 detector can be used for the measurement of the neutron flux as a function of time.
- N_t is the number of nuclei of the measuring target X
- N_p is the number of the produced radioactive nucleus Y
- λ is the decay constant of the produced radioactive nucleus Y

The solution of the differential equation A.1 is as follows:

$$\begin{aligned}
\frac{dN_p}{dt} &= \sigma \cdot f(t) N_t - \lambda \cdot N_p \xrightarrow{e^{\cdot \lambda t}} \\
\frac{dN_p}{dt} \cdot e^{\lambda t} &= \sigma \cdot f(t) \cdot N_t \cdot e^{\lambda t} - \lambda \cdot N_p \cdot e^{\lambda t} \Rightarrow \\
\frac{dN_p}{dt} \cdot e^{\lambda t} + \lambda \cdot N_p \cdot e^{\lambda t} &= \sigma \cdot f(t) \cdot N_t \cdot e^{\lambda t} \Rightarrow \\
\frac{dN_p}{dt} \cdot e^{\lambda t} + N_p \frac{de^{\lambda t}}{dt} &= \sigma \cdot f(t) \cdot N_t \cdot e^{\lambda t} \Rightarrow \\
\frac{d\left(N_p \cdot e^{\lambda t}\right)}{dt} &= \sigma \cdot f(t) \cdot N_t \cdot e^{\lambda t} \Rightarrow \\
\int \frac{d\left(N_p \cdot e^{\lambda t}\right)}{dt} dt &= \int \sigma \cdot f(t) \cdot N_t \cdot e^{\lambda t} dt \Rightarrow \\
N_p(t) \cdot e^{\lambda t} &= \int \sigma \cdot f(t) \cdot N_t \cdot e^{\lambda t} dt + C \qquad \text{(A.2)}
\end{aligned}$$

Assuming that the irradiation starts at $t = 0$ and ends at $t = t_{irr}$, the initial conditions for $t = 0$ of equation A.2 are:

$$N_p(t = 0) = 0 \Rightarrow C = 0$$

Equation A.2 then becomes:

$$\begin{aligned}
N_p(t_{irr}) &= \frac{\sigma \cdot N_t \cdot \int_0^{t_{irr}} e^{\lambda t} f(t) dt}{e^{\lambda \cdot (t_{irr} - 0)}} \Rightarrow \\
N_p(t_{irr}) &= \sigma \cdot N_t \cdot \left(\int_0^{t_{irr}} e^{\lambda t} f(t) dt \right) \cdot e^{-\lambda t_{irr}} \Rightarrow \\
N_p(t_{irr}) &= \sigma \cdot N_t \cdot \left(\int_0^{t_{irr}} e^{\lambda t} f(t) dt \right) \cdot e^{-\lambda t_{irr}} \frac{\int_0^{t_{irr}} f(t) dt}{\int_0^{t_{irr}} f(t) dt} \Rightarrow
\end{aligned}$$

$$N_p(t_{irr}) = \sigma \cdot N_t \underbrace{\left(\int_0^{t_{irr}} f(t)dt \right)}_{\Phi} \cdot \underbrace{e^{-\lambda t_{irr}} \cdot \frac{\int_0^{t_{irr}} e^{\lambda t} f(t)dt}{\int_0^{t_{irr}} f(t)dt}}_{f_c} \Rightarrow$$

$$N_p(t_{irr}) = \sigma \cdot N_t \cdot \Phi \cdot f_c \tag{A.3}$$

The "D" correction factor After the end of the irradiation, the N_p produced radioactive nuclei, start decaying following the differential equation:

$$\frac{dN_p}{dt} = -\lambda N_p \Rightarrow \frac{1}{N_p}\frac{dN_p}{dt} = -\lambda \Rightarrow \int \frac{1}{N_p}\frac{dN_p}{dt}dt = -\int \lambda dt \Rightarrow$$

$$\ln N_p = -\lambda t + C \Rightarrow N_p(t) = e^{-\lambda t + C} \Rightarrow N_p(t) = e^{-\lambda t} e^{C} \xrightarrow{N_p(0)=0 \Rightarrow e^{C} = N_p(0)}$$

$$N_p(t) = N_0 \cdot e^{-\lambda t} \tag{A.4}$$

which is essentially the radioactive decay law, providing the number of radioactive nuclei that still exist after time "t" with respect to the time of their creation (time "0").

Therefore, the number of nuclei that have decayed (N_d) at a specific time t' after the end of the irradiation (t_{irr}) is:

$$N_d(t') = N_p(t = t_{irr}) - N_p(t') \xrightarrow{A.4} N_d(t') = N_0 - N_0 \cdot e^{-\lambda t'} \Rightarrow$$

$$N_d(t') = N_0 \left(1 - e^{-\lambda t'}\right) \tag{A.5}$$

Now assuming:

- t_1 as the "cooling" or "waiting" time that represents the time interval between the end of the irradiation end the start of the measurement of the sample by the HPGe detector
- t_2 as the time duration between the end of irradiation and the end of the measurement in front of the HPGe detector

and according to equation A.5, the number of nuclei that decayed during the measurement is:

$$N_d = N_d(t_2) - N_d(t_1) = N_0 \left(1 - e^{-\lambda t_2}\right) - N_0 \left(1 - e^{-\lambda t_1}\right) \Rightarrow$$

$$N_d = N_0 \left(1 - e^{-\lambda t_2} - 1 + e^{-\lambda t_1}\right) \Rightarrow$$

$$N_d = N_0 \underbrace{\left(e^{-\lambda t_1} - e^{-\lambda t_2}\right)}_{D} \tag{A.6}$$

The correction factor for the correction of nuclei produced during the irradiation but decayed, during the "cooling" and measurement time is:

$$D = e^{-\lambda t_1} - e^{-\lambda t_2} \tag{A.7}$$

Appendix B

Corrections in the Measured Yield

The experimentally measured γ-ray yield must be corrected for different effects including True Coincidence Summing (TCS), dead time and the contribution of parasitic neutrons.

B.1 Summing Effects

True Coincidence Summing (TCS) effects can be observed in γ-ray measurements, when two (or more) γ-rays are detected simultaneously by the detector. This effect can happen while performing γ-ray spectroscopy in an isotope that emits multiple cascade γ-rays in its decay (see Figure B.1). Generally, the lifetime of the intermediate state (E_B), is very short and the two (or more) γ-rays from the same decay of the residual nucleus are emitted effectively simultaneously, with respect to the response time of the detector and the corresponding electronics. In this case, the energy deposition of both γ-rays takes place simultaneously in the active volume of the detector, resulting in a photopeak corresponding to an energy equal to the sum of the two individual γ-ray energies in the recorded amplitude spectrum. This peak is called sum coincidence peak, while partial loss interactions, will also result in a continuum of sum events at lower amplitudes [58].

This process creates a sum peak by removing at the same time events that would otherwise be recorded in the individual γ-ray peaks of the cascade. The relative number of events expected in the sum peak depends on the following factors:

- the branching ratio and the multiplicity of the γ-rays

- the possible angular correlation that may exist between them
- the solid angle between the sample and the detector

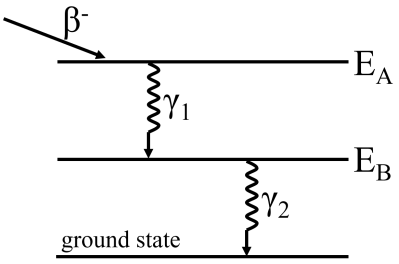

Figure B.1: Simplified decay scheme of a nucleus emitting two cascade γ-rays. Given that the intermediate state E_B is short-lived, γ_1 and γ_2 are emitted with a very small time difference, i.e. "simultaneously".

In order to estimate these effects in the present work, Monte Carlo simulations were performed, implementing the MCNP-CP extension [82] to the MCNP5 Monte Carlo code. MCNP-CP models the radioactive decay of a given nucleus taking into account the emission of cascade γ-rays along with the respective emission times and γ-γ angular correlations. These data are sampled according to the decay scheme of a specific radioactive isotope, taken from the evaluated nuclear structure data file ENSDF [83].

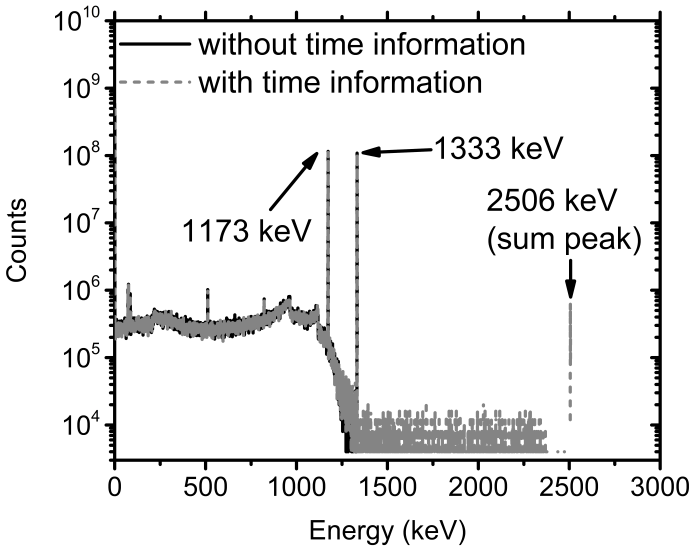

Figure B.2: The spectra obtained from the f8 tally scoring with (grey dotted line) and without (black solid line) time information about the cascade γ-rays emitted from a radioactive nucleus. This example is plotted for a ^{60}Co source.

The first step was to accurately describe the geometry of the γ-ray spectroscopy measurement (HPGe detector and measuring sample). The second

step was to run the Monte Carlo simulation **with** the information of cascade γ-ray emission times. The third step was to run the Monte Carlo simulation **without** the information of cascade γ-ray emission times. In both cases, the γ-rays were scored in the active volume of the HPGe detector with the f8 (pulse height) tally, producing the simulated spectra presented in Figure B.2. In this example, the decay of a ^{60}Co source was simulated, placed at a distance of 10 cm from the HPGe detector. A ^{60}Co source is chosen for the illustration of this example, since it is a nucleus with high intensity cascade γ-rays as presented in Figure B.3.

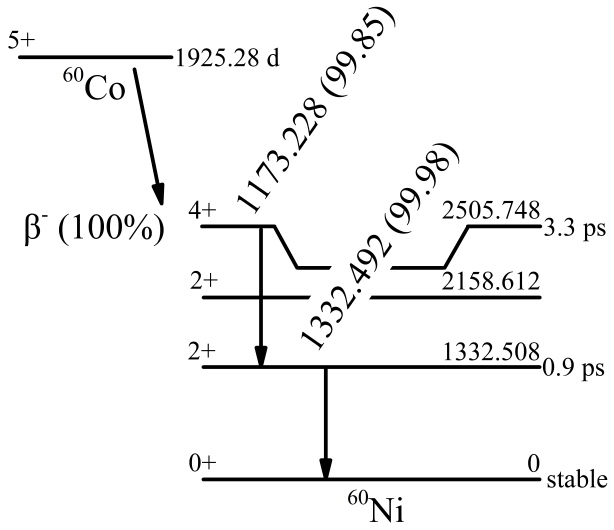

Figure B.3: A simplified decay scheme of ^{60}Co. The γ-ray energies and respective intensities were obtained from IAEA [84].

Following the same methodology, the TCS effect can be estimated for each γ-ray emitted either from a Ge target or a reference foil, as the ratio of the integrals of the γ-ray of interest between the two different simulations. For the example of the ^{27}Al reference foil, the contribution of summing effects was found to be ∼2% at a distance of 10 cm.

B.2 Dead Time

In every detection system, a detected event is recognized as a separate pulse. In general, there is a minimum time needed between two pulses for them to be recognized as separate events. This time limit is related to physical processes within the detector itself, as well as to the associated electronics. Dead time corrections must be applied in the measured γ-ray yield, when the measured sample has high activity, leading to high counting rates. This correction factor is simply given by the ratio:

$$f_{DT} = \frac{\text{live time}}{\text{real time}} \tag{B.1}$$

where "live time" represents the time when the detection system can process pulses, while "real time" represents the actual time duration of the measurement. These two time values will differ if events are recorded at the detector with a time difference smaller than the "minimum time" allowed by the detector and the associated electronics.

B.3 Parasitic Neutrons

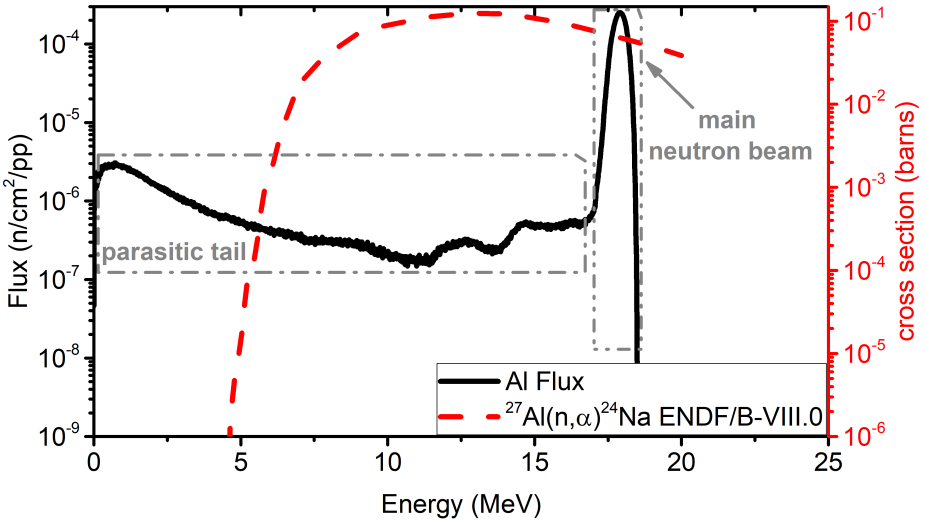

Figure B.4: The Neutron Flux from the MCNP5 code scored at an Al foil, and the ^{27}Al(n,α)^{24}Na reaction cross section, obtained from the ENDF/B-VIII.0 library

In Figure B.4 the main neutron beam (black solid line) is presented, that is accompanied by a low-energy parasitic tail [6] with intensity lower by 2-3 orders of magnitude in comparison with the main beam. However, the reference ^{27}Al(n,α)^{24}Na reaction (as well as the (n,x) ones on the Ge isotopes) have thresholds in the MeV range. In Figure B.4 the cross section for the ^{27}Al(n,α)^{24}Na reference reaction is presented with the red dashed line. The long tail of the parasitic tail is not expected to have a significant contribution on the measured yield of each measured reaction. Nevertheless, the contribution of this effect was calculated via the following equation:

$$f_{par} = \frac{\sum_{\text{main}} \sigma(E) \cdot \Phi(E)}{\sum_{\text{total}} \sigma(E) \cdot \Phi(E)} \tag{B.2}$$

where the numerator is the reaction rate integral of the main neutron beam and the denominator is the integral of the total reaction rate. The cross-section values $\sigma(E)$ are obtained from the ENDF/B-VIII.0 library, and were linearly interpolated to have the same energy binning as the neutron flux, simulated by the MCNP5 code. This correction will insert a systematic uncertainty in the analysis.

Appendix C

Weighted Average & Covariance

According to the formalism mentioned in Appendix 2 of Ref. [62], the weighted average cross section from three different values[1], each stemming from a different γ-ray is given by the following expression:

$$\bar{\sigma} = \Sigma \cdot W^{\intercal} = \begin{bmatrix} \sigma_1 \\ \sigma_2 \\ \sigma_3 \end{bmatrix} \cdot \begin{bmatrix} w_1 & w_2 & w_3 \end{bmatrix} \Rightarrow$$
$$\bar{\sigma} = \sigma_1 \cdot w_1 + \sigma_2 \cdot w_2 + \sigma_3 \cdot w_3 \tag{C.1}$$

, where σ_i are the different cross-section values and w_i are the corresponding weights.

The weights are described by equation C.2:

$$w_i = \frac{\sum_j V_{ji^{-1}}}{\sum_k \sum_l V_{kl}^{-1}} \tag{C.2}$$

, where V_{ij} is the covariance matrix between the different measurements, and V_{ij}^{-1} the respective inverse covariance matrix:

$$V_{ij} = \begin{bmatrix} V_{11} & V_{12} & V_{13} \\ V_{21} & V_{22} & V_{23} \\ V_{31} & V_{32} & V_{33} \end{bmatrix}$$

[1] A similar formalism is applied for four or more different cross-section values.

$$V_{ij}^{-1} = \frac{1}{|V_{ij}|}\begin{bmatrix} \begin{vmatrix} V_{22} & V_{23} \\ V_{32} & V_{33} \end{vmatrix} & \begin{vmatrix} V_{13} & V_{12} \\ V_{33} & V_{32} \end{vmatrix} & \begin{vmatrix} V_{12} & V_{13} \\ V_{22} & V_{23} \end{vmatrix} \\ \begin{vmatrix} V_{23} & V_{21} \\ V_{33} & V_{31} \end{vmatrix} & \begin{vmatrix} V_{11} & V_{13} \\ V_{31} & V_{33} \end{vmatrix} & \begin{vmatrix} V_{13} & V_{11} \\ V_{23} & V21 \end{vmatrix} \\ \begin{vmatrix} V_{21} & V_{22} \\ V_{31} & V_{32} \end{vmatrix} & \begin{vmatrix} V_{12} & V_{11} \\ V_{32} & V_{31} \end{vmatrix} & \begin{vmatrix} V_{11} & V_{12} \\ V_{21} & V_{22} \end{vmatrix} \end{bmatrix} \Rightarrow$$

$$V_{ij}^{-1} = \frac{1}{|V_{ij}|}\begin{bmatrix} V_{22}\cdot V_{33} - V_{23}^2 & V_{13}\cdot V_{32} - V_{12}\cdot V_{33} & V_{12}\cdot V_{23} - V_{13}\cdot V_{22} \\ V_{23}\cdot V_{31} - V_{21}\cdot V_{33} & V_{11}\cdot V_{33} - V_{13}^2 & V_{13}\cdot V_{21} - V_{11}\cdot V_{23} \\ V_{21}\cdot V_{32} - V_{22}\cdot V_{31} & V_{12}\cdot V_{31} - V_{11}\cdot V_{32} & V_{11}\cdot V_{22} - V_{12}^2 \end{bmatrix}$$

The uncertainty in the weighted average value is calculated by equation C.3:

$$(\delta\sigma)^2 = W\cdot V\cdot W^{\intercal} \Rightarrow (\delta\sigma)^2 = \begin{bmatrix} w_1 & w_2 & w_3 \end{bmatrix}\begin{bmatrix} V_{11} & V_{12} & V_{13} \\ V_{21} & V_{22} & V_{23} \\ V_{31} & V_{32} & V_{33} \end{bmatrix}\begin{bmatrix} w_1 \\ w_2 \\ w_3 \end{bmatrix} \Rightarrow$$

$$\begin{aligned}(\delta\sigma)^2 = w_1\cdot(w_1V_{11} + w_2V_{21} + w_3V_{31}) + w_2\cdot(w_1V_{12} + w_2V_{22} + w_3V_{32}) \\ + w_3\cdot(w_1V_{13} + w_2V_{23} + w_3V_{33})\end{aligned} \quad \text{(C.3)}$$

Therefore, in order to calculate the weighted average cross section and its corresponding uncertainty, the only thing that needs to be calculated is the V_{ij} covariance matrix.

Following equation (27) reported in Ref. [61], the V_{ij} elements of the covariance matrix for the weighted average cross-section value (following equation 4.1) are calculated using the equation C.4:

$$\begin{aligned} V_{ij} &= \mathrm{cov}\,(\sigma_1, \sigma_2) \\ &= \left(\frac{\partial\sigma}{\partial\sigma_{ref}}\right)_i \mathrm{cov}\left(\sigma_{ref,i}, \sigma_{ref,j}\right)\left(\frac{\partial\sigma}{\partial\sigma_{ref}}\right)_j + \\ &+ \left(\frac{\partial\sigma}{\partial N_{\gamma,tar}}\right)_i \mathrm{cov}\left(N_{\gamma,tar,i}, N_{\gamma,tar,j}\right)\left(\frac{\partial\sigma}{\partial N_{\gamma,tar}}\right)_j + \\ &+ \left(\frac{\partial\sigma}{\partial N_{\gamma,ref}}\right)_i \mathrm{cov}\left(N_{\gamma,ref,i}, N_{\gamma,ref,j}\right)\left(\frac{\partial\sigma}{\partial N_{\gamma,ref}}\right)_j + \\ &+ \left(\frac{\partial\sigma}{\partial\varepsilon_{ref}}\right)_i \mathrm{cov}\left(\varepsilon_{ref,i}, \varepsilon_{ref,j}\right)\left(\frac{\partial\sigma}{\partial\varepsilon_{ref}}\right)_j + \end{aligned}$$

$$
\begin{aligned}
&+ \left(\frac{\partial\sigma}{N_{t,ref}}\right)_i \operatorname{cov}\left(N_{t,ref,i}, N_{t,ref,j}\right) \left(\frac{\partial\sigma}{N_{t,ref}}\right)_j + \\
&+ \left(\frac{\partial\sigma}{\partial N_{t,tar}}\right)_i \operatorname{cov}\left(N_{t,tar,i}, N_{t_tar_j}\right) \left(\frac{\partial\sigma}{\partial N_{t,tar}}\right)_j + + \\
&+ \left(\frac{\partial\sigma}{\partial\varepsilon_{tar}}\right)_i \operatorname{cov}\left(\varepsilon_{tar,i}, \varepsilon_{tar_j}\right) \left(\frac{\partial\sigma}{\partial\varepsilon_{tar}}\right)_j \\
&+ \left(\frac{\partial\sigma}{\partial I_{\gamma,tar}}\right)_1 \operatorname{cov}\left(I_{\gamma,tar,i}, I_{\gamma,tar_j}\right) \left(\frac{\partial\sigma}{\partial I_{\gamma,tar}}\right)_j + \\
&+ \left(\frac{\partial\sigma}{\partial I_{\gamma,ref}}\right)_i \operatorname{cov}\left(I_{\gamma,ref,i}, I_{\gamma,ref_j}\right) \left(\frac{\partial\sigma}{\partial I_{\gamma,ref}}\right)_j
\end{aligned} \tag{C.4}
$$

As presented in equation C.3, the covariance between the σ_1 and σ_2 values depends on the covariance between the different factors of equation 4.1. These covariances for each "i" and "j" measurement are:

- $\boxed{\operatorname{cov}\left(\sigma_{ref,i}, \sigma_{ref,j}\right)}$
  The reference cross-section value is the same for both measurements. Therefore:
  $$\operatorname{cov}\left(\sigma_{ref,i}, \sigma_{ref,j}\right) = (\delta\sigma)_i^2 = (\delta\sigma)_j^2 = (\delta\sigma)^2$$

- $\boxed{\operatorname{cov}\left(N_{\gamma,tar,i}, N_{\gamma,tar,j}\right) = 0}$
  The integrals of the two different γ-rays used for the calculation of the two different cross-section values σ_i and σ_j are considered to be fully uncorrelated.

- $\boxed{\operatorname{cov}\left(N_{\gamma,ref,i}, N_{\gamma,ref,j}\right)}$
  The γ-ray peak integral for the reference target is the same for both measurements. Therefore:
  $$\operatorname{cov}\left(N_{\gamma,tar,i}, N_{\gamma,tar,j}\right) = \left(\delta N_{\gamma,ref}\right)_i^2 = \left(\delta N_{\gamma,ref}\right)_j^2 = \left(\delta N_{\gamma,ref}\right)^2$$

- $\boxed{\operatorname{cov}\left(\varepsilon_{ref,i}, \varepsilon_{ref,j}\right)}$
  For the same reason mentioned previously:
  $$\operatorname{cov}\left(\varepsilon_{ref,i}, \varepsilon_{ref,j}\right) = (\delta\varepsilon_{ref})_i^2 = (\delta\varepsilon_{ref})_j^2 (\delta\varepsilon_{ref})^2$$

- $\boxed{\operatorname{cov}\left(N_{t,ref,i}, N_{t,ref,j}\right)}$
  Following the same logic:
  $$\operatorname{cov}\left(N_{t,ref,i}, N_{t,ref,j}\right) = \left(\delta N_{t,ref}\right)_i^2 = \left(\delta N_{t,ref}\right)_j^2 = \left(\delta N_{t,ref}\right)^2$$

- $\boxed{\mathrm{cov}\left(N_{t,tar,i}, N_{t,tar,j}\right)}$
  Similarly:

$$\mathrm{cov}\left(N_{t,tar,i}, N_{t,tar,j}\right) = \left(\delta N_{t,tar}\right)_i^2 = \left(\delta N_{t,tar}\right)_j^2 = \left(\delta N_{t,tar}\right)^2$$

- $\boxed{\mathrm{cov}\left(I_{\gamma,tar,i}, I_{\gamma,tar_j}\right) = 0}$
  The intensities of the two different γ-rays used for the calculation of the two different cross-section values σ_i and σ_j are considered to be fully uncorrelated.

- $\boxed{\mathrm{cov}\left(I_{\gamma,ref,i}, I_{\gamma,ref_j}\right)}$
  For the same reasons as mentioned above:

$$\mathrm{cov}\left(I_{\gamma,ref,i}, I_{\gamma,ref_j}\right) = \left(\delta I_{\gamma,ref,i}\right)^2 = \left(\delta I_{\gamma,ref,j}\right)^2 = \left(\delta I_{\gamma,ref}\right)^2$$

- $\boxed{\mathrm{cov}\left(\varepsilon_{tar,i}, \varepsilon_{tar_j}\right)}$
  The two efficiency values corresponding to the two-at-the-time different γ-ray energies (E_1, E_2) are correlated, since they are calculated from a fitting process in the experimental efficiency points (Figure 3.18). The fitting function used, is the one proposed by IAEA [8]:

$$\varepsilon(E) = A_0 + \frac{A_1}{E} + \frac{A_2}{E^2} + \frac{A_3}{E^3} \tag{C.5}$$

  Once again, following the formalism of equations (37) and (38) used in Ref. [61] the covariance between the two efficiency points for γ-ray energies E_1 and E_2 is:

$$\begin{aligned}
\mathrm{cov}(\varepsilon(E_1), \varepsilon(E_2)) = &\left(\frac{\partial\varepsilon}{\partial A_0}\right)_{E_1}\left(\frac{\partial\varepsilon}{\partial A_0}\right)_{E_2}\delta A_0^2 + \\
&+\left(\frac{\partial\varepsilon}{\partial A_1}\right)_{E_1}\left(\frac{\partial\varepsilon}{\partial A_1}\right)_{E_2}\delta A_1^2 + \\
&+\left(\frac{\partial\varepsilon}{\partial A_2}\right)_{E_1}\left(\frac{\partial\varepsilon}{\partial A_2}\right)_{E_2}\delta A_2^2 + \\
&+\left(\frac{\partial\varepsilon}{\partial A_3}\right)_{E_1}\left(\frac{\partial\varepsilon}{\partial A_3}\right)_{E_2}\delta A_3^2 + \\
+\left(\frac{\partial\varepsilon}{\partial A_0}\right)_{E_1}&\left(\frac{\partial\varepsilon}{\partial A_1}\right)_{E_2}\mathrm{cov}(A_0, A_1) + \\
+\left(\frac{\partial\varepsilon}{\partial A_0}\right)_{E_1}&\left(\frac{\partial\varepsilon}{\partial A_2}\right)_{E_2}\mathrm{cov}(A_0, A_2) +
\end{aligned}$$

$$
\begin{aligned}
&+\left(\frac{\partial \varepsilon}{\partial \mathrm{A}_0}\right)_{\mathrm{E}_1}\left(\frac{\partial \varepsilon}{\partial \mathrm{A}_3}\right)_{\mathrm{E}_2}\operatorname{cov}(\mathrm{A}_0,\mathrm{A}_3)+\\
&+\left(\frac{\partial \varepsilon}{\partial \mathrm{A}_1}\right)_{\mathrm{E}_1}\left(\frac{\partial \varepsilon}{\partial \mathrm{A}_2}\right)_{\mathrm{E}_2}\operatorname{cov}(\mathrm{A}_1,\mathrm{A}_2)+\\
&+\left(\frac{\partial \varepsilon}{\partial \mathrm{A}_1}\right)_{\mathrm{E}_1}\left(\frac{\partial \varepsilon}{\partial \mathrm{A}_3}\right)_{\mathrm{E}_2}\operatorname{cov}(\mathrm{A}_1,\mathrm{A}_3)+\\
&+\left(\frac{\partial \varepsilon}{\partial \mathrm{A}_2}\right)_{\mathrm{E}_1}\left(\frac{\partial \varepsilon}{\partial \mathrm{A}_3}\right)_{\mathrm{E}_2}\operatorname{cov}(\mathrm{A}_2,\mathrm{A}_3)+\\
&+\left(\frac{\partial \varepsilon}{\partial \mathrm{A}_0}\right)_{\mathrm{E}_2}\left(\frac{\partial \varepsilon}{\partial \mathrm{A}_1}\right)_{\mathrm{E}_1}\operatorname{cov}(\mathrm{A}_0,\mathrm{A}_1)+\\
&+\left(\frac{\partial \varepsilon}{\partial \mathrm{A}_0}\right)_{\mathrm{E}_2}\left(\frac{\partial \varepsilon}{\partial \mathrm{A}_2}\right)_{\mathrm{E}_1}\operatorname{cov}(\mathrm{A}_0,\mathrm{A}_2)+\\
&+\left(\frac{\partial \varepsilon}{\partial \mathrm{A}_0}\right)_{\mathrm{E}_2}\left(\frac{\partial \varepsilon}{\partial \mathrm{A}_3}\right)_{\mathrm{E}_1}\operatorname{cov}(\mathrm{A}_0,\mathrm{A}_3)+\\
&+\left(\frac{\partial \varepsilon}{\partial \mathrm{A}_1}\right)_{\mathrm{E}_2}\left(\frac{\partial \varepsilon}{\partial \mathrm{A}_2}\right)_{\mathrm{E}_1}\operatorname{cov}(\mathrm{A}_1,\mathrm{A}_2)+\\
&+\left(\frac{\partial \varepsilon}{\partial \mathrm{A}_1}\right)_{\mathrm{E}_2}\left(\frac{\partial \varepsilon}{\partial \mathrm{A}_3}\right)_{\mathrm{E}_1}\operatorname{cov}(\mathrm{A}_1,\mathrm{A}_3)+\\
&+\left(\frac{\partial \varepsilon}{\partial \mathrm{A}_2}\right)_{\mathrm{E}_2}\left(\frac{\partial \varepsilon}{\partial \mathrm{A}_3}\right)_{\mathrm{E}_1}\operatorname{cov}(\mathrm{A}_2,\mathrm{A}_3)
\end{aligned}
\tag{C.6}
$$

Substituting the partial derivatives and taking into account equation C.5, equation C.6 becomes:

$$
\begin{aligned}
\operatorname{cov}\left(\varepsilon\left(\mathrm{E}_1\right),\varepsilon(\,\mathrm{E}_2\,)\right) = 1\cdot 1\cdot \delta\mathrm{A}_0^2+&\\
+\frac{1}{\mathrm{E}_1}\cdot\frac{1}{\mathrm{E}_2}\cdot\delta\mathrm{A}_1^2+&\\
+\frac{1}{\mathrm{E}_1^2}\cdot\frac{1}{\mathrm{E}_2^2}\cdot\delta\mathrm{A}_2^2+&\\
+\frac{1}{\mathrm{E}_1^3}\cdot\frac{1}{\mathrm{E}_2^3}\cdot\delta\mathrm{A}_3^2+&\\
+1\cdot\frac{1}{\mathrm{E}_2}\cdot\operatorname{cov}\left(\mathrm{A}_0,\mathrm{A}_1\right)+&\\
+1\cdot\frac{1}{\mathrm{E}_2^2}\cdot\operatorname{cov}\left(\mathrm{A}_0,\mathrm{A}_2\right)+&\\
+1\cdot\frac{1}{\mathrm{E}_2^3}\cdot\operatorname{cov}\left(\mathrm{A}_0,\mathrm{A}_3\right)+&\\
+\frac{1}{\mathrm{E}_1}\cdot\frac{1}{\mathrm{E}_2^2}\cdot\operatorname{cov}\left(\mathrm{A}_1,\mathrm{A}_2\right)+&
\end{aligned}
$$

$$
\begin{aligned}
&+\frac{1}{E_1}\cdot\frac{1}{E_2^3}\cdot \mathrm{cov}\left(A_1, A_3\right) + \\
&+\frac{1}{E_1^2}\cdot\frac{1}{E_2^3}\cdot \mathrm{cov}\left(A_2, A_3\right) + \\
&+1\cdot\frac{1}{E_1}\cdot \mathrm{cov}\left(A_0, A_1\right) + \\
&+1\cdot\frac{1}{E_1^2}\cdot \mathrm{cov}\left(A_0, A_2\right) + \\
&+1\cdot\frac{1}{E_1^3}\cdot \mathrm{cov}\left(A_0, A_3\right) + \\
&+\frac{1}{E_2}\cdot\frac{1}{E_1^2}\cdot \mathrm{cov}\left(A_1, A_2\right) + \\
&+\frac{1}{E_2}\cdot\frac{1}{E_1^3}\cdot \mathrm{cov}\left(A_1, A_3\right) + \\
&+\frac{1}{E_2^2}\cdot\frac{1}{E_1^3}\cdot \mathrm{cov}\left(A_2, A_3\right)
\end{aligned}
\tag{C.7}
$$

, that can be rewritten as:

$$
\begin{aligned}
\mathrm{cov}\left(\varepsilon\left(E_1\right), \varepsilon\left(E_2\right)\right) = \delta A_0^2 &+ \frac{\delta A_1^2}{E_1 E_2} + \frac{\delta A_2^2}{\left(E_1 E_2\right)^2} + \frac{\delta A_3^2}{\left(E_1 E_2\right)^3} + \\
&+ \mathrm{cov}\left(A_0, A_1\right)\cdot\left(\frac{E_1 + E_2}{E_1 E_2}\right) + \\
&+ \mathrm{cov}\left(A_0, A_2\right)\cdot\left(\frac{E_1^2 + E_2^2}{\left(E_1 E_2\right)^2}\right) + \\
&+ \mathrm{cov}\left(A_0, A_3\right)\cdot\left(\frac{E_1^3 + E_2^3}{\left(E_1 E_2\right)^3}\right) + \\
&+ \mathrm{cov}\left(A_1, A_2\right)\cdot\left(\frac{E_1 + E_2}{\left(E_1 E_2\right)^2}\right) + \\
&+ \mathrm{cov}\left(A_1, A_3\right)\cdot\left(\frac{E_1^2 + E_2^2}{\left(E_1 E_2\right)^3}\right) + \\
&+ \mathrm{cov}\left(A_2, A_3\right)\cdot\left(\frac{E_1 + E_2}{\left(E_1 E_2\right)^3}\right)
\end{aligned}
\tag{C.8}
$$

The covariances $\mathrm{cov}\left(A_i, A_j\right)$ for $i, j = 1, 2, 3$ are provided from the fitting software used

To sum up, the covariance matrix elements can be calculated using equation C.9:

$$
\begin{aligned}
V_{ij} = & \frac{\sigma_i}{\sigma_{ref}} \cdot (\delta\sigma)^2 \cdot \frac{\sigma_j}{\sigma_{ref}} + \\
& + \frac{\sigma_i}{N_{\gamma,ref}} \cdot \left(\delta N_{\gamma,ref}\right)^2 \cdot \frac{\sigma_j}{N_{\gamma,ref}} + \\
& + \frac{\sigma_i}{\varepsilon(E_i)_{tar}} \cdot \mathrm{cov}\left(\varepsilon(E_i), \varepsilon(E_j)\right) \cdot \frac{\sigma_j}{\varepsilon\left(E_j\right)_{tar}} + \\
& + \frac{\sigma_i}{\varepsilon_{tar}} \cdot (\delta\varepsilon_{ref})^2 \cdot \frac{\sigma_j}{\varepsilon_{ref}} + \\
& + \frac{\sigma_i}{N_{t,tar}} \cdot \left(\delta N_{t,tar}\right)^2 \cdot \frac{\sigma_j}{N_{t,tar}} + \\
& + \frac{\sigma_i}{N_{t,ref}} \cdot \left(\delta N_{t,ref}\right)^2 \cdot \frac{\sigma_j}{N_{t,ref}}
\end{aligned}
\tag{C.9}
$$

Bibliography

[1] M. Herman et al. “EMPIRE: Nuclear Reaction Model Code System for Data Evaluation”. In: Nuclear Data Sheets 108.12 (2007). Special Issue on Evaluations of Neutron Cross Sections, pp. 2655–2715. issn: 0090-3752. doi: https://doi.org/10.1016/j.nds.2007.11.003. url: https://www.sciencedirect.com/science/article/pii/S0090375207000981.

[2] Evert Birgersson and Göran Lövestam. NeuSDesc-Neutron Source Description Software Manual. Tech. rep. 2009. url: http://www.jrc.ec.europa.eu/.

[3] Birgersson Evert and L. Goeran. “NeuSDesc-Neutron Source Description Software Manual”. In: Technical Report, EUR 23794 EN (European Comission) (2009).

[4] X-5 Monte Carlo team. “MCNP - A General Monte Carlo N-Particle Transport Code, version 5”. In: LA-UR-03-1987 (Apr. 2005).

[5] Ziegler James F. and Jochen P. Biersack. “SRIM-2008, Stopping Power and Range of Ions in Matter”. In: Nuclear Energy Agency of the OECD (NEA) (May 2008). url: http://inis.iaea.org/search/search.aspx?orig_q=RN:40107606.

[6] Antigoni Kalamara. “Neutron induced reactions on Ir and Au and production of isomeric states”. PhD thesis. Applied Mathematical and Physical Sciences - National Technical University of Athens, 2019.

[7] Philip R Bevington and D Keith Robinson. Data reduction and error analysis for the physical sciences; 3rd ed. New York, NY: McGraw-Hill, 2003. url: https://cds.cern.ch/record/1305448.

[8] Development of a Reference Database for Particle Induced Gamma Ray Emission (PIGE) Spectroscopy. TECDOC Series 1822. Vienna: INTERNATIONAL ATOMIC ENERGY AGENCY, 2017. isbn: 978-92-0-106317-5. url: https://www.iaea.org/publications/12235/development-

of-a-reference-database-for-particle-induced-gamma-ray-emission-pige-spectroscopy.

[9] C.D. Nesaraja. "Nuclear Data Sheets for A=69". In: Nuclear Data Sheets 115 (2014), pp. 1–134. issn: 0090-3752. doi: https://doi.org/10.1016/j.nds.2013.12.001. url: https://www.sciencedirect.com/science/article/pii/S0090375213000938.

[10] D. Abriola and A.A. Sonzogni. "Nuclear Data Sheets for A = 72". In: Nuclear Data Sheets 111.1 (2010), pp. 1–140. issn: 0090-3752. doi: https://doi.org/10.1016/j.nds.2009.12.001. url: https://www.sciencedirect.com/science/article/pii/S0090375209001136.

[11] Balraj Singh and Jun Chen. "Nuclear Data Sheets for A=73". In: Nuclear Data Sheets 158 (2019), pp. 1–257. issn: 0090-3752. doi: https://doi.org/10.1016/j.nds.2019.02.006. url: https://www.sciencedirect.com/science/article/pii/S0090375219300195.

[12] Balraj Singh and Jun Chen. "Nuclear Structure and Decay Data for A=71 Isobars". In: Nuclear Data Sheets 188 (2023), pp. 1–341. issn: 0090-3752. doi: https://doi.org/10.1016/j.nds.2023.02.001. url: https://www.sciencedirect.com/science/article/pii/S0090375223000200.

[13] Alexandru Negret and Balraj Singh. "Nuclear Data Sheets for A = 75". In: Nuclear Data Sheets 114.8 (2013), pp. 841–1040. issn: 0090-3752. doi: https://doi.org/10.1016/j.nds.2013.08.001. url: https://www.sciencedirect.com/science/article/pii/S0090375213000537.

[14] M. Shamsuzzoha Basunia and Anagha Chakraborty. "Nuclear Data Sheets for A=24". In: Nuclear Data Sheets 186 (2022), pp. 3–262. issn: 0090-3752. doi: https://doi.org/10.1016/j.nds.2022.11.002. url: https://www.sciencedirect.com/science/article/pii/S0090375222000576.

[15] Huang Xiaolong. "Nuclear Data Sheets for A = 196". In: Nuclear Data Sheets 108.6 (2007), pp. 1093–1286. issn: 0090-3752. doi: https://doi.org/10.1016/j.nds.2007.05.001. url: https://www.sciencedirect.com/science/article/pii/S0090375207000488.

[16] D. A. Brown et al. "ENDF/B-VIII.0: The 8th Major Release of the Nuclear Reaction Data Library with CIELO-project Cross Sections, New Standards and Thermal Scattering Data". In: Nuclear Data Sheets 148 (Feb. 2018), pp. 1–142. issn: 00903752. doi: 10.1016/j.nds.2018.02.001.

[17] J. Theuerkauf et al. "Program Tv". In: (1993). url: https://www.ikp.uni-koeln.de/~fitz/viewspectra/viewspectra.html.

[18] N. Otuka et al. “Towards a More Complete and Accurate Experimental Nuclear Reaction Data Library (EXFOR): International Collaboration Between Nuclear Reaction Data Centres (NRDC)”. In: Nuclear Data Sheets 120 (2014), pp. 272–276. issn: 0090-3752. doi: https://doi.org/10.1016/j.nds.2014.07.065. url: https://www.sciencedirect.com/science/article/pii/S0090375214005171.

[19] Zhong-Sheng Pu, Guan Qiu-Yun, and Dong Yan. “Cross section measurements for (n,2n), (n,p) and (n,alpha) reactions on germanium isotopes at the neutron energy around 14MeV”. In: High Energy Physics and Nuclear Physics -Beijing- 30 (2006), pp. 1171–1174.

[20] Changlin Lan et al. “Measurement of cross sections for (n, 2n), (n, p) and (n, α) reactions on germanium isotopes induced by 14MeV neutrons”. In: Annals of Nuclear Energy 35.11 (2008), pp. 2105–2108. issn: 0306-4549. doi: https://doi.org/10.1016/j.anucene.2008.05.009. url: https://www.sciencedirect.com/science/article/pii/S0306454908001552.

[21] H. M. Hoang et al. “Energy dependence of the isotopic effect in the (n,p) reaction on the germanium isotopes”. In: Zeitschrift für Physik A Hadrons and Nuclei 342.3 (Sept. 1992), pp. 283–290. issn: 09397922. doi: 10.1007/BF01291511. url: https://link.springer.com/article/10.1007/BF01291511.

[22] Chikara Konno et al. Activation cross section measurements at neutron energy from 13.3 to 14.9MeV using the FNS facility. 1993.

[23] E. Steiner et al. “(n, 2n)-Querschnitte und Isomer-Querschnittsverhaltnisse von 76Ge und 165Ho im Energiebereich von 12, 5 bis 18, 5 MeV”. In: Helv.Phys.Acta 43 (1970), p. 17.

[24] S. Chasapoglou et al. “On the accuracy of cross-section measurements of neutron-induced reactions using the activation technique with natural targets: The case of Ge at En=17.9 MeV”. In: Applied Radiation and Isotopes 203 (2024), p. 111077. issn: 0969-8043. doi: https://doi.org/10.1016/j.apradiso.2023.111077. url: https://www.sciencedirect.com/science/article/pii/S096980432300430X.

[25] A.J. Koning et al. “TENDL: Complete Nuclear Data Library for Innovative Nuclear Science and Technology”. In: Nuclear Data Sheets 155 (2019). Special Issue on Nuclear Reaction Data, pp. 1–55. issn: 0090-3752. doi: https://doi.org/10.1016/j.nds.2019.01.002. url: https://www.sciencedirect.com/science/article/pii/S009037521930002X.

[26] Osamu Iwamoto, Nobuyuki Iwamoto, Satoshi Kunieda, Futoshi Minato, Shinsuke Nakayama, Yutaka Abe, Kohsuke Tsubakihara, Shin Okumura, Chikako Ishizuka, Tadashi Yoshida, Satoshi Chiba, Naohiko Otuka, Jean-Christophe Sublet, Hiroki Iwamoto, Kazuyoshi Yamamoto, Yasunobu Nagaya, Kenichi Tada, Chikara Konno, Norihiro Matsuda, Kenji Yokoyama, Hiroshi Taninaka, Akito Oizumi, Masahiro

Fukushima, Shoichiro Okita, Go Chiba, Satoshi Sato, Masayuki Ohta and Saerom Kwon. “Japanese evaluated nuclear data library version 5: JENDL-5”. In: Journal of Nuclear Science and Technology 60.1 (2023), pp. 1–60. doi: 10.1080/00223131.2022.2141903. eprint: https://doi.org/10.1080/00223131.2022.2141903. url: https://doi.org/10.1080/00223131.2022.2141903.

[27] A J M Plompen et al. “The joint evaluated fission and fusion nuclear data library, JEFF-3.3”. In: The European Physical Journal A 56.7 (July 2020), p. 181.

[28] J.-Ch Sublet et al. EASY Documentation Series The European Activation File: EAF-2010 neutron-induced cross section library. Tech. rep. 2010.

[29] Arjan Koning et al. JEFF Report 21: The JEFF-3.1 Nuclear Data Library. Jan. 2006. isbn: 92-64-02314-3.

[30] G. Zhigang et al. “CENDL-3.2: The new version of Chinese general purpose evaluated nuclear data library”. In: EPJ Web Conf. 239 (2020), p. 09001. doi: 10.1051/epjconf/202023909001. url: https://doi.org/10.1051/epjconf/202023909001.

[31] RA Forrest et al. “FENDL-3 Library–Summary documentation”. In: INDC (NDS)-628, IAEA Nuclear Data Section (Jan. 2012).

[32] Keiichi Shibata et al. “Japanese Evaluated Nuclear Data Library Version 3 Revision-3: JENDL-3.3”. In: Journal of Nuclear Science and Technology 39.11 (2002), pp. 1125–1136. doi: 10.1080/18811248.2002.9715303. eprint: https://doi.org/10.1080/18811248.2002.9715303. url: https://doi.org/10.1080/18811248.2002.9715303.

[33] A.J. Koning et al. “TENDL: Complete Nuclear Data Library for Innovative Nuclear Science and Technology”. In: Nuclear Data Sheets 155 (2019). Special Issue on Nuclear Reaction Data, pp. 1–55. issn: 0090-3752. doi: https://doi.org/10.1016/j.nds.2019.01.002. url: https://www.sciencedirect.com/science/article/pii/S009037521930002X.

[34] Walter Hauser and Herman Feshbach. “The Inelastic Scattering of Neutrons”. In: Phys. Rev. 87 (2 July 1952), pp. 366–373. doi: 10.1103/PhysRev.87.366. url: https://link.aps.org/doi/10.1103/PhysRev.87.366.

[35] J. Raynal. “Technical Report No. SMR-9/8”. IAEA (unpublished).

[36] J. Raynal. “Computing as a language of physics. ICTP International Seminar Course”. (IAEA, ICTP, Trieste, Italy, 1972), p. 281.

[37] H. A. Bethe. “Nuclear Physics B. Nuclear Dynamics, Theoretical”. In: Rev. Mod. Phys. 9 (2 Apr. 1937), pp. 69–244. doi: 10.1103/RevModPhys.9.69. url: https://link.aps.org/doi/10.1103/RevModPhys.9.69.

[38] A. Gilbert and A. G. W. Cameron. “A COMPOSITE NUCLEAR-LEVEL DENSITY FORMULA WITH SHELL CORRECTIONS”. In: Canadian Journal of Physics 43.8 (1965), pp. 1446–1496. doi: 10.1139/p65-139. eprint: https://doi.org/10.1139/p65-139. url: https://doi.org/10.1139/p65-139.

[39] A V Ignatyuk, K K Istekov, and G N Smirenkin. “Role of collective effects in the systematics of nuclear level densities”. In: Sov. J. Nucl. Phys. (Engl. Transl.); (United States) 29 (Apr. 1979). url: https://www.osti.gov/biblio/5770504.

[40] A. V. Ignatyuk et al. “Density of discrete levels in ^{116}Sn”. In: Phys. Rev. C 47 (4 Apr. 1993), pp. 1504–1513. doi: 10.1103/PhysRevC.47.1504. url: https://link.aps.org/doi/10.1103/PhysRevC.47.1504.

[41] A D’Arrigo et al. “Semi-empirical determination of the shell correction temperature and spin dependence by means of nuclear fission”. In: Journal of Physics G: Nuclear and Particle Physics 20.2 (Feb. 1994), p. 365. doi: 10.1088/0954-3899/20/2/015. url: https://dx.doi.org/10.1088/0954-3899/20/2/015.

[42] T. Tamura, T. Udagawa, and H. Lenske. “Multistep direct reaction analysis of continuum spectra in reactions induced by light ions”. In: Phys. Rev. C 26 (2 Aug. 1982), pp. 379–404. doi: 10.1103/PhysRevC.26.379. url: https://link.aps.org/doi/10.1103/PhysRevC.26.379.

[43] H Nishioka et al. “Statistical theory of precompound reactions: The multistep compound process”. In: Annals of Physics 172.1 (1986), pp. 67–99. issn: 0003-4916. doi: https://doi.org/10.1016/0003-4916(86)90020-5. url: https://www.sciencedirect.com/science/article/pii/0003491686900205.

[44] J. J. Griffin. “Statistical Model of Intermediate Structure”. In: Phys. Rev. Lett. 17 (9 Aug. 1966), pp. 478–481. doi: 10.1103/PhysRevLett.17.478. url: https://link.aps.org/doi/10.1103/PhysRevLett.17.478.

[45] J.J. Griffin. “Energy dependence of average direct reaction cross sections and partial nuclear level densities”. In: Physics Letters B 24.1 (1967), pp. 5–7. issn: 0370-2693. doi: https://doi.org/10.1016/0370-2693(67)90319-X. url: https://www.sciencedirect.com/science/article/pii/037026936790319X.

[46] B. Morillon and P. Romain. “Bound single-particle states and scattering of nucleons on spherical nuclei with a global optical model”. In: Phys. Rev. C 76 (4 Oct. 2007), p. 044601. doi: 10.1103/PhysRevC.76.044601. url: https://link.aps.org/doi/10.1103/PhysRevC.76.044601.

[47] A.J. Koning and J.P. Delaroche. “Local and global nucleon optical models from 1 keV to 200 MeV”. In: Nuclear Physics A 713.3 (2003), pp. 231–310. issn: 0375-9474. doi: https://doi.org/10.1016/S0375-9474(02)01321-0. url: https://www.sciencedirect.com/science/article/pii/S0375947402013210.

[48] R. Vlastou et al. “Neutron induced reactions at the Athens Tandem Accelerator NCSR ”Demokritos””. In: Journal of Radioanalytical and Nuclear Chemistry 272.2 (2007), pp. 219–222. issn: 02365731. doi: 10.1007/s10967-007-0503-8.

[49] V. Avrigeanu, P. E. Hodgson, and M. Avrigeanu. “Global optical potentials for emitted alpha particles”. In: Phys. Rev. C 49 (4 Apr. 1994), pp. 2136–2141. doi: 10.1103/PhysRevC.49.2136. url: https://link.aps.org/doi/10.1103/PhysRevC.49.2136.

[50] url: https://nmi3.eu/neutron-research/techniques-for-/chemical-analysis.html.

[51] url: https://en.irsn.fr/EN/Research/Scientific-tools/experimental-facilities-means/GF-amande-facility/Pages/default.aspx.

[52] V. Gressier et al. “AMANDE: a new facility for monoenergetic neutron fields production between 2 keV and 20 MeV”. In: Radiation Protection Dosimetry 110.1-4 (Aug. 2004), pp. 49–52. issn: 0144-8420. doi: 10.1093/rpd/nch185. eprint: https://academic.oup.com/rpd/article-pdf/110/1-4/49/4529556/nch185.pdf. url: https://doi.org/10.1093/rpd/nch185.

[53] url: https://www.irsn.fr/savoir-comprendre/sante/amande.

[54] V. Lacoste. “Design of a new long counter for the determination of the neutron fluence reference values at the IRSN AMANDE facility”. In: Radiation Measurements 45.10 (2010). PROCEEDINGS OF THE 11TH SYMPOSIUM ON NEUTRON AND ION DOSIMETRY, pp. 1250–1253. issn: 1350-4487. doi: https://doi.org/10.1016/j.radmeas.2010.06.026. url: https://www.sciencedirect.com/science/article/pii/S1350448710002179.

[55] url: http://www.inp.demokritos.gr/.

[56] url: http://tandem.inp.demokritos.gr/index.html.

[57] url: https://www-nds.iaea.org/exfor/endf.htm.

[58] Glen Knoll. Radiation Detection and Measurement (4th ed.) Hoboken, NJ: John Wiley, 2010. isbn: 978-0-470-13148-0.

[59] P. Bossew. “A very long-term HPGe-background gamma spectrum”. In: Applied Radiation and Isotopes 62.4 (2005), pp. 635–644. issn: 0969-8043. doi: https://doi.org/10.1016/j.apradiso.2004.09.006. url: https://www.sciencedirect.com/science/article/pii/S0969804304005299.

[60] url: https://www.nndc.bnl.gov/nudat3/NuDatBandPlotServlet?nucleus=152Eu&unc=NDS.

[61] N. Otuka et al. “Uncertainty propagation in activation cross section measurements”. In: Radiation Physics and Chemistry 140 (Jan. 2017). doi: 10.1016/j.radphyschem.2017.01.013.

[62] Wolf Mannhart. “A Small Guide to Generating Covariances of Experimental Data (INDC(NDS)–0588)”. In: International Atomic Energy Agency (IAEA) (2011).

[63] Megha Bhike and W Tornow. “Total and isomeric-state cross sections for the 76 Ge(n,2n) 75 Ge reaction from threshold to 14.8 MeV”. In: Physical Review C 95 (2017), p. 54605. doi: 10.1103/PhysRevC.95.054605.

[64] M. Herman, A. Marcinkowski, and K. Stankiewicz. “A program for calculation of spectra and cross sections within the combined pre-equilibrium/ compound nucleus model of nuclear reactions”. In: Computer Physics Communications 33.4 (1984), pp. 373–398. issn: 0010-4655. doi: https://doi.org/10.1016/0010-4655(84)90144-9. url: https://www.sciencedirect.com/science/article/pii/0010465584901449.

[65] Changlin Lan et al. “Measurement of cross sections for (n, 2n), (n, p) and (n, α) reactions on germanium isotopes induced by 14MeV neutrons”. In: Annals of Nuclear Energy 35.11 (2008), pp. 2105–2108. issn: 0306-4549. doi: https://doi.org/10.1016/j.anucene.2008.05.009. url: https://www.sciencedirect.com/science/article/pii/S0306454908001552.

[66] Md Shuza Uddin. In: Radiochimica Acta 110.1 (2022), pp. 1–7. doi: doi:10.1515/ract-2021-1085. url: https://doi.org/10.1515/ract-2021-1085.

[67] Kenneth S Krane. Introductory nuclear physics. New York, NY: Wiley, 1988. url: https://cds.cern.ch/record/359790.

[68] E. Soukhovitskii et al. “Technical report, JAERI-Data/Code 2004-002”. Japan Atomic Energy Research Institute (unpublished).

[69] E. Soukhovitskii et al. “Technical Report No. JAERI-Data/Code 2005-002”. Japan Atomic Energy Research Institute (unpublished).

[70] E. Soukhovitskii et al. “Technical report, JAERI-Data/Code 2008-025”. Japan Atomic Energy Research Institute (unpublished).

[71] R. Capote et al. “RIPL – Reference Input Parameter Library for Calculation of Nuclear Reactions and Nuclear Data Evaluations”. In: Nuclear Data Sheets 110.12 (2009). Special Issue on Nuclear Reaction Data, pp. 3107–3214. issn: 0090-3752. doi: https://doi.org/10.1016/j.nds.2009.10.004. url: https://www.sciencedirect.com/science/article/pii/S0090375209000994.

[72] A.J. Koning and D. Rochman. “Modern Nuclear Data Evaluation with the TALYS Code System”. In: Nuclear Data Sheets 113.12 (2012). Special Issue on Nuclear Reaction Data, pp. 2841–2934. issn: 0090-3752. doi: https://doi.org/10.1016/j.nds.2012.11.002. url: https://www.sciencedirect.com/science/article/pii/S0090375212000889.

[73] Arjan Koning, Stephane Hilaire, and Stephane Goriely. “TALYS: modeling of nuclear reactions”. In: The European Physical Journal A 59.6 (June 2023), p. 131.

[74] C.K. Cline. “The Pauli exclusion principle in pre-equilibrium decay”. In: Nuclear Physics A 195.2 (1972), pp. 353–360. issn: 0375-9474. doi: https://doi.org/10.1016/0375-9474(72)91063-9. url: https://www.sciencedirect.com/science/article/pii/0375947472910639.

[75] F.C. Williams. “Intermediate state transition rates in the Griffin model”. In: Physics Letters B 31.4 (1970), pp. 184–186. issn: 0370-2693. doi: https://doi.org/10.1016/0370-2693(70)90097-3. url: https://www.sciencedirect.com/science/article/pii/0370269370900973.

[76] C.K. Cline and M. Blann. “The pre-equilibrium statistical model: Description of the nuclear equilibration process and parameterization of the model”. In: Nuclear Physics A 172.2 (1971), pp. 225–259. issn: 0375-9474. doi: https://doi.org/10.1016/0375-9474(71)90713-5. url: https://www.sciencedirect.com/science/article/pii/0375947471907135.

[77] A. V. Ignatyuk, G. N. Smirenkin, and A. S. Tishin. In: Sov. J. Nucl. Phys. 21 (1975), p. 255.

[78] A. Gilbert and A. G. W. Cameron. “A COMPOSITE NUCLEAR-LEVEL DENSITY FORMULA WITH SHELL CORRECTIONS”. In: Canadian Journal of Physics 43.8 (1965), pp. 1446–1496. doi: 10.1139/p65-139. eprint: https://doi.org/10.1139/p65-139. url: https://doi.org/10.1139/p65-139.

[79] S. Goriely, M. Samyn, and J. M. Pearson. “Further explorations of Skyrme-Hartree-Fock-Bogoliubov mass formulas. VII. Simultaneous fits to masses and fission barriers”. In: Phys. Rev. C 75 (6 June 2007), p. 064312. doi: 10.1103/PhysRevC.75.064312. url: https://link.aps.org/doi/10.1103/PhysRevC.75.064312.

[80] Haixia An and Chonghai Cai. “Global deuteron optical model potential for the energy range up to 183 MeV”. In: Phys. Rev. C 73 (5 May 2006), p. 054605. doi: 10.1103/PhysRevC.73.054605. url: https://link.aps.org/doi/10.1103/PhysRevC.73.054605.

[81] Jr. F.D.Becchetti and G.W.Greenlees. Annual Report. J.H.Williams Lab., Univ. Minnesota, 1969.

[82] Andrey Berlizov. “MCNP-CP: A Correlated Particle Radiation Source Extension of a General Purpose Monte Carlo N-Particle Transport Code”. In: vol. 945. Nov. 2006, pp. 183–194. isbn: 0-8412-3982-7. doi: 10.1021/bk-2007-0945.ch013.

[83] J. K. Tuli. Evaluated nuclear structure data file: A manual for preparation of data sets. Tech. rep. BNL-NCS–51655-Rev87. United States, 1987, p. 67. url: http://inis.iaea.org/search/search.aspx?orig_q=RN:19000921.

[84] E. Browne and J.K. Tuli. “Nuclear Data Sheets for A = 60”. In: Nuclear Data Sheets 114.12 (2013), pp. 1849–2022. issn: 0090-3752. doi: https://doi.org/10.1016/j.nds.2013.11.002. url: https://www.sciencedirect.com/science/article/pii/S0090375213000823.